Production and Sympathetic Cooling of Complex Molecular Ions

Inaugural-Dissertation

zur
Erlangung des Doktorgrades der
Mathematisch-Naturwissenschaftlichen Fakultät
der Heinrich-Heine-Universität Düsseldorf

vorgelegt von

Chaobo Zhang

aus Zhejiang, China

Mai 2008

Aus dem Institut für Experimentalphysik
der Heinrich-Heine-Universität Düsseldorf

Gedruckt mit der Genehmigung der
Mathematisch-Naturwissenschaftlichen Fakultät der
Heinrich-Heine-Universität Düsseldorf

Referent: Prof. S. Schiller, Ph.D.

Koreferent: Prof. Dr. T. Heinzel

Tag der mündlichen Prüfung: 24. Juni 2008

Abstract

This thesis reports on experimental and theoretical studies of the sympathetic cooling of complex molecular ions demonstrating that this general method for cooling atomic and molecular ions is reliable and efficient.

For this purpose, complex molecular ions and barium ions have been confined simultaneously in a linear Paul trap. The complex molecular ions are generated in an electrospray ionization system and transferred to the trap via a 2 m long octopole ion guide. These molecular ions are pre-cooled by room temperature helium buffer gas so that they can be captured by the trap. The atomic barium ions are loaded from a barium evaporator oven and are laser-cooled by a 493 nm cooling laser and a 650 nm repumping laser. Due to the mutual Coulomb interaction among these charged particles, the kinetic energy of the complex molecular ions can be reduced significantly.

In our experiments we have demonstrated the sympathetic cooling of various molecules (CO_2, Alexa Fluor 350, glycyrrhetinic acid, cytochrome c) covering a wide mass range from a few tens to 13000 amu. In every case the molecular ions could be cooled down to millikelvin temperatures.

Photo-chemical reactions of the $^{138}Ba^+$ ions in the $(^2P_{1/2})$ excited state with gases such as O_2, CO_2, or N_2O, could be observed. If the initial $^{138}Ba^+$ ion ensemble is cold, the produced $^{138}BaO^+$ ions are cold as well, with a similar temperature as the laser-cooled barium ions (a few tens of millikelvin). The back-reaction of $^{138}BaO^+$ ions with neutral CO to $^{138}Ba^+$ is possible and was observed in our experiments as well.

A powerful molecular dynamics (MD) simulation program has been developed. With this program dynamic properties of ion ensembles, such as sympathetic interactions or heating effects, have been investigated and experimental results have been analyzed to obtain, for example, ion numbers and temperatures. Additionally, the feasibility of nondestructive spectroscopy via an optical dipole excitation and the lineshape of rovibrational transitions of 1.4 and 5.1 μm have been studied.

Dedication

to my wife, Fanzhen Meng.

Contents

Abstract i

1 Introduction 1
1.1 Motivation . . . 1
1.2 Outline . . . 2

2 The linear radiofrequency (rf) trap 3
2.1 Trap types . . . 3
2.2 Trap theory of the linear Paul trap . . . 6
2.2.1 Quadrupole mass filter . . . 6
2.2.2 Longitudinal confinement . . . 7
2.2.3 Mathieu equations . . . 8
2.2.3.1 Solution to the Mathieu equations . . . 10
2.2.3.2 Stability diagrams . . . 10
2.2.4 Ion trajectories . . . 12
2.2.4.1 Secular motion . . . 13
2.2.4.2 Micromotion . . . 14
2.2.4.3 Rf heating . . . 15

3 Cooling of trapped ions 17
3.1 Laser cooling . . . 17
3.1.1 Doppler laser cooling . . . 18
3.1.1.1 Notation for the atom-laser interaction . . . 19
3.1.1.2 Basic theory of Doppler laser cooling . . . 21
3.1.1.3 Doppler cooling limit . . . 22
3.1.2 Doppler cooling of $^{138}Ba^{+}$ . . . 24
3.1.2.1 Barium element . . . 24
3.1.2.2 Transitions of $^{138}Ba^{+}$ . . . 25
3.1.2.3 Laser cooling of a three-level system . . . 26
3.1.2.4 Zeeman splitting . . . 27
3.2 Buffer gas cooling . . . 29
3.3 Sympathetic cooling . . . 30
3.3.1 Overview of sympathetic cooling . . . 30
3.3.2 Mass dependency of sympathetic cooling . . . 32

4 Experimental setup 39
4.1 Vacuum system . . . 39
4.1.1 Main vacuum chamber . . . 39
4.1.2 Differential vacuum system . . . 43
4.2 Ion trap . . . 44
4.2.1 Mechanical design . . . 44

4.2.2 Electrical power supplies . . . 44
4.2.2.1 Rf power supply . . . 45
4.2.2.2 DC power supply . . . 47
4.2.3 Magnetic field . . . 48
4.3 Ion sources . . . 48
4.3.1 Barium ion source . . . 48
4.3.2 Ions from background gas . . . 49
4.3.3 Complex molecular ion source - ESI . . . 49
4.3.3.1 Principles of ESI . . . 50
4.3.3.2 Advantages of ESI . . . 50
4.3.3.3 Structure of ESI . . . 51
4.3.3.4 Mass spectra . . . 52
4.3.3.5 Ion flux . . . 52
4.4 Transport of complex molecular ions . . . 53
4.4.1 Theoretical background of octopoles . . . 53
4.4.2 Structure of the octopole . . . 54
4.4.3 Octopole parameters . . . 55
4.5 Ion detection . . . 57
4.5.1 CEM . . . 57
4.5.2 CCD . . . 57
4.5.3 PMT . . . 58
4.6 Laser system . . . 59
4.6.1 The 650 nm laser - repumping laser . . . 60
4.6.2 The 493 nm laser - cooling laser . . . 61
4.6.3 Laser stabilization . . . 63

5 Preparation and properties of laser-cooled barium Coulomb crystals 65
5.1 Preparation of barium Coulomb crystals . . . 65
5.2 Laser detuning . . . 67
5.3 Secular frequency . . . 67
5.3.1 Radial secular excitation . . . 68
5.3.2 Axial secular excitation . . . 69
5.4 Trap parameters . . . 70
5.4.1 Ion confinement . . . 71
5.4.2 Compensation voltages . . . 72
5.5 Spatial distribution . . . 73
5.5.1 Axial spatial distribution . . . 73
5.5.2 Radial spatial distribution . . . 74
5.6 Lifetime of ion ensembles . . . 75

6 Chemical reactions of $^{138}Ba^{+}$ 77
6.1 Introduction . . . 77
6.2 Investigation of chemical reactions with He, N_2, and H_2 gases . . . 80
6.3 Chemical reaction with O_2 . . . 83
6.4 Chemical reaction with CO_2 . . . 87
6.5 Chemical reaction with N_2O . . . 91
6.6 Back-reaction with CO . . . 91

7 Sympathetic cooling of medium sized organic molecular ions 95
7.1 Loading of molecular ions . . . 95
7.2 Photofragmentation of Rhodamine ions . . . 99
7.3 Sympathetic cooling of Alexa Fluor 350 ions . . . 101
7.4 Sympathetic cooling of glycyrrhetinic acid ions . . . 108

8 Sympathetic cooling of proteins 115
8.1 Protein molecule - cytochrome c . . . 115
8.2 Loading of cyt c molecular ions . . . 117
8.3 Sympathetic cooling of cyt17 protein ions . . . 118
8.3.1 Simultaneous trapping of cyt17 and barium ions . . . 119
8.3.2 Evidences of the sympathetic cooling of cyt17 ions . . . 119
8.3.2.1 Ion extraction . . . 121
8.3.2.2 Visible evidence . . . 121
8.3.2.3 Secular excitation . . . 122
8.4 Temperature determination via MD simulations . . . 122
8.5 Sympathetic cooling of cyt12 ions . . . 126

9 Molecular dynamics simulations 129
9.1 Introduction . . . 129
9.2 Basic approach . . . 130
9.2.1 Equations of motion and forces . . . 130
9.2.2 Algorithms . . . 131
9.2.3 The leapfrog algorithm . . . 131
9.2.4 The velocity Verlet algorithm . . . 132
9.3 Time scales . . . 133
9.4 Initial conditions . . . 134
9.5 Simulation models . . . 136
9.5.1 Heating effects . . . 137
9.5.2 Modelling of heating effects . . . 140
9.5.3 Cooling model . . . 145
9.6 Simulation of CCD images . . . 147
9.7 Ion number and temperature determination . . . 148
9.7.1 Determination of ion numbers . . . 148
9.7.2 Sympathetic heating and cooling . . . 149
9.7.3 Temperature determination of laser-cooled ions . . . 151
9.7.4 Temperature determination of sympathetically cooled ions . . . 153
9.8 Advanced cooling of complex molecular ions . . . 154
9.9 Micromotion effect . . . 156
9.10 Ion diffusion . . . 157
9.11 Conclusion . . . 161

10 Simulation of secular excitation spectra 163
10.1 Introduction . . . 163
10.2 Model for the secular excitation . . . 166
10.3 Space charge effects . . . 166
10.3.1 Weak coupling . . . 168
10.3.2 Strong coupling . . . 168

10.4 Alternative model for the secular excitation 173

11 Simulation of nondestructive state-selective detection and spectroscopy 177
11.1 Optical dipole potential 179
11.2 Simulations of the optical excitation with different beam configurations . 181
11.2.1 Modulated single beam case 181
11.2.2 Standing-wave case 184
11.2.2.1 Intensity modulation 184
11.2.2.2 Frequency detuning of one individual beam 185
11.3 Conclusion of the optical dipole excitation 189
11.4 Simulation of HD^+ vibrational spectroscopy 190
11.5 Conclusion of the simulations of the spectroscopy 194

12 Summary 197

Bibliography 201

Acknowledgements 211

1 Introduction

1.1 Motivation

In the last two decades, an enormous success in the field of laser cooling of neutral and charged atoms has been achieved [1, 2, 3]. Significant efforts are under way to cool molecules, since in the new accessible ion temperature regime molecules are very interesting to be used for performing high-precision spectroscopy, studying molecular structure and chemical reactions, testing fundamental theories, measuring fundamental constants [4], and observing quantum mechanical effects. Additionally, there is a variety of applications in biology and quantum chemistry.

Although laser cooling has proved to be an excellent technique for reducing the temperature of atoms, it can not be directly applied to molecules due to the lack of closed optical transitions or suitable laser sources [5]. Thus, to cool molecules indirect methods are used, for example, creating cold few-atom molecules from pre-cooled atoms via Feshbach resonances or photoassociation [6, 7, 8, 9], cooling pre-existing molecules using buffer gas [10, 11, 12], or decelerating dipolar molecules by a time-dependent electric field [13, 14, 15, 16]. However, these methods are limited to some particular species, or depend on the internal nature of the particles, or bring in disturbing factors such as strong magnetic fields. Our challenge is to develop a universal way, which can lead to high-resolution spectroscopy and is applicable for any molecular species from the simplest molecule H_2^+ to complex molecules such as proteins and polymers.

We therefore make use of the technique of laser cooling to cool an atomic ion species to millikelvin temperatures and take these cold ions as coolant to reduce the translational temperature of the molecular ions, which are simultaneously confined in a radio frequency (rf) ion trap, to a similar temperature as the laser-cooled ions via the strong long range mutual Coulomb interactions. This is the so-called sympathetic cooling technique. It is a powerful tool and can be applied to various types of applications ranging from mass spectrometry to quantum computing after the first demonstration for ions in Penning traps [17, 18].

In the experimental work, different types of molecular ions with masses from a few hundred to more than ten thousand amu, are demonstrated to be sympathetically cooled to the millikelvin regime by laser-cooled $^{138}Ba^+$ ions (mass 138 amu), which stay in a crystal state. To generate complex molecular ions without damaging them, a soft ionization method - electrospray ionization (ESI), is used. Thus, an ion guide is developed to transfer the molecular ions from the ESI system to the Paul trap and a differential vacuum system is added to make a vacuum transition from atmospherical pressure (ESI) to ultra-high-vacuum (UHV) pressure (Paul trap).

In order to analyze the produced particle ensembles models were developed and im-

plemented within a simulation program - SOSC. With this program various molecular dynamics (MD) simulations are performed to explain phenomena observed in the experiment and to better understand the ion systems in the Paul trap.

1.2 Outline

This thesis is organized as follows. In Chapter 2-4, the theoretical background and basic setup for our project are described. In Chapter 5-8, experimental results of the project are presented. Efforts on simulations and related results are addressed in Chapter 9-11. The last chapter (Chapter 12) is summary of this thesis and gives an outlook.

Chapter 2: a brief overview of different types of traps is made and the advantages of using linear Paul traps are addressed, the geometry and basic theory of the linear Paul trap are introduced.

Chapter 3: the Doppler laser cooling technique is introduced followed by a detailed description of the laser-cooling of $^{138}Ba^{+}$ ions. Another two cooling methods - buffer gas cooling and sympathetic cooling, which are also used in our project, are described as well.

Chapter 4: our experimental setup mainly consists of vacuum systems, the ion trap, ion sources, ion detection devices, an octopole ion guide, laser systems, and electronics, which are discussed.

Chapter 5: the preparation of laser-cooled $^{138}Ba^{+}$ ion ensembles is described and some of their properties are studied.

Chapter 6: chemical reactions of the laser-cooled $^{138}Ba^{+}$ ions with some neutral gases are presented.

Chapter 7: the sympathetic cooling of medium size organic molecular ions (Rhodamine 6G, Rhodamine 101, Alexa Fluor 350, and glycyrrhetinic acid) is described.

Chapter 8: sympathetic cooling of protein molecular ions - cytochrome c, is addressed.

Chapter 9: some basic theories about MD simulation are introduced followed by the development of cooling and heating models. Then, results on simulation of CCD images, determination of ion numbers and temperatures for different ion species, micromotion effects, and ion diffusion are presented.

Chapter 10: the secular excitation spectra are studied via MD simulations.

Chapter 11: investigation of a nondestructive detection method (optical dipole excitation) via MD simulations followed by simulations of the Doppler broadening spectroscopy.

Chapter 12: a summary of the work discussed in this thesis.

2 The linear radiofrequency (rf) trap

In our experiments ions are trapped, cooled and studied in a linear rf trap (Paul trap or quadrupole rf trap). Thus, it is the key apparatus in our experiment. In this chapter a concise introduction to this type of trap including the geometry and basic theory is presented. Since many different trapping techniques have been developed until today, in the beginning of this chapter a brief overview of other trap types is given and the advantages of choosing linear Paul traps are shown.

2.1 Trap types

In order to study well the properties of a molecular species, we need to confine the molecules in a container. If we only focus on a few number of molecules at very low temperatures and do precise measurements such as molecule-molecule, molecule-atom, and molecule-radiation interaction, special traps are necessary to isolate them from the disturbance of surroundings.

Magneto-optical traps (MOT) and optical dipole traps (ODT) have been widely used in the research of atomic and optical physics, especially, as a cooling and trapping method in achieving Bose-Einstein condensates [3] or atom optics experiments [19, 20]. However, those traps only work on atoms with a simple effective two-level electronic structure. On the other hand through the atom-to-molecule conversion method, ultra-cold neutral di-, tri-, tetra-atomic neutral molecules can be produced and trapped [21]. Lately, magnetic traps were built to trap cold paramagnetic neutral particles [14], which are pre-cooled by buffer gas. However, only a certain fraction of neutral magnetic molecules and atoms are applicable for this kind of trap. Furthermore, the strong magnetic field is a big disadvantage for some experiments, e.g. fundamental tests of physics.

Thus, it is better to find a universal way to cool molecules or atoms to the millikelvin regime or even lower. Fortunately, many atomic ions such as $^{138}Ba^+$, $^{9}Be^+$, $^{24}Mg^+$, $^{200}Hg^+$, $^{174}Yb^+$, $^{40}Ca^+$, $^{88}Sr^+$,$^{111}Cd^+$, ..., can be cooled by lasers to the Doppler limit and other ion species can be cooled by these cold atomic ions via the long range Coulomb interaction. So we need a trap to confine ions. However, trapping of a charged particle cannot be achieved with an electrostatic field alone. The Laplace equation

$$\nabla^2\Phi = 0 \tag{2.1}$$

shows that there is no potential minimum of an electrostatic field in all three dimensions of space. With the help of a magnetostatic field, an electrostatic field can confine any kind of ions, which results in the Penning trap, first introduced by Dehmelt in 1961 [23, 24]. The principle of the Penning trap is shown in Fig. 2.1 [22].

Although by using an electrostatic together with a magnetostatic field it is possible to confine charged particles in free space, the influence of the magnetostatic field on high

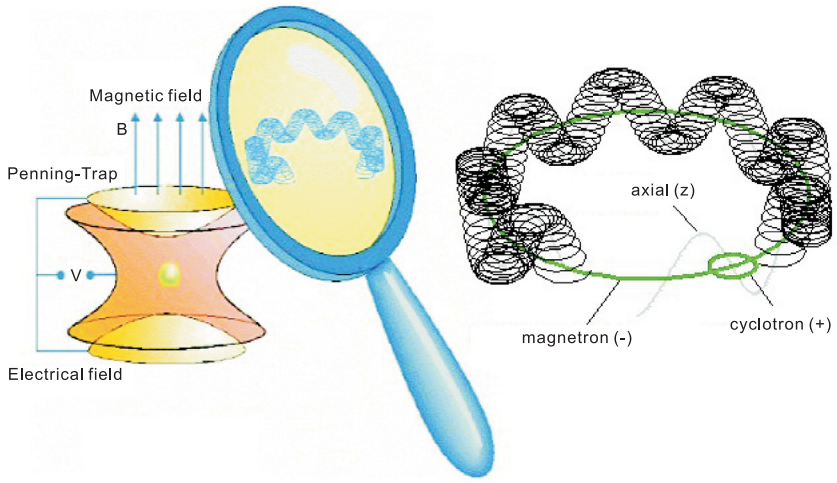

Figure 2.1: A standard Penning trap consists of an axial magnetic field and an electric field that provides radial confinement of the charged particle [22].

resolution spectroscopy measurement is a big disadvantage.

An oscillating radiofrequency (rf) field can create a so-called time-averaged harmonic pseudopotential, which is capable of trapping charged particles. The idea was proposed by Wolfgang Paul in 1958 [25]. The principle is illustrated in Fig. 2.2 by a mechanical analogue. If a ball is placed on a saddle as shown in Fig. 2.2(a), it only can stand on the middle point or oscillate along one symmetric axis, which is energetically unstable and any small disturbance might make it leave the saddle. However, if the saddle is rotated with a suitable mass-dependent frequency around the arrow direction, there is an average force which can keep the ball on the saddle. Fig. 2.2(b) is the illustration of the created potential well and the ball's trace, which is shown as the black line. Likewise, if a saddle-shape electrostatic potential which fulfills Laplace's law is oscillating with the right rf frequency, charged particles can be confined as well.

There are two kinds of rf ion traps called Paul traps (or quadrupole ion trap, QIT): the 3D and the linear Paul trap. The 3D trap generally consists of two hyperbolic metal electrodes with their foci facing each other and a hyperbolic ring-shaped electrode halfway between the other two electrodes as shown in Fig. 2.3. Normally, an rf AC field $V_0 \cos(\Omega t)$ (V_0 is the amplitude and Ω is the angular frequency) is applied to the ring electrode, while the endcap electrodes are held at rf ground. The applied rf voltage creates a potential well to confine charged particles.

However, for the 3D Paul trap only the point of the trap center has a zero rf field. When the ion deviates from the center point, it experiences a time dependent force and is driven to the trap center back and forth, which is also illustrated on the ball's trace in Fig. 2.2(b). For trapping large numbers of ions or several ion species with a higher mass-to-charge ratio difference, due to the strong Coulomb repelling interaction, they cannot occupy the central point of the trap. Thus, they experience a large rf driven motion (micromotion). If this motion becomes too large, it might lead to heating the

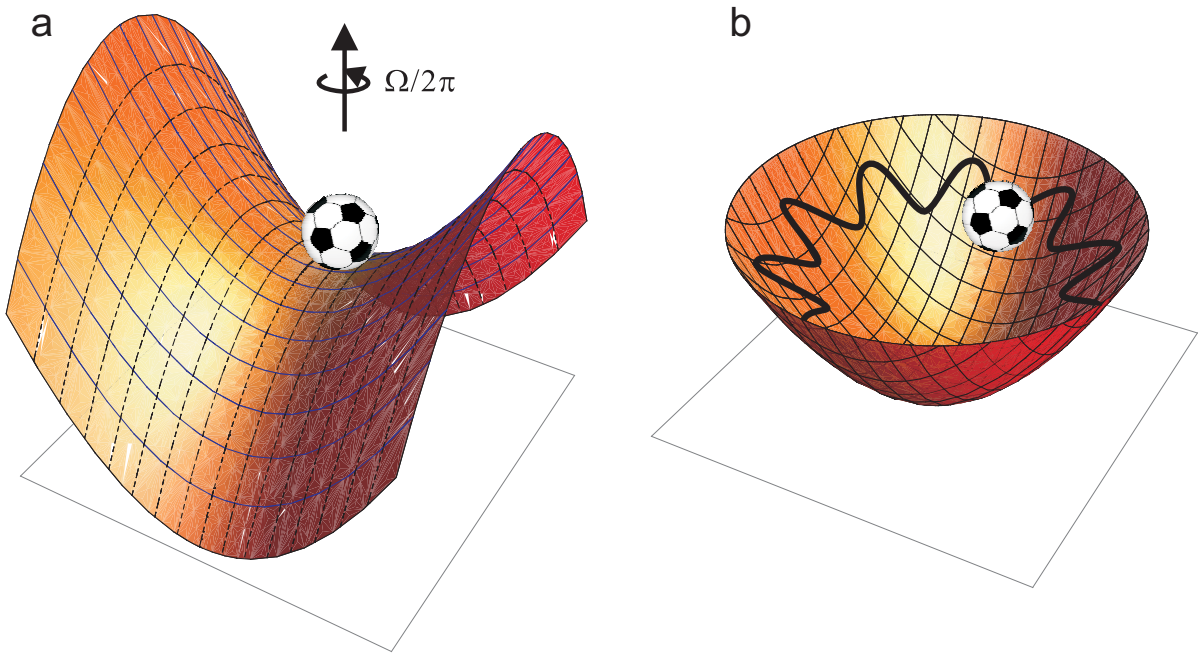

Figure 2.2: Mechanical analog to the rf Paul trap. A ball on the saddle point is in unstable equilibrium, but if the saddle is rotated with a suitable frequency, it can be confined on the saddle point. The right image shows the resulting effective potential well.

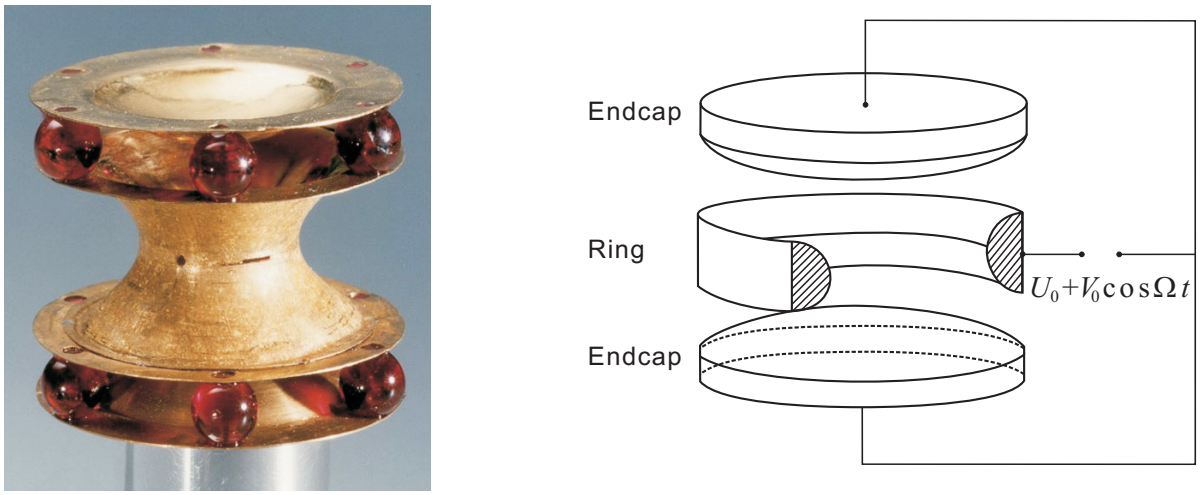

Figure 2.3: Typical 3D Paul trap. The left image shows the ion trap from Wolfgang Paul and the right one the electrode structure.

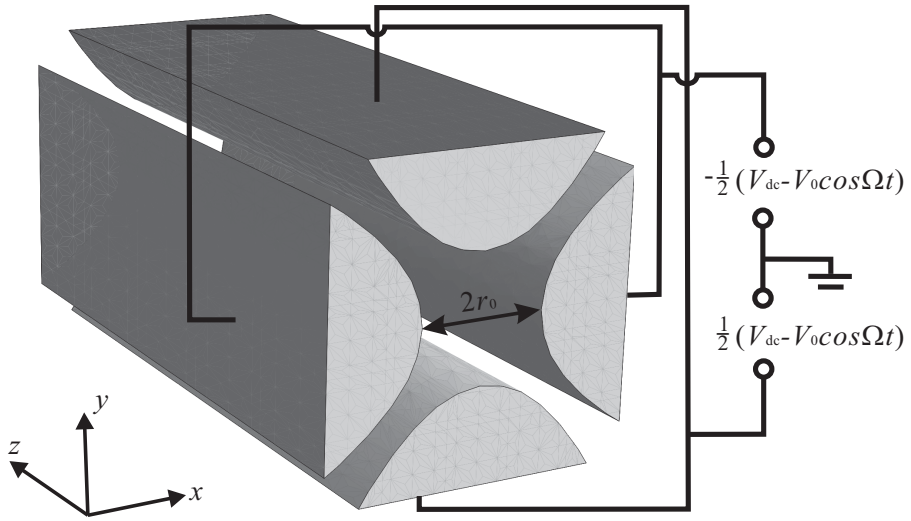

Figure 2.4: A standard quadrupole mass filter.

harmonic oscillator normal modes.

For this reason, we focus on another type of ion trap: the linear Paul trap. There is no rf field along the longitudinal axis (trap axis) of the linear Paul trap gaining the advantages of reduced space charge effects, an increased ion trapping efficiency and a much higher ion storage volume [26]. Moreover, its simple structure is convenient for shining the working lasers and for monitoring and detecting the trapped ions.

2.2 Trap theory of the linear Paul trap

There are linear Paul traps [27] with many kinds of geometries [28, 29, 22, 30], but the basic idea is the combination of a quadrupole mass filter plus longitudinal trapping electrodes. The movement of the ions in the trap can be described by the so-called Mathieu equations.

2.2.1 Quadrupole mass filter

The quadrupole mass filter consists of four parallel hyperbolically shaped electrodes. The geometry is shown in Fig. 2.4. When there are no charges in the trap, the potential distribution $V(x, y, z)$ is quadratic [31]:

$$V(x, y, z) = \frac{\Phi}{r_0^2}(\lambda x^2 + \sigma y^2 + \gamma z^2), \tag{2.2}$$

where Φ is the applied electric potential, r_0 is the distance from the trap center to the surface of the electrodes, λ, σ, and γ are the weight for the coordinates of x, y, and z, respectively [32]. Typically, the applied potential to the two orthogonal pairs of the trap electrodes is the combination of an rf potential $\frac{1}{2}V_0 \cos \Omega t$ and a DC potential $\frac{1}{2}V_{dc}$ with opposite phase (see the electric circuit in Fig. 2.4), Hence, Φ has the form

$$\Phi = \frac{1}{2}(V_{dc} - V_0 \cos \Omega t), \tag{2.3}$$

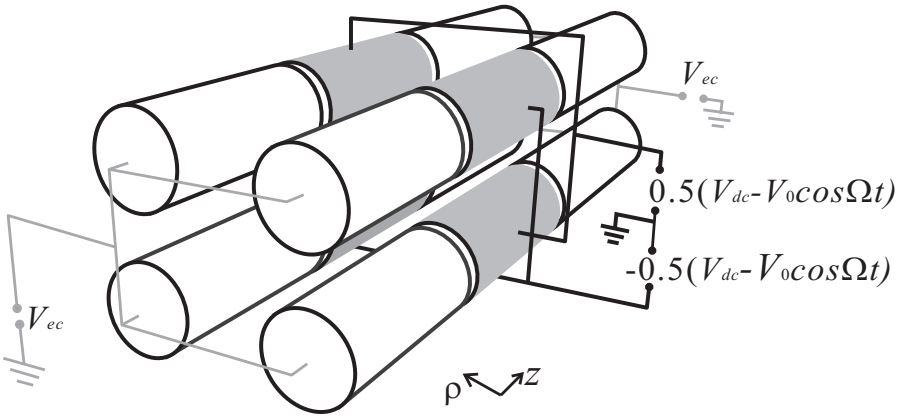

Figure 2.5: Structure of our linear Paul trap.

where V_0 is the peak-to-peak amplitude of the rf voltage, and Ω is the angular frequency of the rf field.

Eq. (2.2) always fulfills the Laplace equation Eq. (2.1). Thus,

$$\nabla^2 V(x,y,z) = \frac{\Phi}{r_0^2}(2\lambda + 2\sigma + 2\gamma), \tag{2.4}$$

from which we get

$$\lambda + \sigma + \gamma = 0 \tag{2.5}$$

or $\Phi = 0$. When $\Phi \neq 0$, λ, σ, and γ cannot have the same sign simultaneously. Consequently, if ions are confined in one dimension, they escape in at least one of the other two dimensions. In our case of the linear Paul trap, the rf field only confines the ions in the xy plane, $\gamma = 0$. Therefore, if we set λ to be 1, σ is -1. The potential V at any point (x, y) in the quadrupole field is [22]:

$$V(x,y) = \frac{\Phi}{r_0^2}(x^2 - y^2) = \frac{V_{dc} - V_0 \cos\Omega t}{2r_0^2}(x^2 - y^2). \tag{2.6}$$

2.2.2 Longitudinal confinement

Confinement of ions in the axial (z) direction is achieved by electrostatic fields applied to the endcap electrodes. In some linear Paul traps, the endcap electrodes are two pin or ring electrodes placed at both ends of the mass filter [33]. This kind of trap structure limits or even blocks the access of laser beams along the axial direction and the loading of the complex molecular ions from an specific ion source. Therefore, we use another two sets of quadrupole electrodes as the endcap electrodes, which are shown in Fig. 2.5.

As it is hard to build hyperbolic electrodes, most of the quadrupole electrodes are replaced by circular rods [34] with radius

$$r = 1.1478\, r_0. \tag{2.7}$$

Although the aberration due to the approximation is inevitable, the agreement of the

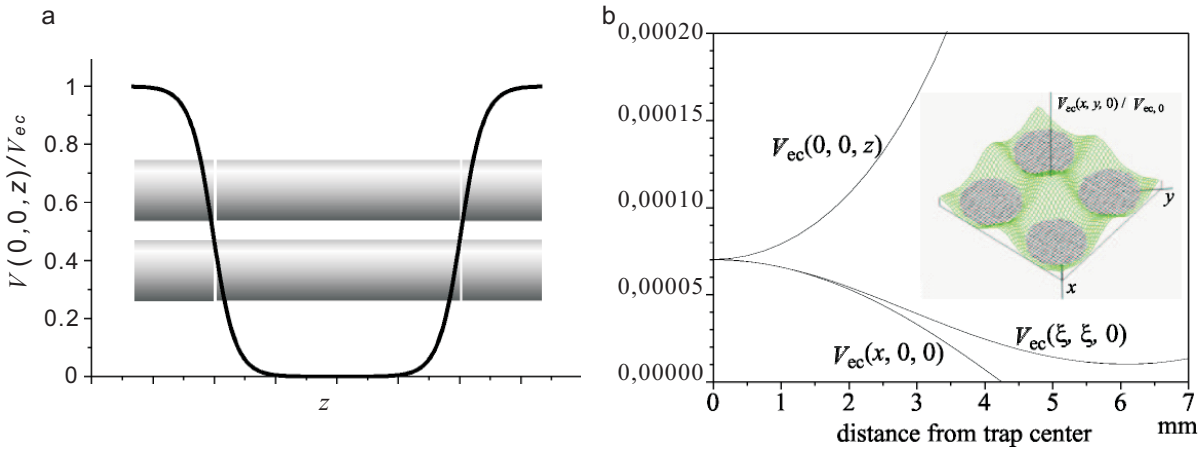

Figure 2.6: Electric field distribution due to the electrostatic potential applied on the endcap electrodes of a linear Paul trap. The difference of the applied electrostatic voltages between the endcap and central electrodes is V_{ec}. (a) Electric field distribution along the trap axis. (b) Simulated defocusing effect of the endcap voltage in the xy plane [35].

potential distribution near the trap center is good enough.

Three electrodes in a line share the same rf potential. Therefore, the whole setup also can be taken as a quadrupole mass filter being divided into three electrically isolated segments. The difference is that an electrostatic offset voltage is applied to the eight endcap electrodes, while a lower electrostatic offset voltage is acted on the central electrodes. The difference of these two voltages is defined as the endcap voltage, V_{ec}, which creates a static trapping potential well as demonstrated in Fig. 2.6(a). In our experiments, normally, 2 and -5 volts are applied to the endcap and central electrodes, respectively. Thus, V_{ec} is 7 volts. Through numerical solution via the widely used commercial software SIMION, this electrostatic field distribution in a specific trap along the axial direction can be approximated to be a harmonic well with the depth of κV_{ec}. Here parameter κ is a characteristic factor of a specific linear Paul trap and it only depends on the geometry of the trap. In our case, it is 0.15.

However, the presence of the electrostatic voltage on the endcap electrodes weakens the confinement of the rf field in the transverse (radial) direction. A related simulation is done with SIMION and the result is plotted in the Fig. 2.6(b) [35]. Actually, this defocusing effect is quite small, as will be discussed in the following section.

2.2.3 Mathieu equations

Considering the rf field and the electrostatic field V_{ec} the potential distribution $V(x, y, z, t)$ of the trap has the form

$$V(x, y, z, t) = \frac{V_{dc} - V_0 \cos \Omega t}{2r_0^2}(x^2 - y^2) + \frac{\kappa V_{ec}}{2z_0^2}(2z^2 - x^2 - y^2). \tag{2.8}$$

Here, $2z_0$ is the length of the central electrodes.

From the above equation we know that the field is uncoupled in the three coordinate directions, and the forces acting on a charged particle may be determined separately with

$$F_x = ma_x = m\frac{d^2x}{dt^2} = -Q\frac{\partial V(x,y,z,t)}{\partial x} = -Q\left(\frac{V_{dc} - V_0\cos\Omega t}{r_0^2} - \frac{\kappa V_{ec}}{z_0^2}\right)x, \tag{2.9}$$

$$F_y = ma_y = m\frac{d^2y}{dt^2} = -Q\frac{\partial V(x,y,z,t)}{\partial y} = Q\left(\frac{V_{dc} - V_0\cos\Omega t}{r_0^2} + \frac{\kappa V_{ec}}{z_0^2}\right)y, \tag{2.10}$$

$$F_z = ma_z = m\frac{d^2z}{dt^2} = -Q\frac{\partial V(x,y,z,t)}{\partial z} = -Q\left(\frac{2\kappa V_{ec}}{z_0^2}\right)z. \tag{2.11}$$

Rearrangement of Eq. (2.9), Eq. (2.10), and Eq. (2.11) leads to the equations of motion of a charged positive ion.

$$\frac{d^2x}{dt^2} + \frac{Q}{m}\left(\frac{V_{dc} - V_0\cos\Omega t}{r_0^2} - \frac{\kappa V_{ec}}{z_0^2}\right)x = 0, \tag{2.12}$$

$$\frac{d^2y}{dt^2} - \frac{Q}{m}\left(\frac{V_{dc} - V_0\cos\Omega t}{r_0^2} + \frac{\kappa V_{ec}}{z_0^2}\right)y = 0, \tag{2.13}$$

$$\frac{d^2z}{dt^2} + \frac{2Q\kappa V_{ec}}{mz_0^2}z = 0. \tag{2.14}$$

Eq. (2.14) directly tells us the axial harmonic frequency ω_z, which is expressed as

$$\omega_z = \sqrt{\frac{2Q\kappa V_{ec}}{mz_0^2}}. \tag{2.15}$$

To simplify Eq. (2.12) and Eq. (2.13), the definition of the dimensionless parameters is introduced

$$\tau = \frac{\Omega t}{2}, a_x = \frac{4Q}{m\Omega^2}\left(\frac{V_{dc}}{r_0^2} - \frac{\kappa V_{ec}}{z_0^2}\right), a_y = -\frac{4Q}{m\Omega^2}\left(\frac{V_{dc}}{r_0^2} + \frac{\kappa V_{ec}}{z_0^2}\right), q = q_x = -q_y = \frac{2QV_0}{mr_0^2\Omega^2}, \tag{2.16}$$

Eq. (2.12) and Eq. (2.13) can be written as

$$\frac{d^2x}{d\tau^2} + (a_x - 2q_x\cos 2\tau)x = 0, \tag{2.17}$$

$$\frac{d^2y}{d\tau^2} + (a_y - 2q_y\cos 2\tau)y = 0. \tag{2.18}$$

Finally, they become the canonical form of Mathieu's differential equations.

2.2.3.1 Solution to the Mathieu equations

We rewrite the equations of (2.17) and (2.18) as

$$\frac{d^2u}{d\tau^2} + (a_u - 2q_u \cos 2\tau)u = 0, \quad u = x, y. \tag{2.19}$$

In a general case, the complete solution $u(\tau)$ is given as

$$u(\tau) = \alpha_1 e^{\mu\tau} \sum_{n=-\infty}^{n=\infty} C_{2n} e^{2in\tau} + \alpha_2 e^{-\mu\tau} \sum_{n=-\infty}^{n=\infty} C_{2n} e^{-2in\tau}, \tag{2.20}$$

where α_1 and α_2 are constants of integration depending on the initial conditions of position u_0, velocity $\dot{u}_0$, and rf phase τ_0, while the C_{2n} coefficients are the factors describing the amplitudes of ion motion. They depend on the parameters a and q only. μ is a characteristic exponent depending on a and q as well.

2.2.3.2 Stability diagrams

When $\tau \to \infty$, the particle's trajectory u stays finite. Then we take this as a stable solution. μ determines the stability of the solutions of the Mathieu equations. Normally, μ is expressed as a complex number

$$\mu = \xi + i\beta, \tag{2.21}$$

here, ξ and β are real. If $\xi \neq 0$, one of the factors $e^{\pm\mu\tau}$ diverges and the trajectory is unstable. In the case of $\xi = 0$, μ is a purely imaginary. And if β is not an integer, it results in periodic and stable trajectories, which are enveloped by the boundaries corresponding to integers of β.

The stable solutions can be plotted using a_u and q_u as the coordinate axes. Such graphical representations of stable solutions to the Mathieu equation are called stability diagrams [32]. Fig. 2.7 gives an example. The characteristic values for these even and odd numbers divide the plane into regions of stability and instability (the stable area is shaded). Constructing such diagrams for each of the coordinate axes by plotting the appropriate a, q pairs, the stable trajectories in 3D are found leading to stable trapping.

Since in the experiment lower voltages can be realized easier, we only consider the first stable zone, which is found by the characteristic curves of $\beta_x = 0, 1$ and $\beta_y = 0, 1$ as shown in Fig. 2.8(a). For simplicity, only the positive first stable zone is shown in Fig. 2.8(b). This diagram tells us that without the rf voltage ($V_0 = 0$) charged particles can not be trapped and if all the electrostatic voltages on the electrodes are zero ($V_{dc} = V_{ec} = 0$) and q parameter is less than 0.908, the particles always stay in the stable region. This means that only mass-to-charge ratios less than $0.908\frac{2V_0}{r_0^2\Omega^2}$ can possibly be trapped radially.

For a quadrupole mass filter, there are no endcap electrodes or V_{ec} is set to zero. Therefore, a_x equals to $-a_y$ and the (a, q)-diagram leads to (V_{dc}, V_0)-diagram through the relationship of $a/q = 2V_{dc}/V_o$. If the ratio of the voltages applied to the central

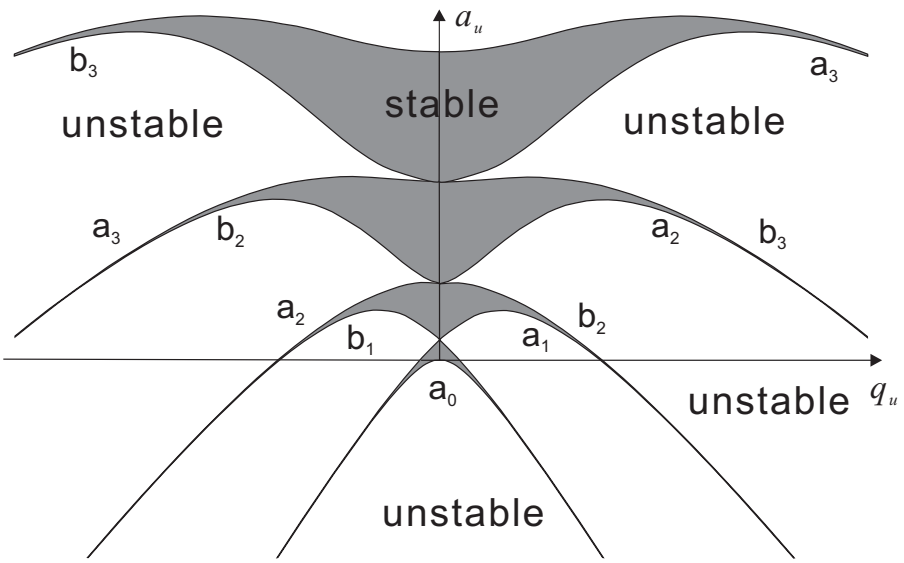

Figure 2.7: Mathieu stability diagram in one dimension.

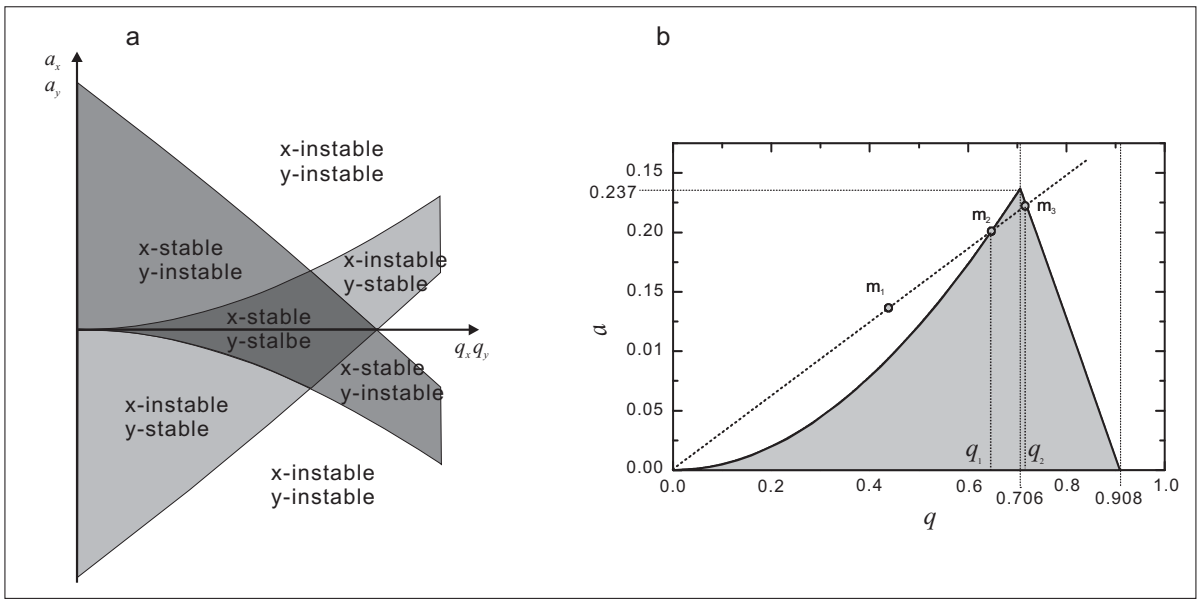

Figure 2.8: Mathieu stability diagram of the first region in two dimensions (x and y). (a) The first stable region in x and y dimensions. (b) The positive part of the shared first stable region in x and y dimensions. For a fixed ratio of V_{dc} to V_0 only ions with mass-to-charge ratio between m_2 and m_3 are able to be trapped radially.

electrodes (V_{dc}/V_0) is fixed, the value of a/q is determined. Then, only the ions whose q value is in between q_1 and q_2 can be trapped. This means only the ions whose mass-to-charge ratio is bigger than m_2 and smaller than m_3 can be trapped radially as shown in Fig. 2.8(b). By scanning V_{dc} and V_0 from low to high with a fixed ratio V_{dc}/V_0 we can bring in one mass-to-charge ratio ion species after another into the stability region and also can only bring in the charged particles we want as we do in the loading of the complex molecular ions.

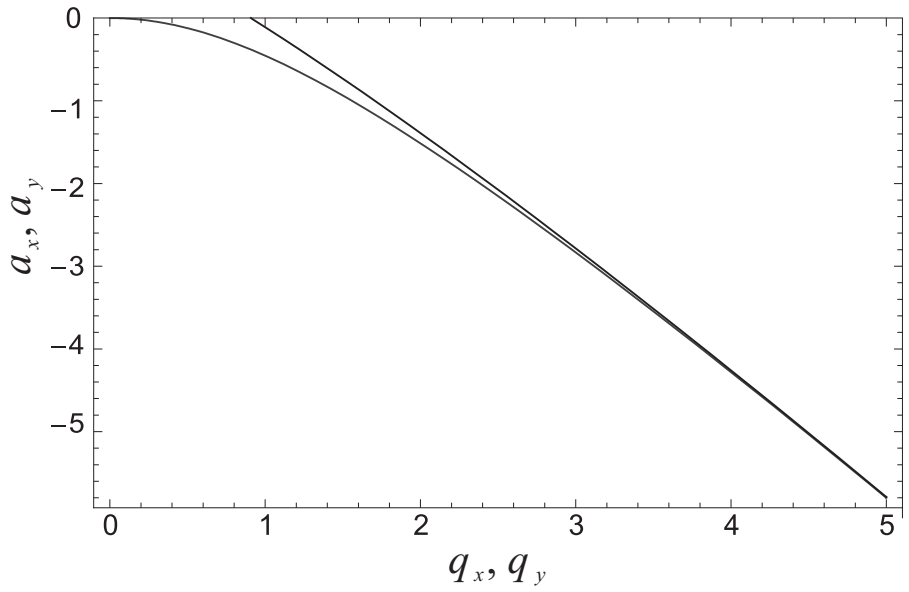

Figure 2.9: Stability diagram of our linear Paul trap at the first region when V_{dc} is zero.

To trap ions along the axial direction, V_{ec} cannot be zero. When we assume $V_{dc} = 0$ (as we always do in our experiment), the a parameter is only determined by V_{ec}. From Eq. (2.16) we obtain

$$a = a_x = a_y = -\frac{4Q\kappa V_{ec}}{m\Omega^2 z_0^2}. \tag{2.22}$$

Hence, the stability of the ions is determined by V_{ec} and V_0 and its stability diagram at the lowest region is shown in Fig. 2.9. Since a_x and a_y are equal and the sign is negative, the stable region is only in the negative a side [36]. Generally, the a parameter is quite small in our experiment. When V_{ec} is set to be 7 Volts to confine barium ions longitudinally, the κ parameter is 0.15 for our specific trap, and the angular frequency Ω is $2\pi \times 2.5$ MHz, the calculated value of a is about 0.000374, which is negligible compared to the q parameter.

2.2.4 Ion trajectories

Since one is typically looking at the stable solutions of the Mathieu equations, as we discussed in the previous section, μ is a purely imaginary and β is a value between 0 and 1. Therefore, the Eq. (2.20) can be rewritten as

$$u(\tau) = \alpha_1 \sum_{n=-\infty}^{n=\infty} C_{2n} e^{i(2n\tau+\beta\tau)} + \alpha_2 \sum_{n=-\infty}^{n=\infty} C_{2n} e^{-i(2n\tau+\beta\tau)}. \tag{2.23}$$

Using Euler's theorem, we may write this equation alternatively as

$$u(\tau) = A \sum_{n=-\infty}^{n=\infty} C_{2n} \cos(2n+\beta)\tau + iB \sum_{n=-\infty}^{n=\infty} C_{2n} \sin(2n+\beta)\tau, \tag{2.24}$$

where $A = \alpha_1 + \alpha_2$ and $B = \alpha_1 - \alpha_2$. The motion frequencies are

$$\omega_{n,u} = \mid 2n + \beta_u \mid \frac{\Omega}{2} \qquad n = 0, \pm 1, \pm 2, \ldots \tag{2.25}$$

The lowest-frequency motion, that for which $n = 0$, is given as $\omega_{0,x} = \omega_{0,y} = \frac{1}{2}\beta\Omega$ and is known as the ion's fundamental secular frequency. The higher order frequencies (n>0) give rise to the micromotion of the trajectory. We see from the above formula, any order motional frequency can be solved, if the characteristic frequency β is determined.

By inserting Eq. (2.24) into the Mathieu equation Eq. (2.19) one obtains a recursion relation,

$$C_{2n+2} + C_{2n-2} - D_{2n}C_{2n} = 0, \tag{2.26}$$

where

$$D_{2n} = \frac{a_u - (2n + \beta_u)^2}{q_u}. \tag{2.27}$$

Simple rearrangements and recursive use of Eq. (2.26) yield continued expressions for C_{2n},

$$C_{2n} = \frac{C_{2n-2}}{D_{2n} - \frac{1}{D_{2n-2} - \frac{1}{\cdots}}}, \tag{2.28}$$

$$C_{2n+2} = \frac{C_{2n}}{D_{2n} - \frac{1}{D_{2n+2} - \frac{1}{\cdots}}}, \tag{2.29}$$

and β_u^2,

$$\beta_u^2 = a_u - q_u \left(\frac{1}{D_0 - \frac{1}{D_2 - \frac{1}{\cdots}}} + \frac{1}{D_0 - \frac{1}{D_{-2} - \frac{1}{\cdots}}} \right). \tag{2.30}$$

Using Eq. (2.27) to replace the D_{2n} [37],

$$\begin{aligned} \beta_u^2 = a_u + & \frac{q_u^2}{(\beta_u + 2)^2 - a_u - \frac{q_u^2}{(\beta_u+4)^2 - a_u - \cdots}} \\ & + \frac{q_u^2}{(\beta_u - 2)^2 - a_u - \frac{q_u^2}{(\beta_u-4)^2 - a_u - \cdots}}. \end{aligned} \tag{2.31}$$

2.2.4.1 Secular motion

In principle, with the increase of the order the contribution of the higher order frequency motion to the energy becomes much smaller and is of little practical significance. β_u and the coefficients can be extracted by truncating the continued fractions after the desired accuracy is reached [38]. If ($|a_u|$, q_u^2)$\ll 1$ (normally, $q_u \leq 0.4$), the fundamental secular frequency

$$\beta_u \approx \sqrt{a_u + \frac{q_u^2}{2}}, \tag{2.32}$$

and the trajectory is expressed from Eq. (2.24) as

$$u(t) = AC_0 \cos\frac{\beta_u \Omega t}{2} + iBC_0 \sin\frac{\beta_u \Omega t}{2}. \tag{2.33}$$

A and B are determined by the initial conditions. If we assume that at $t = 0$, $\dot{u}(0) = 0$, the trajectory has the form

$$u(t) = u(0) \cos\frac{\beta_u \Omega t}{2}. \tag{2.34}$$

Thus,

$$\frac{d^2u(t)}{dt^2} = -\frac{\beta_u^2\Omega^2}{4}u(t) = -\frac{(a_u + \frac{q_u^2}{2})\Omega^2}{4}u(t) = -\omega_u^2 u(t), \tag{2.35}$$

which is a typical harmonic oscillation formula. If $V_{dc} = 0$, and a_u and q_u are replaced by the expressions in Eq. (2.16), its frequency, named radial secular frequency, is written as

$$\omega_r = \omega_x = \omega_y = \sqrt{-\frac{Q\kappa V_{ec}}{mz_0^2} + \frac{Q^2V_0^2}{2m^2r_0^4\Omega^2}}, \tag{2.36}$$

and the pseudopotential has the form as follows

$$\Psi(x,y) = \frac{1}{2}\frac{m\omega_r^2}{Q}(x^2+y^2) = \left(\frac{QV_0^2}{4mr_0^2\Omega^2} - \frac{\kappa r_0^2 V_{ec}}{2z_0^2}\right)\frac{x^2+y^2}{r_0^2} = \bar{D}_r\frac{x^2+y^2}{r_0^2}, \tag{2.37}$$

where $\bar{D}_r$ is the depth of the potential well in the radial direction. Via Eq. (2.15) a similar treatment in the axial direction yields

$$\bar{D}_z = \kappa V_{ec}, \tag{2.38}$$

which, unlike $\bar{D}_r$, is independent of the masses and charges of the trapped ions. Then we are able to write the pseudopotential well of the linear Paul trap as

$$\Psi(x,y,z) = \frac{1}{2}\frac{m}{Q}(\omega_x^2x^2 + \omega_y^2y^2 + \omega_z^2z^2) = \left(\frac{QV_0^2}{4mr_0^4\Omega^2} - \frac{\kappa V_{ec}}{2z_0^2}\right)(x^2+y^2) + \frac{\kappa V_{ec}}{z_0^2}z^2. \tag{2.39}$$

2.2.4.2 Micromotion

If the first order ($n = \pm 1$) is also kept by assuming $C_{\pm 4} = 0$ in Eq. (2.28) and Eq. (2.29), the characteristic frequency β is still approximated as Eq. (2.32). However, the trajectory has the form

$$u(t) \approx AC_0 \cos\frac{\beta_u \Omega t}{2}\left[1 - \frac{q_u}{2}\cos(\Omega t)\right]. \tag{2.40}$$

Besides the secular motion as described in Eq. (2.39) the trajectory includes an additional micromotion term, whose frequency is the rf driven frequency. The maximum amplitude of the micromotion is $1/2AC_0q_u$, which is $q_u/2$ times smaller than the moving amplitude of the secular motion. Fig. 2.10 shows a trajectory of a barium ion, which is released at $x = 200$ μm, with different q_u parameters including the secular motion and micromotion. The secular frequency is about 100 kHz and the rf frequency is 2.5 MHz. The corresponding q parameters of Fig. 2.10(a) and Fig. 2.10(b) are 0.1 and 0.01,

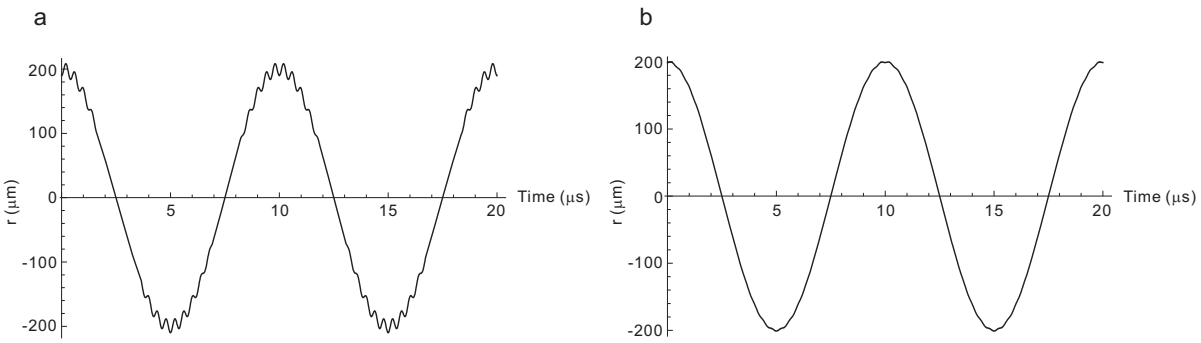

Figure 2.10: Ion trajectory including secular motion and micromotion with different q_u parameters, 0.1 and 0.01 for (a) and (b), respectively.

respectively. The amplitude of micromotion in Fig. 2.10(a) is 20 times smaller than that of the secular motion, but 10 times higher than that of the micromotion in Fig. 2.10(b), where the micromotion is hard to be distinguished.

2.2.4.3 Rf heating

Although an ion is confined and driven by the rf field at the frequency Ω, no energy is coupled into its secular motion. However, when electric noise and ion-residual gas collisions kick the ion out of phase with the rf field and produce chaotic motion, the secular motion of the ion absorbs some kinetic energy from the rf field. This is an irreversible process. The secular energy cannot be returned to the rf field. In this sense, the ion is heated up by the rf field. This phenomenon is called rf heating [39, 40, 41].

When more than one ion is trapped simultaneously, most of the ions might be pushed far away from the rf-free trap axis, which makes the amplitude of the ions' micromotion substantial. Together with the ion-ion Coulomb interaction the rf heating effect increases significantly [42, 43]. This ion coupling is strongly dependent on the trap parameters and the ion temperature as well as the ion numbers. By choosing appropriate trap parameters, improving the trap symmetry and loading lower numbers of ions the rf micromotion can be minimized to decrease the rf heating [44]. One of the most important advantages of choosing a linear Paul trap is its large trapping volume with a relatively low rf field. The rf heating effect is very serious at high temperatures and might help ions to overcome the trapping potential well and escape. In this thesis, I concentrate on relatively low temperatures, less than 1 K, and simulations about rf heating have been performed and are discussed in Chapter 9 [45].

3 Cooling of trapped ions

Generally, at the moment when the ions are captured by the trap, their temperatures are quite high. Then they gain additional kinetic energy as they move to the trap center, which has the minimum potential for positive ions. In the meantime, these ions absorb energy from the rf field (rf heating effect) and via collision processes with residual gas molecules. They can easily overcome the trap potential wall, whose height was specified by Eq. (2.37) and Eq. (2.38) ($\bar{D}_r \approx 6$eV and $\bar{D}_z \approx 1$ eV for our usual trap settings). In order to prolong the ion storage time, the kinetic energy of the ions need to be reduced as much as possible.

Up to now a large variety of cooling techniques has been developed to cool trapped particles. Temperatures below the Bose-Einstein condensation temperature, at $\simeq$40 nK, were already achieved [46]. However, these methods are mainly applied to atoms. Our work focuses on the cooling of complex molecular ions. Thus, the cooling schemes must be available for ions. There are several techniques including laser cooling, resistive cooling [24, 47], which is suitable for the Penning trap, collisional cooling [48], and sympathetic cooling [17]. In our work these three cooling techniques are used.

In this chapter, the first main section is about the laser cooling technique, which is used cool the atomic barium ions. The large mass-to-charge ratio of barium ions makes the sympathetic cooling of much heavy complex molecular ions relatively efficient. Due to the large mass-to-charge ratio of the complex molecular ions, coming from the ion source, it is hard to capture them before they leave the ion trap. Thus, helium buffer gas is used to slow them down to improve the capture probability. This buffer gas cooling method is briefly introduced in the second section. Finally, the decelerated complex molecular ions and laser cooled barium ions are confined in the trap simultaneously. The barium ions are continuously cooled to low temperatures by our working lasers (493 nm cooling laser and 650 nm repumping laser) and the complex molecular ions are cooled via the Coulomb interaction, sympathetic cooling. It is discussed in the last section.

3.1 Laser cooling

Laser cooling of trapped ions was first proposed in 1975 by D. J. Wineland, H. Dehmelt, and A. L. Schawlow, T. Hänsch, [49, 50]. In the last two decades, it was widely used and has played a significant role in atomic physics. However, most scientific reports on using this technique are concentrated on atomic gases, since the application on ions or molecules has some limits. The ion species which can be laser cooled, has to have a resonance transition reachable by a continuous-wave (CW) laser and an electronic structure which allows the ion to be excited from its ground state to an excited state and return to the ground state with a spontaneous radiation process in a short time. Molecules usually have many ro-vibrational levels. These levels can have long lifetimes and relax with radiationless transitions, so it is hard to realize laser cooling. Electronic levels, on

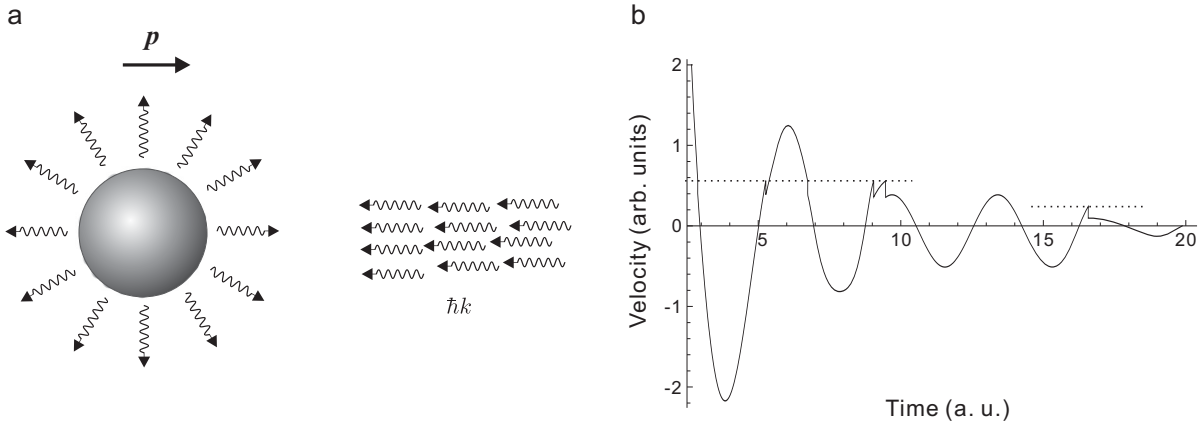

Figure 3.1: Illustration of Doppler cooling. (a) Ions are moving towards a laser beam and the absorption of the photons gives them recoils which slow them down. The absorbed energy is released by spontaneous emission. However, the recoils caused by the emission are counteracted over many cycles. (b) Illustration of how the secular oscillating motion of a trapped ion is reduced through the Doppler cooling.

the other hand, are the main reason why we have to cool the molecules in an indirect way.

Ions are confined in a trap by a harmonic potential well with resonance frequencies ω_u ($u = x$, y, or z) (see Eq. (2.39)). In our experiments, the cooling laser is directed along the z direction. When the atomic ions are at high temperature, the linewidth Γ of the cooling transition is much greater than the ion's axial motional frequency ω_z. Red-shifting the cooling laser and making use of the Doppler effect, the atomic ions can be cooled efficiently. When the atomic ions are cooled down to less than a few millikelvin, they are confined to a region of dimension much less than the wavelength of the radiation and Γ becomes much smaller than ω_z. Now the ions are in the Lamb-Dicke confinement regime [51] (see Chapter 11). The first-order Doppler effect disappears and is replaced by a series of sidebands spaced by the oscillation frequency ($\approx \omega_z$). In our experiments, we only employ the Doppler cooling technique. So the minimum temperature of a pure barium ion ensemble is limited to a few millikelvin.

3.1.1 Doppler laser cooling

Doppler laser cooling, is based on the Doppler effect in the photon scattering probability of generating a recoil to retard a moving ion. A graphical illustration is shown in Fig. 3.1. The scattering of a photon from a laser beam is subject to energy conservation and momentum conservation. When an ion runs to the right against a monochromatic laser beam, as shown in Fig. 3.1(a), whose frequency is ω_L red-detuned from the transition frequency of the ion at rest ω_{eg}, due to the Doppler effect the transition frequency is red-shifted, and at the right velocity the resonance with the laser frequency occurs. In this case a photon is absorbed and this ion gains a photon momentum $\hbar k_L = \hbar\omega_L/c$ in the direction of the laser beam. Thus, the ion is decelerated by the recoil. The absorbed photon is released by the decay through spontaneous emission. However, this emission is random but spherical symmetric. Thus, if this absorption-emission process repeats

enough times, the recoils from the emissions are counteracted. Finally, the net effect is that the ion is retarded in a direction opposite to the laser beam propagation. When the velocity of the ion becomes larger or smaller or the ion moves along the same direction as the laser beam, the Doppler shifted transition frequency is off resonance with the laser frequency resulting in low absorption probabilities. The ion can only be decelerated or accelerated with a much smaller probability. Fig. 3.1(b) demonstrates the process of how the ion is decelerated. The deceleration occurs at one particular velocity point where the transition frequency shifts to the resonance with the laser frequency. When the ion is cooled down below the velocity point, no resonance with the laser frequency can happen. However, the laser frequency can be tuned a little bit to the blue to continue the ion cooling procedure.

3.1.1.1 Notation for the atom-laser interaction

In order to deeply understand the Doppler laser cooling process, a quantitative analysis needs to be done. For simplicity, the atom is assumed to constitute of a closed two-level system with a stable ground state $|g\rangle$ and an excited state $|e\rangle$, whose lifetime is $\tau = 1/\Gamma$. The dipole transition frequency between these two levels is ω_{eg}. Since $|g\rangle$ and $|e\rangle$ are the atom's eigenstates, the atomic Hamiltonian has the form

$$\hat{H}_{atom} = |g\rangle\langle g| + |e\rangle\langle e|, \tag{3.1}$$

and the atomic wavefunction Ψ can be written as a superposition of the two eigenstates

$$\Psi(\boldsymbol{r}, t) = c_g|g\rangle + c_e|e\rangle, \tag{3.2}$$

where the coefficients c_g and c_e in general are complex numbers. $|c_g|^2$ and $|c_e|^2$ mean the probabilities of the atom to be in the ground or excited state, respectively. Their sum is 1.

The electric field $\boldsymbol{E}_L(z,t)$ coming from a laser beam is given by

$$\boldsymbol{E}_L(z,t) = \boldsymbol{e}_L(z)E_0(z)\cos(\omega_L t + k_L z), \tag{3.3}$$

where $\boldsymbol{e}_L$ is the polarization vector, E_0 is the amplitude and the laser frequency is ω_L. The laser beam running along the axial direction with the wave vector of k_L.

The operator of the atomic dipole moment $\boldsymbol{d}$ along the z direction is expressed as

$$\boldsymbol{d} = d\boldsymbol{e}_z(|e\rangle\langle g| + |g\rangle\langle e|), \tag{3.4}$$

where $\langle e|\boldsymbol{d}|g\rangle = d\boldsymbol{e}_z = \langle g|\boldsymbol{d}|e\rangle$. Then the interaction energy operator Hamiltonian $\hat{H}'$ between the atom and the laser beam has the form

$$\hat{H}' = -e\boldsymbol{d}\cdot\boldsymbol{E}_L(z,t) = \hbar\Omega_R\cdot\cos(\omega_L t + k_L z)\cdot(|e\rangle\langle g| + |g\rangle\langle e|), \tag{3.5}$$

here, Ω_{eg} is Rabi-frequency defined as

$$\Omega_R = \frac{d}{\hbar}eE_0(z)\boldsymbol{e}_z\cdot\boldsymbol{e}_L, \tag{3.6}$$

which determines the interaction strength.

Thus, the time evolution of the atomic wavefunction Ψ is governed by the time-dependent Schrödinger equation

$$i\hbar\frac{\partial\Psi}{\partial t} = (\hat{H}_{atom} + \hat{H}')\Psi. \tag{3.7}$$

To evaluate the probabilities of states with spontaneous emission of a two-level atom interacting with a travelling-wave light-field, the coefficients of c_g and c_e are used to form a density matrix

$$\rho = \begin{bmatrix} \rho_{ee} & \rho_{eg} \\ \rho_{ge} & \rho_{gg} \end{bmatrix} = \begin{bmatrix} c_e c_e^* & c_e c_g^* \\ c_g c_e^* & c_g c_g^* \end{bmatrix}. \tag{3.8}$$

where the time evolution of the matrix elements is governed by the equations of motion known as the optical Bloch equations (OBE) [52]:

$$\begin{aligned} \frac{d\rho_{ee}}{dt} &= -\frac{d\rho_{gg}}{dt} = -\Gamma\rho_{ee} - \frac{i}{2}(\Omega_R^* e^{-i\Delta\omega t}\rho_{eg} - \Omega_R e^{i\Delta\omega t}\rho_{ge}) \\ \frac{d\rho_{ge}}{dt} &= -(\frac{\Gamma}{2} + i\Delta\omega)\rho_{ge} + \frac{i}{2}\Omega_R^* e^{-i\Delta\omega t}(\rho_{ee} - \rho_{gg}) \\ \frac{d\rho_{eg}}{dt} &= -(\frac{\Gamma}{2} - i\Delta\omega)\rho_{eg} - \frac{i}{2}\Omega_R e^{i\Delta\omega t}(\rho_{ee} - \rho_{gg}). \end{aligned} \tag{3.9}$$

The optical Bloch equations can be solved numerically [53, 54]. If the laser frequency is detuned by $\Delta\omega$ from the resonance, in the steady state the population in the excited state is given by

$$\rho_{ee} = \frac{\Omega_R^2/4}{\Delta\omega^2 + \Omega_R^2/2 + \Gamma^2/4}. \tag{3.10}$$

Therefore, in the steady state the decay rate from the excited state to the ground state, $\Gamma\rho_{ee}$, is equal to the excitation rate from the ground state to the excited state, which is called the scattering rate γ, photons from the light are scattered by an atom, given by

$$\gamma = \Gamma\rho_{ee} = \Gamma\frac{\Omega_R^2/4}{\Delta\omega^2 + \Omega_R^2/2 + \Gamma^2/4} = \frac{\Gamma}{2}\frac{s}{1+s}. \tag{3.11}$$

where

$$s = \frac{\Omega_R^2/2}{\Delta\omega^2 + \Gamma^2/4} \tag{3.12}$$

is the so-called saturation parameter. In the case of $\Delta\omega = 0$, the saturation parameter becomes

$$s_0 = \frac{2\Omega_R^2}{\Gamma^2} = \frac{I}{I_{sat}}, \tag{3.13}$$

where

$$I_{sat} = \frac{\hbar\Gamma\omega_{eg}^3}{12\pi c^2} \approx \frac{2\pi^2\hbar c\Gamma}{3\lambda_L^2} \tag{3.14}$$

is the saturation intensity. So the Rabi-frequency can be expressed by the saturation

intensity as

$$\Omega_R^2 = \Gamma^2 \frac{I}{2I_{sat}}. \tag{3.15}$$

3.1.1.2 Basic theory of Doppler laser cooling

The light force due to the absorption of the photons is equal to the photon momentum $\hbar k_L$ multiplied by the scattering rate γ. When the ion is moving against the laser beam with a velocity v_z, the Doppler shift needs to be taken into account with $\Delta\omega$ replaced by $\Delta\omega + k_L v_z$ in Eq. (3.11). Finally, the light force is given as

$$F_z(v_z) = -\hbar k_L \Gamma \frac{\Omega_R^2/4}{(\Delta\omega + k_z v_z)^2 + \Omega_R^2/2 + \Gamma^2/4}. \tag{3.16}$$

Near $v_z = 0$, this light force can be expanded around $v_z = 0$ and the new expression is

$$F_z(v_z) = F_z(0) + \beta v_z + O(v_z), \tag{3.17}$$

with

$$F_z(0) = -\hbar k_L \Gamma \frac{\Omega_R^2/4}{\Delta\omega^2 + \Omega_R^2/2 + \Gamma^2/4} = -\hbar k_L \frac{\Gamma}{2} \frac{s}{1+s}, \tag{3.18}$$

and

$$\beta = \hbar k_L^2 \frac{s}{(s+1)^2} \frac{\Delta\omega\Gamma}{\Delta\omega^2 + \Gamma^2/4}. \tag{3.19}$$

The light force $F_z(v_z)$ has a constant light pressure force $F_z(0)$ and a velocity dependent friction force, whose damping coefficient is β. $F_z(0)$ is determined by the properties of the cooling laser and the linewidth of the transition frequency. It can be counteracted by using a counter-propagating laser beam with the same frequency and intensity. In our experiments, we use a running wave beam, since the space at the other end of the trap is occupied by the octopole ion guide. Therefore, this force is always present, pushing the laser cooled ion ensemble along the beam direction. Through molecular dynamics simulations, the magnitude of the light pressure force can be simulated (see Chapter 9).

Fig. 3.2(a) plots the light force expressed in Eq. (3.16) as a function of the ion's velocity with different laser intensities when $\Delta\omega = -\Gamma/2$. At near zero velocity the force curve can be approximated to be linear with the slope β as we obtained in Eq. (3.17). If the ion's velocity is quite large, leading to a large Doppler shift, the cooling force is relatively weak. Through a laser detuning further to lower frequencies, the Lorentz shaped force curve moves away from the origin but towards the optimal cooling to cool the ions much more efficiently as shown in Fig 3.3. Therefore, via a frequency scan the width of the ion velocity distribution can be reduced.

The damping coefficient β depends on the laser detuning which is depicted in Fig. 3.2(b). The red-detuning corresponding to $\beta < 0$ leads to the deceleration of the ions' motion, whereas the blue detuning results in heating. For each laser red-detuning $\Delta\omega$ one always can find a maximum value of -β (maximum cooling efficiency). For example, when $\Delta\omega = -\frac{1}{2}\Gamma$, -$\beta_{max} = \frac{1}{4}\hbar k_L^2$ with $s_0 = 2$. In the low intensity limit, $s \ll 1$, the expression

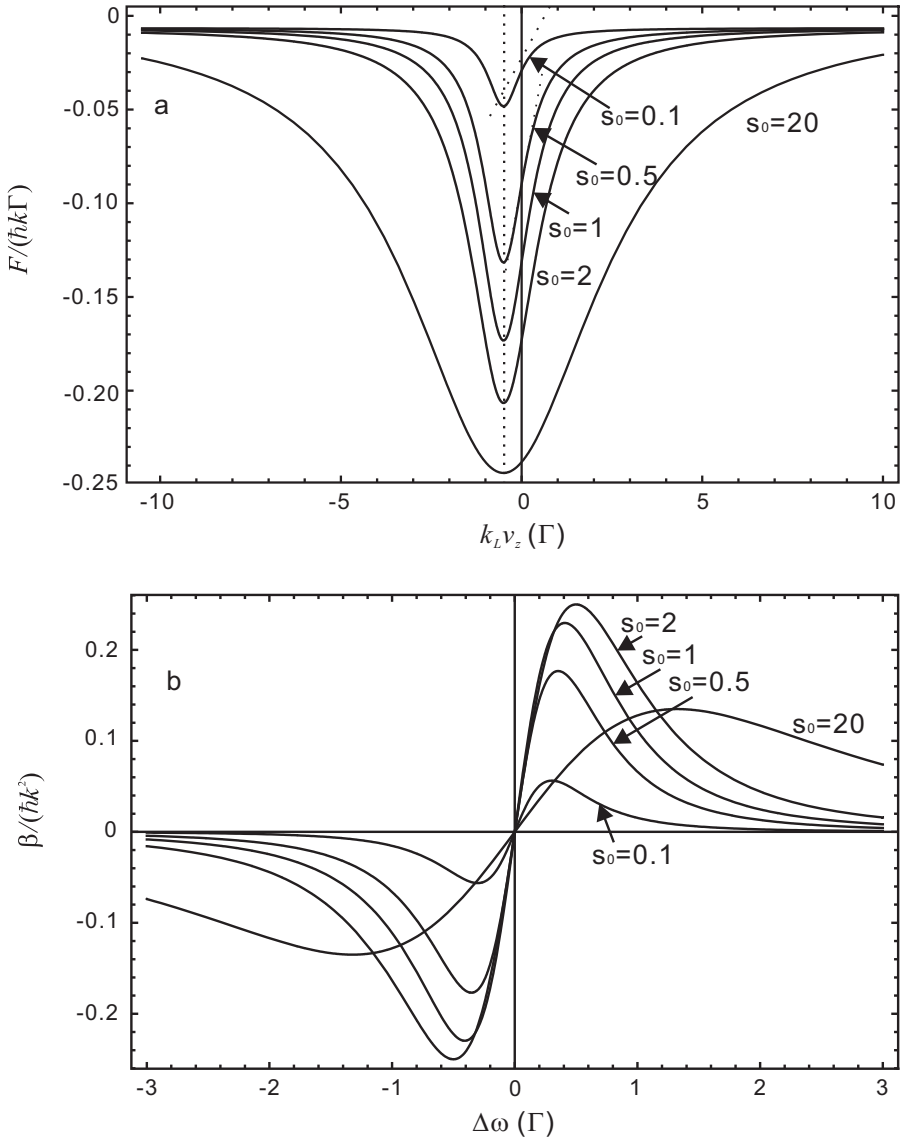

Figure 3.2: Light force of a running wave. (a) The force is plotted as a function of the Doppler shift. (b) The damping coefficient β as a function of the laser detuning $\Delta\omega$.

of β in Eq. (3.19) is reduced to be

$$\beta = \hbar k_L^2 s \frac{\Delta\omega\Gamma}{\Delta\omega^2 + \Gamma^2/4}, \tag{3.20}$$

which shows that the damping coefficient β is proportional to the intensity. On the other hand, when $s \gg 1$, β becomes reverse proportional to the intensity.

3.1.1.3 Doppler cooling limit

As we discussed above, the realization of the Doppler cooling relies on the randomness of the spontaneous emission recoils, which makes the ion undergo a random walk in momentum space. In fact this momentum diffusion has a heating effect on the ion

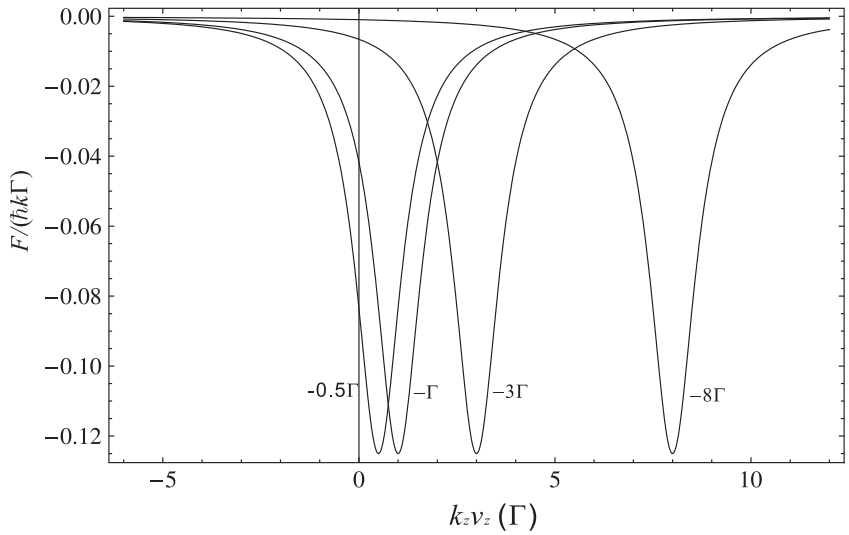

Figure 3.3: Light force as a function of the Doppler shift at different red detunings.

motion. For each recoil of a photon emission the velocity change of an ion is $\Delta \boldsymbol{p}/m$ and the kinetic energy change is

$$\Delta E = \frac{1}{2} m \left\langle (\boldsymbol{V} + \frac{\Delta \boldsymbol{p}}{m})^2 - \boldsymbol{V}^2 \right\rangle = \left\langle \boldsymbol{V} \Delta \boldsymbol{p} + \frac{\Delta \boldsymbol{p}^2}{2m} \right\rangle, \tag{3.21}$$

where m is the mass of the ion and $\boldsymbol{V}$ is its velocity before the photon emission. Since the ion velocity and the recoil are uncorrelated, the first term is zero, so

$$\Delta E = \left\langle \frac{\Delta \boldsymbol{p}^2}{2m} \right\rangle = \frac{\hbar^2 k_L^2}{2m}. \tag{3.22}$$

If we also consider the heating from the photon absorption and assume it has the same contribution, then the total heating rate h is given as

$$h = 2\Delta E \gamma = \frac{\hbar^2 k_L^2}{m} \gamma. \tag{3.23}$$

When the ion is cooled, the laser cooling rate c_l decreases linearly ($c_l = -\frac{2\beta}{3m}\langle E \rangle_l$, see Eq. (9.26) and Eq. (9.28)). Therefore, the ion cannot be cooled infinitely. When the cooling rate reaches the heating rate, the ion reaches an equilibrium state and has minimum temperature, which can be calculated as

$$\frac{\hbar^2 k_L^2}{m} \gamma = -\frac{2\beta}{3m} \langle E \rangle_l = -\frac{2\beta}{3m} \frac{3}{2} k_B T_{min} = -\frac{\beta}{m} k_B T_{min}, \tag{3.24}$$

$$T_{min} = -\frac{\hbar^2 k_L^2 \gamma}{\beta k_B} = -\frac{\hbar(s+1)}{2k_B} \frac{\Delta\omega^2 + \Gamma^2/4}{\Delta\omega}, \tag{3.25}$$

here the definition of temperature is $E_{kinetic} = 3/2 k_B T$. In the case of $\Delta\omega = -\Gamma/2$ and $\Omega_R^2 \to 0$, the minimum temperature is $\frac{\hbar\Gamma}{2k_B}$.

This is the minimum temperature, which can be achieved by Doppler cooling. If one

iso	^{130}Ba	^{132}Ba	^{133}Ba	^{134}Ba	^{135}Ba	^{136}Ba	^{137}Ba	^{138}Ba
NA	0.106%	0.101%	Syn	2.417%	6.592%	7.854%	11.23%	71.7%
spin	0	0	$\frac{1}{2}\hbar$	0	$\frac{3}{2}\hbar$	0	$\frac{3}{2}\hbar$	0

Table 3.1: Stable barium isotopes with their natural abundance (NA) and nuclear spin [55, 56, 57]

wants to achieve lower temperatures, other cooling techniques such as sideband cooling are necessary.

This minimum temperature is obtained for a single ion only in the axial direction. Using the same principle, the ion can be cooled by another two lasers radially. Thus, to cool a single ion to the minimum temperature in three dimensions, at least three identical laser systems are necessary. When more than one ion is confined in the trap simultaneously, after some kinetic energy being extracted by a laser beam along the axial direction, via the thermalization process a part of the radial kinetic energy redistributes to the axial direction. With the cooling continuing like this all the ions can be cooled in all dimensions.

3.1.2 Doppler cooling of $^{138}Ba^{+}$

3.1.2.1 Barium element

Barium is a silvery white, metallic, alkaline earth metal. Its atomic number is 56 with a standard atomic weight of 137.327 atomic mass unit (amu). Its first ionization energy is 5.2117 eV. It is a very reactive chemical element; when it is exposed to the air, it oxidizes easily. Moreover, it is highly reactive with water and alcohol. Normally, barium is kept under a petroleum-based fluid (such as kerosene) or other suitable oxygen-free liquids that exclude air. In our lab, we keep it in a vacuum chamber ($< 10^{-4}$ mbar) until we fill it into the oven; this operation is done in an argon atmosphere.

There are twenty-two isotopes, however, most of them are highly radioactive and have half-lives in the range of several milliseconds to several minutes. Synthetic radioisotope ^{133}Ba is the only exception, which has a half-life of about 10.51 years. Naturally occurring barium is a mix of seven stable isotopes which are shown in Table 3.1 with their natural abundance (NA) and a nuclear spin. From Table 3.1 we can see that the odd barium isotopes have nuclear spin, which causes the hyperfine structure in their ground and excited states.

As we discussed above the momentum change of an ion experiencing a single excitation followed by spontaneous emission is $\hbar k_L$, and the corresponding velocity change is $v_r = \hbar k_L/M$ along the axial direction. This is a small amount. Thus, in order to cool the atom sufficiently, many units of photon momentum on the same ion need to be accumulated. That means the excitation process needs to be repeatable and the spontaneous decay process always needs to bring the ion to the ground state. Otherwise, the cycle of the cooling is broken. Therefore the ground state splitting of the

Transition	Wavelength λ (nm)	Decay rate $\Gamma/2\pi$ (MHz)
$6^2S_{1/2} \leftrightarrow 6^2P_{1/2}$	493.4	15.1
$6^2S_{1/2} \leftrightarrow 6^2P_{3/2}$	455.4	18.8
$6^2P_{1/2} \leftrightarrow 5^2D_{3/2}$	649.7	5.3
$6^2P_{3/2} \leftrightarrow 5^2D_{3/2}$	585.4	0.7
$6^2P_{3/2} \leftrightarrow 5^2D_{5/2}$	614.2	5.9
$6^2S_{1/2} \leftrightarrow 5^2D_{3/2}$	2051	$4{\cdot}10^{-9}$
$6^2S_{1/2} \leftrightarrow 5^2D_{5/2}$	1761.7	$5{\cdot}10^{-9}$

Table 3.2: Wavelengths and decay rates of selected $^{138}Ba^+$ transitions [59, 60].

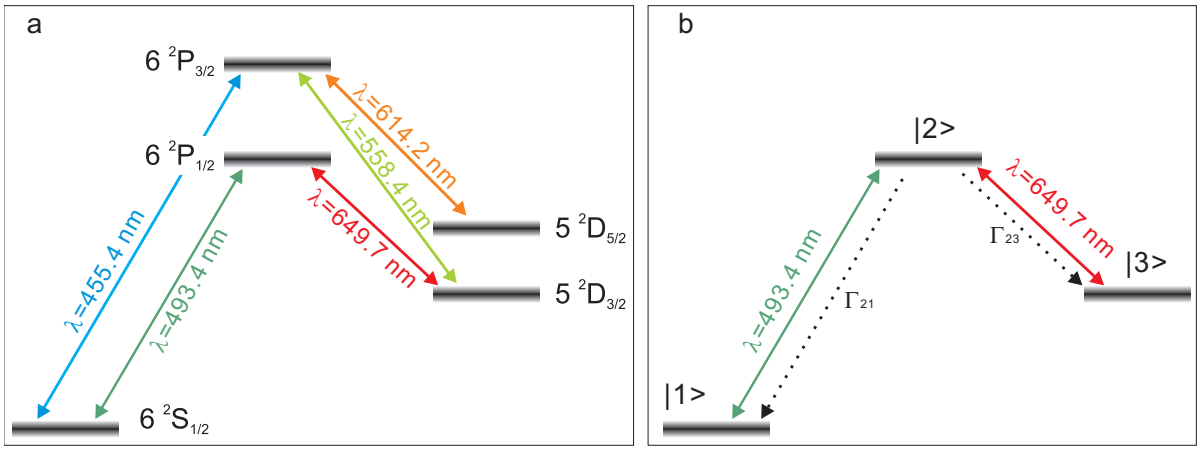

Figure 3.4: Level scheme for Doppler laser cooling of $^{138}Ba^+$ with wavelengths for the dipole allowed transitions [61].

odd isotopes due to the hyperfine structure makes them not suitable for the laser cooling.

The isotope shift between ^{138}Ba and ^{136}Ba or ^{136}Ba and ^{134}Ba at the $6^2S_{1/2}$ - $6^2P_{1/2}$ transition is greater than 100 MHz [58]. Therefore, we use the most abundant barium ^{138}Ba, whose natural abundance is about 72%, to be laser cooled. Other isotopes are sympathetically cooled.

3.1.2.2 Transitions of $^{138}Ba^+$

The electron configuration of a singly ionized ^{138}Ba atom is similar to that of the noble gas xenon, but with one additional valence electron in the 6s shell ([Xe]$6^2S_{1/2}$). Some main transitions between its low energy levels and the corresponding wavelengths together with their decay rates are listed in Table 3.2. The relevant level scheme is shown in Fig. 3.4(a). It is not a two-level system. When the ^{138}Ba ion is excited from the ground state to the P state, it might decay to a metastable D-state (lifetimes are 30 s and 40 s, respectively) first, then decay to the ground state via an electric quadrupole transition.

Thus, the laser cooling cycle is broken. However, since the transitions between P and D are also dipole-allowed, with the help of a repumping laser a closed system is constructed. We use the transitions of $6^2S_{1/2}$ - $6^2P_{1/2}$ and $5^2D_{3/2}$ - $6^2P_{1/2}$, whose transition frequencies are at 493 nm and 650 nm, respectively, where three energy levels are coupled by two laser beams as shown in Fig. 3.4(b).

3.1.2.3 Laser cooling of a three-level system

The three-level system is quite similar to the two-level system. We define the ground state $6^2S_{1/2}$ as state $|1\rangle$, the excited $6^2P_{1/2}$ and $5^2D_{3/2}$ as state $|2\rangle$ and state $|3\rangle$, respectively. The decay rate from $|2\rangle$ to $|1\rangle$ is Γ_{21} and the corresponding Rabi-frequency is Ω_{R21}, so do Γ_{23} and Ω_{R23} for $|2\rangle$ to $|3\rangle$. Thus, the Hamiltonian is

$$\hat{H}_{ion} = |1\rangle\langle 1| + |2\rangle\langle 2| + |3\rangle\langle 3|, \tag{3.26}$$

and the electric field of Eq. (3.3) becomes

$$\boldsymbol{E}_L(z,t) = \boldsymbol{E}_{Lg}(z,t) + \boldsymbol{E}_{Lr}(z,t), \tag{3.27}$$

where $\boldsymbol{E}_{Lg}(z,t)$ and $\boldsymbol{E}_{Lr}(z,t)$ are the electric field from green and red laser, respectively. The dipole operator is

$$\boldsymbol{d} = d_{21}\boldsymbol{e}_z(|2\rangle\langle 1| + |1\rangle\langle 2|) + d_{23}\boldsymbol{e}_z(|2\rangle\langle 3| + |3\rangle\langle 2|). \tag{3.28}$$

The interaction Hamiltonian is expressed as

$$\hat{H}' = \hbar\Omega_{21}\cos(\omega_{Lg}t + k_{Lg}z)(|2\rangle\langle 1| + |1\rangle\langle 2|) + \hbar\Omega_{23}\cos(\omega_{Lr}t + k_{Lr}z + \theta)(|2\rangle\langle 3| + |3\rangle\langle 2|) \tag{3.29}$$

In classical statistics, the subsystem is no longer in a pure state and must be described with a density operator $\hat{\rho}$

$$\hat{\rho} = \sum_{a,b=1,2,3} \rho|a\rangle\langle b|. \tag{3.30}$$

The time evolution of the density operator is governed by the Liouville equation

$$\frac{d\rho}{dt} = -\frac{i}{\hbar}[H,\rho] + \pounds_{damp}(\rho). \tag{3.31}$$

The first term corresponds to the Schrödinger equation and the second term $\pounds_{damp}(\rho)$ includes the damping terms. By choosing the phases of lasers to be 0 and setting the zero point of energy at $|2\rangle$ level, the complete Hamiltonian finally is

$$H' = \hbar\begin{pmatrix} \Delta\omega_g & \Omega_{21} & 0 \\ \Omega_{21} & 0 & \Omega_{23} \\ 0 & \Omega_{23} & \Delta\omega_r \end{pmatrix}, \tag{3.32}$$

where $\Delta\omega_g$ ($\equiv \omega_{Lg} - \omega_{21}$) and $\Delta\omega_r$ ($\equiv \omega_{Lr} - \omega_{23}$) are the laser detunings of the green and the red laser, whose frequencies are ω_{Lg} and ω_{Lr}, respectively.

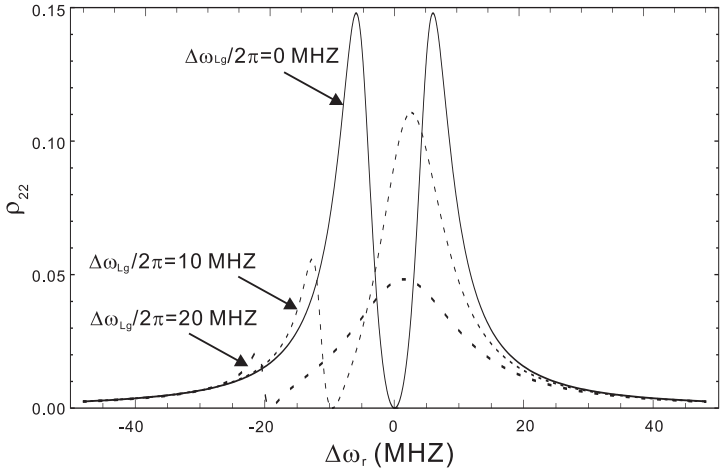

Figure 3.5: Resonance fluorescence excitation spectrum of a three level system with different detunings of the 493 nm laser. Here, $\Omega_{21} = 10$ MHz, $\Omega_{23} = 5$ MHz, laser linewidth $\Gamma_{Lg}$is 0, $\Gamma_{21} = 15.1$ MHz, and $\Gamma_{23} = 5.3$ MHz.

The elements can be described by the coupled optical Bloch equations [62], which can be solved numerically. The light force on the ion has the form

$$F_z(v_z) = -\hbar k_{Lg}\Gamma_{21}\rho_{22} - \hbar k_{Lr}\Gamma_{23}\rho_{22}. \tag{3.33}$$

When the detunings of the 493 nm laser and the 650 nm laser are equal, $\Delta\omega_g = \Delta\omega_r$, which satisfies the condition of a Raman transition between level $|1\rangle$ and level $|3\rangle$, no photons spontaneously emit from level $|2\rangle$. This effect is a so-called dark resonance. Fig. 3.5 shows the population in state $|2\rangle$, ρ_{22}, as a function of the detuning of the 650 nm laser with the detuning of the 493 nm laser at 0, 10, an 20 MHz. At the dark resonances ρ_{22} is zero and

$$\rho_{11} = \frac{\Omega_{23}^2}{\Omega_{21}^2 + \Omega_{23}^2}, \quad \rho_{33} = \frac{\Omega_{21}^2}{\Omega_{21}^2 + \Omega_{23}^2}, \quad \rho_{13} = -\frac{\Omega_{21}\Omega_{23}}{\Omega_{21}^2 + \Omega_{23}^2}, \quad \rho_{12} = \rho_{23} = 0. \tag{3.34}$$

In this case, the light field has no interaction with the ion and the ion is transparent.

Normally, the laser linewidths are not exactly 0. A finite linewidth results in some probabilities of exciting the ion to level $|2\rangle$. Therefore, the fluorescence will not vanish completely.

3.1.2.4 Zeeman splitting

As a matter of fact, the energy levels of a $^{138}Ba^+$, $6^2S_{1/2}$, $6^2P_{1/2}$ and $5^2S_{3/2}$ as shown in Fig. (3.4)(b), have eight degenerate substates, which are shown in Fig. (3.6). $6^2S_{1/2}$ and $6^2P_{1/2}$ are duplicate degeneracy, while $5^2S_{3/2}$ is fourfold degeneracy. These degenerate substates are described by the magnetic quantum number m_j. The optical excitations between these substates depend on the polarization of the lasers. Due to conservation of the angular momentum, the transitions with $m_j = \pm 1$, i.e. σ^+ and σ^- transitions, transfer an additional angular momentum $\hbar$. Thus, in a $^{138}Ba^+$ ion only transitions with $m_j = 0$, π can be excited with linear polarized 493 nm and 650 nm lasers. Populations

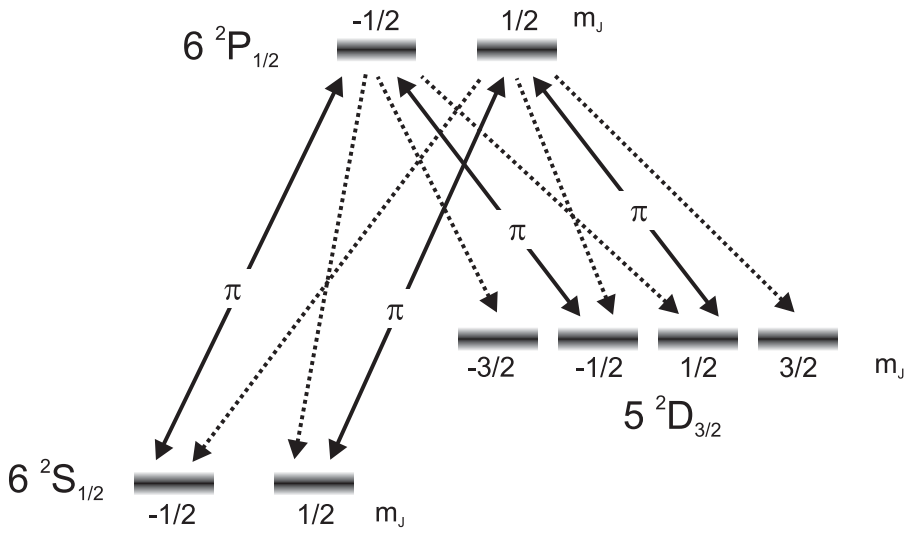

Figure 3.6: Level scheme of $^{138}Ba^{+}$ transitions without an external magnetic field [61].

in states $5^2S_{3/2}$ (with $m_j = \pm 3/2$) are accumulated via the spontaneous decay from the states of $6^2S_{1/2}$ ($m_j = \pm 1/2$) following the rule $\Delta m_j = \pm 1$. Finally, the substates of $6^2P_{1/2}$ become empty and the laser cooling process is stopped.

However, this situation can be prevented by implementing a homogenous magnetic field whose direction is not parallel to the polarization direction of our laser beams. The applied magnetic field splits up these substate energy levels. This effect is the Zeeman splitting. The energy change for each substate is

$$E_{zeeman} = m_j g_j \mu_B |B| \tag{3.35}$$

when expressed in frequency

$$\Delta\omega_{zeeman} = m_j g_j \frac{\mu_B |B|}{\hbar} = m_j g_j \mu, \tag{3.36}$$

where μ_B is is the Bohr magneton. g_j is the Landé factor given by

$$g_j = 1 + \frac{J(J+1) + S(S+1) - L(L+1)}{2J(J+1)}. \tag{3.37}$$

In our case, g_j for $6^2S_{1/2}$, $6^2P_{1/2}$, and $5^2D_{3/2}$ are 2, $\frac{2}{3}$, and $\frac{4}{5}$, respectively. All the information is shown in Fig. (3.7).

If the direction of the applied magnetic field is parallel to the propagation direction of the laser beams while perpendicular to their polarization (the polarizations of our two lasers are parallel to each other), the Zeeman splitting happens along the axial direction. In this case, all the photons seen radially are linear polarized. Therefore, σ transitions as well as π transitions can be optical excited. Of course, the dark resonance also splits and the corresponding positions depend on the ion species and the magnitude of the applied external magnetic field [63, 64, 65].

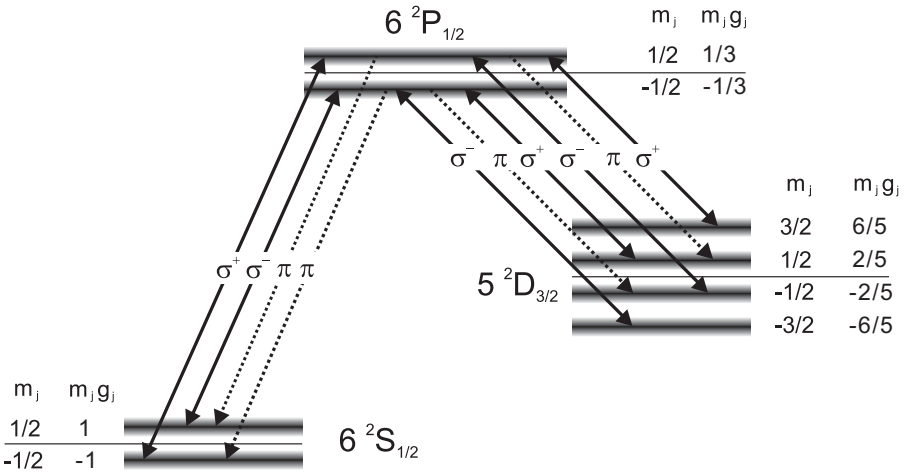

Figure 3.7: Level scheme of $^{138}Ba^{+}$ with Zeeman splitting and the possible transitions [61].

3.2 Buffer gas cooling

Our complex molecular ions are produced in an electrospray ionization system from where they are transferred to the ion trap via an octopole ion guide. Normally, their secular energy is about a few eV after the entrance of the trap for singly charged molecular ions. Ions pass the middle segment of the trap and leave trap through the trap exit easily. If we raise the endcap voltage at the exit end to stop the escaping, they bounce and escape from the other end, which is kept at relative low voltage to leak in the ions (see Fig. 7.2). More details are presented in Chapter 7. Meantime, due to the rf phase mismatch between the octopole and quadrupole, when the molecular ions leave the octopole guide and go into the trap, they gain some instantaneous rf energy into the secular energy, which might kick them out of the trap. Therefore, the complex molecular ions need to be slowed down in the trap, so that they can be captured.

Buffer gas cooling, which was introduced more than forty years ago [23], is a powerful tool to realize this goal. It relies on the elastic scattering of the ions on the buffer-gas molecules transferring a part of their energy to them. Thus, the motion of the ions is damped until they finally reach thermal equilibrium with the buffer gas. In principle, this cooling technique is applicable to any ion species, as long as the ion species is able to remain in the trap after multiple collisions with low energy buffer gas molecules. Finally, the molecular ions need to be sympathetically cooled by laser cooled ions, for which ultra-high vacuum conditions are necessary. The buffer gas can be removed in a few seconds (much shorter than the lifetime of the molecular ions staying in the trap).

At low temperatures ($T < 300$ K) the most important ion-neutral interaction arises from an induced dipole attraction which has a potential $\varphi = -\frac{\alpha}{2}(\frac{e}{4\pi\epsilon_0 r^2})^2$ [66] for a singly charged ion. Here α is the polarizability of the neutral atom or molecule, e the electron charge, and r the radial separation. Using classical collision theory one can derive an

expression for the ion-neutral collision heating or cooling rate [66] as

$$h_{coll} = \frac{3 \cdot 2.21}{4} \frac{e k_B}{\epsilon_0} n_n \sqrt{\alpha \mu} \frac{T_n - T_c}{m_n + m_c}, \tag{3.38}$$

and the momentum transfer collision rate

$$\gamma_{elastic} = \frac{2.21}{4} \frac{e}{\epsilon_0} n_n \sqrt{\frac{\alpha}{\mu}}, \tag{3.39}$$

where n_n is the particle density of the neutral gas, m_n (m_c) and T_n (T_c) are the masses and temperatures of the neutrals (charged particles), $\mu = m_n m_c/(m_n + m_c)$ is the reduced mass. Fig. (3.8) gives an example of the cooling process of a $^{39}K^+$ ion entering the trap with a kinetic energy of 10 eV, for details, see the work of F. Herfurth [67].

In fact, the collisions between the buffer gas and ions cause rf heating. When the mass of the molecular ions is greater than that of the buffer gas, the buffer gas cooling overcomes the rf heating. If their masses are close or the mass of the molecular ions is smaller, the rf heating becomes very serious. This is the main reason why we use helium gas as buffer gas. Of course, in our case, the complex molecular ions are relatively heavy, so nitrogen, argon, krypton and even xenon could be chosen, too.

3.3 Sympathetic cooling

3.3.1 Overview of sympathetic cooling

As we discussed in the Chapter 2, due to the limits of the availability of tunable, narrow-band laser sources and the fundamental problems such as complicated level structures (presence of ro-vibrational levels in molecules) or the absence of optical structures (as in protons and negative atomic ions) [17], only a few ion species can be laser cooled directly. Furthermore, the laser-cooling process itself strongly perturbs the levels of an atom or ion so that the precision of measurements is limited. Other cooling techniques are also limited to certain specific species. However, sympathetic cooling offers a solution to these problems. With this technique two or more ion species are confined in a trap simultaneously and one atomic ion species is directly cooled by lasers, while the others (atomic or molecular ions) are cooled via the long-range Coulomb interaction with the laser cooled ions. Fig. (3.9) gives an illustration of sympathetic cooling. It is very universal and should be applicable to cool nearly any ion species to the subkelvin regime.

In principle, sympathetic cooling can be realized in either a Penning or a Paul trap. The first demonstration in a Penning trap was provided in 1980 (isotopes $^{26}Mg^+$ were sympathetically cooled by laser cooled $^{24}Mg^+$ to about 0.5 K [18]). Experiments using laser-cooled $^9Be^+$ to cool $^{198}Hg^+$ [17, 68], laser cooled $^{24}Mg^+$ to cool $^9Be^+$ [69], and $^{40}Cd^+$ to cool diverse isotopes [70], were performed in Penning traps later.

However, most of the sympathetic cooling experiments are done in Paul traps since the observation by accident in 1992 [71]. Generally, in a Paul trap ordered and crystal-like structures can easily be observed through the fluorescence of the laser cooled ion

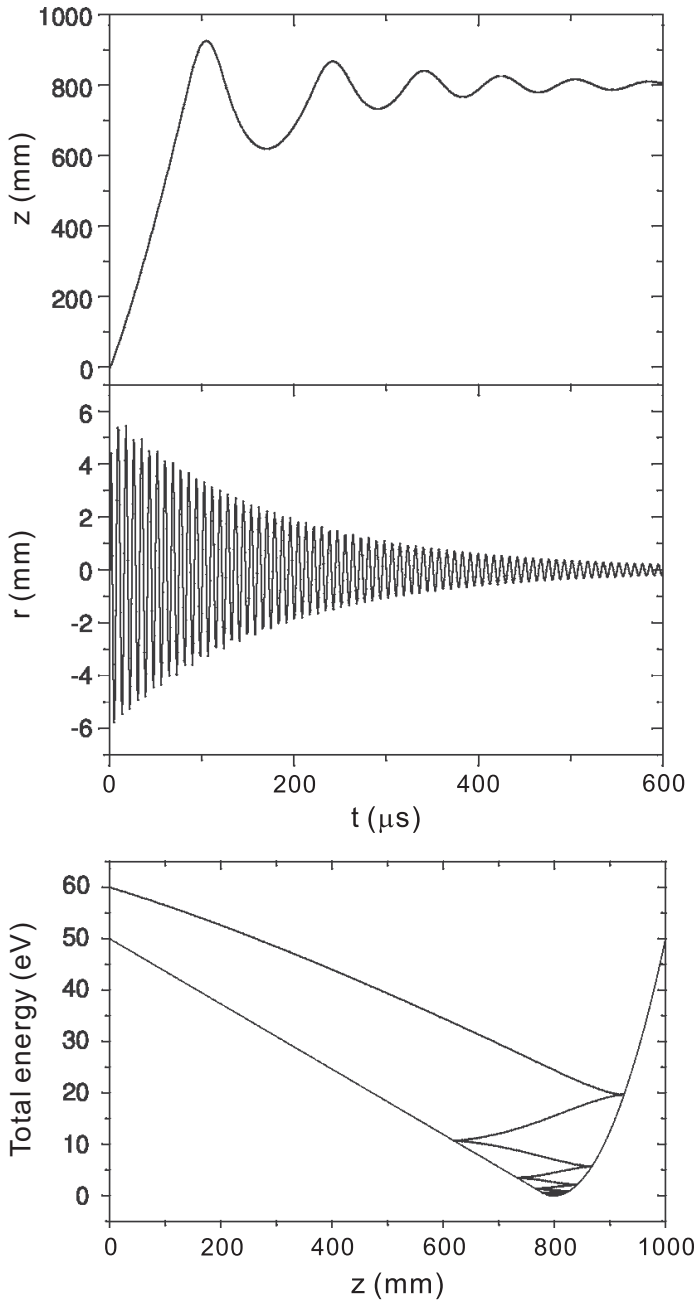

Figure 3.8: Simulation of the cooling process in a linear Paul trap in the presence of buffer gas. (a) The axial oscillation of a particle as a function of time, (b) the radial oscillation as a function of time, and (c) the total axial energy as a function of the axial position (shown together with the axial trap potential). The kinetic energy of the particle is reduced gradually and finally reaches the equilibrium state at the trap bottom (minimum trap potential). [67].

species at very low temperatures. The sympathetically cooled ions might occupy some "lattice" sites that appear dark. If they were not cooled to a temperature close to that of the laser cooled ion species, the crystal structure, at least near them, would be absent. In 1992, some dark spots were observed in a laser cooled $^{24}Mg^{+}$ ion crystal. Another important demonstration was that the molecular ions (from the background gas) were

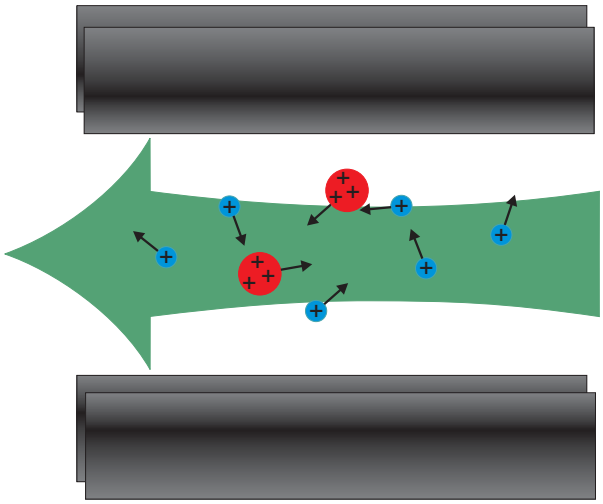

Figure 3.9: Illustration of sympathetic cooling. Molecular ions (in red) are loaded into the trap together with the laser-cooled atomic ions (in blue). The momentum transfer between charged particles is quite effective due to the strong Coulomb interaction. Thus, the momentum of the molecular ions will be transferred to the ions that are laser-cooled and then be removed from the laser cooled species "by the laser" as described in the first section. Thereby cooling of both species is achieved. In reality, the laser beam is usually wider than the ion ensemble once it is cold.

first sympathetically cooled by a laser-cooled $^{24}Mg^+$ ion crystal in 1996 [72] and the molecular species were identified. Up to now, a series of atomic ions and molecular ions with ion numbers from one to several thousand were sympathetically cooled and studied. In one experiment even 90% ions were sympathetically cooled [35]. Table 3.3 gives an overview of the atomic ions and molecular ions already being sympathetically cooled in Paul traps [78]. We extended this to complex molecules and we succeeded to cool the translational temperature of singly-charged Alexa Fluor 350 (Mass 410 amu) [61] and glycyrrhetinic acid (Mass 471 amu) and highly charged (charges from 12 to 17) cytochromes *c* (Mass about 13000 amu) to the millikelvin regime.

3.3.2 Mass dependency of sympathetic cooling

Sympathetic cooling, unlike buffer gas cooling, allows to use laser cooled ions to cool heavier ones, as well the lighter ones. In order to understand the sympathetic cooling quantitatively, the mass-to-charge ratio, m/Q, is used as the characteristic quantity of an ion species in an ion trap. The sympathetic cooling between two ion species is characterized by the quotient of their characteristic quantities, χ:

$$\chi = \left(\frac{m}{Q}\right)_{SC} : \left(\frac{m}{Q}\right)_{LC} . \tag{3.40}$$

In principle, any ion species is able to be sympathetically cooled. However, under specific parameters, only the ion species whose m/Q lies in the Mathieu stability diagram are available. The minimum χ for the trap parameter reported in Reference [72] is about 0.54 [79]. $^9Be^+$ ion species can be used to cool HD^+, and even protons leading to

Sympathetically cooled atomic ions		
Research Group	Crystallization achieved	fluid state only
Our group (HHU, Germany)	H^+, D^+, $^3He^+$, $^4He^+$, N^+, O^+, Ne^+, Ar^+, Ar^{2+}, Kr^+, Xe^+, $^{135-137}Ba^+$	
Sympathetically cooled molecular ions		
Our group (HHU, Germany)	H_2^+, HD^+, D_2^+, H_3^+, D_3^+, H_2D^+, HD_2^+, BeH^+, BeD^+, NeH^+, NeD^+, N_2^+, OH^+, O_2^+, O_2H^+, H_2O^+, ArH_2^+, ArD^+, CO_2^+, KrH^+, KrD^+, BaO^+, $C_4F_8^+$, $AF350^+$, GA^+, $R6G^+$, Cyt^{12+} - Cyt^{17+}	
Aarhus University (Denmark)	MgH^+, O_2^+, MgO^+, CaO^+ [73, 74]	
Hitachi Research Center (Japan)		NH_4^+, H_2O^+, H_3O^+, $C_2H_5^+$, COH^+, O_2^+ [75, 72]
NIST (U.S.)	BeH^+ [76]	
Texas A & M University (U.S.)		C_{60}^+ [77]

Table 3.3: Cold atomic ions and molecular ions produced by sympathetic cooling [78].

$\chi = 1:9$. In our experiments, CO_2^+ from residual gas are always loaded with Ba^+ and sympathetically cooled, in this case, the corresponding χ is about 0.29. $\chi = 1:6$ was achieved through simulations using $^{24}Mg^+$ to cool D_2^+ [35] and $\chi = 7.85$ was realized in our experiment (the cyt c protein ions in the 12 charge state were sympathetically cooled by the laser-cooled $^{138}Ba^+$ ions).

When several ion species with the minimum mass-to-charge difference ($\chi = 1$) are confined in a linear Paul trap and cooled to sufficiently low temperatures, all the ions mix and the momentum transfer between these ion species is most efficient. In most cases, their mass-to-charge ratios are different, so they are spatially separated (radially) as shown in Fig. 3.10. The higher the mass-to-charge difference between two ion species, the further they are located from each other, which leads to a lower sympathetic cooling efficiency. The separation is determined by the q parameter. Higher mass-to-charge ratio ion species suffer weaker trap pseudopotential than lighter ones, so lighter ion ensembles stay more close to the trap axis and repel heavier ones away from the trap axis. The heavier of the ions, the easily of them to be pushed further away from the trap axis. To better under stand this, a two-ion-species system is considered, for example, a system with barium and complex molecular ions. Their mass-to-charge ratios are m_1/Q_1 and m_2/Q_2, respectively, with $m_1/Q_1 < m_2/Q_2$. The trap confinement force on the heavier ions is $m_2 q^2 \Omega^2 r/8$ and the Coulomb repelling force from the lighter ions is approximately

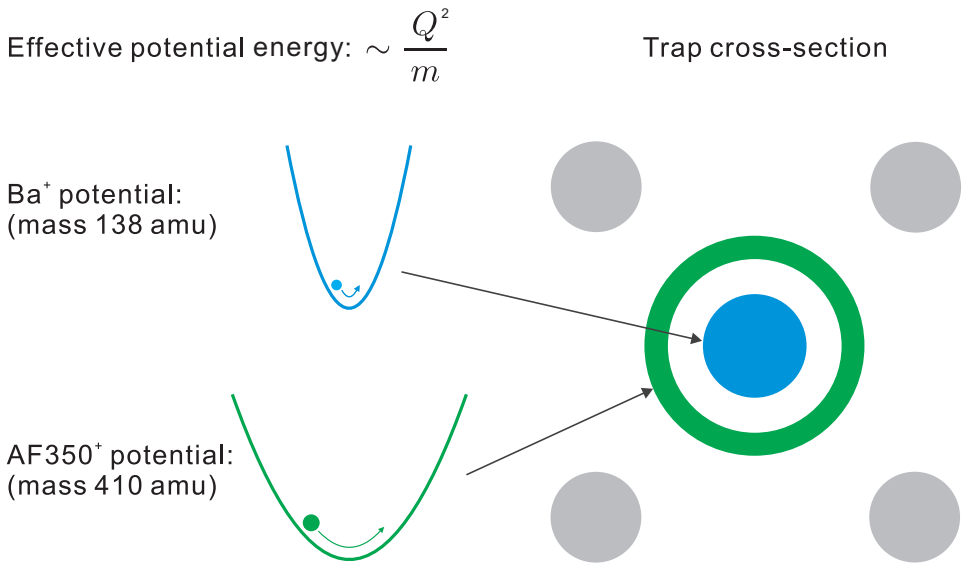

Figure 3.10: Scheme of the spatial distribution of different ion species and their corresponding effective trap potentials (proportional to Q/m in absence of space charge effects, i.e. the presence of other species). Lower mass-to-charge ratio ions experience a stronger pseudopotential.

$\frac{1}{4\pi\varepsilon_0}\frac{NQ_1Q_2}{r^2}$ in the case of the distance (the width of the gap) between these two ion species r, much big comparing to the size of the ion ensemble of the lighter ions. The N lighter ions are taken as a point charge at the trap center. At equilibrium state, we can obtain

$$r = \sqrt[3]{\frac{1}{4\pi\varepsilon_0}\frac{8NQ_1Q_2}{m_2q^2\Omega^2}} = \sqrt[3]{\frac{1}{4\pi\varepsilon_0}\frac{2NQ_1r_0^4\Omega^2}{V_0^2}\frac{m_2}{Q_2}}. \tag{3.41}$$

We can see that r is proportional to the cube root of the mass-to-charge ratio of the heavier ions. This equation also tells us that a larger number of lighter ions can enlarge the gap width leading to a weaker momentum transfer efficiency. Therefore, if the lighter ions are the laser-cooled barium ions and the heavier ions are the sympathetically cooled complex molecular ions, too many barium ions do not means to cool the molecular ions more efficiently.

In fact, m/Q of the complex molecular ions confined in our trap can not be more than 1500 amu/e, so the width of the gap between a barium ion ensemble and an ion ensemble of complex molecular ions is comparable or even much less than the dimensions of the barium ion ensemble. In this case, r is no longer simply proportional to the cube root of m_2/Q_2 due to the strong space charge effects. Therefore, we study ion systems via MD simulations.

Fig. 3.11 shows a simulation of the dependence of the sympathetic cooling efficiency on the the mass-to-charge ratio. A barium ion ensemble, whose ion number is 500, and another ion species (mass 200, 400, or 1000 amu) including 100 singly-charged ions are trapped simultaneously and heated up to 160 mK. When the heating is switched off and the laser cooling with a cooling rate $\beta/m_{Ba} = 4330\ \mathrm{s}^{-1}$ (5 times higher than actual) is

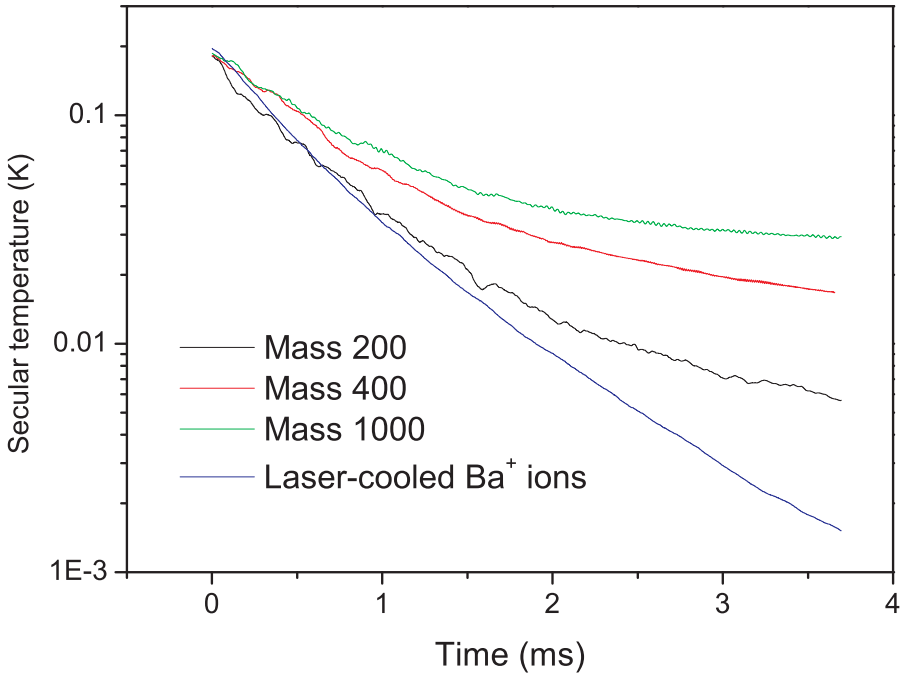

Figure 3.11: Temperature decay of different sympathetically cooled ion species together with 500 laser-cooled barium ions cooled by lasers from 160 mK. It is evident that ions, whose mass is close to that of the laser-cooled $^{138}Ba^{+}$ ions, are sympathetically cooled more efficiently. Heavier ions crystallize at larger distance from the coolant ions and are cooled less efficiently.

turned on, the barium ion ensemble is laser cooled and the other ion ensemble is sympathetically cooled. When the sympathetically cooled ions are heavier, the gap between the two ion species becomes larger, and the sympathetic cooling efficiency decreases, which is represented by smaller temperature decrease. Fig. 3.11 also shows that the sympathetic cooling efficiency depends on the temperatures of the ion species. With the temperatures going down the sympathetic cooling efficiencies decrease as well. Thus, higher temperatures have higher sympathetic cooling efficiencies.

If the mass-to-charge ratio of the species is too large, for example, some thousand amu or even more (proteins), ions will stay far away from trap axis with a very weak sympathetic cooling efficiency. Moreover, when the ions stay further away from the trap axis, the rf heating becomes more and more serious. Finally the rf heating rate overcomes the sympathetic cooling rate and the ions will not be trapped any more. Highly charging the molecules to decrease the mass-to-charge ratio is one solution to move ions closer to the axis. This effect is simulated in Fig. 3.12. To be more realistic, in the simulations a same ion ensemble as above is used, but the mass of the molecular ions is set to be 4000 amu and an additional heating rate $k_B(37.5\ \mathrm{K/s})$ is applied to both ion species. The molecular ions here are singly, doubly and fourfold charged, respectively. Since the sympathetic cooling rates are smaller than the heating rate, the molecular ions are heated up. If we do not consider the potential energy change (see Chapter 9) in the heating process, via these heating curves the sympathetic cooling rate for each case is achievable. For example, for the singly charged molecular ions, they stay further away from the trap

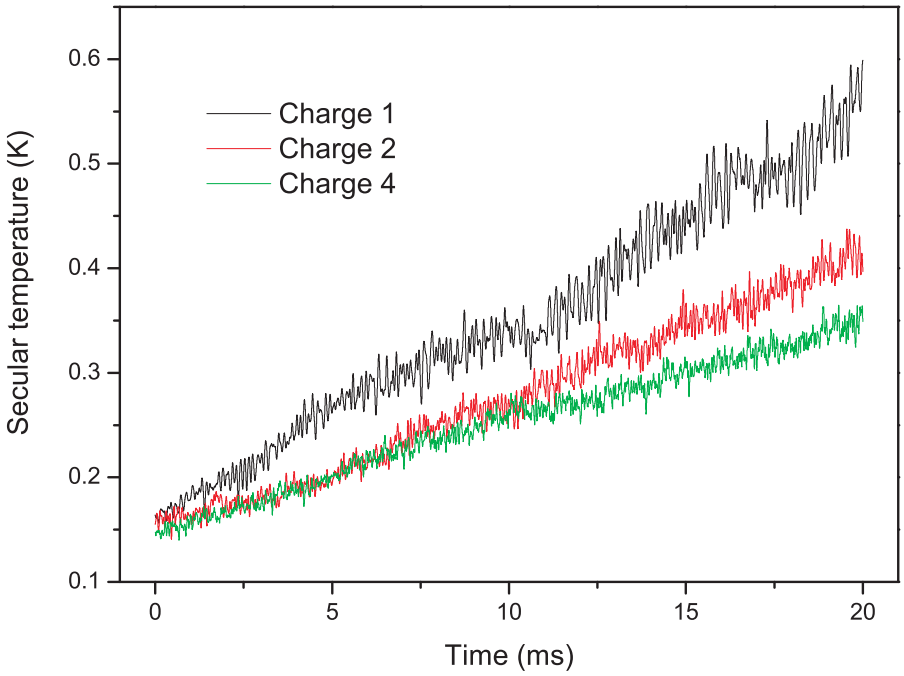

Figure 3.12: The dependence of the sympathetic cooling efficiency on Q. The ensembles including 100 molecular ions with mass 4000 amu and 500 laser-cooled barium ions initially evolve at about 160 mK. The implemented laser cooling rate is $\beta/m_{Ba} = 4330\ \mathrm{s}^{-1}$ and the heating rates for both ion species are $k_B(37.5\ \mathrm{K/s})$. The molecular ions are singly, doubly, and fourfold charged, respectively. A higher charge state forces the molecular ions closer to the trap axis and improves sympathetic cooling efficiency.

axis and have a weaker sympathetic cooling efficiency. Their fitted heating rate from the black curve is $k_B(28.5\ \mathrm{K/s})$, thus, the corresponding sympathetic cooling rate is about $k_B(9\ \mathrm{K/s})$ (= external heating rate - actual heating rate). When the molecular ions are doubly charged, they move towards the laser-cooled barium ions and the corresponding sympathetic cooling efficiency increases to approximately $k_B(17.4\ \mathrm{K/s})$. Finally, if the molecular ions are fourfold charged, sympathetic cooling rate becomes $k_B(22.5\ \mathrm{K/s})$.

It is also interesting to investigate the relationship between the sympathetic cooling efficiency and the mass, for constant mass-to-charge ratio. For this case, the gap between the coolant ions and the molecular ions is similar. Fig. 3.13(a) shows the temperature changes of different molecular ion species (masses 1000, 2000, and 4000 amu). Since their charge states are 1, 2, and 4 correspondingly, they have the same mass-to-charge ratio m/Q. The gap between the barium and the molecular ion species is approximately constant under these conditions. Accordingly, the obtained sympathetic cooling rates are $k_B(16.5\ \mathrm{K/s})$, $k_B(19.2\ \mathrm{K/s})$, and $k_B(22.5\ \mathrm{K/s})$. Thus, with a same m/Q the sympathetic cooling rates can be different, but they depend only weakly with m or Q, especially if the initial heating is considered. Actually, these differences arise from the spatial distribution of these molecular ions. Under same trap conditions, the molecular ions with a higher charge state repel each other more strongly and therefore have a broader distribution (mainly along the axial direction in our trap) leading to a more efficient energy transfer

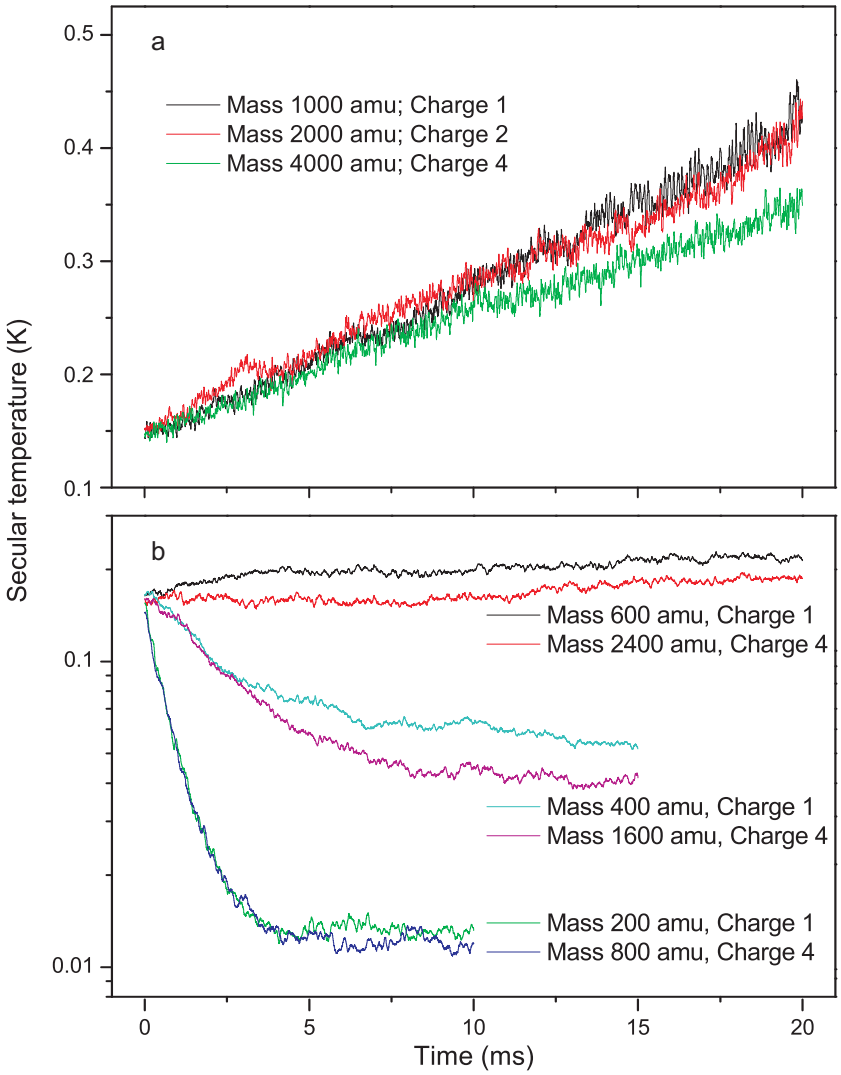

Figure 3.13: The dependence of the sympathetic cooling efficiency on the mass m and charge state Q of the molecular ions for constant mass-to-charge ratio. The ensembles including 100 molecular ions and 500 laser-cooled barium ions initially evolve at about 150 and 175 mK, respectively. The implemented laser cooling rate is $\beta/m_{Ba} = 4330\ \mathrm{s}^{-1}$ and the heating rates on both ion species are $k_B(37.5\ \mathrm{K/s})$. (a) Temperature evolutions of the molecular ions with masses 1000, 2000, and 4000 amu and in the corresponding charge states 1, 2, and 4. They have somewhat different sympathetic cooling efficiencies, which arise from their different spatial distributions. (b) Temperature evolutions of the molecular ions with masses 200 and 800 amu. The charge states are 1 and 4 correspondingly. Since the charge-to-mass ratio is similar to that of barium ions, there is only a small gap between the species and cooling takes place more efficiently. Another two groups (masses 400 and 1600 amu and masses 600 and 2400 amu) are also simulated. Their larger gaps weaken the sympathetic cooling efficiencies. When $m/Q \approx 600$ amu/e, the sympathetic cooling rate almost equals to the heating rate. Here, if the simulation time is long enough, all the final temperatures of the molecular ions will approach absolute zero.

with the barium ions.

However, when m/Q of the molecular ions becomes close to that of the barium ions, the gap between the molecular ions and the barium ions is small enough to neglect this spatial distribution effect, as the green and blue curves shown in Fig. 3.13(b). In this particular simulation, the molecular ion species masses 200 and 800 amu are chosen, but their mass-to-charge ratios are 200 amu/e. Fig. 3.13(b) shows that their sympathetic cooling curves are overlapped very well. Here, although the implemented heating rates on the ions are still $k_B(37.5\ \mathrm{K/s})$, the sympathetic cooling rates are strong enough to overcome the external heating rate. The further simulations show that under the specific trap settings used here when $m/Q \approx 600$ amu/e the sympathetic cooling rate and the external heating rate reach balance at near 200 mK (see the black and red temperature curves).

On the other hand, when the mass-to-charge ratio of the sympathetically cooled ion species is smaller than that of the laser cooled ion species, the ion ensemble always sits inside the laser cooled ion ensemble, so rf heating is low. Thus, when choosing a laser cooled atomic ion species as an efficient coolant two aspects need to be considered: One aspect is that the mass-to-charge ratio of the target species should be smaller than that of coolant. The other aspect, also the most important one, is that the mass-to-charge ratios of the two species should be as close as possible. Of course, in the experiment some other factors such as the accessible equipments are also need to be taken into account. In our group, to cool lighter species such as HD^+, the lightest coolant $^9Be^+$ is chosen. However, for the heavier complex molecular ions, $^{138}Ba^+$ is quite appropriate as coolant.

4 Experimental setup

In this chapter the experimental setup used in the experiment is discussed. It mainly consists of vacuum systems, an ion trap, ion sources, ion detection devices, an octopole ion guide, laser systems, and electronics. The block diagram of the experimental setup is shown in Fig.4.1. In the following sections the functions and parameters of each device will be introduced individually. We first discuss the vacuum system, which consists of a main vacuum chamber and a differential vacuum system with a pressure transition from atmospheric pressure to below 5×10^{-10} mbar. In Sec. 4.2 the linear Paul trap and its external electrical circuits are described. Then, different ion generation methods used in our experiment are addressed (Sec. 4.3). Since complex molecular ions are required to be generated in a universal and soft way, the electrospray ionization method protonates the complex molecules without fragmentation. However, the ionization process happens at atmospheric pressure. Thus, the molecular ions need to be transferred to the trap in a UHV chamber in an opposite way. Sec. 4.4 introduces the octopole ion guide used for this purpose. The fluorescence of the $^{138}Ba^{+}$ ions can be detected by a photomultiplier tube (PMT) or collected to be imaged by an Intensified CCD (ICCD) camera. Ions from the trap can be collected by a channeltron electron multiplier (CEM). These ion detection techniques are presented in Sec. 4.5. In the last section, Sec. 4.6, the working lasers are mentioned briefly. For more details please check the dissertation of Alexander Ostendorf [61]. Other lasers mentioned in this thesis such as UV lasers (266 nm or 313 nm), are provided by other groups [80, 81].

4.1 Vacuum system

Fig. 4.2 shows the scheme of a partial but central part of the experimental setup. Both the top and the side views are given. The main vacuum chamber is the centrum, since the linear Paul trap is located there. Due to the generation of the complex molecular ions under atmospheric pressure, the ions need to be transferred into the trap. However, the crystallization of the barium ion ensemble occurs under the working background pressure at about 5×10^{-10} mbar. Thus, all these components (ESI, differential vacuum chambers, the octopole ion guide, the ion trap, an electron gun, the barium oven, and the main chamber) are required to be enclosed in the vacuum chamber.

4.1.1 Main vacuum chamber

Since the pressure in the chamber needs to be less than 5×10^{-10} mbar, which is in the ultra high vacuum range (UHV), it is important that the chamber and the flange components are clean. Our main chamber is made of a low carbon grade stainless steel noted for high purity and hardness, with CF-flanges. All the flange connections are sealed with oxygen-free high conductivity copper (OFHC) gaskets. It is necessary to use only low-outgassing and low vapor pressure materials for other components. All materials should be able to stand the baking at 250°C for removing water and hydrocarbons adsorbed to

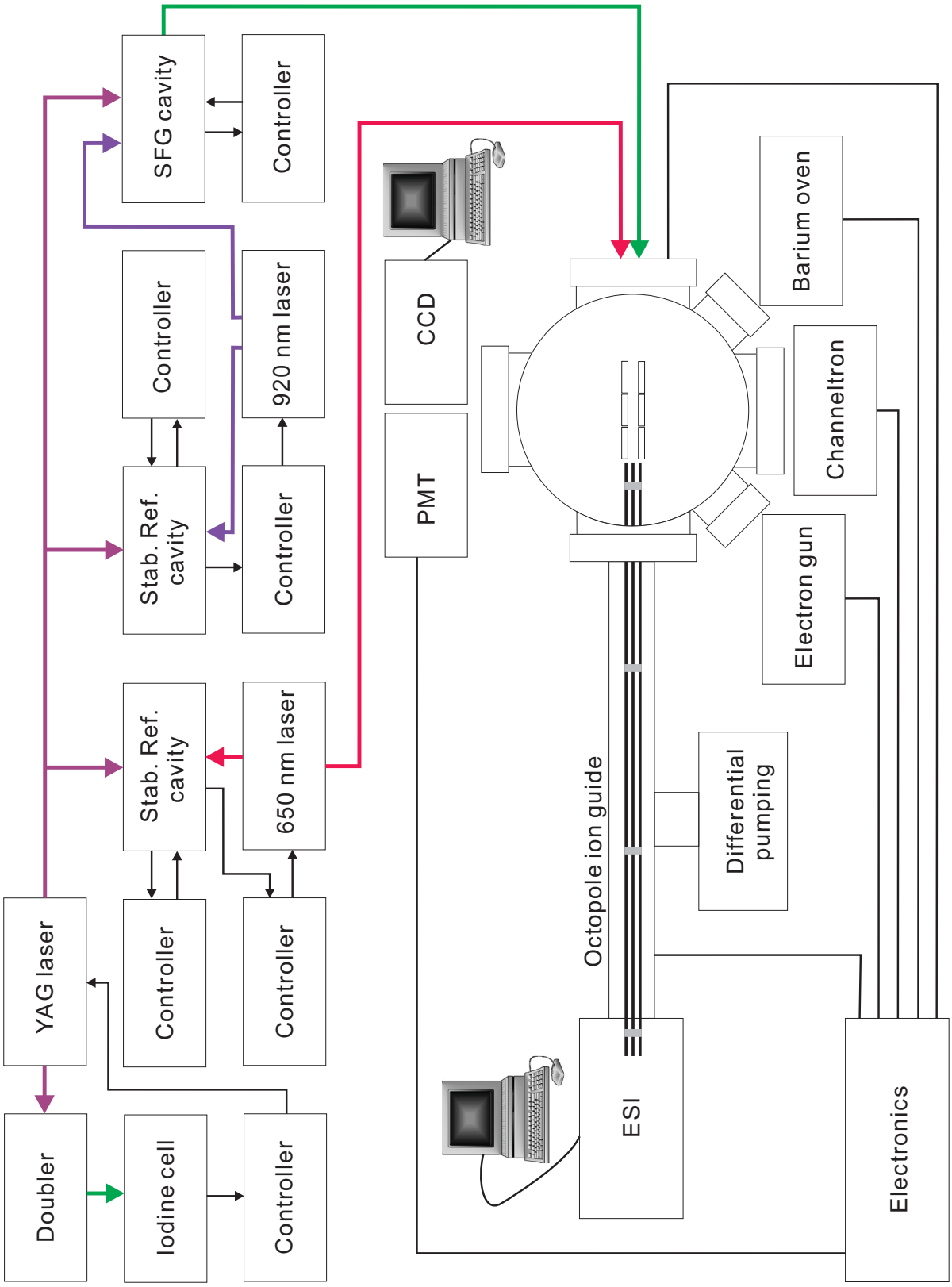

Figure 4.1: Block diagram of the experimental setup.

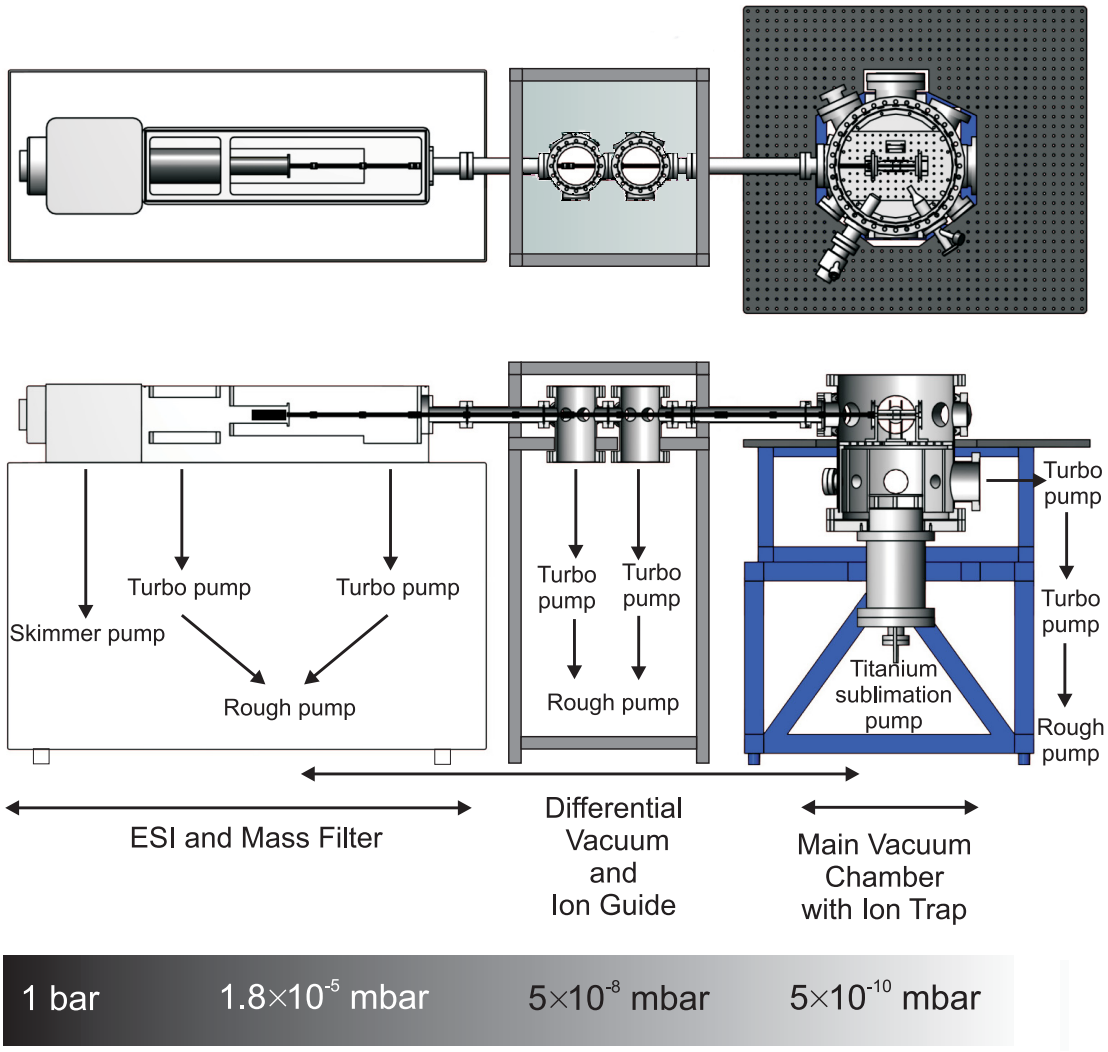

Figure 4.2: Scheme of the entire vacuum setup including ESI, the octopole ion guide, and the main vacuum chamber with the linear Paul trap, an electron gun, and the barium oven [61].

the walls.

The mechanical design of our main chamber is shown in Fig. 4.3. It is a pipe with 300 mm inner diameter and a 3 mm thick wall. The two ends are 300 CF-flanges. Around the side wall there are two virtual planes (Layer 1 and Layer 2), each contains 10 CF-flanges of three types (CF 35, CF 63, and CF 100). As designed the trap center is at the same height level as Layer 1. The laser beams enter into the chamber from the center of the right CF 63 flange and leave it from that of the left, opening for the octopole and connection to the differential vacuum system. Thus, the laser beam is overlapped with the trap axis. The CF 100 flange in Layer 1 and its opposite CF 63 flange are occupied by the fluorescence detectors, an ICCD camera and a PMT. Two flanges with their axes passing through the trap center are used for the barium oven and the electron gun, which can be used as an optical access for other laser beams. Another four flanges can be used for the connections of electrical wires. Here, we use one CF 35 flange lo-

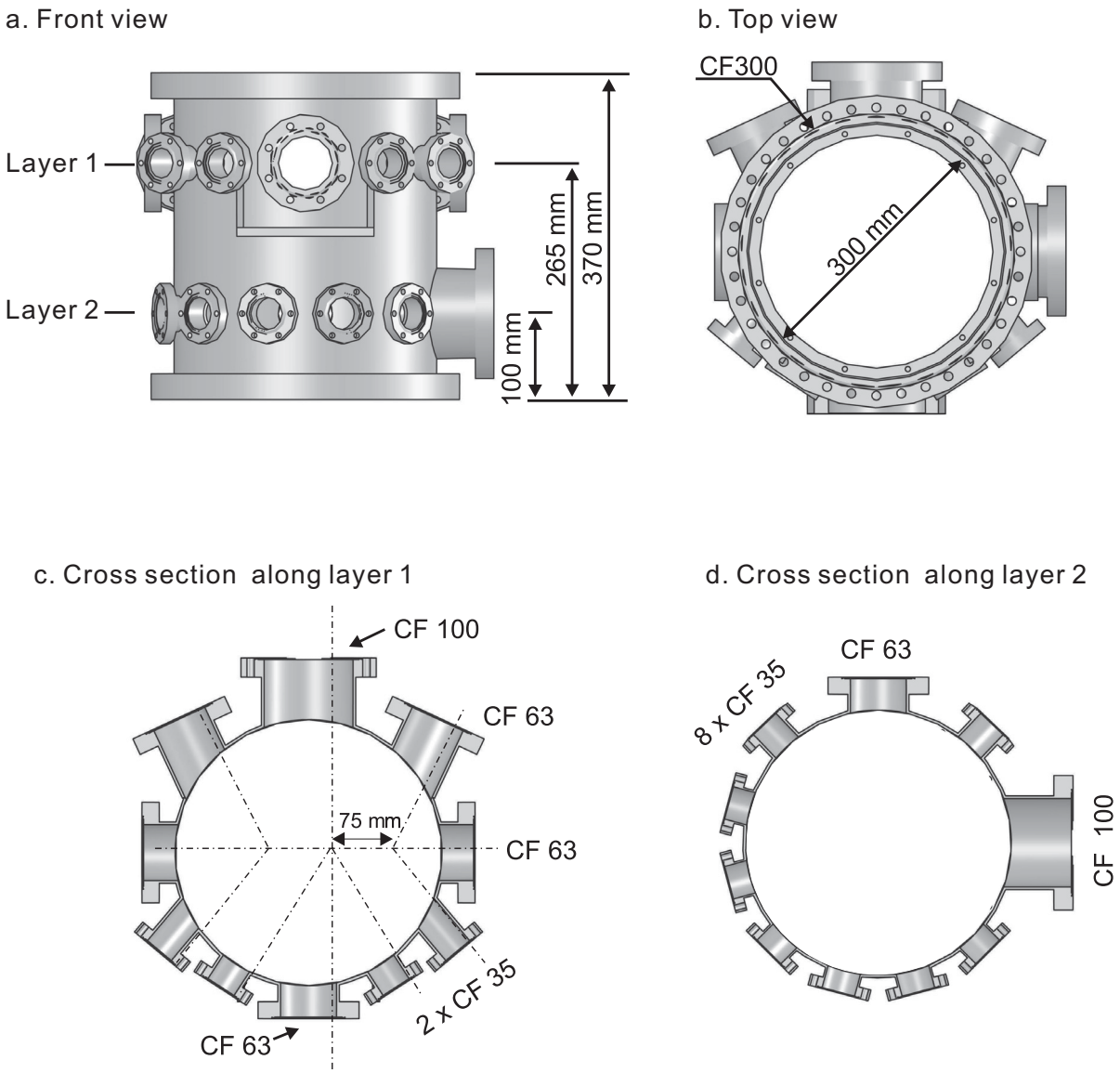

Figure 4.3: Mechanical drawings of the main chamber [61].

cated at the bottom left in Fig. 4.3(c) and another one at the bottom right for the wire connections of the channeltron and the copper wire coils. The flanges in Layer 2 are supplements. Flanges of CF 100 and CF 63 are connected to a turbo molecular pump (Pfeiffer, TMU520) and a restgas analyzer (RGA), respectively. One CF 35 flange is used as a wire connector between trap and its external electronics. One is employed by a leak valve. Another one is used by an ion gauge to measure the pressure of the main chamber.

The main chamber is mounted in a hole of an optical table as shown in Fig. 4.2. This optical table is not only the worktable for coupling the laser beams to the trap but also a height reference. It becomes much more convenient than taking the trap center as the height reference due to its enclosure by the chamber.

In order to achieve the (UHV) condition around 5×10^{-10} mbar, a turbo molecular pump (Pfeiffer, TMU520, 520 L/s) is implemented. The low pressure limit for this kind

of pump is about 5×10^{-11} mbar. When it works, another turbo molecular pump (Pfeiffer, TMU261, 210 L/s) is required to create a prevacuum, which is 10^{-5} mbar. A prevacuum ($\approx 8\times10^{-3}$ mbar) for this turbo pump is created by a rotary vane pump. Normally, in our case, the minimum pressure directly created by these pumps is about 2-3$\times10^{-9}$ mbar after one week bakeout at around 200 °C. The bottom of the main chamber is connected with a home-made titanium sublimation pump (three removable hairpin shaped filaments mounted on low electrical resistance electrodes). After running the titanium sublimation pump once or twice (each time one filament works at 40 A for about 20 minutes and the wall of the pump, about 500 cm^2, is cooled by water all the time at 12°C), the pressure of the main chamber is brought down to the working pressure 5×10^{-10} mbar. In best cases, 2×10^{-10} mbar are reachable. The pressure is monitored by an ion gauge. And the content of the residual gas can be checked via a restgas analyzer (Balzers, QME 112).

Since the main chamber is connected to the atmosphere via the ESI system, even worse, the ionization process of the complex molecules is realized just before the vacuum, i.e, water molecules have much higher possibility to enter into the main chamber, the vacuum degree of the main chamber becomes worse and worse with time. Usually, another bakeout of the main chamber is better to be done after serval months depending on the frequency of the loading of the complex molecular ions.

4.1.2 Differential vacuum system

If the main chamber was connected with the ESI system directly, its reachable minimum pressure would be in the order of 10^{-8} mbar or even worse. With such high background pressure it would be impossible to cool a barium ion ensemble to the crystalline state by laser cooling due to the strong heating effect from the collisions with the neutral residual gas molecules. Thus a differential vacuum system is necessary to offer a pressure transition from atmospheric pressure to the required working pressure for the laser cooling of a barium ion ensemble to crystalline state.

The differential vacuum system consists of two connecting tubes (CF 35) and two differential vacuum chambers (65 mm inner diameters, CF 100), (see Fig. 4.4). A turbo molecular pump (Pfeiffer, TMU261, 210 L/s) is connected to the differential vacuum chamber close to the ESI system. Another differential vacuum chamber is connected with a second turbo molecular pump (Pfeiffer, TMU520, 520 L/s). The prevacuum for these two turbo molecular pumps is created by a rotary vane pump. The scheme of the differential vacuum system and the pressure transition are also shown in Fig. 4.2.

Since the ESI system itself has two turbo molecular pumps, normally, the pressure at the end of the system is about 1×10^{-5} mbar. Therefore, the created pressure transition by the differential vacuum system is from 1×10^{-5} mbar to 5×10^{-10} mbar. If the faster turbo pump for the differential vacuum system is omitted, only 7.5×10^{-9} mbar minimum pressure can be reached [61].

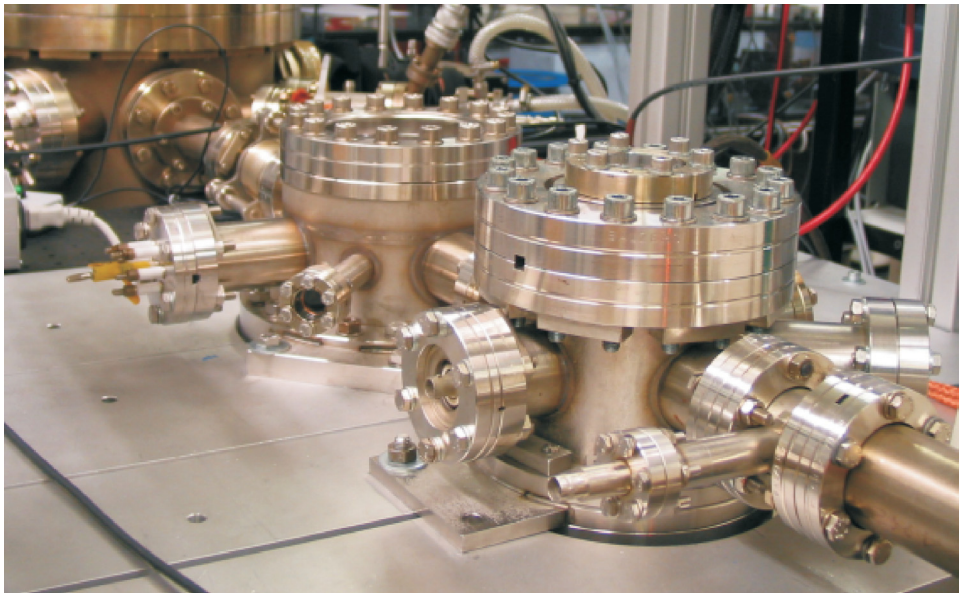

Figure 4.4: Differential chambers. Turbo molecular pumps are mounted under the table.

4.2 Ion trap

A stainless steel plate with threaded holes is mounted in the vacuum chamber parallel to the optical table. The core device is the linear Paul trap, which is mounted in the center of the plate as shown in Fig. 4.5. The trap center is to be kept in Layer 1, which is described in the last section and shown in Fig. 4.3. The trap axis is superposed on the axis of the two opposite CF 63 flanges.

4.2.1 Mechanical design

Our linear Paul trap consists of three quadrupole mass filters in series and two identical sets work as endcap electrodes (as described in Chapter 2). All the 12 quadrupole electrodes are circular rods with a diameter of 10 mm. The lengths of the endcap and middle electrodes are 30 and 20 mm, respectively. Three electrodes from each quadrupole mass filter form a group longitudinally and are mounted together by a polar holder with small macor rings keeping them out of contact (gap width 0.5 mm). Each electrodes has two vent holes, and a thread hole for attaching a wire for electronic connection. The mechanical design and the alignment of all electrodes are shown in Fig. 4.6. According to the rule of Eq. (2.7) the distance from the trap axis to the surface of the electrodes is about 4.36 mm. The distance between the trap center and the base plate is 70 mm.

4.2.2 Electrical power supplies

In order to operate the trap, appropriate power supplies are necessary. An rf power supply is used to generate the rf voltage to confine the ions radially. For different purposes, other various types of DC power supplies are used, for example, using quadrupole DC voltages for mass selection, individual small DC voltages on middle electrodes to correct voltage offsets, and DC voltages on the endcap electrodes giving the longitudinal confinement of ions. In our case, secular excitation (see Chapter 9) is usually used to

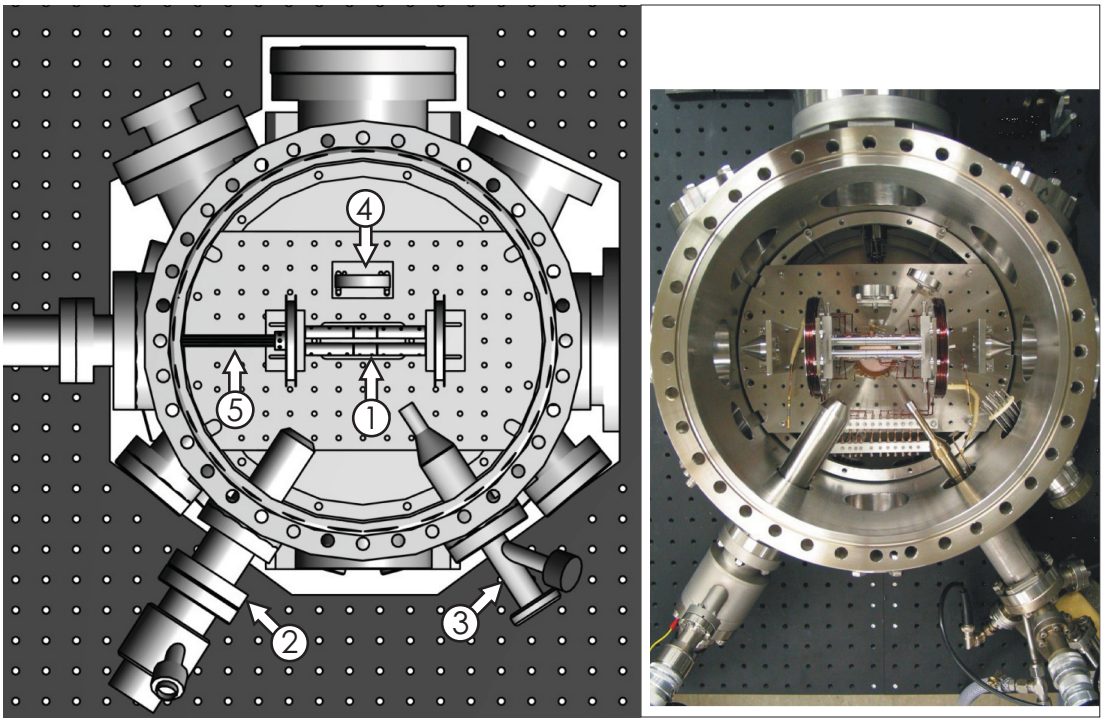

Figure 4.5: Main chamber with the linear Paul trap inside [61]. The elements: 1. trap, 2. electron gun, 3. barium evaporator oven, 4. optics, 5. octopole ion guide.

detect the ion species or to remove specific ion species. Thus, an AC power supply with frequency sweeping from 10 kHz to about 1 MHz is required. The wiring diagram of all the electronics connected for the trap is shown in Fig. 4.7.

4.2.2.1 Rf power supply

The rf voltage is required to confine the charged particles in the linear Paul trap (see Sec. 2.2 of Chapter 2). In our trap, the three mass filters share one rf voltage. The longitudinal confinement is realized by the difference of the DC potentials between the endcap electrodes and the middle electrodes.

The sine rf voltage is initially generated by a function generator (Agilent, 33220A). The low-amplitude rf signal is amplified by a 25 W rf power amplifier (Amplifier Research) and sent to a transformer to be resonantly enhanced. The resonant frequency and amplitude of this circuit are determined by the diameter and the number of windings of the coils and the trap capacities. In our case, the resonant frequency is 2.5 MHz and the maximum output amplitude is about 500 V. Out of the resonance, the maximum amplitude decreases and the rf voltage on the trap is no longer proportional to the signal amplitude behind the rf function generator.

The transformer has a ferrite ring and is housed in an aluminium box, which keeps other sensitive instruments in the lab, such as the laser-locking circuits, out of the rf radiation. The printed circuit board is located in another housing, which is at ground. In order to reduce capacitances associated with cable length, this box is mounted above the vacuum feedthroughs directly.

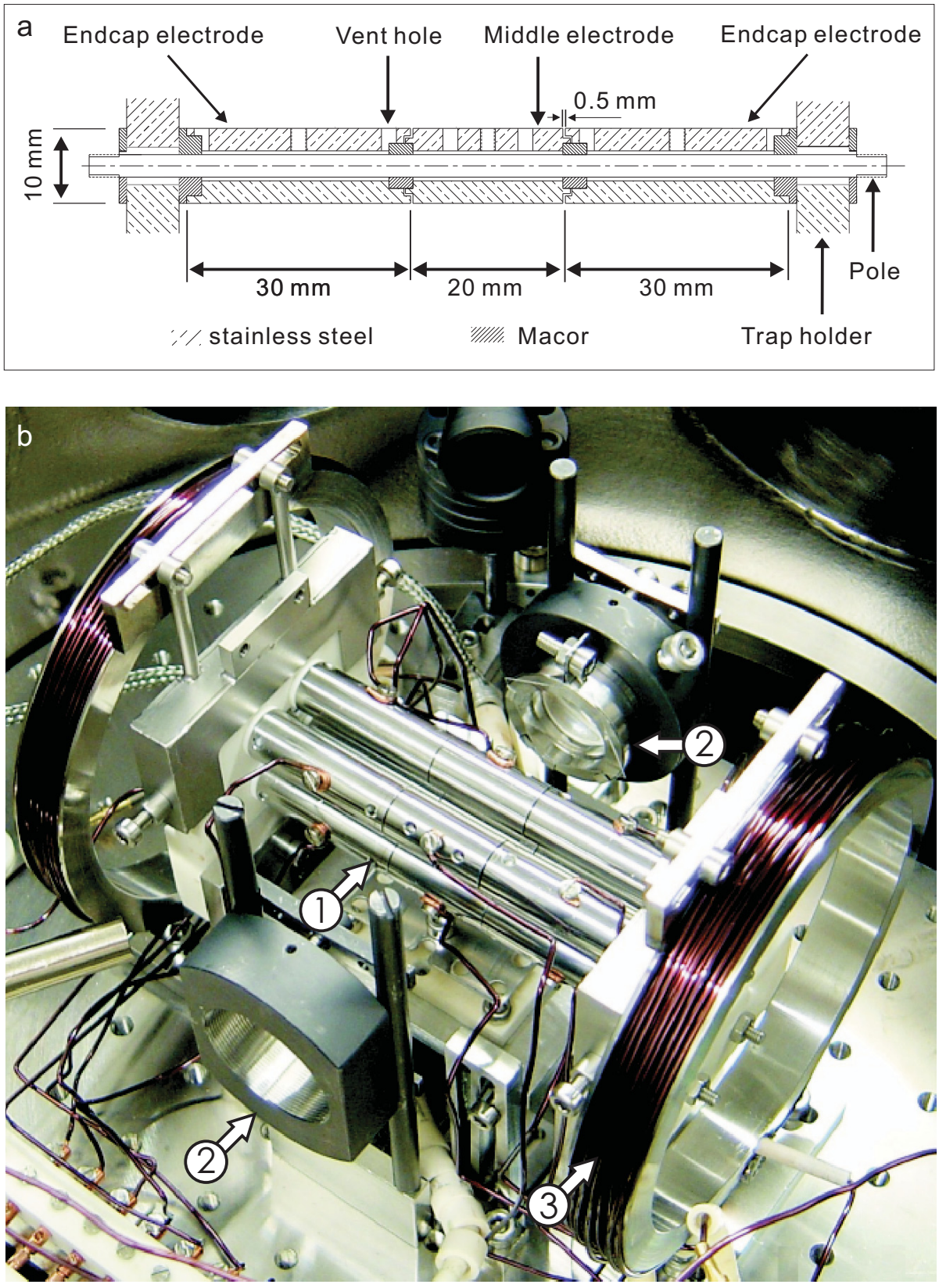

Figure 4.6: Linear Paul trap and the mechanical drawing of the electrodes. The elements: 1. trap, 2. optics, 3 coils.

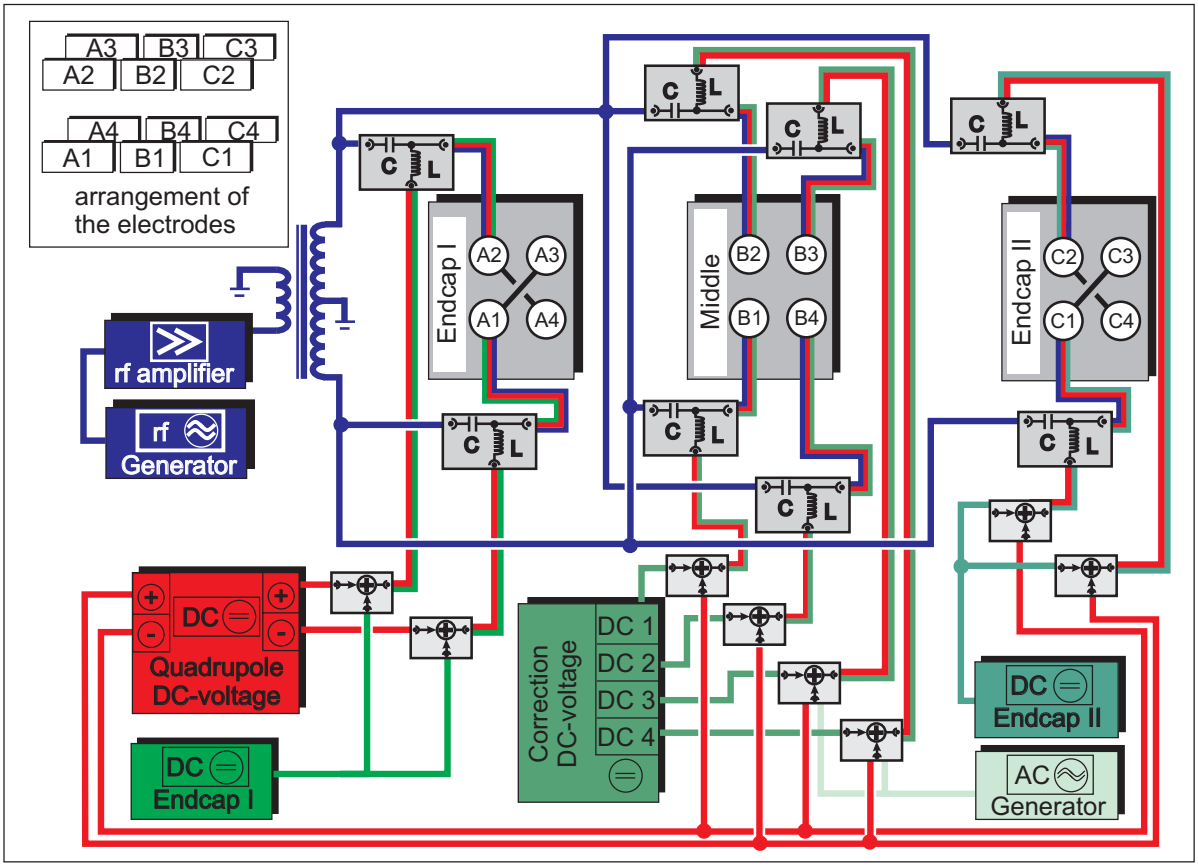

Figure 4.7: Block diagram of the trap power electronics [61].

The rf voltages on the trap electrodes are displayed on an oscilloscope have the following calibration: 1 V on the oscilloscope and gives 100 V to the trap. Through the comparison with some experimental results, this calibration drifts within approximately 5%. More precise calibration for a specific case can be done via a measurement of the secular resonance frequency of a pure barium ion ensemble.

4.2.2.2 DC power supply

The quadrupole DC voltage ($V_{dc} = 0 \ldots 20V$), as shown in Fig. 4.7, is implemented to all electrodes symmetrically increasing the potential of the one half of electrodes by $V_{dc}/2$ and lowering the other half by $-V_{dc}/2$. By varying this voltage, ion species change their position in the stability diagram (see Sec. 2.2 of Chapter 2). Thus, some ion species can be moved to an instability area and kicked out from the trap. This is an additional mass selection option. In our experiments, we normally remove unwanted ion species via strong excitation of their resonance frequencies or by lowering the rf voltage whereupon the trap depth decreases and ions of a high mass-to-charge ratio escape first. Hereby V_{dc} is always set to be zero in our experiments.

Due to electrostatic charges or contact potentials on the electrode surfaces the electrical field in the trap can drift. The position of an ion ensembles would shift accordingly. A DC power supply offers individual correction voltages (-24 V...24 V) to each middle

electrodes. On the other hand, with the help of this DC power supply we can easily control the position of ion ensembles radially to better understand their properties and mutual interactions.

Another DC power supply is used for the endcap electrodes. Not each electrode has an individual DC potential as the middle the electrodes do, but four electrodes at one trap end share one DC potential. This DC power supply helps to confine the ions in the axial direction and by varying the potentials the ion ensembles can be pushed to the left or right side.

Besides the rf power supply and several other DC power supplies, we have another AC power supply, whose oscillation frequency, from 10 kHz to 1 MHz, covers the secular frequencies of our interested ion species. This AC voltage is used to modulate the rf amplitude on the two top central electrodes. By a frequency sweep in a certain range with an appropriate amplitude, the ion species, whose secular resonance frequency is within this range, can be excited. For this, an AC signal with a few millivolts or several volts is generated by a function generator (Agilent, 33220A) and attenuated to some millivolts or even a few micro-volts.

4.2.3 Magnetic field

As discussed in Chapter 3, in order to cool $^{138}Ba^{+}$ ions by lasers, a weak magnetic field is required to generate the Zeeman splitting of the energy levels of the ions. This magnetic field is generated by two coils, which are mounted on the two trap holders as shown in Fig. 4.6. The mean diameter of the 56 windings of the two coils is about 87.5 mm. A current I passing through the coils results in a magnetic field B along the trap axis. B (in the unit of Gauss) near the trap center is expressed as

$$B = 10^4 \mu_0 N I \frac{R^2}{\sqrt[3]{R^2 + (d/2)^2}} = 3.92 \times I, \tag{4.1}$$

here μ_0 is magnetic permeability of vacuum and N is the number of windings. R and d are the diameter of the two coils and their distance, respectively. In our case, the current I is set be 1.5 A. Thus, the magnetic field in the trap center is about 5.87 Gauss. Therefore, the corresponding energy change for each substate is given by Eq. (3.36), for example, the energy change of the two substates of the ground state $6^2S_{1/2}$ is ± 8.2 MHz.

4.3 Ion sources

In this section we introduce three different techniques, which are used in our experiment, for the production of ions to be trapped and cooled.

4.3.1 Barium ion source

The barium ions are produced in an UHV suitable electron beam evaporator. Fig. 4.8 shows the wiring diagram of the barium oven. Solid barium metal is filled in a tungsten crucible, to which a high voltage of 2 kV is applied. In front of the crucible there is a tungsten filament. When the filament is ignited, electrons are emitted and accelerated

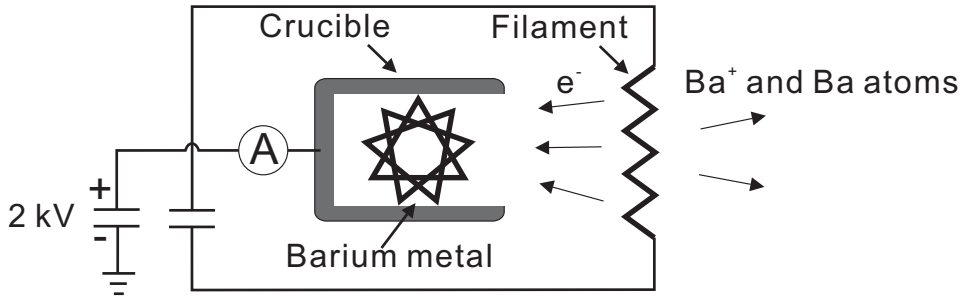

Figure 4.8: Wiring diagram of the barium oven.

by the positive high voltage on the crucible to hit the barium sample. Barium atoms are evaporated from the sample and some of them are singly ionized. These barium ions are pushed away from the crucible and guided to the trap by a metal tube, which is mounted behind the filament and points to the trap center.

There are three disadvantages of using this technique. One is the low ionization coefficient. Small fractions of the evaporated barium atoms are ionized and many barium ions are lost on the way to the trap. Another disadvantage is that in the ionization process not only the barium atoms but also some residual gas such as CO_2, are charged and trapped. The presence of the sympathetically cooled ions slows down the barium cooling process and even prevents the barium ion ensemble from crystallization. The third disadvantage is that when the barium ions approach the trap, it can be accelerated by the rf voltage. The gained kinetic energy might be several hundred eV. Thus, some ions escape before being captured and some hit the trap electrodes being absorbed.

Comparing to the case of being charged by a electron gun or photoionization, this method is more convenient to operate and the loading of the barium ions is more controllable and efficient.

4.3.2 Ions from background gas

An electron gun is mounted orthogonally to the barium oven. Produced electrons with energies between 50 and 1500 eV are focused to the trap center. Normally, the diameter of the electron beam is a few mm and the beam current is about 100 μA. Behind the trap there is a phosphor plate. The electron beam is stopped by this plate generating fluorescence, which can be used to check the characteristic of the electron gun.

If neutral atoms or molecules collide with electrons there, they can be ionized. Gas phase molecules or atoms can be easily injected into the main chamber through a leak valve. Usually, the vacuum pressure arising to 10^{-8} mbar is enough to generate a sufficient number of charged gas molecular ions in a few seconds. By closing the leak valve, most types of the residual neutral molecules can be pumped away in a short time.

4.3.3 Complex molecular ion source - ESI

The main goal of our experiment is to sympathetically cool big molecular ions (masses from hundreds to tens of thousands amu). Typically, these are biomolecules such as

dyes, amino acid, proteins and peptides, and exist as the form of solid or dissolved in a suitable solvent. An appropriate way needs to be found to charge and transfer them into the gas phase without damaging their molecular structures and characteristic properties.

Traditionally, to charge molecules, besides the method of electron impact (EI) ionization, photon impact ionization [82] and chemical ionization (CI) are options. However, in most cases, due to the relatively strong delivered external energy and the complexities of the molecules, they can be fragmented easily.

Thus, several other techniques such as secondary ion mass spectrometry (SIMS) [83], field ionization (FI) [84], fission fragment ionization (also called plasma desorption ionization mass spectrometry, PDMS) [85, 86], and matrix-assisted laser desorption/ionization (MALDI) [87] have been developed to avoid fragmentation. Due to individual disadvantages of each method for our experiment, we finally decide for the widely used electrospray ionization (ESI) method.

4.3.3.1 Principles of ESI

In the electrospray ionization process, the target compound is dissolved in a solvent, which is usually much more volatile than the target sample. The solution is pushed through a small metal capillary by a syringe, which is driven by a motor. Since a positive high voltage is applied to the capillary, in order to balance the electric field between the capillary and the surface of the solution, positive charges are pushed to the tip and negative charges are dragged back. A so-called Taylor cone is formed at the end of the capillary. Droplets are ejected from this cone and collide with air forming an aerosol. A neutral sheath gas such as nitrogen is used to nebulize the droplets and evaporate the neutral solvent. The capillary behind the needle is heated to evaporate the solvent. As the solvent evaporates, the volume of droplets becomes smaller and smaller. Thus, the charge density of the droplets becomes higher and higher. At a critical volume, the charge repulsive force breaks it into some smaller droplets. This phenomenon is the so-called Coulomb fission. The process repeats until the molecules of the target sample are free of solvent and become a single ion. The principle is also shown in Fig. 4.9. In fact, the exact mechanism of the process is still in debate [88]. The development of electrospray ionization for the analysis of biological macromolecules was rewarded [89] with the Nobel Prize in Chemistry to John Bennett Fenn in 2002.

Actually, the final singly charged ions are quasi-molecular ions protonated by adding a proton, a hydrogen ion, and denoted $[M+H]^+$, or sodium adducts ($[M+Na]^+$), or the proton is removed ($[M-H]^-$). More complex ions are normally multi-protonated ($[M+NH]^{N+}$). In our case, only the protonated ions are selected. Usually, to charge the target molecules, acids are added to the solution.

4.3.3.2 Advantages of ESI

Why from our point of view is the ESI in combination with a mass spectrometer (ESI/MS) our best choice? Because the ESI/MS has some advantages:

- ESI is applicable to both small and large complex molecules with a mass higher

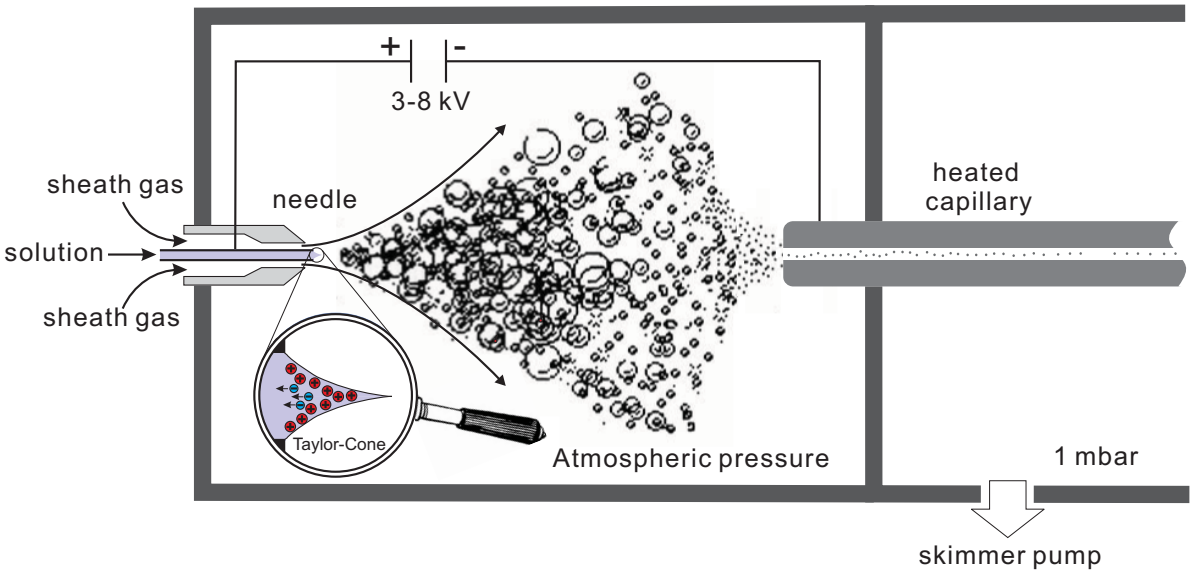

Figure 4.9: Principle of the electrospray ionization (ESI).

than 20.000 amu.

- ESI is a soft ionization method preserving the molecule structure.
- Commercial ESI sources with an integrated mass spectrometer are available.
- Impurities of the target molecular ions can be removed before loading them into the trap.
- The target sample is easily replaced by changing the solution.
- ESI allows producing highly charged ions and molecular ions of a certain charge number can be selected instantly.

4.3.3.3 Structure of ESI

In our experiment, the commercial ESI/MS system Finnigan SSQ700 is used. The central part is shown in Fig. 4.10. The solution in a syringe is pumped by a motor (Harvard Apparatus, model 22) passing through an fused-silica capillary (50 μm inner diameter and 190 μm outer diameter) and the high voltage needle to form an aerosol under the atmospheric pressure with the help of a nitrogen sheath gas at a pressure of 5 bar. The infusion rate of the solution is usually 5 or 20 μl$\cdot$min^{-1}. Behind the needle (15 mm) there is a heated capillary (inner diameter 250 μm) at a temperature of 200...400°C. A rotary vane pump is connected to the cell wit the capillary lowering the pressure to about 1 mbar. When the molecular ions leave the capillary, they are transferred into the quadrupole mass filter by a short octopole ion guide, below which there is a turbo pump to generate a lower pressure - in the order of 10^{-3} mbar. The quadruple mass filter selects the molecular ions with a chosen mass-to-charge ratio. Behind the mass filter there is a big cell with another turbo pump. The pressure in this area is in the order of 10^{-5} mbar, which is acceptable for an ion counting device (channeltron, discussed in

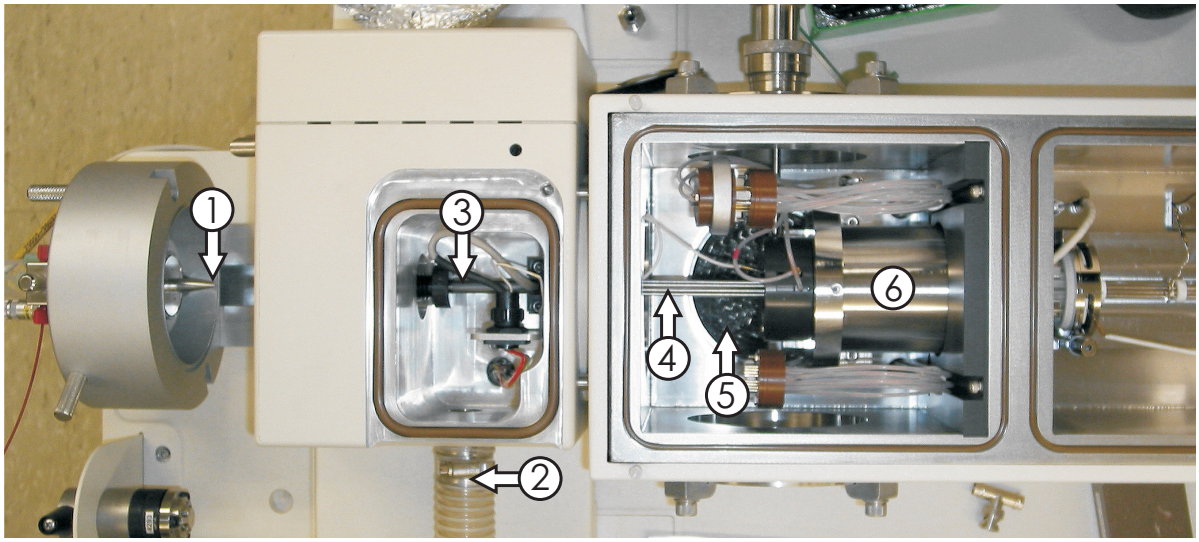

Figure 4.10: Central part of ESI/MS. The elements: 1. needle, 2. tube to a rotary vane pump, 3. heated capillary, 4. octopole ion guide, 5. turbo molecular pump, 6. quadrupole mass filter.

Sec. 4.5).

In principle, all the parameters of this ESI/MS system such as voltages for different elements, temperature, air flux and solution pumping speed, can be set, monitored, and modified by a host computer.

4.3.3.4 Mass spectra

Fig. 4.11 shows a mass spectrum obtained in our ESI/MS system. The solution is a mixture of peptide MRFA (methionine-arginine-phenylalanine-alanine, mass 523.7 amu) and horse skeletal muscle myoglobin with a concentration of 20 and 5 pmol·μl^{-1}, respectively. The solvent is a 50 : 50 methanol/water solution containing 0.5% acetic acid. This solution is usually used for a routine calibration of the system. There are two mass peaks at 524 and 263 amu/e corresponding to singly and doubly charged MRFA, respectively. In the higher mass range, a series of mass peaks are from the highly charged myoglobin. Since the mass of myoglobin is 16955 amu, from the peak positions the number of attached protons can be found. In Fig. 4.11 the corresponding charge numbers from 14 to 25 are distinguishable. No fragments are shown in this figure.

4.3.3.5 Ion flux

The ion flux or the charging efficiency for different ion species varies depending on the molecular species, concentration of the molecule and acid in the solution, and ESI settings parameters such as the needle voltage, sheath gas flux, and capillary temperature. Taking MRFA as an example, under an optimal setting a flux of more than 100 thousand ions per second is possible behind the quadrupole mass filter. In principle, the ion flux itself is not so important, since the extension of the loading time or an increase the buffer gas pressure can compensate the low flux, but higher fluxes make it easy for us to control the loading of the molecular ions in the experiment.

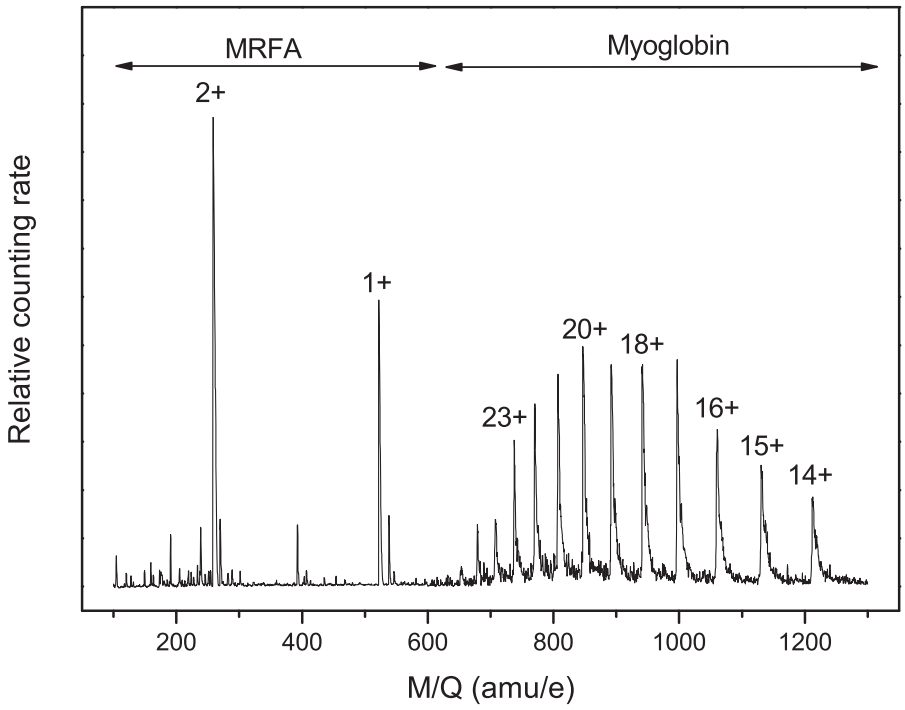

Figure 4.11: Mass spectrum of a mixture of MRFA and myoglobin.

4.4 Transport of complex molecular ions

To realize the pressure transition from the atmospherical pressure to about 5×10^{-10} mbar, a differential vacuum system is implemented resulting in a big gap between the ion source and the linear Paul trap. Therefore, an ion guide is required to transfer the molecular ions from the ion source to the trap. In Chapter 2, the ion confinement of a quadrupole in the radial direction was discussed. Here, we use another rf ion guide - an octopole, which is widely used for guiding slow ions.

4.4.1 Theoretical background of octopoles

For $N > 2$, the rf potentials $\frac{1}{2}(V_{dc} - V_0 \cos\Omega t)$ and $-\frac{1}{2}(V_{dc} - V_0 \cos\Omega t)$ are applied to adjacent electrodes as in case of the quadruple. The x and y motions are no longer decoupled. The pseudopotential is given by [90]

$$\Psi_{2N}(\widehat{r}) = \frac{N^2 Q (V_0/2)^2}{4m\Omega^2 r_0^2}\widehat{r}^{2N-2} + \frac{1}{2}V_{dc}\widehat{r}^N \cos n\varphi, \tag{4.2}$$

here $\widehat{r} = \boldsymbol{r}/r_0$. $2N$ is the number of electrodes, for example, $N = 4$ for an octopole. $(\widehat{r}, \varphi)$ represents the plane polar coordinates. In the case of $V_{dc} = 0$, the second term vanishes. When $N = 2$, the pseudopotential is consistent with the form of quadrupole (Eq. (2.37) with $V_{ec} = 0$).

Fig. 4.12 shows the normalized pseudopotentials of quadrupole and octopole as a function of the distance from the centerline with $V_{dc} = 0$ (plotted according to Eq.4.2). The octopole has a flatter pseudopotential near the octopole axis and a steeper one close to

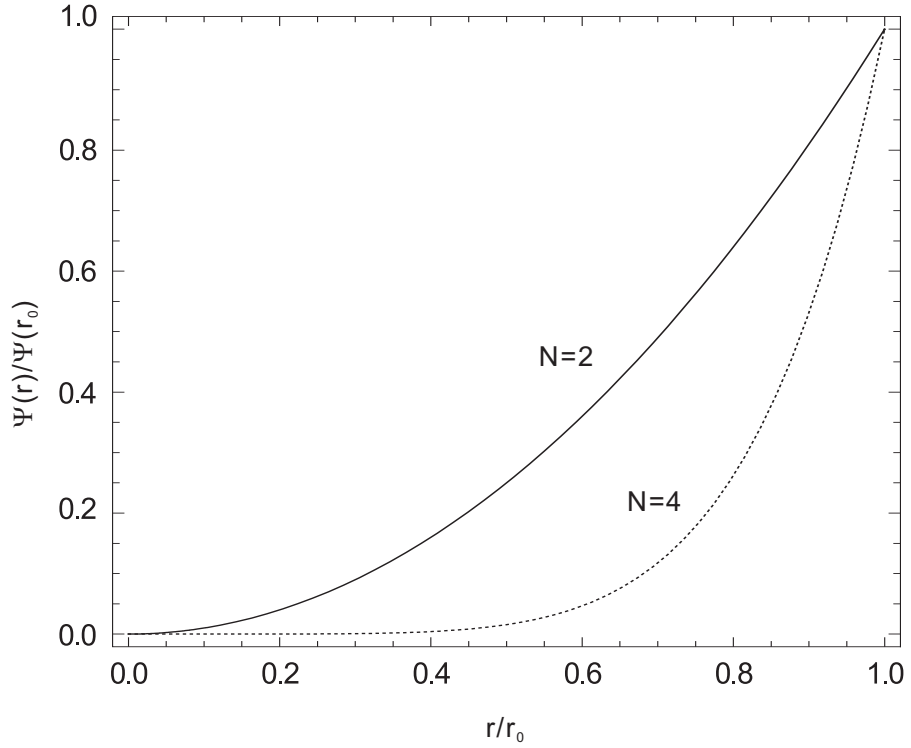

Figure 4.12: Pseudopotential of quadrupole ($N = 2$) and octopole ($N = 4$) obtained from Eq. (4.2).

the electrodes, which helps to minimize the ion loss.

The adiabaticity parameter η (see Gerlich-review) [90] is given as

$$\eta = 2N(N-1)\frac{Q(V_0/2)}{m\Omega^2 r_0^2}\widehat{r}^{N-2}, \tag{4.3}$$

and the reduced amplitude of micromotion, $\widehat{a} = \boldsymbol{a}/r_0$, has the form

$$\widehat{a} = \frac{NQ(V_0/2)}{m\Omega^2 r_0^2}\widehat{r}^{N-1}(-\cos(n-1)\varphi, \sin(n-1)\varphi). \tag{4.4}$$

For an octopole, $\eta < 0.3$ is the stability condition extracted from numerical simulations [90].

4.4.2 Structure of the octopole

One end of our octopole (just behind the mass filter) is shown in Fig. 4.13. The whole octopole is about 1900 mm long, passing through the entire differential vacuum system. Since the other end of the octopole is plugged about 10 mm into the trap to improve the capturing efficiency of the molecular ions, the outer diameter of the octopole should be less than $2r_0$ of the trap. Furthermore, a small diameter of the octopole decreases the inner cross-section of the air passage (also the passage for the complex molecular ions) benefiting the pressure transition. The octopole in our setup is designed to have 5.52 mm inner diameter and 8.69 mm outer diameter. The diameter of the electrodes is 1.58

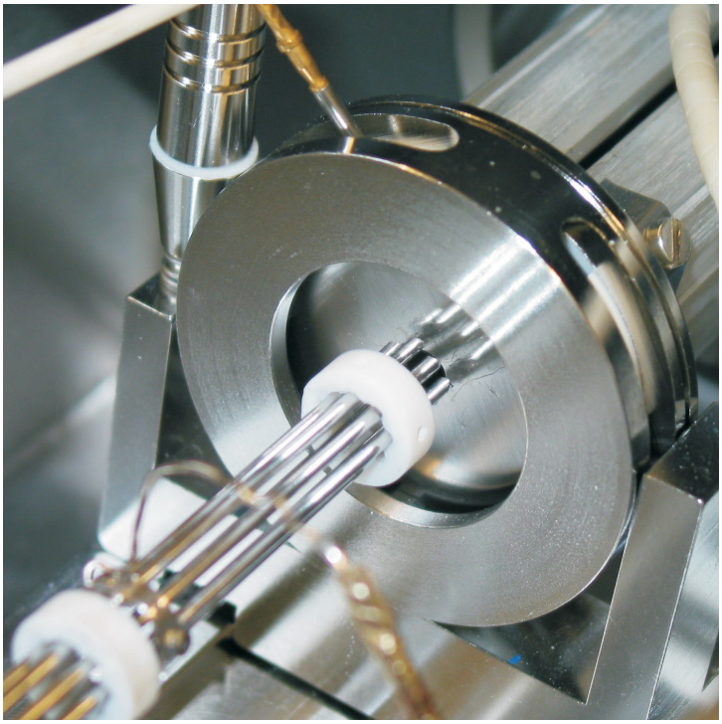

Figure 4.13: End part of the octopole together with the mass filter.

mm. Each of the two four-electrode groups is assembled by metal rings with an interval of 200 mm. Macor rings are used to keep the two electrode groups apart and also act as holders for the octopole. Some of these macor rings fit with the vacuum tube very well only leaving the inner cross-section of the octopole open.

In fact, an octopole has several additional advantages. One is the multi-pole structure that helps shielding the disturbance of external fields more efficiently. Another one is the multi-pole structure which makes such a long setup to be mechanically more robust. Furthermore, the symmetry of the octopole field is relatively insensitive to deviations from the ideal arrangement of electrodes.

4.4.3 Octopole parameters

Ions can be transferred by this octopole guide only when the stability condition $\eta < 0.3$ is satisfied and the potential well of the octopole is deep enough. From Eq. (4.3) we can see that η is proportional to the magnitude of the applied voltage and inversely proportional to the square of the frequency. For a specific voltage a higher frequency is helpful to reduce the η value.

For our setup a rf generator has been developed as shown in Fig. 4.14. Frequencies between 2.8 MHz and 3.7 MHz are available. The voltage is tunable from 0 to 600V (peak-to-peak). The DC voltage is set to be zero normally. However, we have an additional DC offset, from 0 to -30 V, applied to all eight electrodes for the acceleration of ions along the guide to improve the transfer efficiency. In most cases, the rf voltage is set to be 240 V at 3.3 MHz with -27 V DC offset. With this set of parameters,

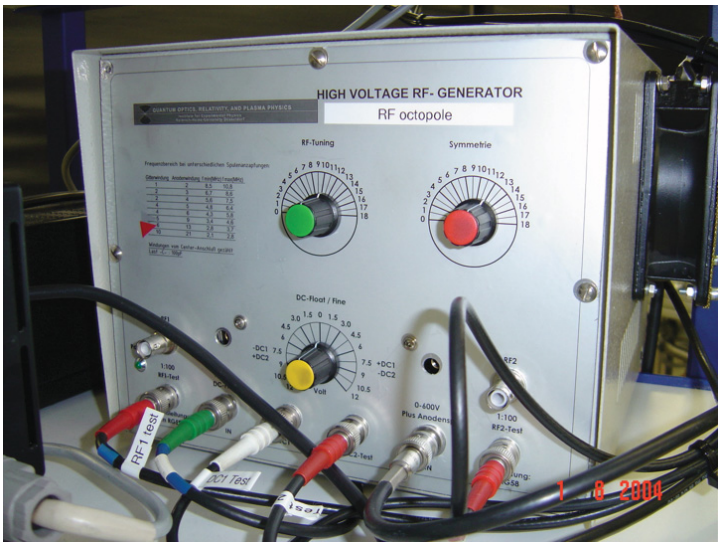

Figure 4.14: Rf generator for the octopole ion guide.

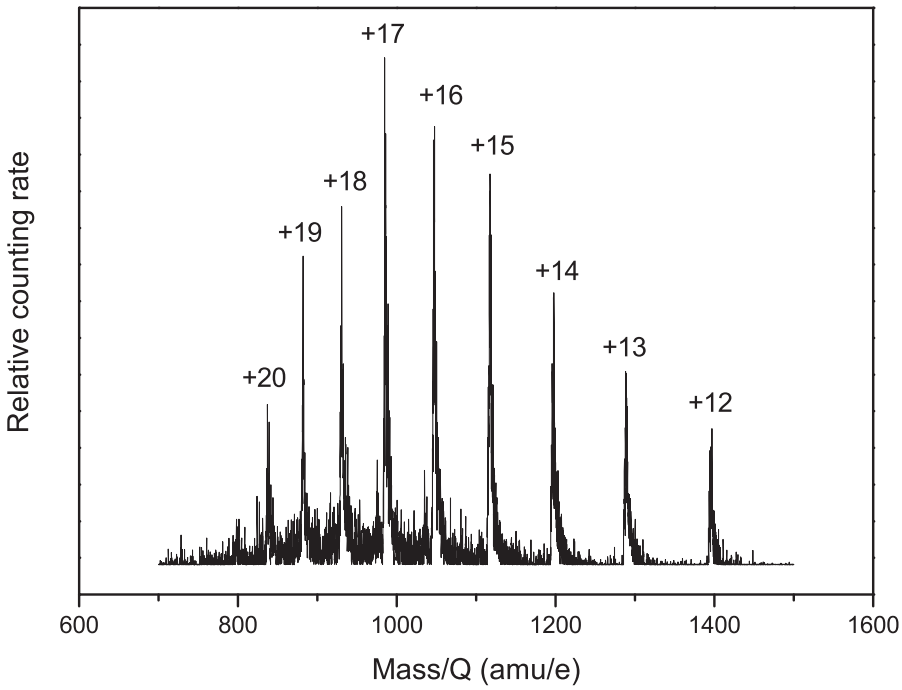

Figure 4.15: Mass spectrum of myoglobin behind the long octopole ion guide.

the stability condition is satisfied for the ions in our range of interest and an ion flux greater than thousand ions per second is always obtainable with the mass-to-charge ratio between a few hundred to about a thousand amu/e. Fig. 4.15 shows an example of the mass spectrum of myoglobin (here the deviation of the peak position is from the ESI system, which requires to be calibrated). In doing this mass spectrum a detector is set behind the long octopole ion guide. This spectrum shows that the octopole can transfer the ions efficiently.

4.5 Ion detection

Ions can be detected and counted by a channeltron electron multiplier (CEM) directly. Using laser cooling there is a by-product - the fluorescence, which can be detected by a photomultiplier tube (PMT). When the laser-cooled ion ensemble is cooled to liquid or crystal state, it can be imaged by a CCD camera as well.

These detection method enable us to obtain a lot of information such as ion numbers of each ion species (in combination with simulations) and even dynamics of the ion cluster. With the help of other techniques such as secular excitation and molecular dynamics simulations, more properties can be studied.

4.5.1 CEM

When a positive ion leaves the octopole or is extracted from the ion trap, it is accelerated by an extraction plate (a hole in the center as the ion passage), which is mounted under the central trap electrodes and operates with a negative high voltage (about -1.5 kV). When an ion strikes the inner side of the CEM, electrons are created and multiplied. Finally, the electron flux pulse is sent to the electronics as the signal to be amplified, discriminated, and converted to TTL pulses, which are counted by counting electronics and recorded using a LabView program. The voltage applied on the CEM is about 3 kV. Thus, a CEM can be used to count the ion number or the ion flux.

Additionally, the destructive method can also be used to get the information about the temperatures and ion species of an ion system qualitatively. The velocity of ions has a distribution, especially, at high temperatures the distribution is quite broad. When do a extraction by lowering the rf voltage gradually (means lowering potential depth (see Eq. (2.37))), the hotter and heavier ions escape from the ion trap first, so different ion species should be distinguishable in an ion extraction spectrum and the peak width for each ion species indicates its temperature. Actually, the mass spectrum done through this method is not expected to have a very high resolution for the determination of the temperatures of ion ensembles and their mass-to-charge ratios.

4.5.2 CCD

In our experiment, barium ions scatter 493 nm light. The emitted photons passing through a gap of two adjacent central trap electrodes are collected by a lens with a short focal length (50 mm) and focused into the ICCD camera (Andor iStar, DH734) by another lens, which focal length is 400 mm. The first lens is mounted inside the vacuum chamber with the distance of its focal length from the trap center as shown in Fig. 4.16. Thus, the magnification factor is about 8. The ICCD camera has a 1024×1024 pixel CCD with a pixel size of $13\ \mu m \times 13\ \mu$m. The achieved resolution is about 1.6 μm. Since the typical Wigner-Seitz radius of our barium crystals is about 20 μm, it is possible to resolve individual ions in the small crystals and the shell structures in the large crystals.

In order to determine the size of the barium ion ensemble from the CCD images precisely, a microscope slide with a scale is mounted in the trap center. The imaged scale is shown in Fig. 4.17. The minimum scale (10 μm) is discriminable. Thus, the resolution

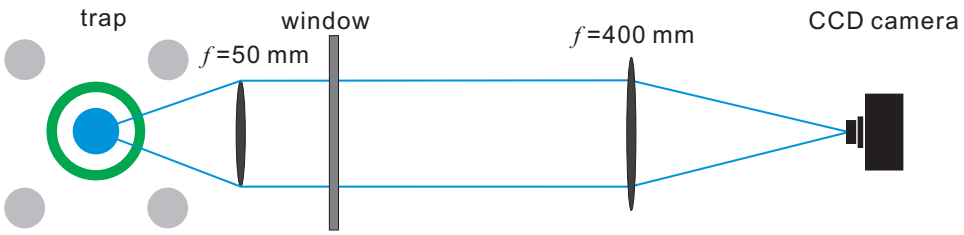

Figure 4.16: Imaging scheme of the CCD camera.

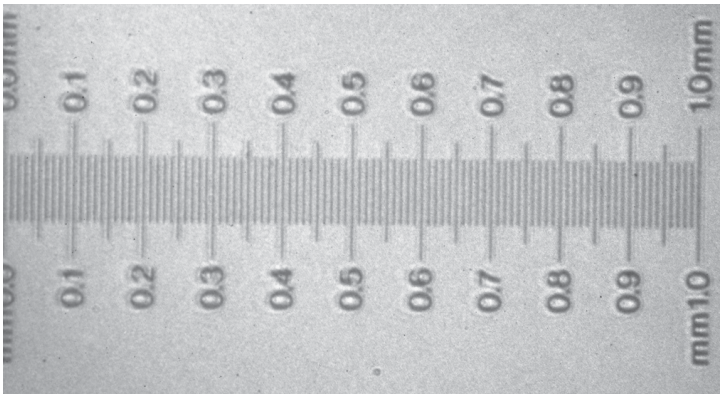

Figure 4.17: Calibration image. The length of the scale is 1 mm and the corresponding pixels in a CCD image are about 980. The minimum scale 10 μm is shown very clearly. Here, the scale is placed in the trap center.

of such system is much better than 10 μm (theoretical value is 1.6 μm). The scaling factor is 100 pixels in a CCD image corresponding to about 104 μm.

To improve the quantum efficiency of the ICCD camera, it runs at a temperature of -20°C. The integrating time is usually set be to 2 s. Additionally, at the optical entrance of the ICCD camera a narrowband 493 nm light-passing filter is mounted to block the repumping laser light and other background light.

Since the fluorescence light (scattered 493 nm light) is collected from the side of the trap and the CCD camera is placed 90° with respect to the trap axis, all the CCD images from the experiments in this thesis are the projection of the intensity of the fluorescence light onto the horizontal $x - z$ plane.

4.5.3 PMT

The fluorescence light can also be detected by a PMT. In our setup a PMT is installed outside of the main chamber. A lens with 50 mm focal length is mounted at the side of trap opposite to the lens for CCD camera to collect the fluorescence light. Then the collimated light beam passes a window and is focused into an aperture by another lens (f = 100mm). Behind an aperture the PMT is mounted. There is also a narrow gap filter for 493 nm set in front of the PMT.

The individual photons generate electron pulses, which are amplified and sent to a

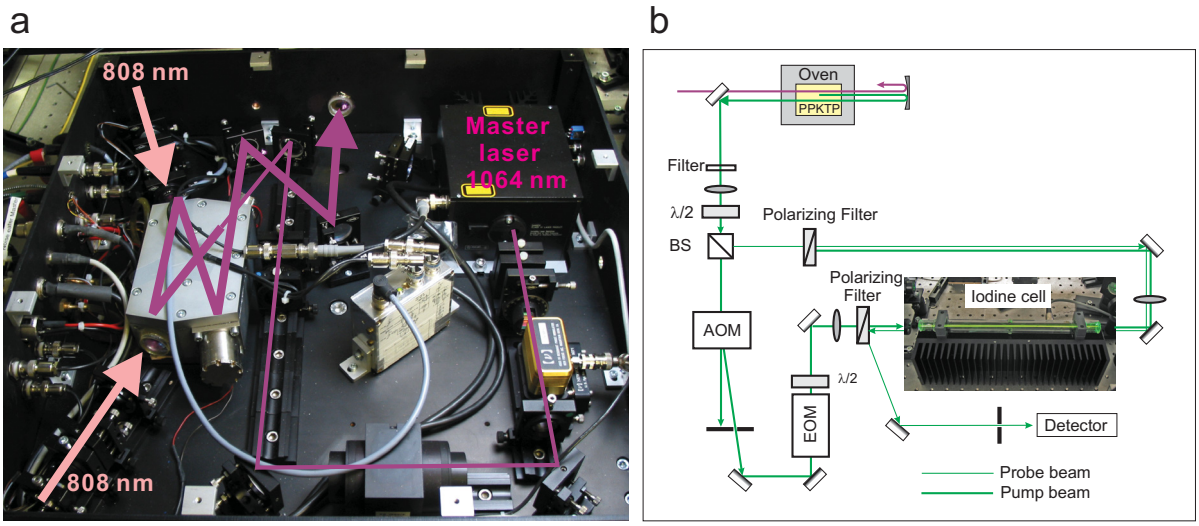

Figure 4.18: Setup of the Nd:YAG laser and its frequency stabilization system [61].

discriminator, after then, converted to TTL pulses. The pulses are counted by a counting electronics as done for the signal from the CEM. The magnitude of the counting is the indication of the ion number and the laser cooling efficiency. With the help of the fluorescence intensity, the optimal detunings of the working lasers can easily be found. The PMT is also used for the non-destructive secular excitation method to identify the ion species (see Chapter 10).

4.6 Laser system

As mentioned in the last chapter, a cooling laser (493 nm) and a repumping laser (650 nm) are required for the laser cooling of $^{138}Ba^{+}$ ions. Here, an overview of their setups is given. Details are described in the thesis of Alexander Ostendorf [61].

Unlike a normal laser system, a laser for laser cooling needs to satisfy several conditions: First of all, sufficient and constant output power is necessary. The most important point is that the laser frequency should be well-stabilized for a long time ($>$ 2 hours) and tunable in a small range ($>$ some hundred MHz). Furthermore, the laser linewidth needs to be narrower than 1 MHz.

The block diagram of the whole laser system is shown in Fig. 4.1. The 650 nm laser is generated directly by a semiconductor laser diode. However, the 493 nm laser is obtained by sum-frequency generation (SFG) of 1064 and 920 nm laser beams, which are generated by a Nd:YAG laser and a semiconductor laser diode, respectively. Moreover, to stabilize the two laser diodes two ring cavities (transfer cavities) are used. The lengths of these cavities are stabilized to the 1064 nm laser. Thus, the Nd:YAG laser is the master laser.

The setup of the Nd:YAG laser is shown in Fig. 4.18(a). Its seed is delivered by a Non-Planar Ring Oscillator (NPRO) master laser. It is amplified in a cavity (two Nd:YAG crystals are end-pumped by 808 nm lasers). The final amplified output power is about 12-14 W. This laser is frequency stabilized using a hyperfine transition in molecular iodine

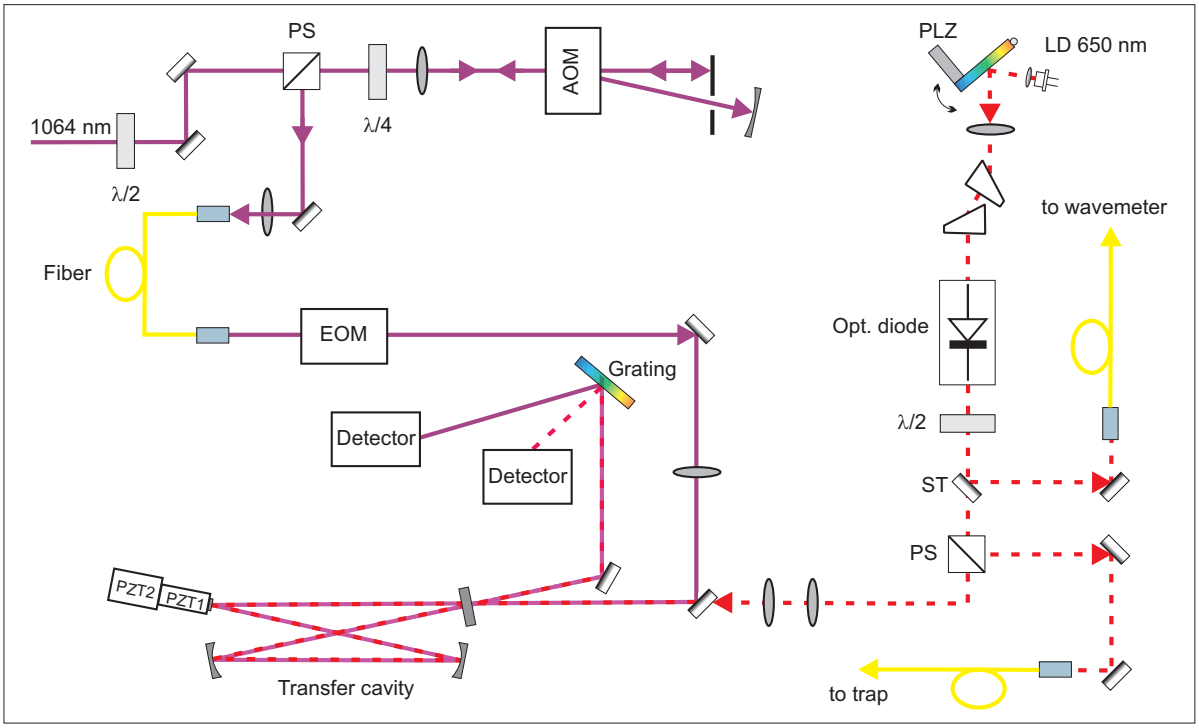

Figure 4.19: Scheme of the optical setup for the frequency stabilization of the 650 nm laser.

at 532 nm. Therefore, a portion of the 1064 nm laser (≈ 1 W) is used to be frequency doubled (SHG) achieving about 18 mW output power at 532 nm. The main portion of the 532 nm laser beam, modulated by an electro-optic modulator (EOM), doubly passes the iodine cell, which is kept at 0°C and 4 Pa gas pressure obtaining about 300 kHz effective linewidth. Another small portion of 532 nm laser beam works as a probe beam. The signal from the photodetector is sent to the electronics to stabilize the frequency of the seed laser through the Pound-Drever-Hall stabilization method [91, 92, 93]. The optical setup for the frequency stabilization of the 1064 nm laser is shown in Fig. 4.18(b).

4.6.1 The 650 nm laser - repumping laser

The laser diode used in our experiment is a commercial one (Sacher, TEC-100-645-10). It is an External Cavity Diode Laser (ECDL) in Littrow configuration and is designed for the applications, which require a high output power as well as a low linewidth. Its central wavelength is about 645 nm with maximum 12 mW output power. The maximum output power after the grating is about 8 mW at the wavelength of 649.94 nm. The beam is linearly polarized and its profile is elliptical (ratio = 1 : 4), which is corrected by a anamorphic prism pair to the ratio of 1 : 1.5.

The scheme of the optical setup for the 650 nm laser is shown in Fig.4.19. The original beam is divided into three parts. The main beam is guided to the trap and one of the other two is delivered to a wavemeter via optical fibers. The last one is sent to a transfer cavity, whose cavity length is stabilized to the 1064 nm laser (a small portion, about 200 μW, is used). The transmission power of the 650 nm laser from the coupling mirror is monitored by a photodiode. The detected signal is sent to the controller to identify the

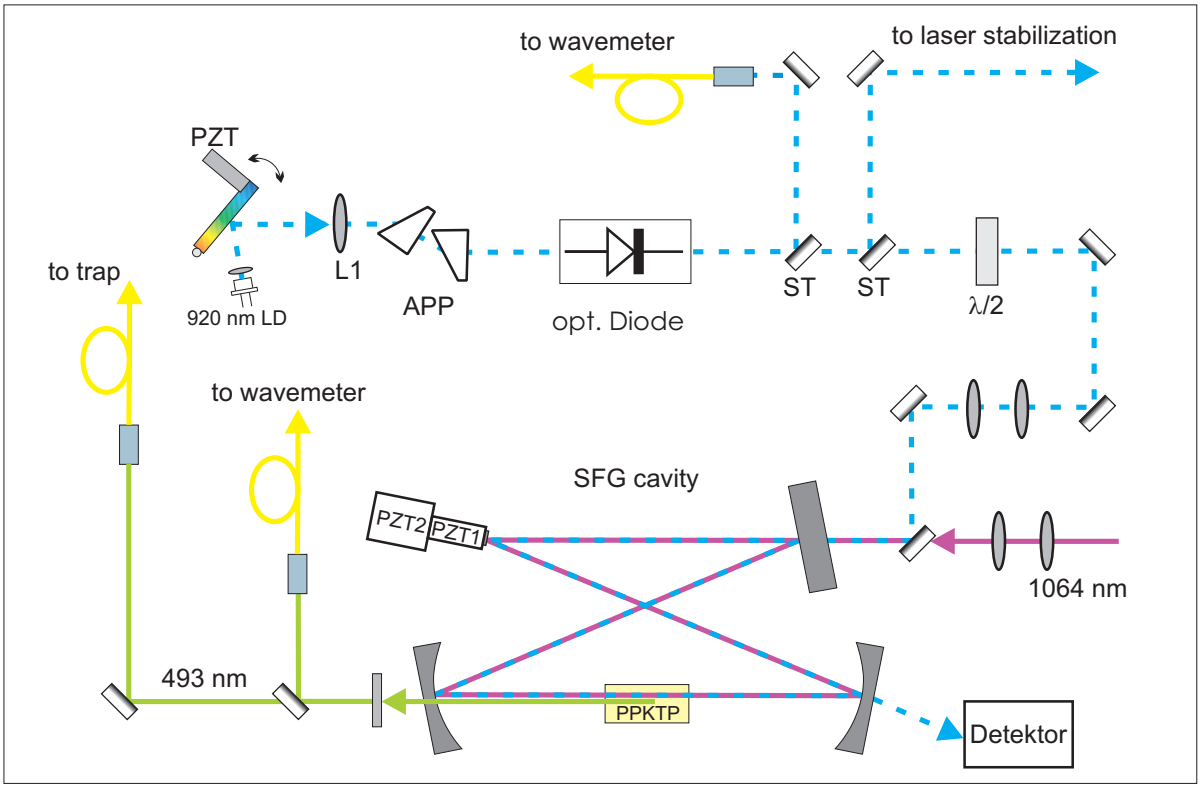

Figure 4.20: Optical setup for the generation of the 493 nm cooling laser radiation.

frequency drift and a corresponding feedback will be sent to the laser diode to recover the frequency. This technique is well known as the Pound-Drever-Hall stabilization method.

When the length of the cavity and the 650 nm laser frequency are locked, an acousto-optical modulator (AOM) can be used to shift the frequency of 1064 nm laser beam to the transfer cavity. Subsequently, the length of cavity is adjusted accordingly resulting in a shift of the frequency of the stabilized diode laser. The maximum shift for our 650 nm laser is about 200 MHz.

The frequency stabilization for to 920 nm diode laser has an identical setup. The AOM is independent from that for the frequency stabilization of the 650 nm laser. The maximum tuning range for the 920 nm laser is about 150 MHz.

4.6.2 The 493 nm laser - cooling laser

Semiconductor laser diodes at 493 nm are still not available. Thus, this cooling laser is obtained on the principle of nonlinear frequency conversion, via sum-frequency generation (SFG) of a Nd:YAG laser and a 920 nm laser diode (Toptica, DL100) in a nonlinear crystal (PPKTP). The optical setup is shown in Fig. 4.20. The output power of the laser diode is about 100 mW at a wavelength of 920 nm. The main portion of the power (about 80%) is used for the SFG. The left portion is sent to the wavemeter and the transfer cavity. The power of the 1064 nm laser delivered to the SFG cavity is about 10 W. To maximize the 493 nm output, the cavity is resonant for 920 nm, but not for 1064 nm. The length of this cavity is locked to the 920 nm laser. Finally, about 50 mW

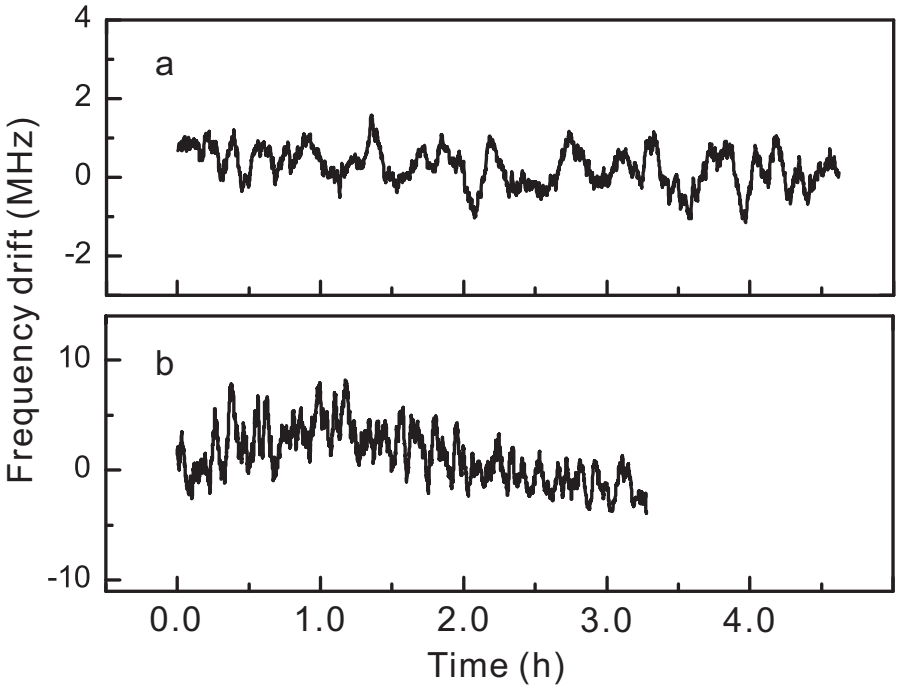

Figure 4.21: Long-time frequency stability of the diode lasers, which are stabilized to the transfer cavity. (a) The central wavelength is 649.869494 nm. (b) The central wavelength is 920.18688 nm [61].

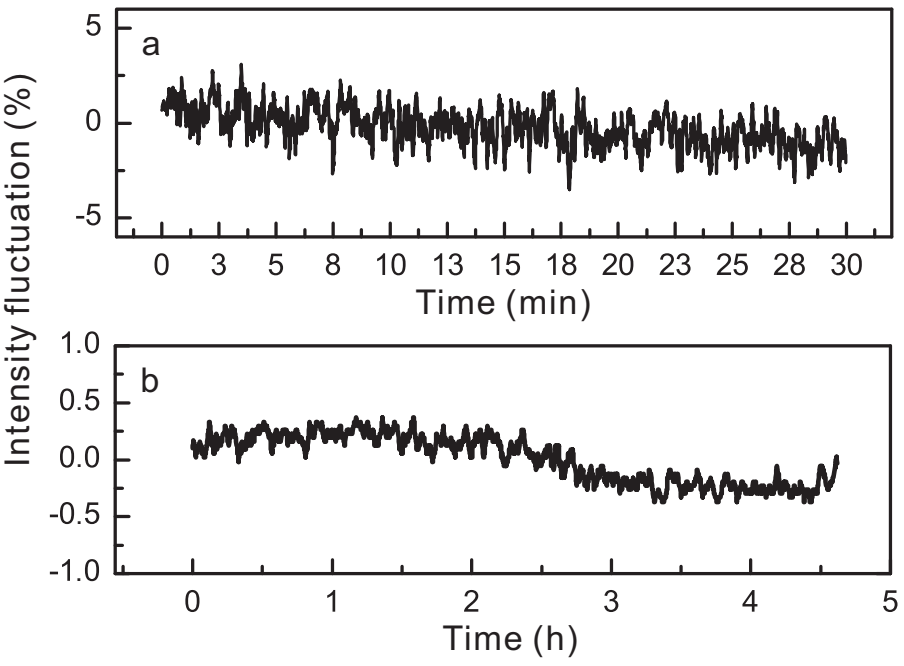

Figure 4.22: Intensity stability of the cooling laser (a) and the repumping laser (b) [61].

output power of 493 nm laser can be achieved.

4.6.3 Laser stabilization

All the lasers mentioned here are frequency stabilized. The seed of the 1064 nm laser is generated by using a NPRO (company: Innolight). This monolithic design of the laser cavity helps to achieve stability. The long-time stability (> 1 hour) for the iodine stabilization is expected to be less than 100 kHz.

The frequency stabilities of the diode lasers in several hours under the stabilization of transfer cavities are shown in Fig. 4.21. The frequency drift is about 2 MHz for the 650 nm laser and 10 MHz for the 920 nm laser, respectively.

Besides the frequency stability of the lasers, a good intensity stability over a long period of time is also necessary. The intensity fluctuations of the cooling laser and the repumping laser are shown in Fig. 4.22. The relative laser power fluctuation for the 493 nm laser is about ± 0.02 and ± 0.005 for the 650 nm laser. In the frequency locked cases, the noise is much smaller.

5 Preparation and properties of laser-cooled barium Coulomb crystals

Laser cooling of barium ion ensembles is the prerequisite for the sympathetic cooling of other ion ensembles. In the beginning of this chapter the experimental procedure for the preparation of pure barium ion crystals is explained (Sec. 5.1). The effects of laser detunings and trap parameters are addressed in Sec. 5.2 and Sec. 5.3, respectively. Aspects such as the secular frequencies (see Chapter. 2), the spatial distribution, and the lifetime of barium ion ensembles are discussed in Sec. 5.4, Sec. 5.5, and Sec. 5.6, respectively.

5.1 Preparation of barium Coulomb crystals

To laser cool a barium ion ensemble, a 493 nm cooling laser and a 650 nm repumping laser are required. They need to be linearly polarized and overlapped passing through the trap center along the trap axis. Moreover, they are tuned to the wavelengths up to several hundred MHz below the atomic resonances for the optical Doppler cooling on the $6^2S_{1/2} \leftrightarrow 6^2P_{1/2}$ and $6^2P_{1/2} \leftrightarrow 5^2D_{3/2}$ transitions to realize the laser cooling. The laser detunings are set with the assistance of a wavemeter (Burleigh, WA-1500).

Subsequently, the barium oven (electron beam evaporator) is switched on. Then, barium ions are generated and pass the trap as described in the last chapter. Due to the presence of the cooling lasers, the barium ions passing through the laser beam lose kinetic energy so that they are captured in the trap. This barium ion loading procedure is simple but effective.

Typically, light molecular ions (most of them are $CO_2{}^+$ ions) are generated by the heated filament during the ion loading procedure as well. These charged particles reduce cooling efficiency of the barium ion ensembles. Therefore, in order to get a pure cold barium crystal, it is necessary to get rid of these pollutant ions from the ion trap.

Since charged particles with different mass-to-charge ratios have different secular frequencies, they can be selectively excited by an additional excitation force running at these frequencies. If the force is strong enough, the selected ions can be removed from the trap (the principle is explained in Chapter 10). Usually, in our case, the secular frequency of a barium ion ensemble is about 105 kHz. Thus, a frequency sweep from 120 kHz to 1 MHz for 10 s with an amplitude of $100 - 300$ mV can eject the light ions efficiently. If necessary, another frequency sweep from 100 kHz to 50 kHz can be used to remove some possible heavier molecular ions such as BaO^+. Normally, after experiencing one or two sweeps the barium ion ensemble is quite pure.

Fig. 5.1 shows an example of the preparation of a pure cold barium Coulomb crystal. After loading the barium ions, the ion ensemble stays in the cloud state (gas or liquid

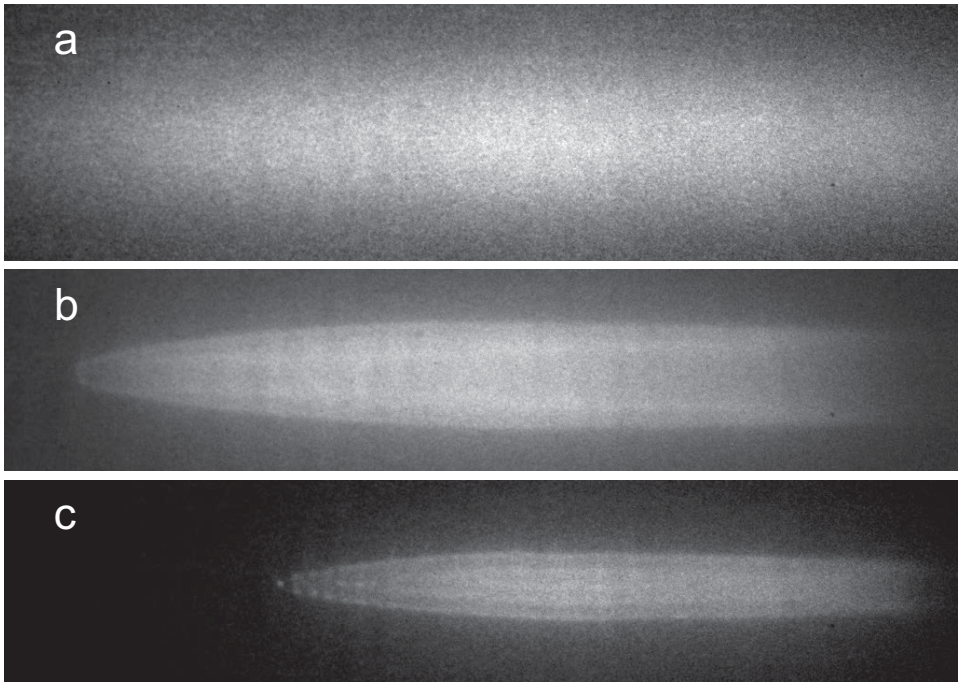

Figure 5.1: Preparation of a pure cold barium ion crystal. (a) Ion cloud after the loading of barium ions. Since the cooling lasers are not optimized, the barium ion ensemble stays at the cloud state. In most cases, due to the disturbance of the light molecular ions the barium ion ensembles cannot be cooled to the crystal state even with optimal laser detunings. (b) The barium ion ensemble is crystallized with the light ions under optimal laser detunings. (c) Only barium ions are left in the trap after the cleaning of the light ions. The ion crystal becomes colder.

state, no long range-order structure) as shown in Fig. 5.1(a). Then the cooling lasers are tuned to optimize the laser cooling rate resulting in a further cooling of the barium ion ensemble. Fig. 5.1(b) shows that the barium ensemble is crystalized (long-range order). However, due to the presence of the impurity ions the barium Coulomb crystal cannot be cooled down further. If the impurity ions are removed via a cleaning process, the Coulomb crystal becomes much colder with the optimal laser detunings (see Fig. 5.1(c)). At the left end even single ions are distinguishable. In most cases, when the fraction of impurity ions is relatively high, the barium ion ensemble cannot be crystallized before cleaning. On the other hand, if we want to study the effect of these impurity ions, it is better to clean them first and then load them in a controllable way.

Here, a barium ion ensemble is denoted as pure here when all impurity ions have been removed and there are only $^{138}Ba^{+}$ and the isotope ions left (see Chapter 3). Due to their close masses, it is impossible to remove the isotopes without losing a significant number of $^{138}Ba^{+}$ ions using the secular excitation cleaning method. Since the isotopes are not laser-cooled, they do not no fluoresce. Thus, they are invisible in the CCD images. Because the laser-cooled $^{138}Ba^{+}$ ions experience a light pressure force (see Eq. (3.17)), when the cooling lasers come from the right side, they are pushed to the left. As a result, the isotopes stay at the right side forming a dark area in the CCD images. However,

they can be studied via molecular dynamics simulations (see Chapter 9).

Actually, it is impossible to load an exact number of the barium ions to the trap, but the size of the ion ensemble is roughly proportional to the loading time and the loading current. Under same loading conditions the loaded ion number varies within $10 - 20\%$. The right laser detunings can help improve the loading efficiency greatly. For the sympathetic cooling of the complex molecular ions the ratio of the ion numbers of the barium and molecular ions rather than the precise number of the barium ions is critical in our experiments. If the ion number of a $^{138}Ba^{+}$ ion ensemble is too small, it cannot cool the molecular ions efficiently, while if too many, the complex molecular ions are pushed further away from the barium ion ensemble lowering the sympathetic cooling efficiency and being harder for the detection of the molecular ions via the secular excitation technique. Thus, we usually attempt to load different barium ion ensembles times until finding a favorite size. Fig. 5.2 shows some cold barium Coulomb crystals with different barium ion numbers.

5.2 Laser detuning

As discussed in Chapter 3, a red detuning of the 493 nm cooling and 650 nm repumping laser is necessary to achieve the laser cooling of the $^{138}Ba^{+}$ ion ensemble. Otherwise, it can even lead to heating. In the loading process of the barium ions, without lasers, barium ions can also be captured by the energy dissipation through the collisions with residual gas. The energy dissipation of the barium ions increases greatly in the presence of the red detuned ($100 - 300$ MHz) lasers.

Due to the three-level scheme of the barium ion, the effect of dark resonances (see Chapter 3) on the laser cooling needs to be taken into account. Fig. 5.3 shows the fluorescence intensity at different detunings of the 493 nm laser as a function of the detuning of the 650 nm laser [61]. It is evident that the fluorescence intensity decreases at the dark resonance. Due to the natural linewidth and the saturation broadening this resonance is significantly broadened, so the individual dark resonances of sub-levels arising from the Zeeman splitting cannot be resolved. Among the 6 plotted curves (corresponding to the detuning of the 493 nm laser of -65 MHz, -43 MHz, -21.5 MHz, 0 MHz, 65 MHz, and 109 MHz) the one at -21.5 MHz has a maximum intensity peak. Thus, the optimal cooling efficiency is expected to be achieved around a 20 MHz red detuning of the 493 nm laser (in this specific measurement for each laser a randomly chosen frequency is taken as the reference point).

5.3 Secular frequency

Ions are confined in the trap by the harmonic potential well created by the rf voltage (radially) and the DC endcap voltage (axially) as discussed in Chapter 2. The characteristic secular frequencies are given by Eq. (2.36) and Eq. (2.15), respectively, and they can be detected via secular excitation with a relative small amplitude.

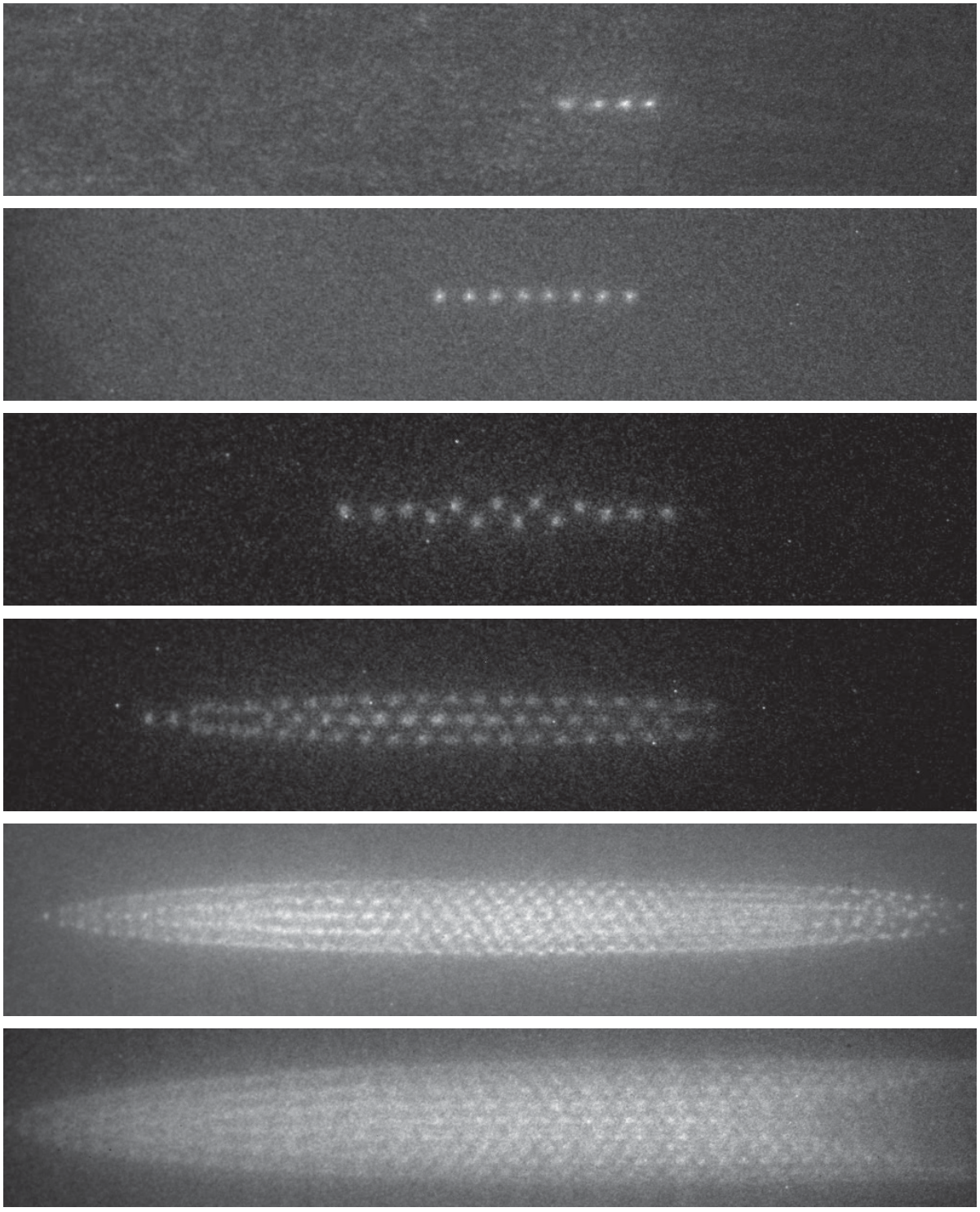

Figure 5.2: Barium ion crystals with different ion number (from 5 to more than 2000 ions). The temperatures of these ion crystals are less than 40 mK.

5.3.1 Radial secular excitation

It is possible to excite the ions radially by applying an AC electric field. In the experiment, this electric field can be applied to the trap electrodes via a modulation of the rf field or to an additional electrode such as a foil with a few hundred μm thickness located

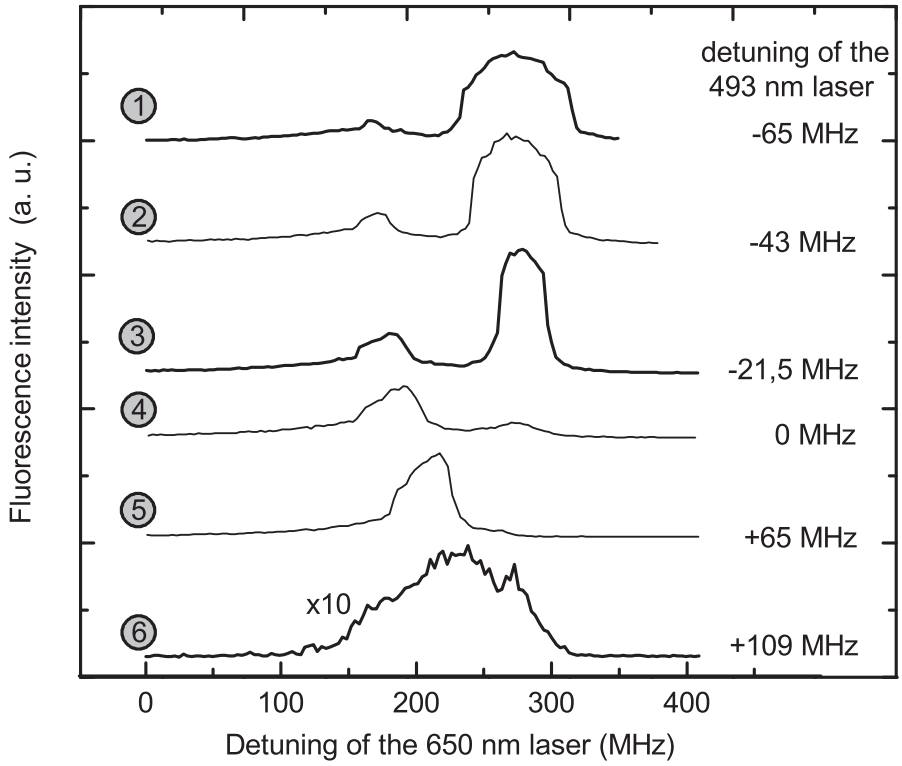

Figure 5.3: Effect of the dark resonances on the fluorescence [61].

in a gap between two adjacent trap electrodes. A metal plate with its edge parallel to the trap axis is another option, but much higher excitation voltages are necessary to penetrate the rf field of the trap. In our setup, the AC voltage is applied on the two top middle trap electrodes. High excitation voltage (above 100 mV) can kick the selected ion species out of the trap, while small excitation voltage (around 1 mV) is used to heat up a particular ion species. Fig. 5.4 gives an example of a secular excitation spectrum of a pure barium ion ensemble, whose calculated secular frequency is about 119 kHz. The frequency is scanned from 80 to 150 kHz with an amplitude of 0.6 mV. The fluorescence intensity drops dramatically when the excitation frequency is near the resonant frequency of the barium ion ensemble. After sweeping over the resonance frequency the heating is small and the ion ensemble cools down again, as shown by the recovery of the fluorescence intensity. More details about the secular excitation are described in Chapter 10.

5.3.2 Axial secular excitation

The axial secular motion can also be excited by an applied external AC electric field as in the radial direction. Due to the presence of the light pressure force the barium ion ensemble can be excited by an intensity modulation of the 493 nm laser as well. The axial direction has four advantages for the implementation of the optical excitation comparing with the excitation in the radial direction.

- The shape of the potential well is shallow. A relatively small force can lead to a big ion position shift.

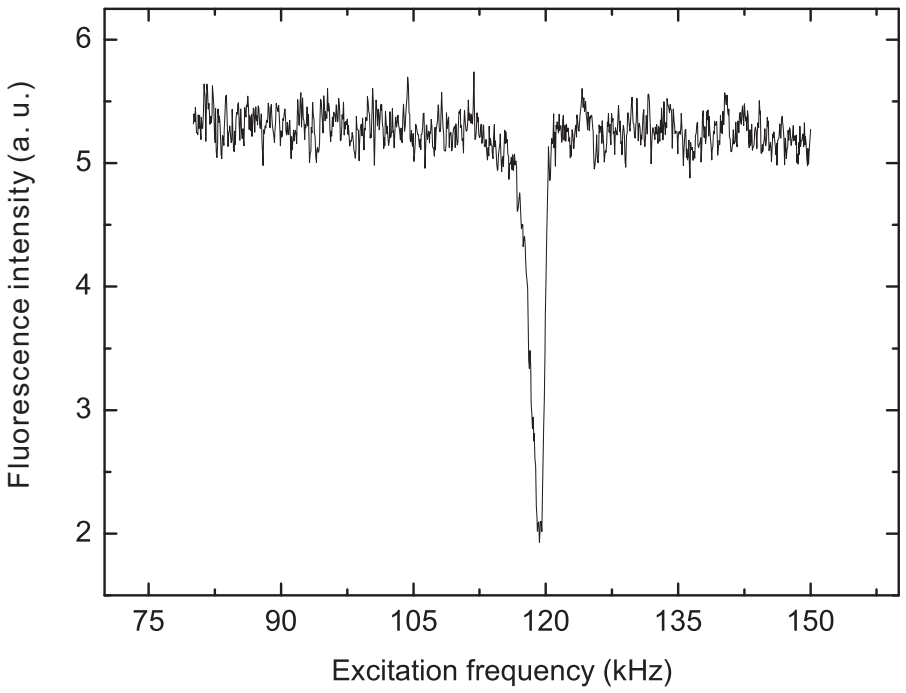

Figure 5.4: Measured fluorescence intensity of a barium ion crystal as a function of the excitation frequency.

- The potential well is created by a DC endcap voltage. So there is no micromotion on the ion motion in the axial direction.
- The ion ensemble usually has a prolate shape. More laser-cooled ions are covered by the laser beams, since the laser beams shine along the axial direction.
- Ions are laser cooled in axial direction. The ion ensemble can be crystalized again more easily after being melted.

Fig. 5.5 shows an axial excitation spectrum. In this measurement the endcap voltage is about 9 V. With a κ parameter of 0.15 in our case the calculated axial secular frequency for a single barium ion is about 21.9 kHz. Both lasers are locked at their optimal laser cooling frequencies and their intensities are 800 μW and 525 μW, respectively. The intensity of the 493 nm laser is modulated by an AOM with the frequency sweep from 15 to 30 kHz and the modulation depth is about 80%. The duration for one scan is 30 s. The spectrum shows a dip at about 22.5 kHz, which is quite close to the calculated value. Actually, the optical excitation only acts on the laser-cooled $^{138}Ba^{+}$ ions. Barium isotopes and other sympathetically cooled ions (if have) are disturbed less strongly. This determines that the optical excitation has a faster response time offering more precise measurements.

5.4 Trap parameters

Several properties of ion ensembles confined in a specific trap such as the structure, the rf heating rate, the cooling efficiency [94], and others, are determined by the trap voltages. With the optimal trap parameters, ion ensembles even with several thousand barium

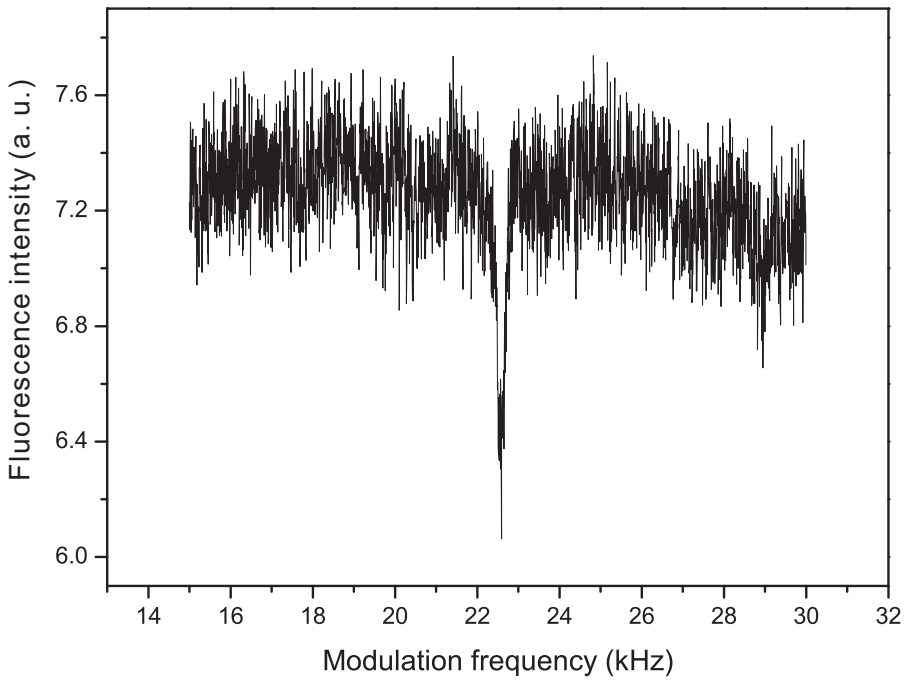

Figure 5.5: Measured fluorescence intensity of a barium ion ensemble during an intensity modulation of the 493 nm laser with the frequency being scanned from 15 to 30 kHz in 30 seconds.

ions can be laser cooled to a few millikelvin in our trap as shown in Fig. 5.2. From their CCD images temperatures of barium ion ensembles, as well as the ion numbers, can be obtained using molecular dynamics simulations. We will address this issue in Chapter 9.

5.4.1 Ion confinement

Fig. 5.6 shows the shape and structure changes of a cold barium Coulomb crystal at different rf and endcap voltages. In order to see the shape change clearly, the barium isotopes are removed by secular excitation (here we started with a big barium ion ensemble as the removal of the isotopes causes a loss of a significant number of $^{138}Ba^{+}$ ions). It is obvious that a higher endcap voltage squeezes the crystals longitudinally, while a higher rf voltage results in a higher radial confinement squeezing the crystal radially.

For the purpose of reducing the rf heating (see Chapter 2) it is more favorable that the ions stay as close to the trap axis as possible. Thus, a lower endcap voltage is always helpful to reduce the size of the crystal radially, since the same amount of the ions occupies a larger space along the axial direction (see the comparison between Fig. 5.6(b) and Fig. 5.6(c)).

Comparing between Fig. 5.6(a) and Fig. 5.6(b), as well as Fig. 5.6(d) and Fig. 5.6(e) shows that a higher rf voltage has the same effect of pushing the ions closer to the trap axis. On the other hand, the increased rf voltage raises the heating effect. When a barium ion ensemble in the cloud state cannot be cooled to the crystal state, lowering the rf voltage reduces the rf heating and can lead to crystallization. After the ion crystallization process the rf voltage can be switched to the previous level without melting

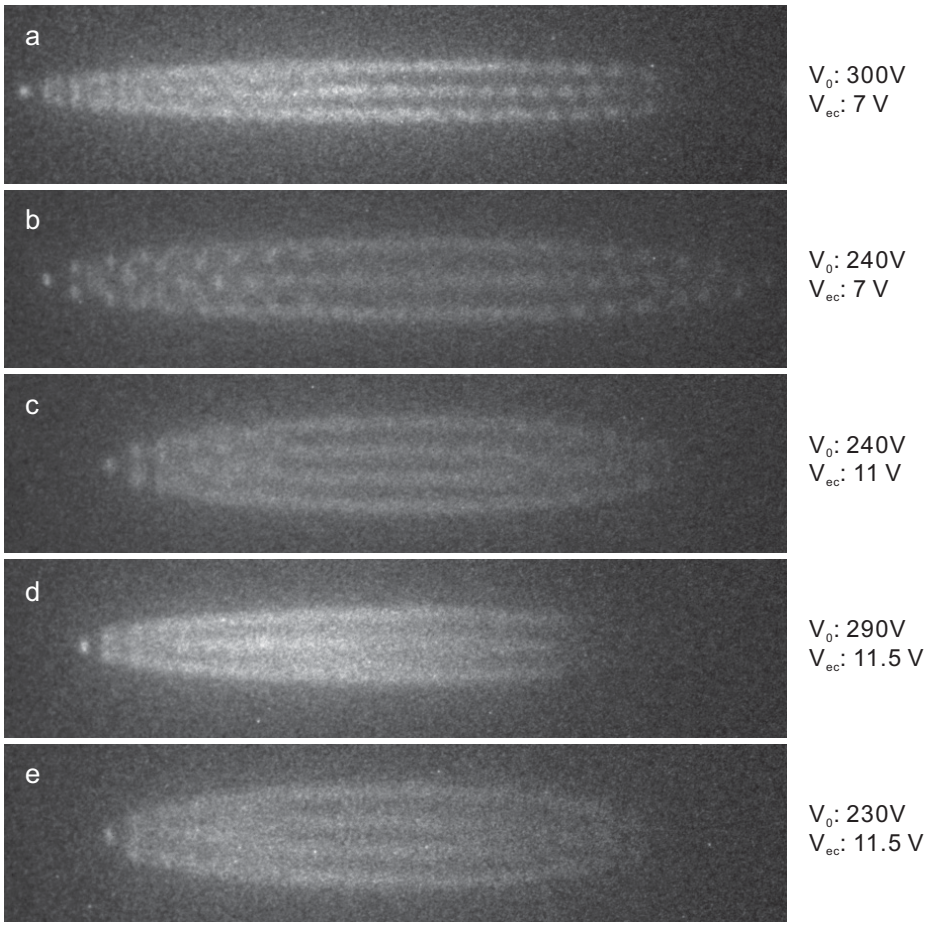

Figure 5.6: Shapes of barium Coulomb crystals at different trap voltages.

the Coulomb crystal, since rf heating is much lower at low temperatures. This operating approach is often used to cool down ion ensembles containing sympathetically cooled complex ion species because they have a stronger rf heating effect (complex molecular ions stay further away from the trap axis). However, since the harmonic pseudopotential well is much shallower for a large mass-to-charge ratio ion species, a lowering of the rf voltage to some extent might cause the loss of such a heavy species.

5.4.2 Compensation voltages

To minimize the rf micromotion of an ion ensemble, the symmetrization of the DC voltages on the four central electrodes is another important issue. Each time loading barium ions, the trap electrodes are coated with neutral barium atoms gradually resulting in contact potentials. They push the ion ensembles away from the trap center so that the rf micromotion increases. This effect is very sensitive, for example, in usual case a voltage drift of 40 mV DC on one middle electrode might shift a barium ion ensemble from the trap axis by 10 μm.

For a pure ion ensemble, the voltage drifts within 100 mV cannot be observed via the CCD images, since the asymmetry of the Coulomb crystal itself is not evident. However, for multi-species ion ensembles, a few mV drift can cause an obvious asymmetry in the

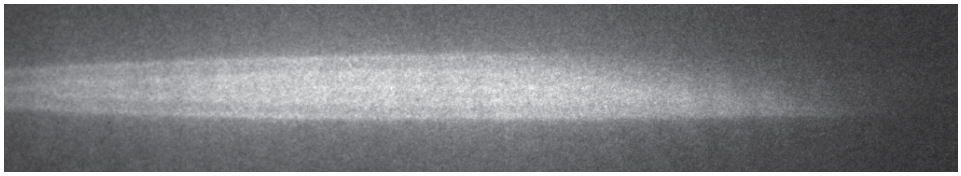

Figure 5.7: An asymmetric barium Coulomb crystal.

CCD images of the laser-cooled ion crystal, because heavier ions have a shallower trap potential well and they are more sensitive to a voltage drift. Fig. 5.7 shows a CCD image of a barium ion ensemble with a few mV DC offset on one middle electrode. In this case, $^{138}Ba^{+}$ ions and barium isotopes are confined in the trap simultaneously. The laser-cooled $^{138}Ba^{+}$ ions are a little bit heavier than the isotopes, thus, with a voltage drift they move further away from the trap axis. The edge shape in the right side of the Coulomb crystal shown in Fig. 5.7 tells us that the $^{138}Ba^{+}$ ions move further downwards and the isotopes finally stay in the top right corner. This is caused by a positive offset voltage on a top middle electrode or a negative one on a lower middle electrode. Therefore, this drift voltage can be compensated by an additional power supply, discussed in Chapter 4.

5.5 Spatial distribution

The spatial distribution of an ion ensemble is determined by the ion number, the temperature, and the trap parameters. Ion ensembles in our trap are normally prolate, since the radial confinement is stronger than the axial one (the axial confining frequency is around 20 kHz and the radial one is around 100 kHz, higher frequency corresponds to a steeper potential well). When only a few barium ions stay in the trap, they form a linear "pearl" chain at low temperature ($<$ 100 mK) or a string at higher temperature along the trap axis. After adding more ions a shell structure appears as shown in Fig. 5.2.

5.5.1 Axial spatial distribution

To investigate the longitudinal distribution, a linear barium chain is shown in Fig. 5.8(a). All the ions (Note that: in all the CCD images or the simulated images of ion crystals single ion points are not real ions but places of high spatial probability) in this chain are distinguishable from each other. The rf voltage in this case is 440 V, which results in a radial secular frequency of about 115 kHz. In order to obtain such a chain, the endcap voltage is lowered to 2 V (corresponding to an axial secular frequency of about 10.3 kHz). A simulation of this ion ensemble is done and a simulated image at 60 mK is shown as Fig. 5.8(b). According to the symmetry of the chain another 3 isotopes are located at the dark area on the right side. Therefore, this linear chain includes 30 barium ions and its total length is about 660 μm. However, the 30 barium ions are not aligned homogenously. Ions near the trap center gain strong Coulomb repulsive forces from both sides, which push ions close to each other, whilst the ions close to the ends are pushed away from the trap center resulting in the distance between two adjacent ions becoming bigger and bigger, as plotted in Fig. 5.8(c). The minimum distance is about 19 μm for the ions located in the middle of the chain, while the two end ions are about 37 μm away from their closest ions.

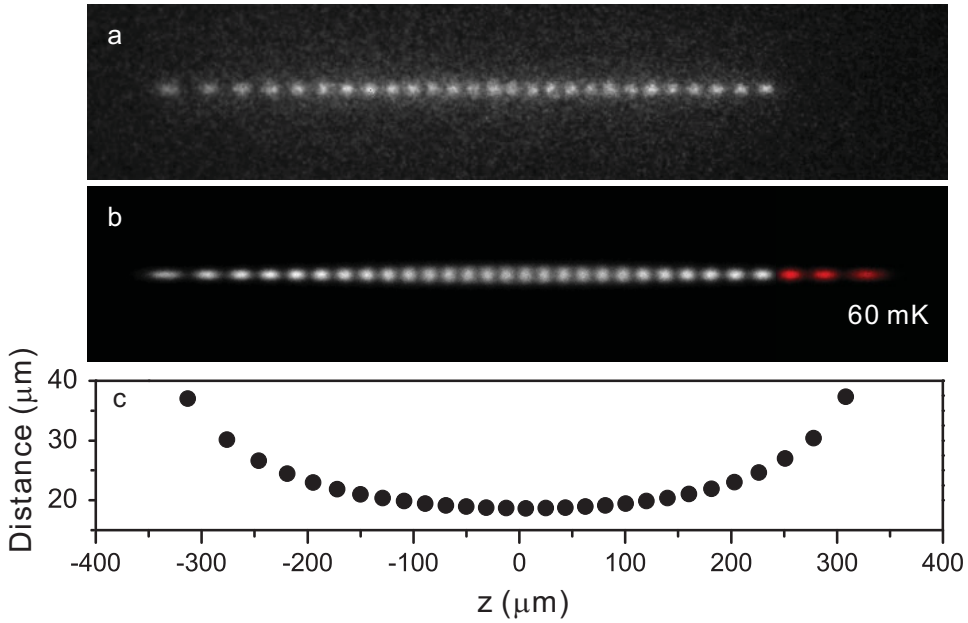

Figure 5.8: A barium ion chain with 27 $^{138}Ba^{+}$ ions and 3 isotopes. (a) CCD image from the experiment. (b) Simulated image with the isotopes shown in red. (c) Distance between two adjacent ions, obtained from the simulation (the positions the ions are represented by their z-coordinates at absolute zero, since this ion string is quite cold and its expansion is negligible).

The ions in this chain are vibrating with a small amplitude around their equilibrium position in the crystal lattices (see Chapter 9). Actually, due to the collisions with the background gas or some electric noises, the ions can exchange their positions sometimes. In presence of the isotopes this phenomenon can be observed as jumps of the dark lattice sites. When the temperature of this barium ion ensemble becomes higher and higher, the possibility of ion diffusion increases and the single-ion resolvable chain starts to be washed out.

5.5.2 Radial spatial distribution

For studying the ion's radial spatial distribution, we consider for simplicity a spherical crystal, by increasing the endcap voltage to 20 V and lowering the rf voltage to 150.5 V ($\omega_x = \omega_y = \omega_z = 30.6$ kHz). At these trap parameters, the ion distributions of a barium ion ensemble containing 550 ions at different temperatures are plotted, as shown in Fig. 5.9. Here, the ion number included in a shell with finite thickness is plotted as a function of the shell diameter. The ion density as a function of the distance from the trap center is plotted in Fig. 5.9(b). At low temperatures of 1 mK and 10 mK the barium ion ensemble has a clear shell structure (5 shells). At 1 mK all the ions are limited in each shell and ion diffusion is forbidden. At 10 mK diffusion is possible. At 100 mK the structure is almost washed out and the spatial distribution is quite homogenous. The outermost shell always has the highest contrast and is the last one to fade out, which is shown in many CCD images, since the ions in this shell are only pushed away from the trap center by the inner ions as the two ions locating at both ends of the string

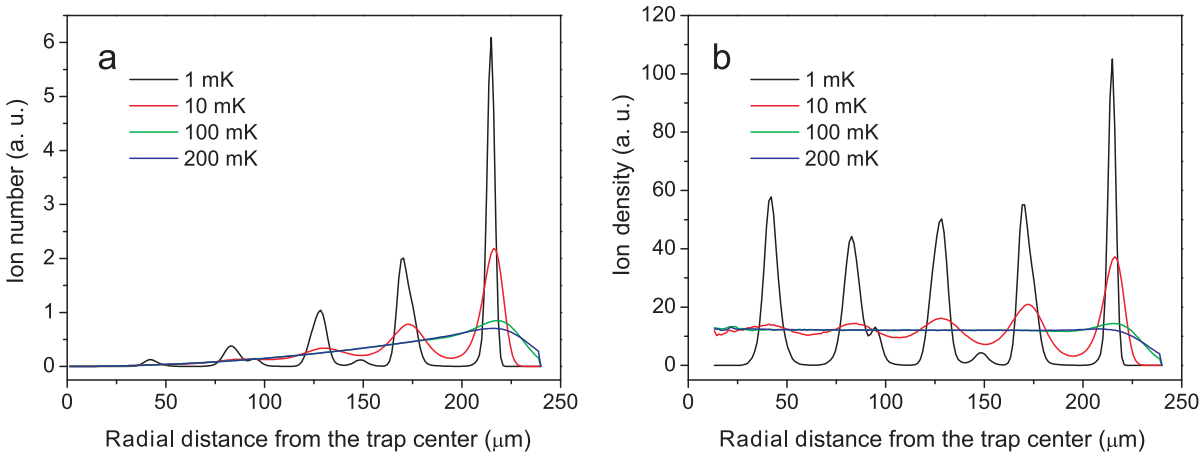

Figure 5.9: Ion distribution of a spherically shaped barium ion ensemble containing 550 ions. (a) Number of ions found at concentric shells with an appointed thickness. (b) Ion density as a function of the distance from the trap center (ion number divided by the shell's volume).

shown in Fig. 5.8. At 200 mK the structure is washed out completely. Another point we can obtain from these images is that even at relatively high temperatures (200 mK) the transition between the ion ensemble and vacuum is very sharp [95]. The simulation results agree with the works done by Dubin and Schiffer [96, 97].

5.6 Lifetime of ion ensembles

The lifetime of barium ion ensembles confined in the trap is quite long (up to several hours), if the lasers are locked. Of course, the ion ensemble loses ions all the times due to collisions, charge exchanges, and chemical reactions with neutral residual background gas molecules. Thus, with an improvement of the vacuum and a reduction of the content of specific gases such as H_2O, O_2, and CO_2, the lifetime of barium ion ensembles can be extended. In our case, a barium ion ensemble is tested. After loading the barium ions, the cooling lasers are optimized and locked. The barium ion crystal is monitored by the ICCD camera for about 20 minutes. No obvious changes are found on the Coulomb crystal [61].

6 Chemical reactions of $^{138}Ba^{+}$

6.1 Introduction

Gas-phase ion-neutral reactions at low temperatures usually occur in interstellar clouds. Via the sympathetic cooling method cold ions can be generated. This offers us a good stage to study the reactions in laboratories, so in the last few years this topic gained more and more interest. In our trap, chemical reactions between laser-cooled barium ions and neutral gas molecules.

In our experiments, when the trap parameters keep constant and the cooling lasers are locked, sometimes shape variations of the barium ion crystals on a time scale of minutes can be observed. Fig. 6.1(a) shows a CCD image of a pure barium crystal. With time, the outer area of the crystal close to the isotopes is flattened gradually - the CCD images after 6 min and 11 min are shown in Fig. 6.1(b) and Fig. 6.1(c), respectively. The obvious crystal deformation is quite serious.

Through the comparison of the crystals in Fig. 6.1(a), Fig. 6.1(b), and Fig. 6.1(c) we can conclude that although some $^{138}Ba^{+}$ ions are lost, the total ion number is almost the same, since the structure and the position of the remaining $^{138}Ba^{+}$ ion ensemble on the left side does not change. Thus, the lost $^{138}Ba^{+}$ ions are replaced by a same amount of heavier ions (mainly $^{138}BaO^{+}$ ions), which are the products of chemical reactions between $^{138}Ba^{+}$ ions and residual background gas molecules. Therefore, to find out which kinds of molecules react with the laser-cooled $^{138}Ba^{+}$ ions it is helpful to reduce the number of possible reaction channels. One advantage, however, is that through the chemical reactions very large translationally cold molecular ion ensembles (comparable to the laser-cooled barium ion ensemble) can be created.

If we do the experiment in another way, following the preparation of a similar sized pure barium crystal and taking a CCD image in the crystal state, the lasers are blocked for about 10 minutes. Subsequently, we unblock in the lasers and recrystallize the barium ion ensemble. A new CCD image is taken to compare with the former one. No obvious deformation appears. Thus, the possible chemical reactions only occur when the barium ions are in the excited states $6^2P_{1/2}$ and $5^2D_{3/2}$. Therefore, this is a photo chemical reaction, which makes use of the energies carried by the cooling lasers, 2.5 eV and 1.9 eV for 493 nm and 650 nm, respectively. Via MD simulations the ion number of each ion species can be fitted according to the CCD images (the determination of the ion numbers for different ion ensembles is discussed in Chapter 9). In any case the obtained ion number of barium isotopes is always almost constant. Since barium isotopes are not excited by our cooling lasers, it confirms that it is a photo chemical reaction.

Considering the main components of the residual gas shown in Fig. 6.2, the possible chemical reaction of the crystalized $^{138}Ba^{+}$ ions with neutral species such as CO_2, He,

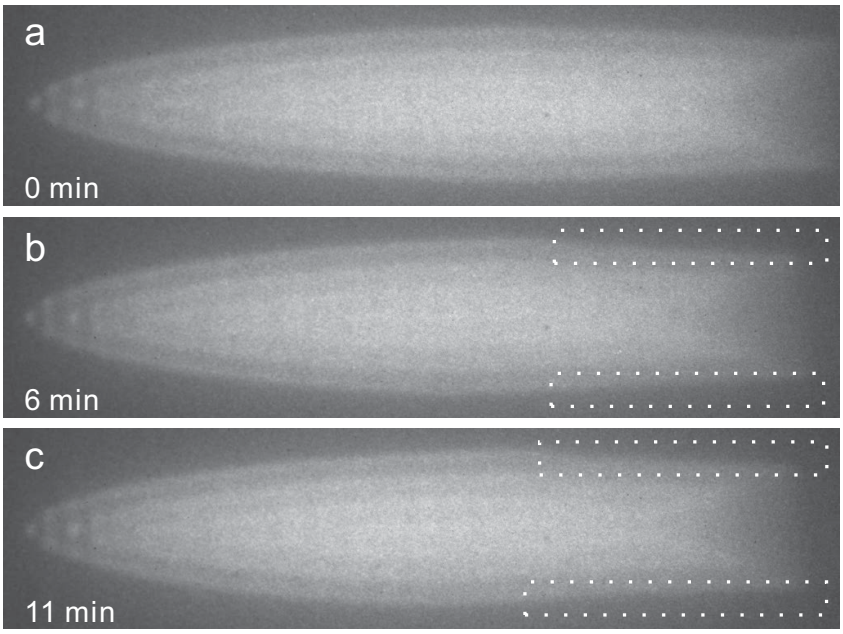

Figure 6.1: Change of shape of a barium crystal as a function of time due to the chemical reactions (see the areas in the dashed boxes).

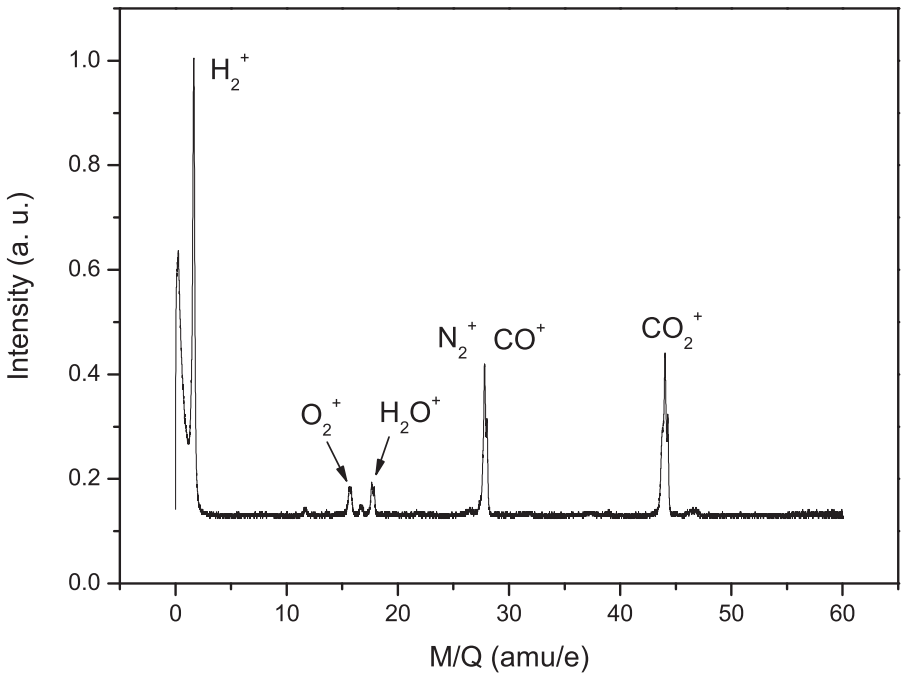

Figure 6.2: Residual gas mass spectrum in the main chamber at 5×10^{-10} mbar.

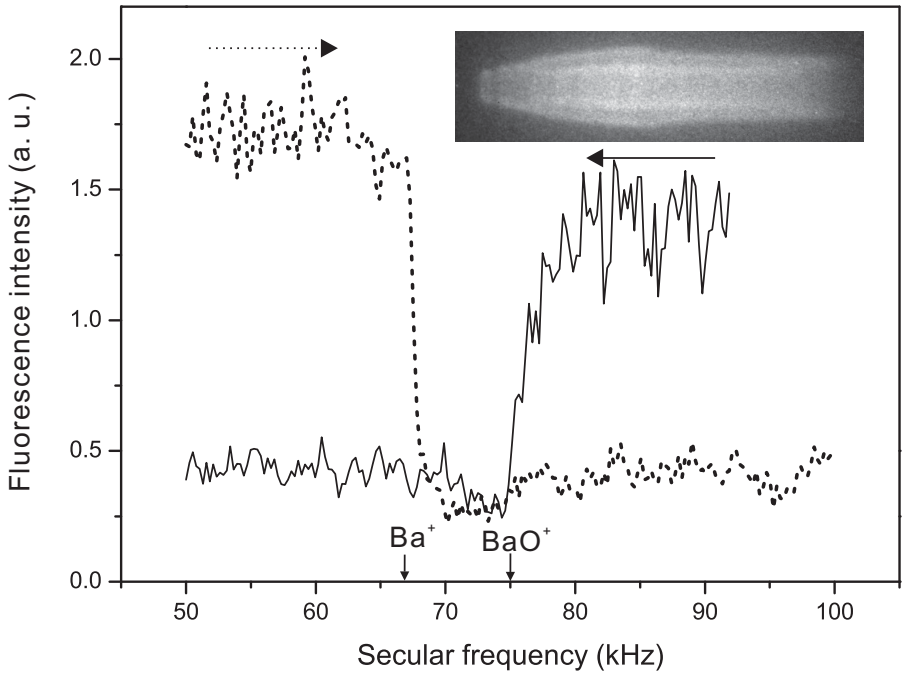

Figure 6.3: Secular excitation spectra scanned from 50 to 100 kHz in forward and backward directions.

O_2, H_2, N_2, and N_2O, are investigated in the following sections. The product of the chemical reaction, BaO^+, is also used to study the back-reaction with CO. Here, we do not study the chemical reaction of barium ions with H_2O, since it is difficult to be removed from the vacuum chamber after experiments due to its high desorption energy at low pressure leading to in a worse vacuum degree.

Since the mass of the reaction product is quite close to that of the barium ions, the ion mass cannot be identified via ion extraction due to the poor resolution of this method. The secular excitation method also has this limit to distinguish between the reaction product. The problem is that the fluorescence intensity of the barium ion ensemble is very sensitive to the excitation near its resonance frequency. Hence a low excitation voltage (below 1 μV) is enough to excite the barium ions. If the barium ion ensemble is excited indirectly by the reaction products, a much higher excitation voltage is necessary to resonantly excite the reaction products. However, since the resonance frequency of the barium ion ensemble is very close to that of the reaction products, a frequency sweep for the detection of the reaction products always covers the resonance frequency of the barium ions. The high excitation voltage easily melts the barium ion crystal. After sweeping over the resonance frequency ion ensembles are still too hot. It will take a longer time (few seconds) to recover the crystal. Thus, if we monitor the intensity of the fluorescence, a dip on the fluorescence curve is replaced by a step.

Fig. 6.3 shows an example. Here, the CCD image of the ion ensemble is shown in the inset in Fig. 6.3. In a frequency sweep from 50 to 100 kHz and a reverse one with an amplitude of 800 μV the barium crystal starts to melt at about 67 kHz and 75 kHz, respectively. The calculated secular frequencies for barium ions and BaO^+ ions are 65.6 kHz and 74.3 kHz, respectively. Although the resolution of the secular excitation method

for determining the reaction product species is not so precise, it still can identify BaO^+ as the product of the chemical reaction. Whether there are any other products, mass between barium and barium oxide, or not is not clear.

6.2 Investigation of chemical reactions with He, N_2, and H_2 gases

Helium (He) gas is normally leaked into the main chamber as a buffer gas to decelerate the molecular ions coming from the ESI ion source. He is a least reactive element and its atoms are easily pumped away. We showed that the barium ions do not react with neutral He atoms by producing a pure barium Coulomb crystal and leaking in helium gas increasing the pressure in the main chamber from 2×10^{-10} to 4×10^{-9} mbar. The time evolution of the crystal is monitored for 38.5 min. Fig. 6.4 shows selected CCD images, which are listed by time. By comparing with Fig. 6.1, it is evident that the deformation of the barium ion crystal has almost the same rate as in the case without leaking in the helium gas. Thus, we have shown that the helium atoms do not chemically react with barium ions.

In the same way we showed that barium ions do not react with neutral nitrogen atoms. The time evolution of a pure crystal is monitored for about 22 min as shown in Fig. 6.5. Although the nitrogen gas rises the pressure of the main chamber from 2×10^{-10} mbar to 4×10^{-9} mbar, the total amount of other residual gas molecules do not change. The chemical reaction rate looks the same as in the case with He. Therefore, nitrogen gas is also nonreactive with the barium ions in the ground state and even $6^2P_{1/2}$ or $5^2D_{3/2}$ excited state.

From the mass spectrum of the residual gas shown in Fig. 6.2 we can obtain that hydrogen is another main component in the residual gas. For hydrogen we observed a slow reaction with the barium ions. Following the preparation of a pure barium crystal, hydrogen gas is leaked in at a pressure of 8×10^{-9} mbar. The time evolution of the crystal is shown in Fig. 6.6. Since the shape deformation in the outmost layers looks a little bit faster than the case of leaking in N_2 or He, the loss rate of $^{138}Ba^+$ ions is higher. Thus, the chemical reaction of $^{138}Ba^+$ ions with hydrogen gas does happen and the product ions are $^{138}BaH^+$. After 15 min a higher flux of hydrogen gas is leaked into the main chamber to increase the pressure to 4×10^{-8} mbar. Due to the relative higher background pressure, the barium Coulomb crystal becomes hotter and its CCD images are blurred. Nevertheless, the change of the outmost layers speeds up. This chemical reaction is an endothermic process with a reaction enthalpy of +2.1 eV. The chemical reaction is given by

$$Ba^+ + H_2 \rightarrow BaH^+ + H, \tag{6.1}$$

and is possible because the $^{138}Ba^+$ ions have an energy of 2.5 eV in the excited state.

However, due to the small cross section of H_2, this reaction happens very slowly. The chemical reaction rate of the barium ions with hydrogen gas at a normal working pressure should be very small. Hence, the shape deformation in our case is mainly caused by other neutral gases such as CO_2, O_2, and H_2O, as shown in the following chapters.

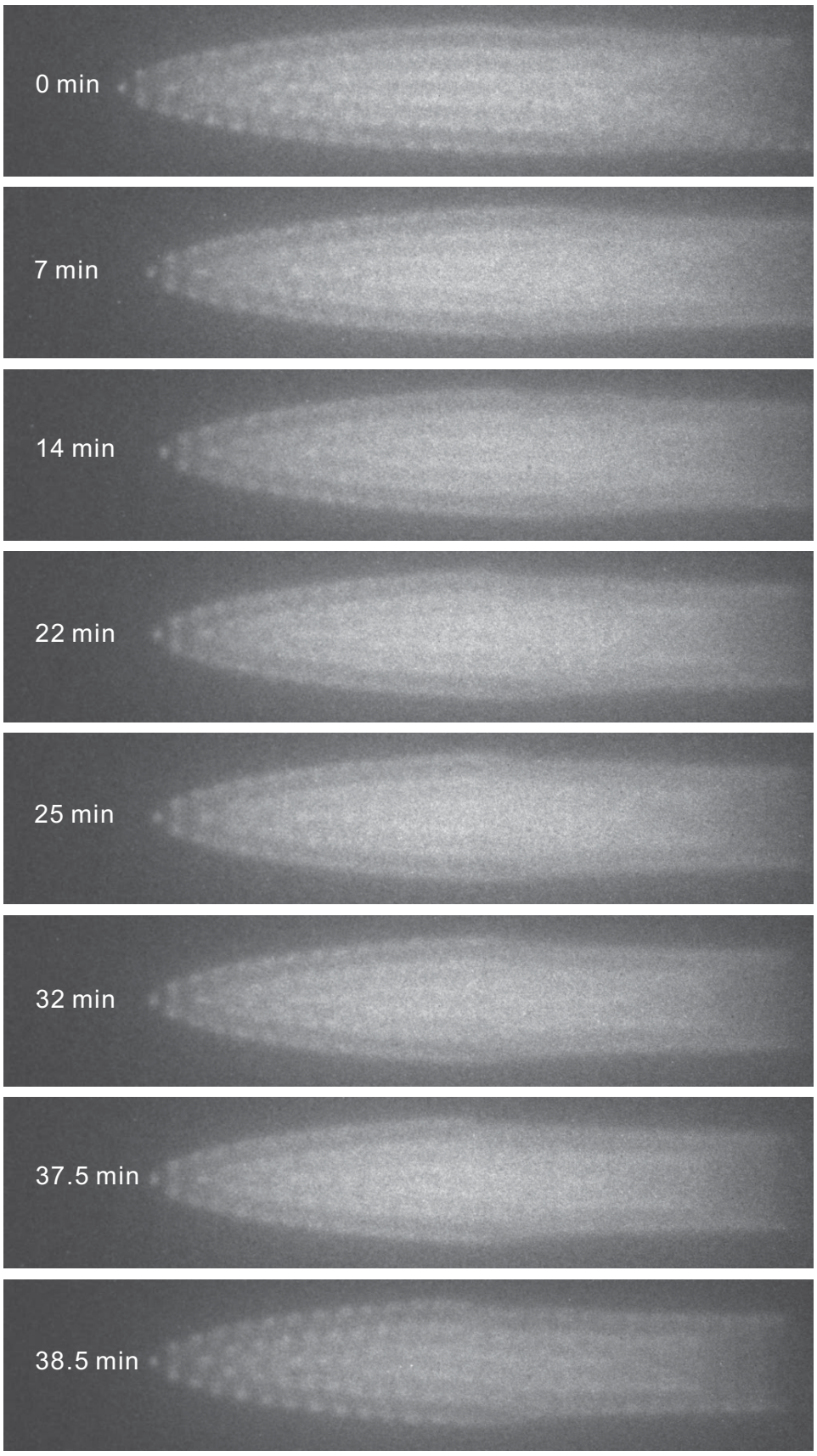

Figure 6.4: Time evolution of a barium ion crystal with He gas at a pressure of 4×10^{-9} mbar.

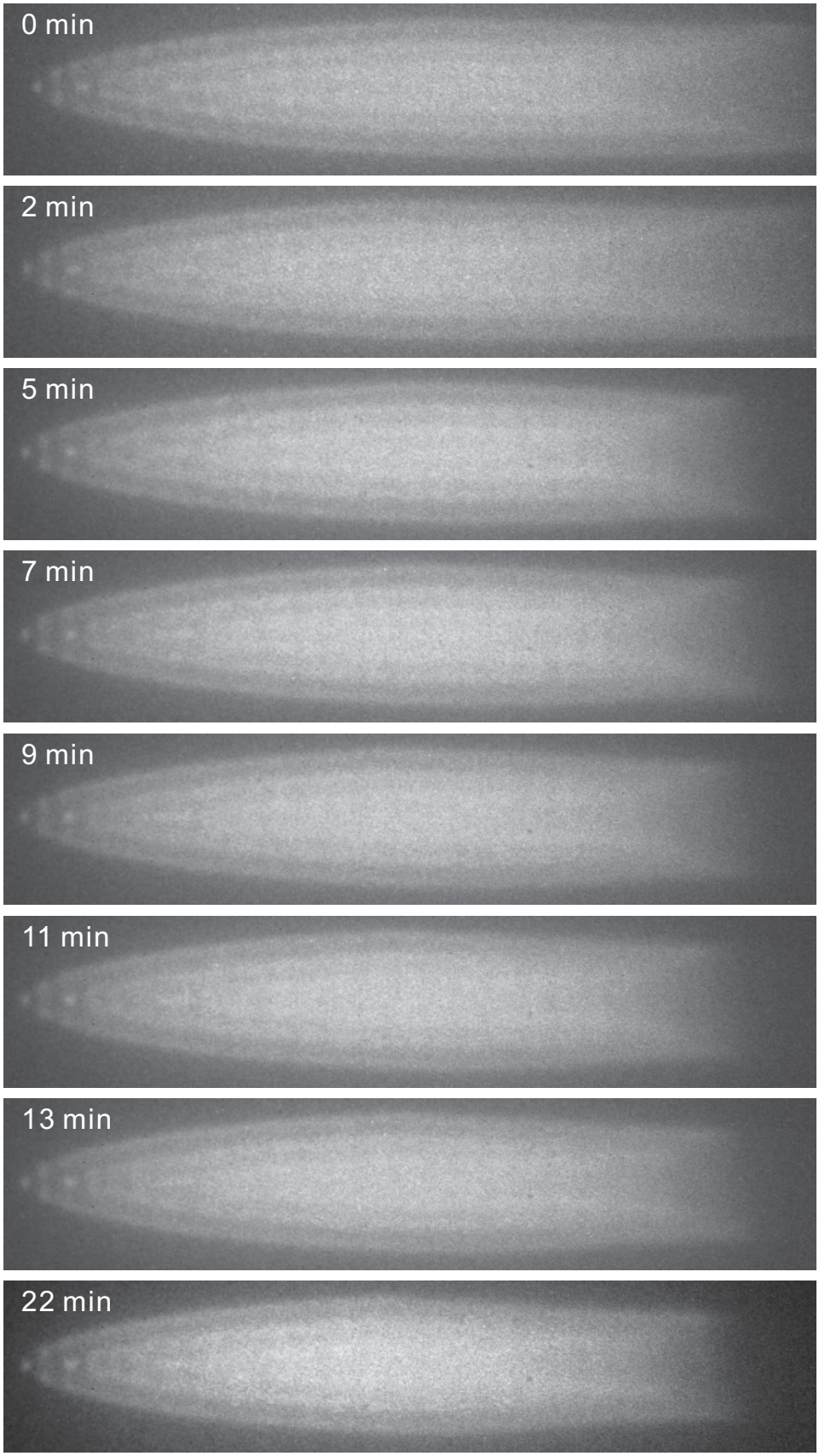

Figure 6.5: Time evolution of a barium ion crystal with N_2 gas at a pressure of $4{\times}10^{-9}$ mbar.

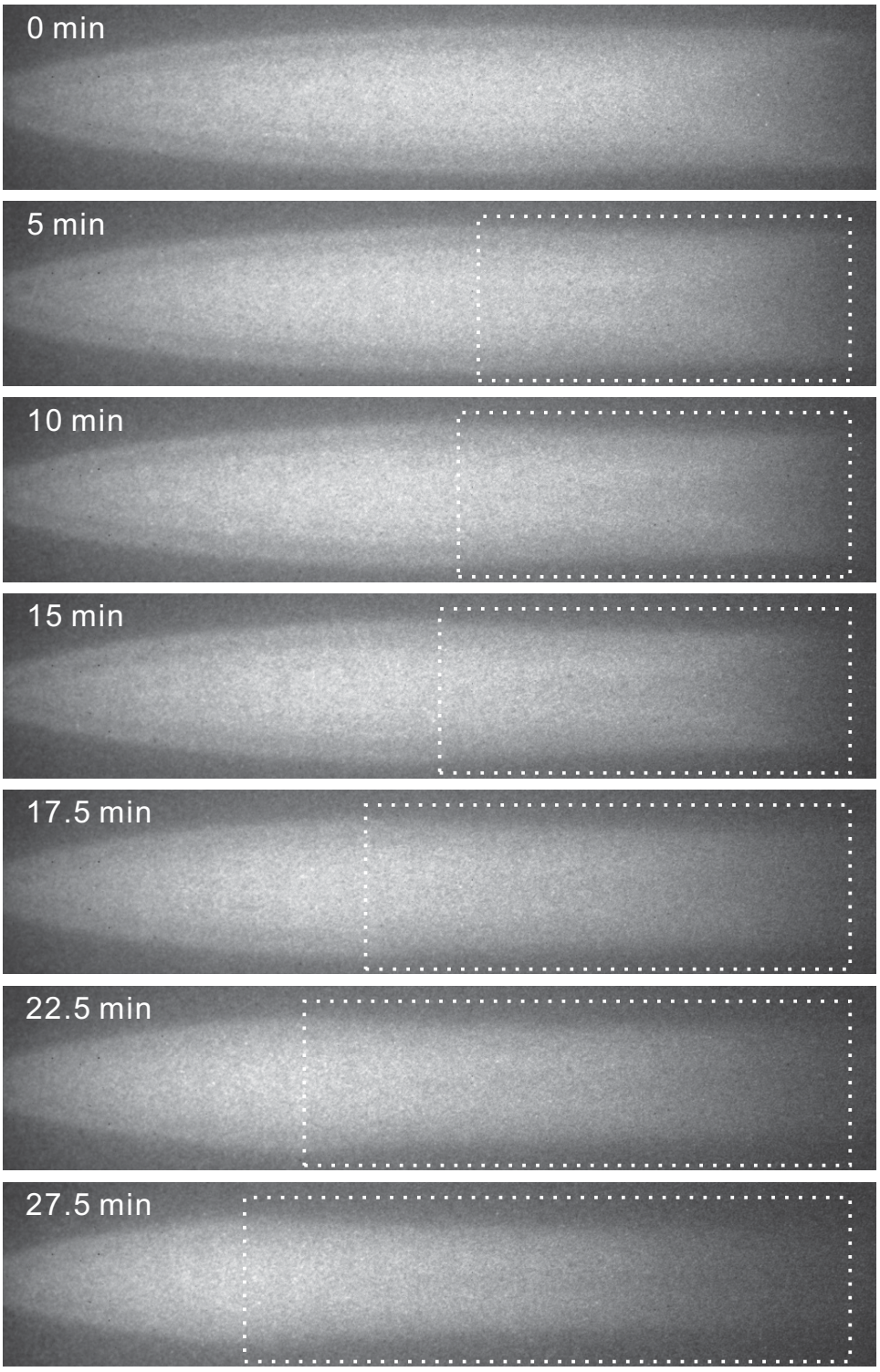

Figure 6.6: Time evolution of a barium ion crystal with H_2 gas at a pressure of 8×10^{-9} mbar (from 0 to 15 min) and 4×10^{-8} mbar (from 15 min to 27.5 min).

6.3 Chemical reaction with O_2

None of the gases introduced so far leads to reactions with laser-cooled barium ions acutely. In this section we study the reaction between laser-cooled barium ions and

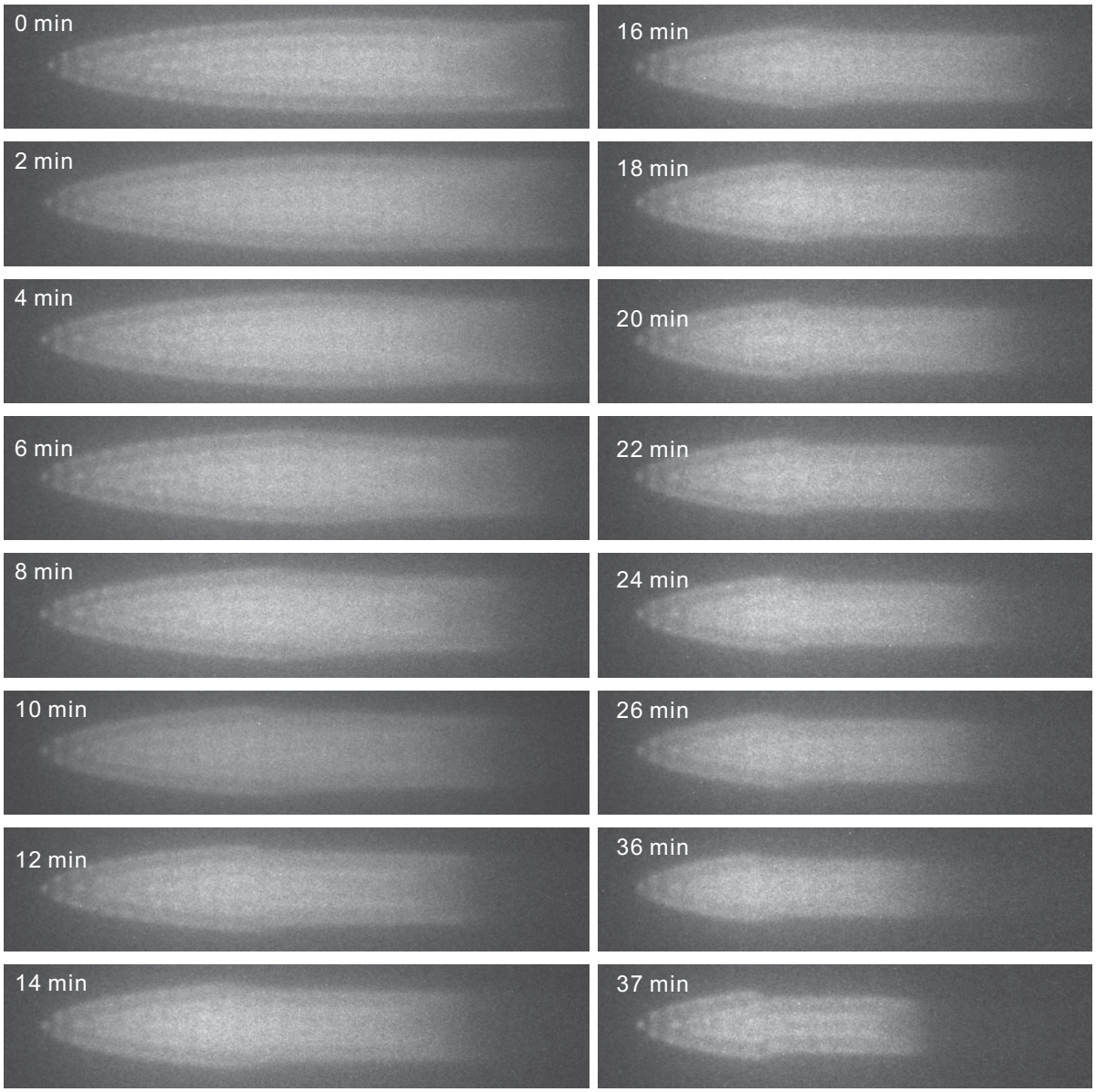

Figure 6.7: Time evolution of a barium ion crystal with O_2 gas at a pressure of 8×10^{-9} mbar. $^{138}Ba^{+}$ ions are replaced by the $^{138}BaO^{+}$ ions gradually due to the chemical reaction with O_2 gas.

neutral room-temperature oxygen molecules. The time evolution of the crystal is shown in Fig. 6.7. It is evident that the chemical reaction rate is faster. The chemical reaction is

$$^{138}Ba^{+} + O_2 \rightarrow {}^{138}BaO^{+} + O. \tag{6.2}$$

The ion number of each ion ensemble can be simulated for each CCD image. Therefore, the rate of the chemical reaction can be extracted. In our case, the ion numbers for $^{138}Ba^{+}$, barium isotopes, and $^{138}BaO^{+}$ ions at 0, 4, 10, 18, 26, and 36 min are simulated and shown Fig. 6.8. The black dots are the simulated ion numbers of the $^{138}Ba^{+}$ ion ensemble and the hollow dots are ones of the $^{138}BaO^{+}$ ion ensemble. The ion number of the barium isotopic ion ensemble is almost constant. Initially, the pure barium ion

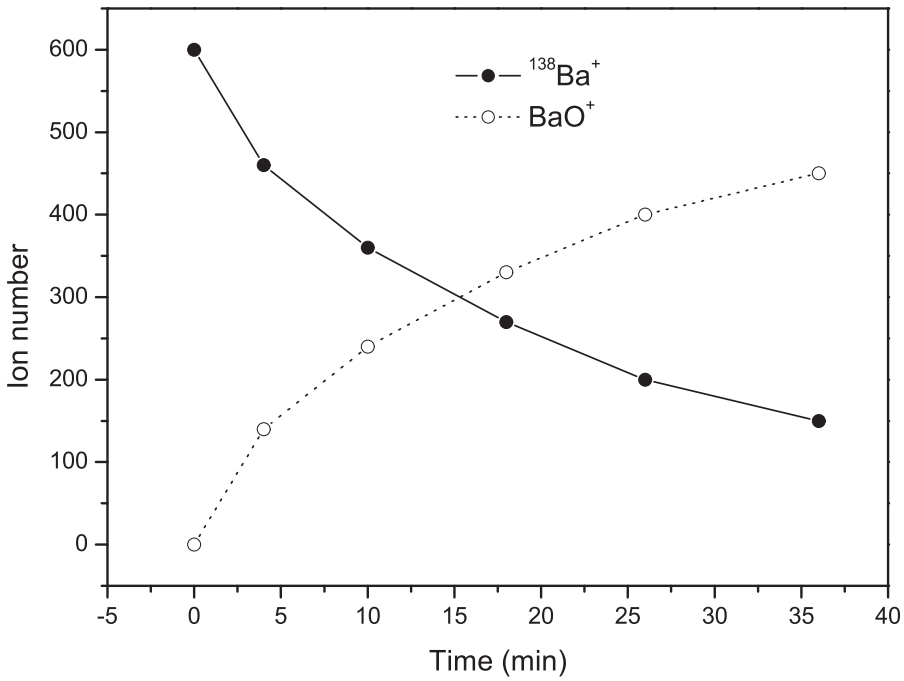

Figure 6.8: Time evolution of the ion numbers of the $^{138}Ba^+$ and $^{138}BaO^+$ ion ensembles. $^{138}Ba^+$ ions react with O_2 gas and generate the same amount of $^{138}BaO^+$ ions.

crystal has about 600 $^{138}Ba^+$ ions and 100 isotopic ions. After leaking in the oxygen the ion number of $^{138}Ba^+$ ions decreases and the ion number of the chemical reaction product $^{138}BaO^+$ increases correspondingly. After 36 min the $^{138}Ba^+$ ion ensemble only has 150 ions. The number of the $^{138}Ba^+$ ions decreases exponentially with a coefficient of $1/t_0 = 0.067\,\mathrm{min}^{-1}$ (fitting the dotted curve shown in Fig. 6.8 with a function of $A_0 e^{-t/t_0}$).

However, the chemical reaction shown in Eq. 6.2 is endothermic by 1 eV [98]. The $^{138}Ba^+$ ions in the ground state do not react with oxygen gas molecules. Thus, the chemical reaction only happens when the $^{138}Ba^+$ stays at the excited states, which have an energy of 2.5 eV and 1.9 eV compared to the ground state. To verify that only excited $^{138}Ba^+$ ions react, following the preparation of a pure barium crystal as shown in Fig. 6.9(a), the cooling laser and the repumping laser are blocked for 15 min with oxygen gas at the pressure of 8×10^{-9} mbar in the main chamber. Subsequently, the leak valve is shut off so that the oxygen gas is pumped away. Finally, the lasers are unblocked resulting in the recrystallization of the barium ion ensemble as shown in Fig. 6.9(b). The two crystals look the same. This proves that the chemical reaction only occurs when the $^{138}Ba^+$ ions stays in the excited state, and the isotopes do not join the chemical reaction.

With the two cooling lasers, the $^{138}Ba^+$ ions are excited to the $6^2P_{1/2}$ and $5^2D_{3/2}$ levels. In order to know which excited state dominates this chemical reaction, we just repeat the experiment, but only the repumping laser is blocked. Thus, the ions at the ground state are excited to the level of $6^2P_{1/2}$ and then decay to the $5^2D_{3/2}$ state. They stay on this level for some time. Finally, they decay to the ground state and are re-excited. So most of the ions are at the $5^2D_{3/2}$ level. The final results are shown in Fig. 6.10(a) and Fig. 6.10(b) accordingly. The chemical reaction rate is negligible in the case of

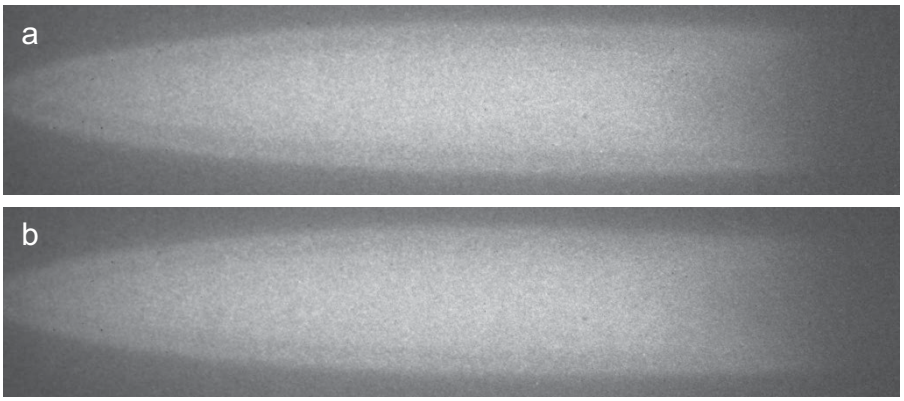

Figure 6.9: Investigation of the effect of the cooling lasers on the chemical reaction of $^{138}Ba^{+}$ ions with O_2. After producing the barium ion crystal shown in (a) the cooling lasers are blocked for 15 min. Then we unblock the cooling lasers and recrystallize the barium ion ensemble as shown in (b). No obvious shape deformation is found. That means only the $^{138}Ba^{+}$ ions in the excited state join the chemical reactions.

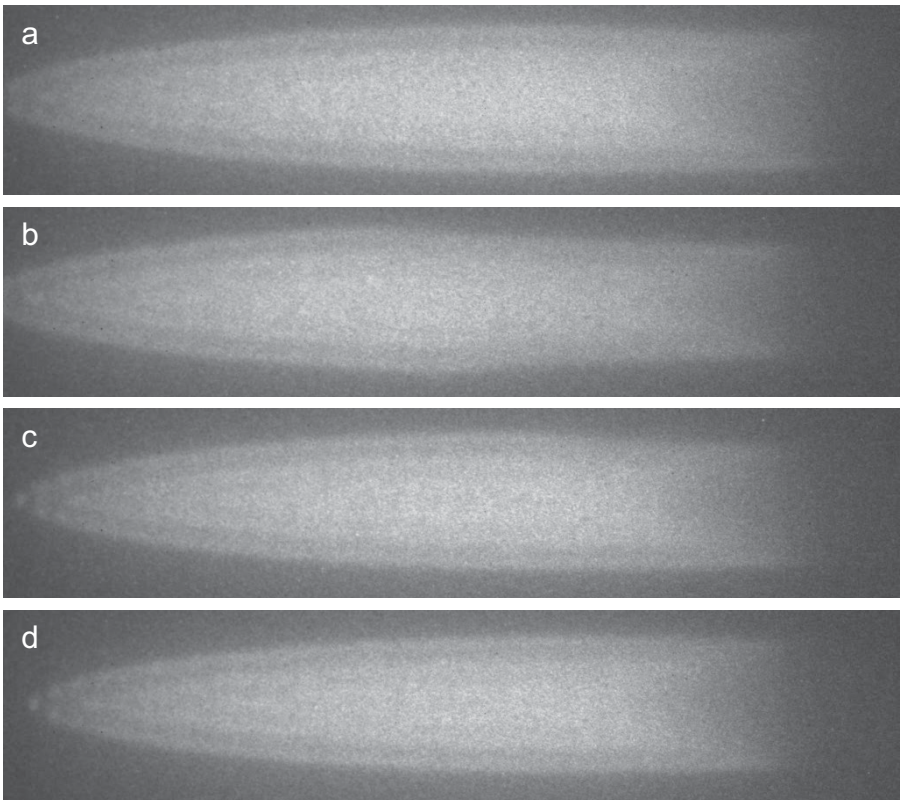

Figure 6.10: Investigation of the role of the cooling lasers on the chemical reaction of $^{138}Ba^{+}$ ions with O_2. Chemical reactions happen with a low reaction rate. (a) A pure barium crystal. (b) The barium crystal after exposure to oxygen gas at 8×10^{-9} mbar for 15 min without the repumping laser. (c) After the cleaning of $^{138}BaO^{+}$ ions once. (d) After the cleaning of $^{138}BaO^{+}$ ions once more.

both lasers being unblocked even with the oxygen pressure doubled. Therefore, the main chemical reaction occurs with the $^{138}Ba^+$ ions at the $6^2P_{1/2}$ excited state

$$^{138}Ba^+(^2P_{1/2}) + O_2 \rightarrow {}^{138}BaO^+ + O. \tag{6.3}$$

Fig. 6.10(c) and Fig. 6.10(d) are CCD images after cleaning the $^{138}BaO^+$ ions once and twice, respectively, via a secular excitation from 50 to 97 kHz with 200 mV AC amplitude. The trap voltage is about 400 V. After the cleaning, the ion cluster becomes a pure barium ion crystal again with a smaller dimensions.

6.4 Chemical reaction with CO_2

Another important issue is to test chemical reactions with neutral carbon dioxide CO_2 molecules, since its content in the residual gas is quite high (see Fig. 6.2). As well as for O_2 we could observe reactions of the excited $^{138}Ba^+$ ions with CO_2 gas. After the preparation of a pure barium crystal CO_2 gas at room temperature is leaked into the main chamber rising the pressure to 4×10^{-9} mbar and the time evolution of the crystal is recorded. Fig. 6.11 shows some CCD images of this barium crystal as a function of time. Neutral CO_2 molecules react with $^{138}Ba^+$ ions. Comparison between Fig. 6.11 and Fig. 6.7 shows that the chemical reaction of a barium ion ensemble with 4×10^{-9} mbar CO_2 gas and 8×10^{-9} mbar O_2 roughly have the same reaction rate.

In this specific experiment, the original barium crystal contains about 450 $^{138}Ba^+$ ions and 120 barium isotopic ions. The ion number of $^{138}Ba^+$ ions decreases to about 260 with CO_2 gas for 9 min and the ion number of the chemical reaction product BaO^+ rises from 0 to 190, while the ion number of the barium isotopes is constant. The time evolution of the ion numbers for each ion species is obtained by fitting CCD images at some time points and the results are shown in Fig. 6.12. The number of the $^{138}Ba^+$ ions decreases exponentially with a coefficient of $A_0 = 0.06$ min^{-1} (fitting the), which is quite close to the case of oxygen gas at 8×10^{-9} mbar.

A longer reaction time of more than one hour is chosen in this case. Finally, only about 20 $^{138}Ba^+$ ions are left but they are still quite cold, since the crystal structure is still distinguishable. All the other ions (about 430 BaO^+ ions and 120 isotopic ions) are sympathetically cooled by this low number of 20 laser-cooled $^{138}Ba^+$ ions. The arrangement of these three ion species in the last CCD image is simulated and shown in Fig. 6.13(c). Fig. 6.13(a) is the CCD image taken in the experiment and Fig. 6.13(b) is the simulation image of Fig. 6.13(a). The corresponding temperature of the $^{138}Ba^+$ ion ensemble is about 25 mK.

As the reaction of barium ions and neutral CO_2 molecules is endothermic with a reaction enthalpy of several eV [99, 100], the reaction should only occur with excited barium ions. Here, the same type of test is made as the case of oxygen. A pure barium crystal is prepared as shown in Fig. 6.14(a) followed by leaking in CO_2 gas to 4×10^{-9} mbar without the cooling lasers for 16 min. Subsequently, the CO_2 gas is pumped away and the cooling lasers are unblocked. The recrystallized barium ion ensemble is shown as Fig. 6.14(b). No big change occurs on this crystal as we expected - only the excited

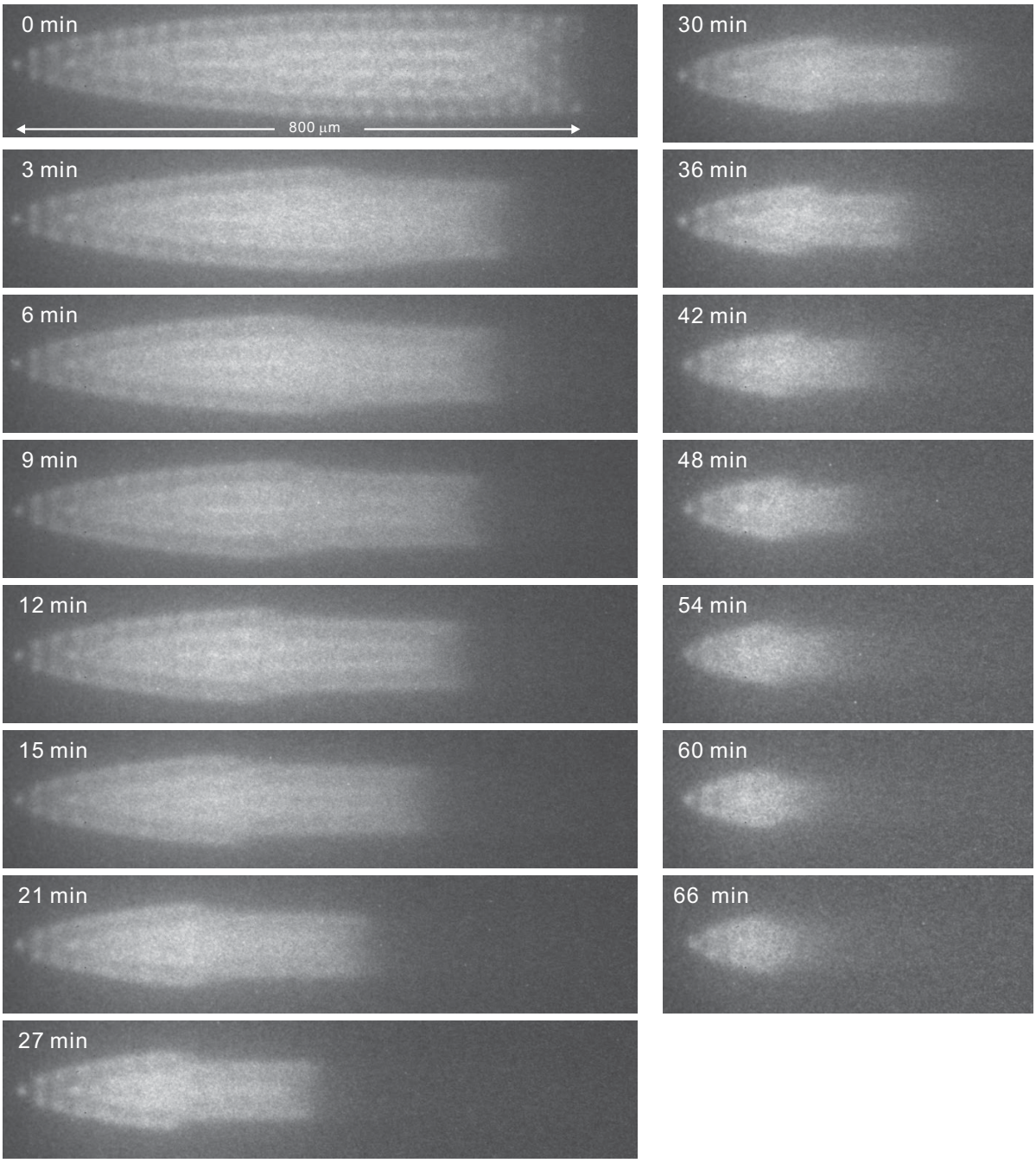

Figure 6.11: Time evolution of a barium ion crystal in presence of CO_2 gas at a pressure of 4×10^{-9} mbar.

barium ions participate in the chemical reaction. Then, with this crystal state we leak in CO_2 gas to 4×10^{-9} mbar for 5 min, the crystal is deformed quickly as shown in Fig. 6.14(c).

Now we repeat the experiment and block the repumping laser after loading a pure barium crystal and then leak CO_2 gas for 15 min into the vacuum chamber. In this case, most of the ions are in the $5^2D_{3/2}$ excited state. The final recrystallized barium crystal is shown in Fig. 6.15. Obviously the chemical reactions are not that fast. This means

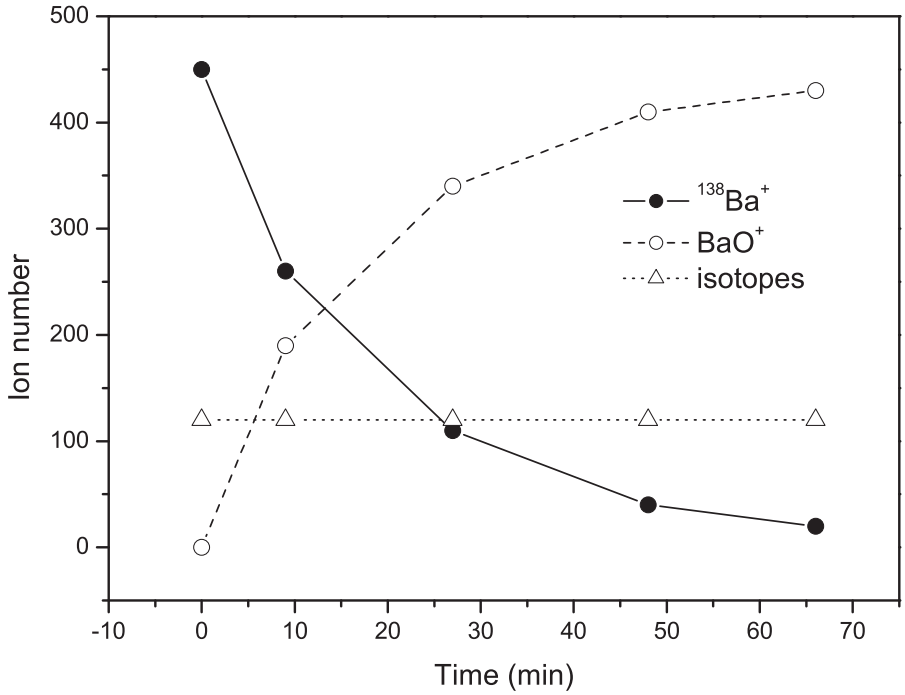

Figure 6.12: Time evolution of the ion numbers for all ion species with CO_2 gas at a pressure of 4×10^{-9} mbar.

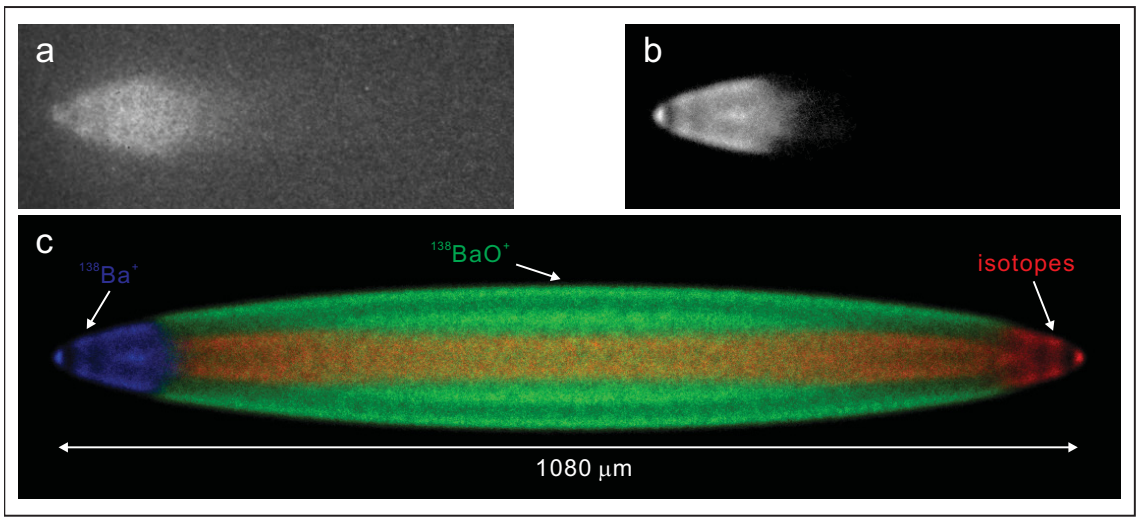

Figure 6.13: Simulation of the ion crystal of Fig. 6.11 after 66 min with CO_2 gas at a pressure of 4×10^{-9} mbar. This ion ensemble contains 20 $^{138}Ba^{+}$, 120 barium isotopes, and 430 $^{138}BaO^{+}$ ions. The temperature of each ion species used here is 25 mK. (a) CCD image from the experiment. (b) Simulated CCD image in order to fit (a). (c) Simulated image with all ion species identified with different colors.

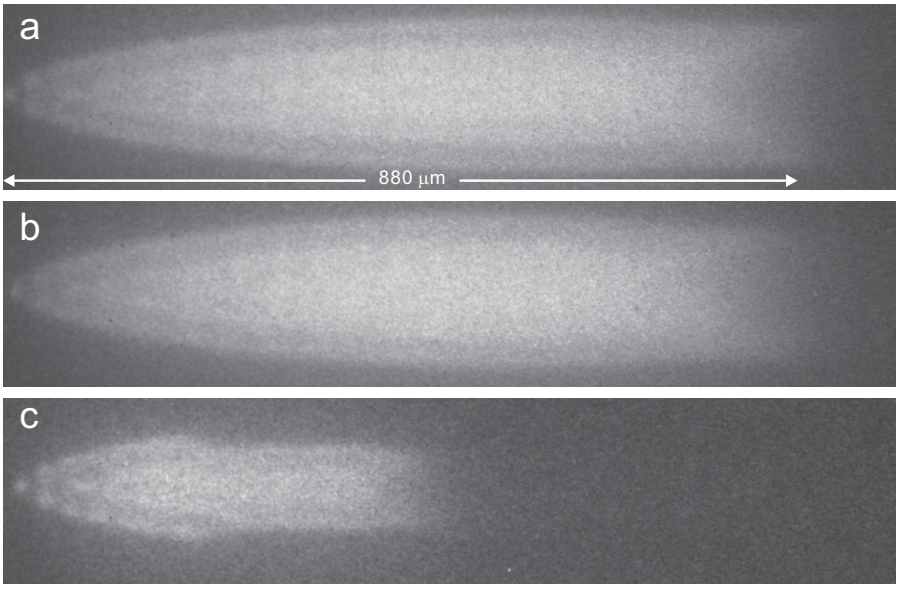

Figure 6.14: Chemical reactions between ground-state barium ions and neutral CO_2 gas. (a) A prepared pure barium crystal. (b) The recrystallized barium ion ensemble after leaking in CO_2 for 16 min without the cooling lasers. (c) The deformation of the barium crystal after leaking in CO_2 for 5 min with the cooling lasers on.

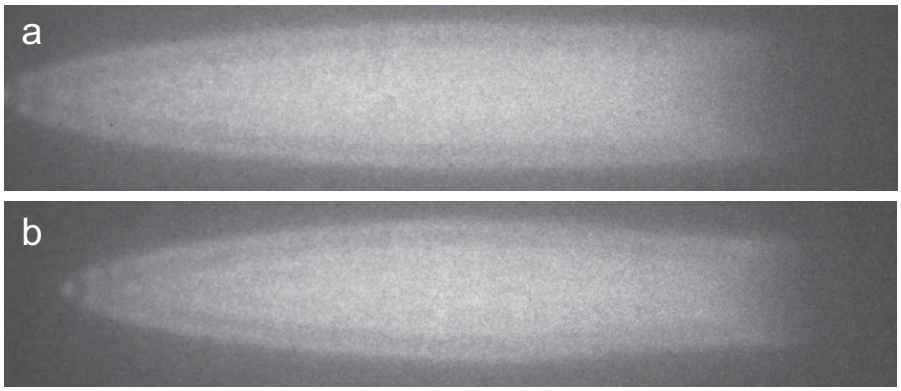

Figure 6.15: Chemical reactions between the barium ions in the $5^2D_{3/2}$ excited state and neutral CO_2 gas.

the $^{138}Ba^{+}$ ions at the $5^2D_{3/2}$ excited state are not as reactive with the neutral CO_2 gas as the oxygen.

Thus, the photo-chemical reaction equation has the form

$$^{138}Ba^{+}(^2P_{1/2}) + CO_2 \rightarrow {}^{138}BaO^{+} + CO. \tag{6.4}$$

We conclude that the shape deformation of the barium crystal is due to the photo-chemical reactions of the $^{138}Ba^{+}$ ions with the residual neutral oxygen and CO_2 gas. Since the content of CO_2 is much higher than oxygen in the residual background gas, the chemical reaction is mainly dominated by the CO_2 gas. The trapped reaction products

are $^{138}BaO^+$ ions.

6.5 Chemical reaction with N_2O

Here, we also study the chemical reactions between $^{138}Ba^+$ ions and neutral N_2O gas, since this reaction should be exothermic by -4.9 eV and should occur even with barium ions in the ground state. After the preparation of a pure barium ion crystal neutral N_2O gas is leaked into the main chamber at a pressure of 4×10^{-9} mbar. The time evolution of the barium crystal is recorded as a movie and frames with the time interval of 10.5 s are selected and sorted by time, as shown in Fig. 6.16. It is evident that the chemical reaction is quite fast and the chemical reaction rate is much higher than in the case of O_2 and CO_2. The ion numbers for each ion ensemble at selected moments are simulated and plotted in Fig. 6.17. Since the original barium crystal has not been cleaned sufficiently , there are some lighter ions (CO_2^+) and BaO^+ ions. Through the simulations we conclude that the ion numbers of the barium isotopes and CO_2 are both about 20 and roughly stay constant all the time (see the green and red triangle plots). The number of the $^{138}Ba^+$ ion ensemble decreases exponentially in the same way as the BaO^+ ion number increases shown as black and blue curve, respectively.

Since the BaO^+ ions are quite cold and do not increase the temperature of the $^{138}Ba^+$ ion ensemble, the intensity of the fluorescence should be proportional to the number of $^{138}Ba^+$ ions. When leaking in N_2O gas, the intensity of fluorescence is recorded using a PMT. The result is shown as the black curve in Fig. 6.18. The intensity of the fluorescence decreases exponentially as expected. The bend of the curve near the end mainly arises from the temperature rise, since with time more ions need to be sympathetically cooled and less barium ions can be laser cooled. We also compare this curve with our simulated ion numbers we obtained from the CCD images (circles in Fig. 6.18). These two curves agree very well.

6.6 Back-reaction with CO

One product of the photo-chemical reaction of the $^{138}Ba^+$ ion with CO_2 gas is neutral CO. This reaction is reversible and the back-reaction is an exothermic process,

$$^{138}BaO^+ + CO \rightarrow {}^{138}Ba^+ + CO_2 \quad -1.42 \text{ eV}. \tag{6.5}$$

In principle, this process can be tested in our experiment. First, we make a barium crystal and leak in CO_2 gas for a while. The barium crystal finally has the shape as shown in Fig. 6.19(a). Then, we pump the CO_2 gas away followed by leaking in CO gas at 1×10^{-8} mbar for about 10 min. In this time, the intensity of the fluorescence is recorded as shown in Fig. 6.20. The reverse reaction is observed, since the barium crystal becomes bigger and the intensity of the barium fluorescence increases. Finally, the chemical reactions reach a balance state. No more $^{138}Ba^+$ ions are released from $^{138}BaO^+$ and the intensity of the fluorescence keeps constant. The CCD image at the equilibrium state is shown in Fig. 6.19(b). In principle, since the concentration of CO is much higher than that of other background gases, almost all the $^{138}BaO^+$ ions should vanish and recover as as $^{138}Ba^+$ ions. Fig. 6.19(b) shows that there are still many $^{138}BaO^+$

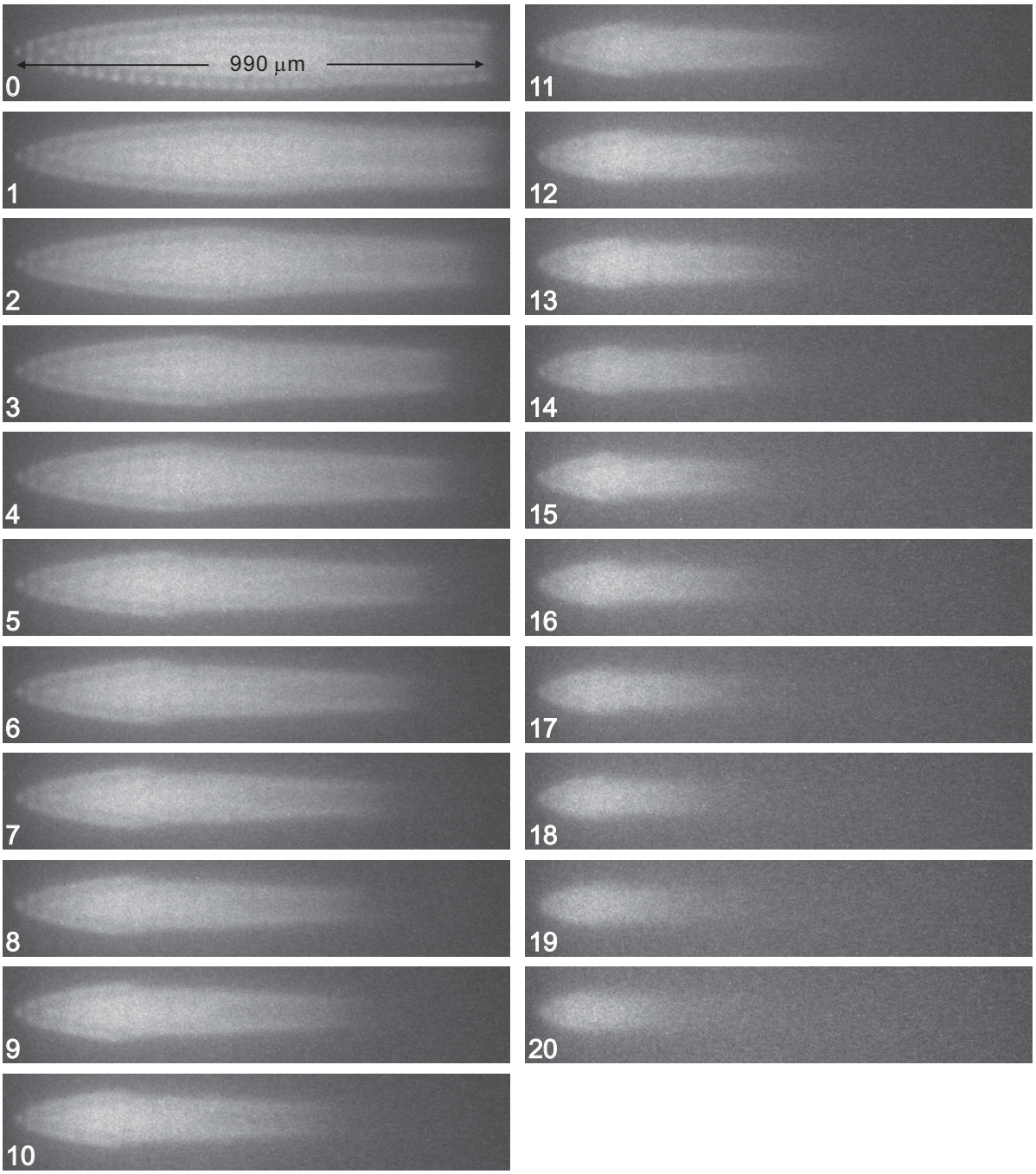

Figure 6.16: Time evolution of a barium ion crystal in the presence of N_2O gas at a pressure of 4×10^{-9} mbar. The time interval between two adjacent CCD images is 10.5 s, thus, the final CCD image was taken about 3.5 min after leaking in N_2O gas. Initially, there are about 540 laser-cooled $^{138}Ba^{+}$ ions and 70 sympathetically cooled ions (20 barium isotopes, 20 CO_2^+ ions and 30 $^{138}BaO^{+}$ ions), but in the final state only approximately 45 $^{138}Ba^{+}$ ions are left and the number of the sympathetically cooled ions increases to 565 (the increment is only from the $^{138}BaO^{+}$ ions)

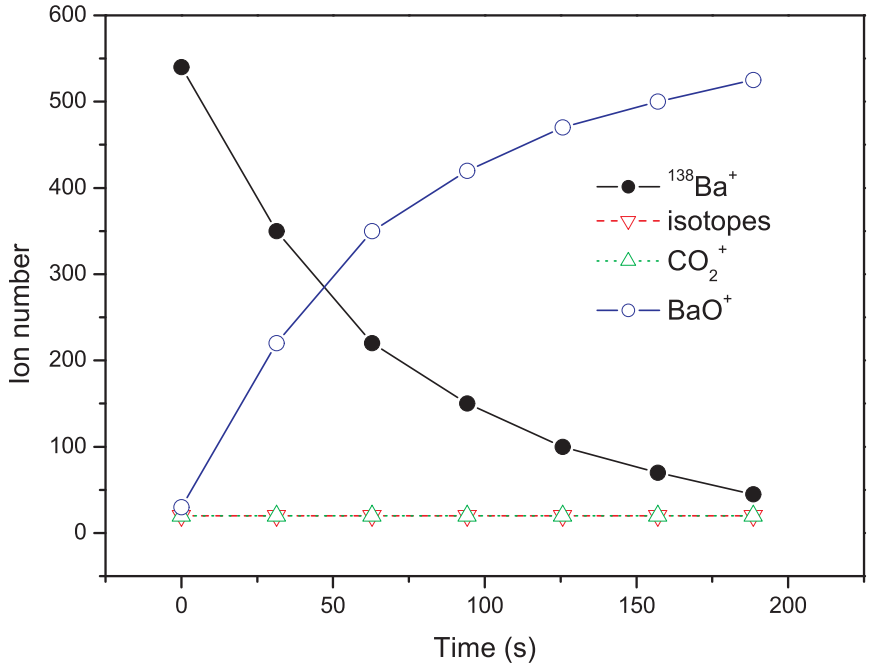

Figure 6.17: Time evolution of the ion numbers for each ion ensemble in the presence of N_2O gas at a pressure of 4×10^{-9} mbar, obtained through a MD analysis of the CCD images.

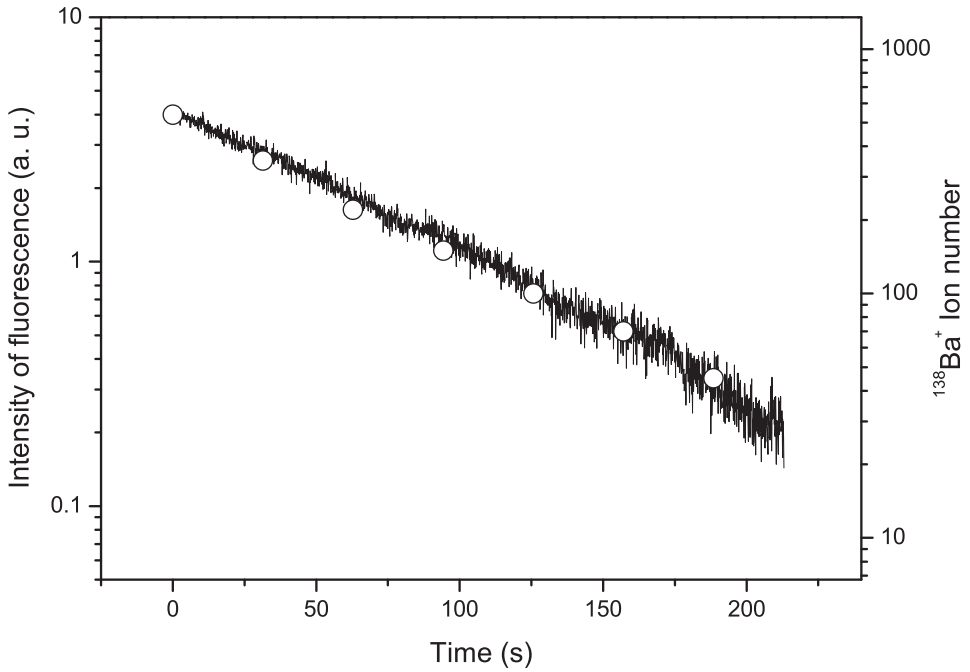

Figure 6.18: Time evolution of the intensity of the barium fluorescence in the presence of N_2O gas at a pressure of 4×10^{-9} mbar. The circles are the simulated ion numbers from CCD images.

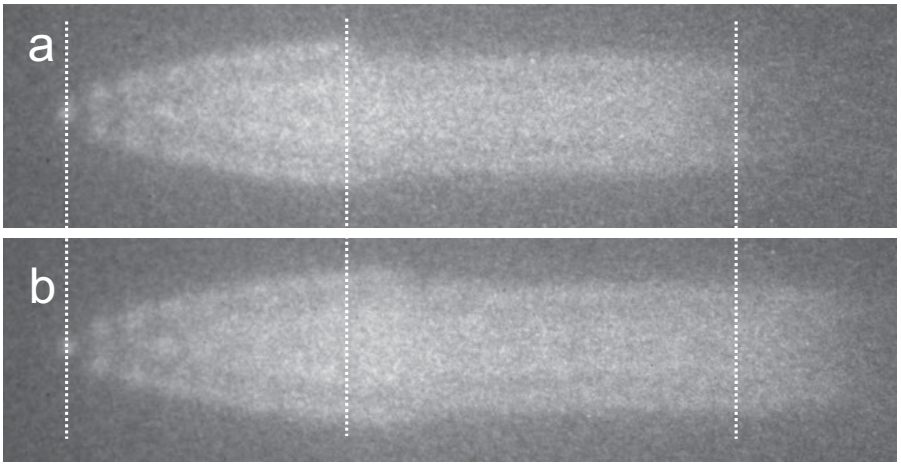

Figure 6.19: Investigation of the back-reaction of $^{138}BaO^{+}$ with CO gas at a pressure of 1×10^{-8} mbar. (a) CCD image of a barium ion crystal together with the product of the chemical reactions between the $^{138}Ba^{+}$ ions and CO_2 gas. (b) CCD image of the ion ensemble after leaking in CO gas for 10 min. Obviously, $^{138}Ba^{+}$ ion ensemble becomes bigger, so some $^{138}Ba^{+}$ ions are released from $^{138}BaO^{+}$ ions. The white dotted lines are only used to help to compare the size change of the $^{138}Ba^{+}$ ion crystal.

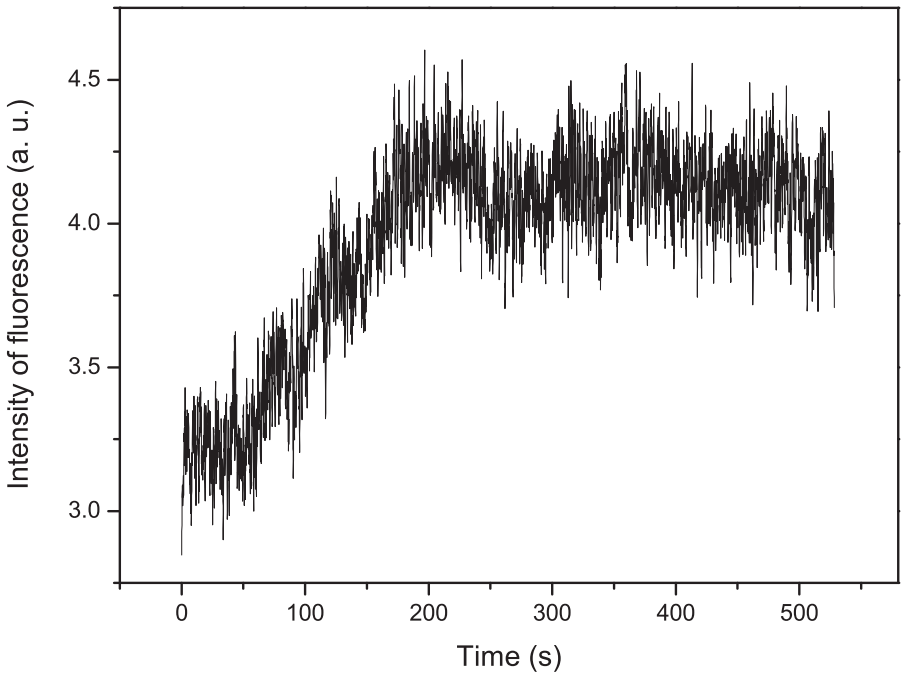

Figure 6.20: Time evolution of the intensity of the barium fluorescence in the presence of CO gas at the pressure of 1×10^{-8} mbar. The intensity of fluorescence indicates the number of $^{138}Ba^{+}$ ions.

left. The possible explanation is that the local CO_2 concentration is high (the released CO_2 molecules react with other $^{138}Ba^{+}$ ions actively before leaving the crystal space) or the $^{138}BaO^{+}$ ions are not the only product of the chemical reaction of the $^{138}Ba^{+}$ ions with the background gas molecules, or both.

7 Sympathetic cooling of medium sized organic molecular ions

In our apparatus, cold pure barium ion crystals have been produced and sympathetic cooling of light molecular ions, such as CO^+, O_2^+, Ar^+ [61], as well as of heavier molecular ions such as BaO^+, has been achieved. In this chapter, the sympathetic cooling of medium sized molecular ions (masses from 400 amu to 500 amu) is presented.

In the first section the loading process for complex molecular ions is introduced. As an example the loading of rhodamine 6G molecular ions is discussed. However, rhodamine 6G, as well as rhodamine 101, ions are not compatible with our cooling laser wavelengths. This will be explained in Sec. 7.2. In Sec. 7.3 and Sec. 7.4 the sympathetic cooling of Alexa Fluor 350 and glycyrrhetinic acid ions are described, respectively.

7.1 Loading of molecular ions

Molecular ions are charged by the ESI system and transferred to the trap through a 1.9 m long octopole (see Chapter. 4). In order to let most of the molecular ions enter the trap, the potential barrier is removed by lowering the endcap voltage at the trap entrance (the trap side close to the octopole is denoted as the entrance and the other side is called the exit side). Accordingly, the potential of the middle electrodes needs to be lower to create a potential well in axial direction. Fig. 7.1 shows the ion flux of rhodamine 6G detected by the channeltron beneath the trap as a function of the endcap voltage at the trap entrance. When the voltage is lower than -4 V, most rhodamine 6G molecular ions can leave the octopole ion guide and enter the trap, while when it is above 3 V most of the ions are blocked. Thus, usually, the endcap voltage at the trap entrance is set to be -2.5 V during the loading of the complex molecular ions and the DC offset voltage of middle electrodes is kept at -5 V all the time.

If the endcap voltage at the trap exit is equal to or even lower than that at the trap entrance, the molecular ions pass through the middle segment of the trap and leave the trap through the trap exit. However, if it is higher than that at the trap entrance, some molecular ions can be stopped, but they will be pushed back and escape from the trap entrance. Therefore, helium is used as a buffer gas to decelerate the molecular ions and accumulate them in the tap (the cooling principle of the buffer gas cooling is described in Chapter 3). The principle of the ion loading with buffer gas is shown in Fig. 7.2. Typically, the endcap voltage at the trap exit end is set be to 2 V.

The DC offset of the octopole is set to about -27 V to shorten the time of passing the octopole for the molecular ions to improve the ion transfer efficiency. Thus, the molecular ions gain $27Q$ eV (Q is the charge number of the molecular ions) kinetic energy along the trap axial direction. -2.5 V for the endcap voltage at the entrance is a good setting to let the main portion of the molecular ions enter the trap, as well to slow the ions down

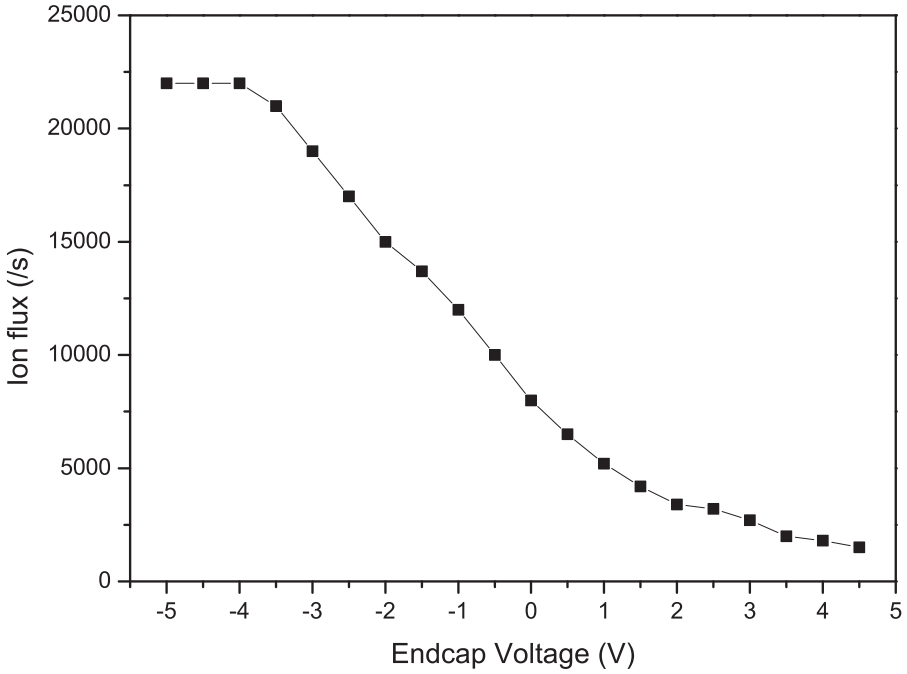

Figure 7.1: Ion flux as a function of the endcap voltage at the trap entrance using rhodamine 6G as an example.

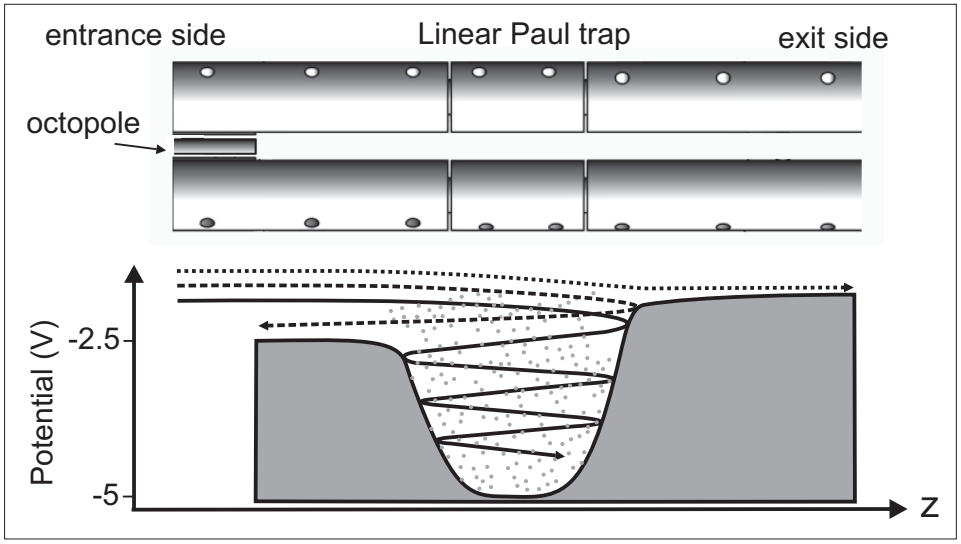

Figure 7.2: Principle of ion loading with the help of buffer gas. The buffer gas decelerate some molecular ions so much that they can be captured by the ion trap [61].

sufficiently before they enter the trap. This makes it possible to trap the molecular ions at an acceptable buffer gas pressure.

As a routine procedure, after the loading of molecular ions, we stop leaking in the helium buffer gas and lift up the endcap voltage at the entrance to the same value as at the exit end. The residual helium buffer gas is pumped away in less than a minute. Whether the molecular ions are trapped or not can be checked by an ion extraction.

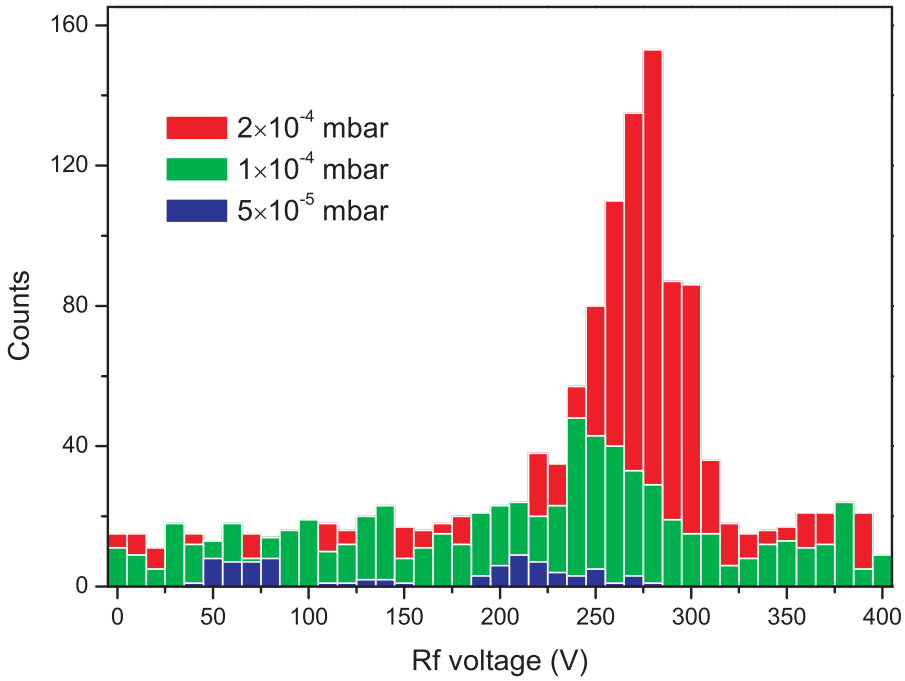

Figure 7.3: Ion extraction spectra of rhodamine 6G molecular ion ensembles loaded at different buffer gas pressures.

The number of loaded molecular ions depends on the buffer gas pressure and the loading time. Fig. 7.3 shows the ion extraction spectra of rhodamine 6G ion ensembles loaded at different buffer gas pressures. Due to the low resolution of the ion extraction technique we need an ion ensemble to be a reference to check the mass-to-charge ratio of the target ion ensemble. Here, we use a laser-cooled barium ion ensemble. Fig. 7.4 is the ion extraction spectrum. The peak position for the light ions is at an rf voltage of about 100 V. The peak for the molecular ions in Fig. 7.11 is at around 270 V. Thus, the molecular ions are much heavier than the barium ions. They should be rhodamine 6G molecular ions.

The ion flux of rhodamine 6G ions is about 10000 counts per second and the loading time is about 1 min in Fig. 7.3. Obviously, the trapping efficiency in this case is quite low (less than 1% rhodamine 6G molecular ions are trapped). Actually, since the octopole and the trap have different rf fields, the coupling between these two multi-pole setups is very critical for the trapping efficiency in the experiment. In this case, with a low buffer gas pressure (less than 5×10^{-5} mbar) only a few complex molecular ions are trapped. However, at 2×10^{-4} mbar we can capture more than 1000 rhodamine 6G ions, which is enough for our experiments. In principle, a higher buffer gas pressure always increases the ion loading efficiency. However, too high buffer gas pressures require a much longer time to achieve ultra-high-vacuum conditions again. Thus, normally, we prefer to leak in the helium buffer gas to less than 1×10^{-4} mbar.

The loading time is another parameter that allows controlling the number of molecular ions loaded. Fig. 7.5 shows ion extraction spectra of rhodamine 6G ion ensembles for different loading times (1, 2, and 4 min) with a helium buffer gas pressure at 2.5×10^{-4}

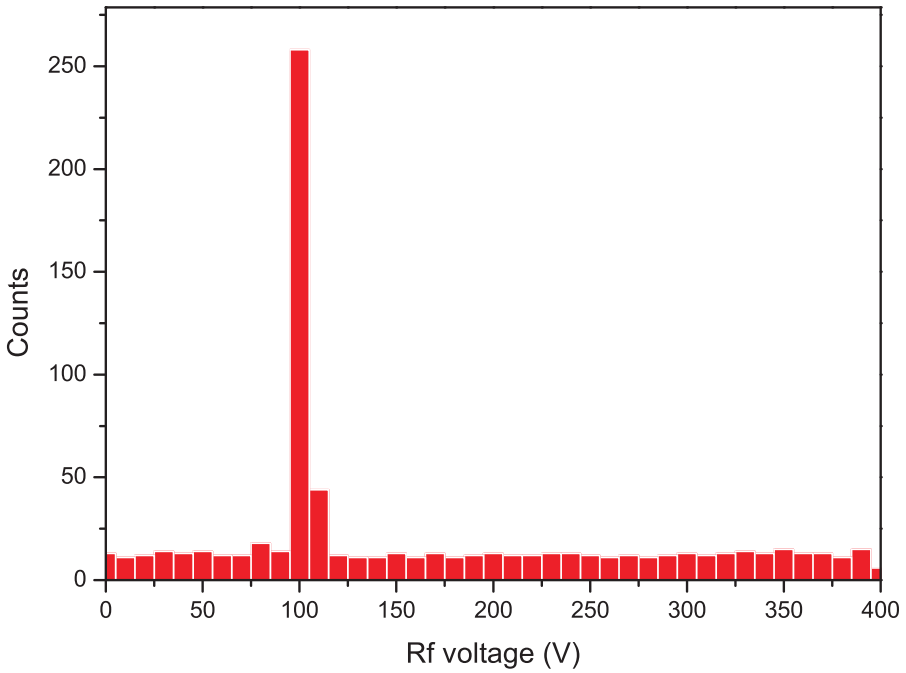

Figure 7.4: An ion extraction spectrum of a laser-cooled pure barium ion ensemble. The peak is narrow due to its low temperature.

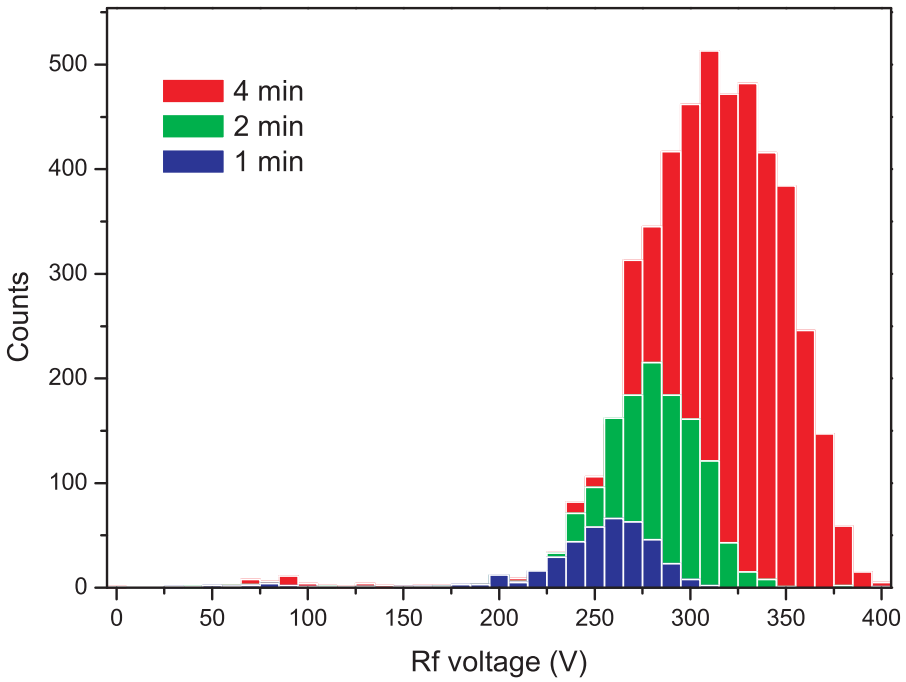

Figure 7.5: Ion extraction spectra of rhodamine 6G molecular ions after different loading times.

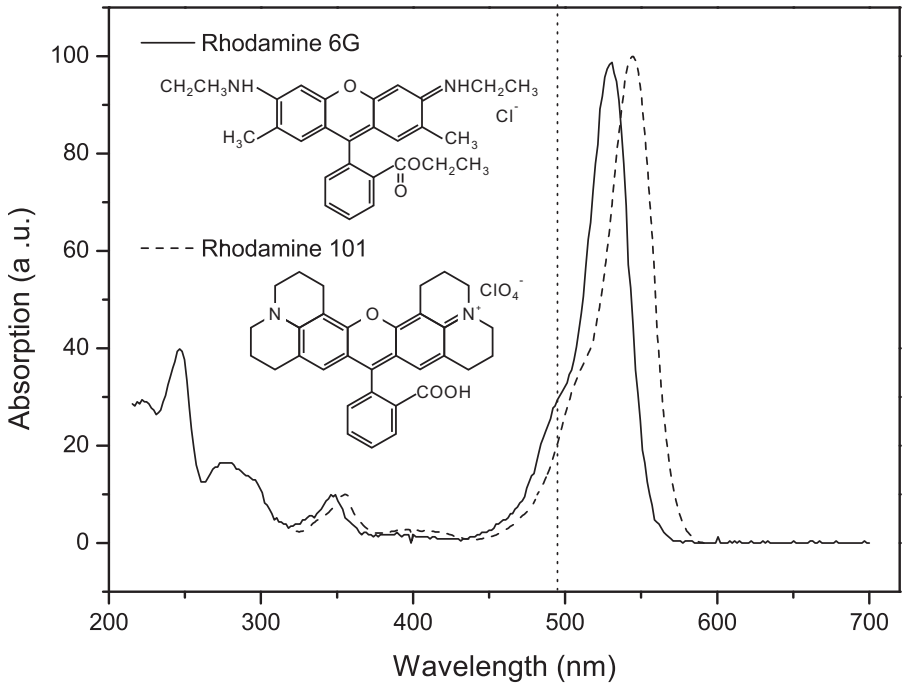

Figure 7.6: Absorption spectra of Rhodamine 6G (full curve) and Rhodamine 101 in solution and their molecular structures [101]. The vertical line is the wavelength of the $^{138}Ba^{+}$ cooling laser.

mbar each time. The counted ion numbers of rhodamine 6G are 400, 1300, and 4700 accordingly.

Thus, by choosing the appropriate loading time and buffer gas pressure enough molecular ions can be captured by the trap. The loaded number of the molecular ions nevertheless is not repeatable varying by $\pm 80\%$.

7.2 Photofragmentation of Rhodamine ions

Rhodamine 6G is a widely used laser dye and its maximum absorption is approximately at 530 nm. The absorption spectrum is shown in Fig. 7.6. Its molecular weight is 479 amu and its molecular formula is $C_{28}H_{31}N_2O_3Cl$. In the solution negatively charged chlorine and the positively charged $C_{28}H_{31}N_2O_3^+$ exist separately. With our electrospray apparatus this positively charged molecule can be transferred to our Paul trap. Moreover, we have succeeded in trapping the rhodamine 6G molecular ions and simultaneous trapping of rhodamine 6G and barium ions is shown in the following: After loading the rhodamine 6G ions, barium ions are loaded without the lasers. Its ion extraction spectrum is shown in Fig. 7.7. The far separated two main peaks indicate that the rhodamine 6G molecular ions stay in the trap with the barium ions simultaneously.

But unfortunately the rhodamine 6G ions photodissociate in the cooling laser light, so that they cannot be sympathetically cooled by laser cooled barium ions. Fig. 7.8 shows a comparison of two ion extraction spectra with and without the 493 nm cooling laser (the 650 nm laser is always unblocked). The extracted ions loaded with the cooling laser

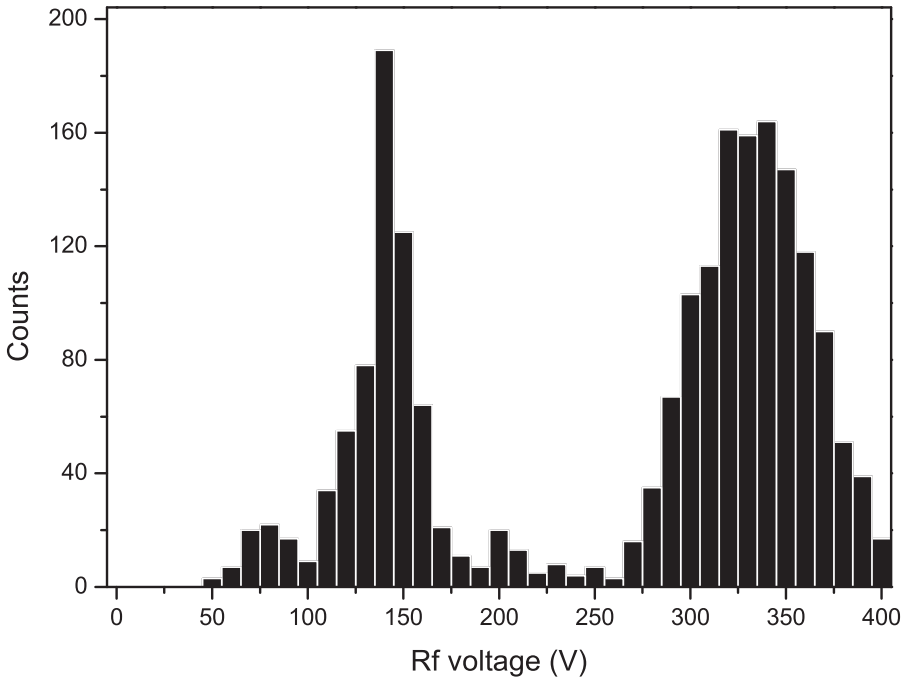

Figure 7.7: An ion extraction spectrum of an ensemble of Rhodamine 6G molecular ions (right peak) and barium ions (left peak).

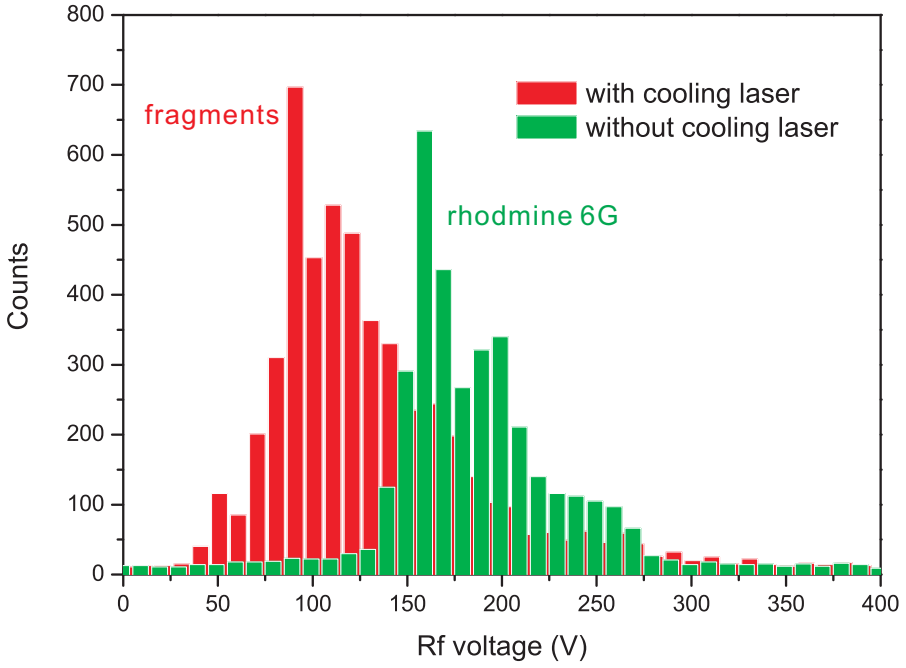

Figure 7.8: Ion extraction spectra of rhodamine 6G ion ensembles with and without exposure to the cooling laser. Since lower rf voltages stand for the ions with lower mass-to-charge ratios, the ions stored with the 493 nm cooling laser on are fragmented.

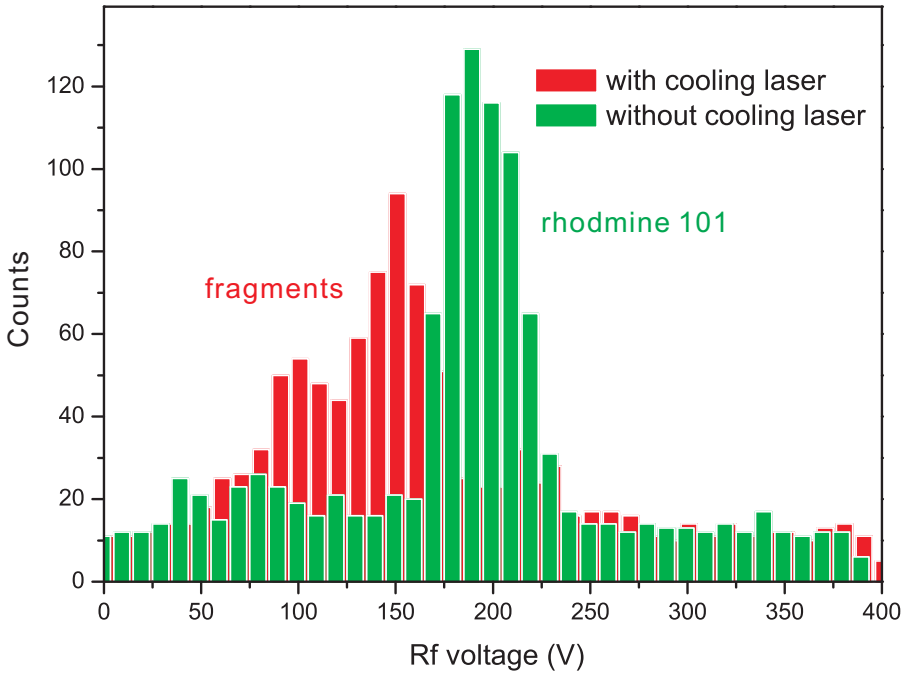

Figure 7.9: Ion extraction spectra of Rhodamine 101 ion ensembles with and without exposure to the cooling laser.

(red histogram) produce a peak in the lower rf voltage range. Since lower rf voltages correspond to ions with lower mass-to-charge ratios, this is the proof for a fragmentation of the rhodamine 6G ions by the cooling laser light.

Normally, if rhodamine 6G molecules dissolved in a solution absorb photons and are excited, they relax by emitting photons and via collisions. Unlike in a solvent, rhodamine 6G molecular ions in a vacuum are quite unstable in the presence of the 493 nm cooling laser as they cannot dissipate their energy via collisions. Since the average binding energy of a C-C bond is 3.6 eV and a C-N bond is 3.0 eV, the photon energies of the cooling lasers of 2.5 and 1.9 eV are not large enough to break up the bonds directly. Anyway, a rhodamine 6G molecular ion can absorb several photons and transfer the energy to vibrational energy via internal energy conversion. Shining the cooling lasers continuously increases the internal energy beyond the dissociation energy, whilst for the case in a solution the internal energy can be dissipated efficiently via the interaction with the other molecules.

Rhodamine 101 has a similar chemical structure and absorption spectrum as shown in Fig. 7.6. Similar to R6G we found for R101 ions that they are also photo fragmented by the 493 nm cooling laser. The ion extraction spectra with (red histogram) and without (green histogram) the cooling laser are shown in Fig. 7.9.

7.3 Sympathetic cooling of Alexa Fluor 350 ions

To avoid photofragmentation by the 493 nm cooling laser and the 650 nm repumping laser, the complex molecular ion species needs to have a low absorption at the wave-

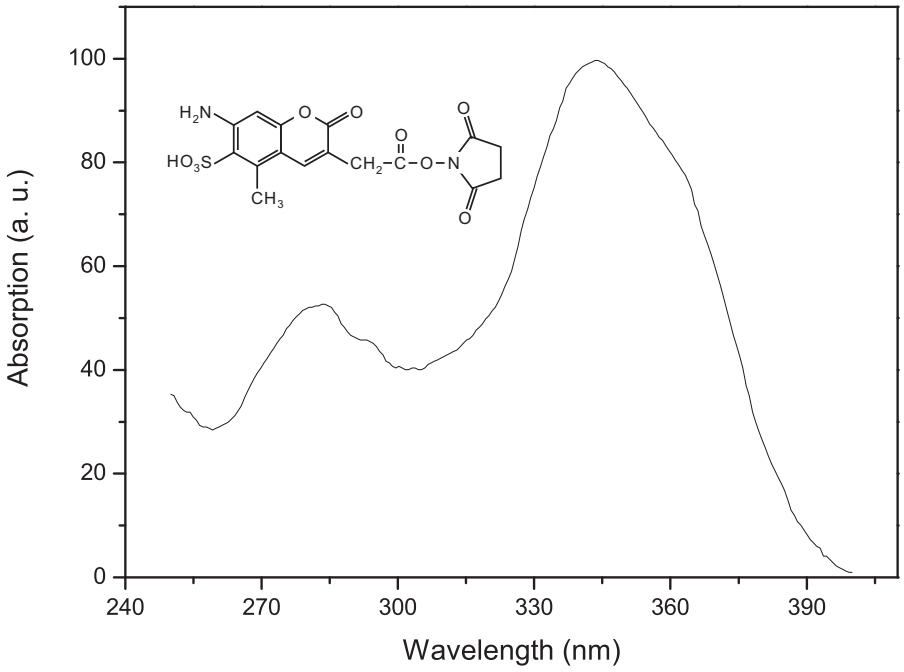

Figure 7.10: Absorption spectrum of Alexa Fluor 350 and its molecular structure.

lengths of our cooling lasers. The dye molecule Alexa Fluor 350 fulfills this requirement. Its strong absorption region is in the UV range as shown in Fig. 7.10 and it can emit blue fluorescence light (observed in solution) when excited by a UV laser.

Alexa Fluor 350 (sometimes denoted as AF) is a dye molecule commonly used for fluorescent labelling in biological research. The compound is water soluble. It has the molecular formula $C_{16}H_{14}N_2O_9S$, its structure is shown in Fig 7.10, and its molecular weight is about 410 amu. In our experiment, the compound is dissolved in a 50 : 50 mixture of methanol and water at a concentration of 250 pmol·ml^{-1}. The volatile methanol is helpful for the electrospray ionization process (it helps to reduce the volume of the charged droplets emitted from the needle of the ESI). Formic acid is added at 1.25% concentration to protonate the Alexa Fluor 350 molecules. Typically, the ion flux of the Alexa Fluor 350 is little bit higher than 100 counts per second. A few hundred Alexa Fluor 350 complex molecular ions can be captured in 4 min with helium buffer gas at a pressure of 1×10^{-4} mbar.

In order to prove the photostability of the Alexa Fluor 350 molecular ions in the vacuum situation, we loaded Alexa Fluor 350 ions to the trap twice. First, after the loading, the molecular ions are left in the trap for 4 min without any exposition to the cooling lasers, followed by an ion extraction. In the second loading, the lasers are unblocked for the same time following the loading of the molecular ions and an ion extraction is done. Comparing these ion extraction spectra shows that both spectra have the same peak position, at about 170 V of rf voltage, as shown in Fig. 7.11. There is no indication of fragmentation. So the Alexa Fluor 350 ions under the vacuum environment are stable against photodissociation by the 493 and 650 nm lasers.

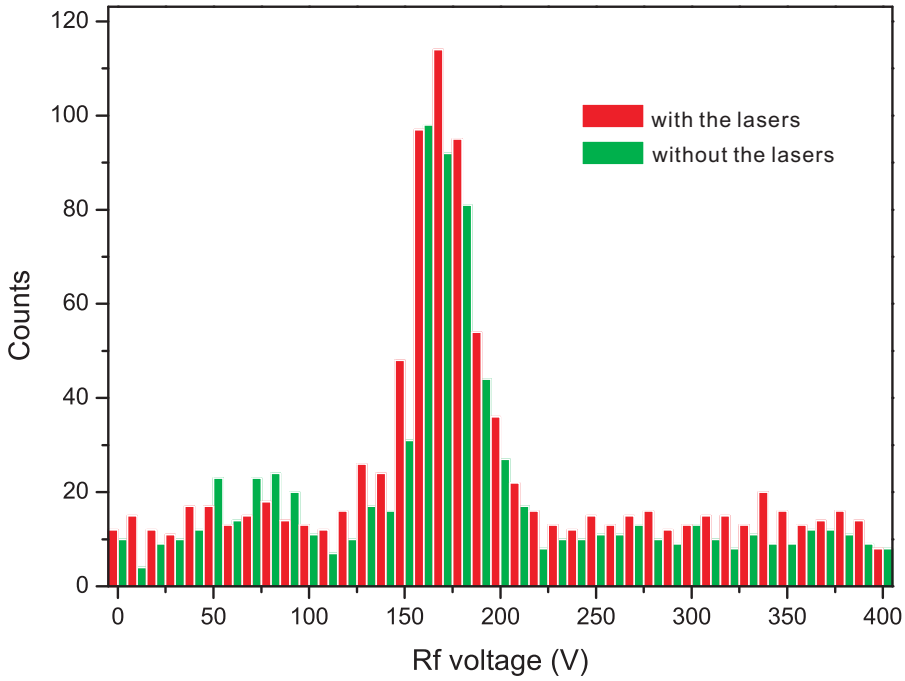

Figure 7.11: Ion extraction spectra of Alexa Fluor 350 ion ensembles with and without exposition to our lasers.

Simultaneous trapping of Alexa Fluor 350 and barium ions is the basic condition for sympathetic cooling of the Alexa Fluor 350 ions. We used the following procedure: After loading the Alexa Fluor 350 ions for 4 min at 1×10^{-4} mbar helium buffer gas pressure, the leak valve is shut off and in a few minutes the background pressure returns to about 5×10^{-10} mbar. Then, the barium ions are loaded. In the whole process the cooling lasers are blocked. An ion extraction is done on the final ion ensemble shown as the red histogram in Fig. 7.12. Three different ion species are distinguishable in this ion ensemble: light ions such as CO_2^+, barium ions, and Alexa Fluor 350 ions. The broadness of the peaks indicates that all ions are quite hot (see Chapter 4).

Therefore, the ion extraction is also a tool to determine the ion temperatures qualitatively. This we show for an ion ensemble of Alexa Fluor 350 and barium ions. We repeat the loading procedure, but in this time the lasers are directed into the trap all the time. Before the ion extraction, light ions are cleaned away followed by a detuning of the lasers to obtain the maximum fluorescence intensity of the $^{138}Ba^+$ ion ensemble, which corresponds to the a high cooling rate. Although the barium ion ensemble is not crystallized, it is already cooled to far below the room temperature (below 1 K as found through simulations). The Alexa Fluor 350 molecular ions are sympathetically cooled through the Coulomb interaction with the barium ions. The ion exaction for this ion ensemble is shown in Fig. 7.12 (green histogram). In this case, the ion peak for the light ions is negligible. The two other peaks are much narrower. This means that not only the barium ions but also the Alexa Fluor 350 ions are cooled. This is the first evidence of the sympathetic cooling of complex molecular ions.

Another indication of the lower thermal energy of the two species is that the maximum

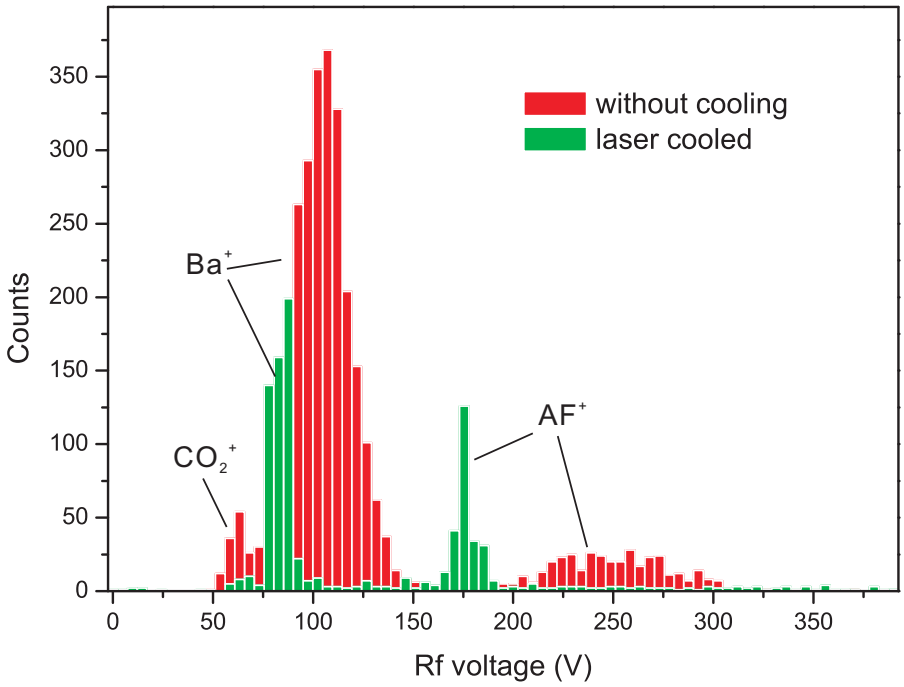

Figure 7.12: Ion extraction spectra of ion ensembles containing barium and Alexa Fluor 350 ions with and without laser cooling. When the barium ion species is laser cooled, all the other ion species present in the trap are sympathetically cooled. The temperatures are reflected by the widths of the peaks.

peak positions move to lower rf voltages, since at low temperature the ion density at a low velocity becomes higher. Nevertheless, the shift of the peak position for the Alexa Fluor 350 ions looks quite large. This is mainly due to the reduction of the size of the barium ion ensemble. Since the Alexa Fluor 350 molecular ions are much heavier than the barium ions, they stay outside the barium ion ensemble. The ion ensemble shown in red contains more barium ions, which pushes the Alexa Fluor 350 ions further away from the trap axis and in the ion extraction process the Alexa Fluor 350 ions are pushed out of the ion trap earlier, when ramping down the rf voltage during the ion extraction process.

Although the Alexa Fluor 350 ions were sympathetically cooled by a laser-cooled barium ion ensemble, the whole ion ensemble was still quite hot, since the barium ion ensemble was not crystallized. The barium ion ensemble is sympathetically heated by the Alexa Fluor 350 molecular ions. In principle, reducing the ion number of Alexa Fluor 350 results in less sympathetic heating. This has been shown experimentally. A new loading of the Alexa Fluor 350 molecular ions is performed, but the loading time is shortened from 4 min to 6 s. In this case, the ensemble of barium and Alexa Fluor 350 ions can be crystallized, as shown in Fig. 7.13(a). This particular two-species ensemble was trapped and cooled for 4 minutes, but this time could be as long as an hour.

The destructive ion extraction method can tell us the mass of the molecular ions only roughly due to its poor resolution. Thus, to determine the mass the molecular ions more precisely the nondestructive method of secular excitation with a small amplitude,

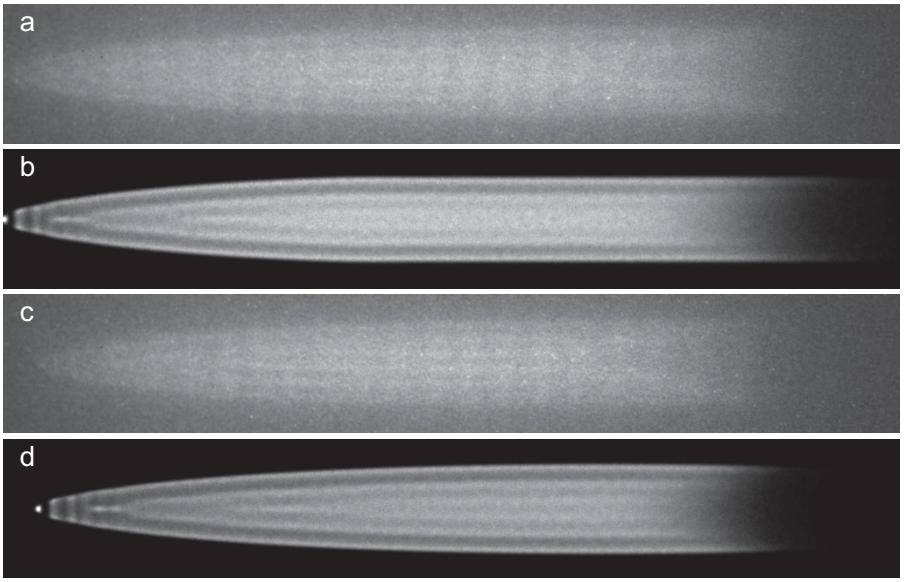

Figure 7.13: CCD images taken from the experiment and their simulated images. (a)(b) Barium ions together with Alexa Fluor 350 molecular ions. (c)(d) Alexa Fluor 350 molecular ions were already removed from the trap.

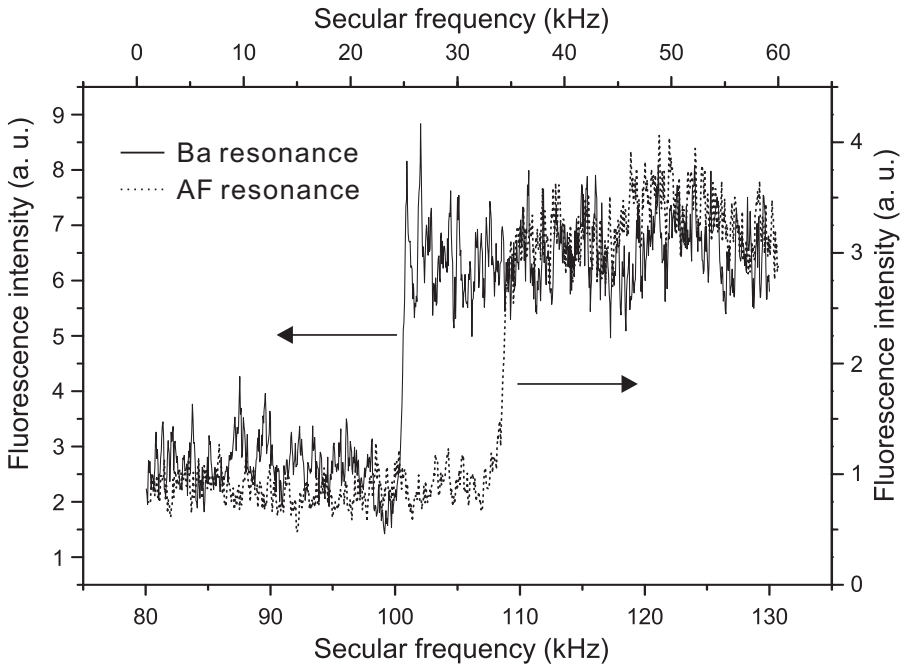

Figure 7.14: Radial secular excitation spectra of an ion cluster containing barium ions and Alexa Fluor 350 complex molecular ions.

is commonly used. Radial resonances were observed at 102 kHz (for direct Ba excitation) and at around 33 kHz (see Fig. 7.14). The latter value implies a mass of the trapped molecules of 418 ± 11 amu, consistent with the value expected for Alexa Fluor 350. The excitation amplitude used here heated the ensemble so strongly that the crystal melted (represented in the step downwards of the recorded fluorescence intensity). When scanning from high to low frequency this permitted the measurement of the single

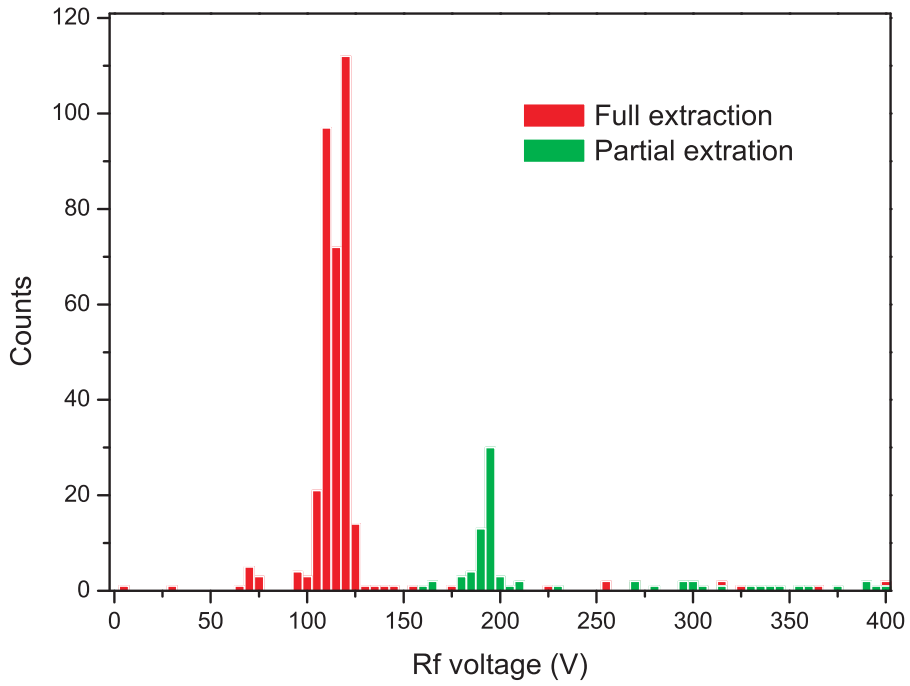

Figure 7.15: Ion extraction spectrum of the barium ion ensemble and partial extraction spectrum of the Alexa Fluor 350 ion ensemble for the calibration of the ion number of each species.

particle secular frequency as opposed to the (shifted) frequency of a strongly coupled two-component crystal [102].

However, the ion extraction can be used to count the ion number of each ion species (if they have a significant large mass difference). For the ion ensemble shown in Fig. 7.13(a), we first do a partial extraction by reducing the rf amplitude from 400 V to 150 V, which is actually still above the extraction rf voltage for the barium ion ensemble. The partial ion extraction spectrum of Alexa Fluor 350 ions is plotted as a green histogram in Fig. 7.15. The counts covering the peak are summed up as the counted Alexa Fluor 350 molecular ions. It is 60.

The rf voltage is turned back to 400 V directly following the ion extraction. The remaining crystal only contains barium ions, its CCD image is shown in Fig. 7.13(c). Since the sympathetic heating from the Alexa Fluor 350 molecular ion ensemble is gone, the barium crystal becomes colder, showing a clearer structure than the crystal in Fig. 7.13(a).

Finally, a full ion extraction is performed by lowering the rf voltage from 400 to 0 V. The barium crystal is ejected from the trap and the ions are counted (see the red histogram in Fig. 7.15). In total 318 barium ions were counted. Thus, the ratio of the ion numbers of the Alexa Fluor 350 ion ensemble to the barium ion ensemble is approximately 1 : 5.3, assuming both ion species having the same detection efficiency (independent of ion mass). The narrow peak for the Alexa Fluor 350 ions indicates this ion ensemble is sympathetically cooled.

In fact, the extraction efficiency is not 100%, i.e. the above absolute numbers are not equal to the numbers of ions originally trapped. Thus, we need to obtain the counting efficiency. Through a molecular dynamics simulation, it is found that the barium ion crystal shown in Fig. 7.13(c) contains 770 ± 20 $^{138}Ba^+$ ions and 410 ± 20 barium isotopes (when doing a partial extraction for the heavier molecular ion, due to the strong changes of the voltages the barium ion ensemble might loose a small portion of ions.). From this real barium ion number of the crystal shown in Fig. 7.13(c), we obtain that the detection efficiency is about 30% and the ion number of the Alexa Fluor 350 ion ensemble can be derived to be 200 ± 20 with the ratio of $1 : 5.3$ derived before. Subsequently, the barium ion number of the ensemble shown in Fig. 7.13(a) can be determined via MD simulation as well: 830 ± 20 $^{138}Ba^+$ ions and 420 ± 20 barium isotopes. It is evident that in the partial ion extraction process a small fraction (5.6%) of the barium ions are lost.

The determination of the Alexa Fluor 350 ions' temperature works as follows: The temperature of the $^{138}Ba^+$ ions can be determined by simulating a consistent image directly. Fig. 7.13(b) and Fig. 7.13(d) are the simulated images for Fig. 7.13(a) and Fig. 7.13(c), respectively. And their corresponding temperatures are 28 and 35 mK, respectively. The temperature determination for other ion ensembles depends on the laser cooling rate of the $^{138}Ba^+$ ions. Theoretically, the laser cooling rate for a barium system is about $\beta/m_{Ba} = 760$ s^{-1} (see Chapter 9). Nonoptimal laser polarizations with respect to the magnetic field and the presence of micromotion may lead to less efficient cooling. If we consider a stronger cooling, $\beta/m_{Ba} = 870$ s^{-1}, the determined temperatures are higher than the actual ones. Thus, these simulated temperatures are taken to be upper limit temperatures.

Since the barium isotopes are similar in mass and near-axis location to the $^{138}Ba^+$ ions, we always assume them having the same heating rate as the $^{138}Ba^+$ ions (see Chapter 9). Therefore, in the case of $\beta/m_{Ba} = 870$ s^{-1}, an intrinsic heating rate of $k_B(10.4$ K/s) per barium ion is needed to obtain the image shown in Fig. 7.13(d). Since the crystal dimensions and its temperature in Fig. 7.13(b) are similar to those of the crystal in Fig. 7.13(d), the cooling and intrinsic heating rates of the barium ion ensemble are reasonably assumed to be the same. Thus, the temperature difference of the two $^{138}Ba^+$ ion crystals is assumed to be caused by the sympathetic heating of the Alexa Fluor 350 ions. To heat the $^{138}Ba^+$ ion ensemble from 28 to 35 mK, a heating rate of $k_B(18.5$ K/s) for each Alexa Fluor 350 ion is required. And the corresponding temperature of the Alexa Fluor 350 ion ensemble is 138 mK. On the other hand, if we repeat the simulations with $\beta/m_{\mathtt{Ba}} = 760$ s^{-1}, the heating rate for the barium ions and the Alexa Fluor 350 molecular ions are $k_B(6.6$ K/s) and $k_B(10.6$ K/s), respectively. The corresponding temperature of the Alexa Fluor 350 ions is found to be 88 mK. Thus, we find an upper limit of the secular temperature for the Alexa Fluor 350 ions of 138 mK. More details about the principle of the temperature determination via MD simulation method are given in Chapter 9.

The finally determined ion ensemble containing barium and Alexa Fluor 350 ions is shown as a simulated image in Fig. 7.16. The Alexa Fluor 350 molecular ions stay around the barium crystal as shown in green. The whole ion cluster is about 1.7 mm long and

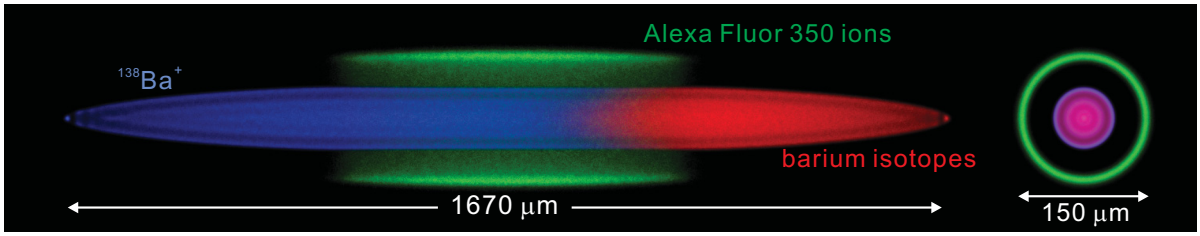

Figure 7.16: Simulated Coulomb crystal containing 830 $^{138}Ba^{+}$, 420 barium isotopes, and 200 Alexa Fluor 350 ions. Their temperatures are approximately 35 mK, 57 mK, and 138 mK, respectively. Here, the ion ensemble is shown in a radial (left) and axial view (right).

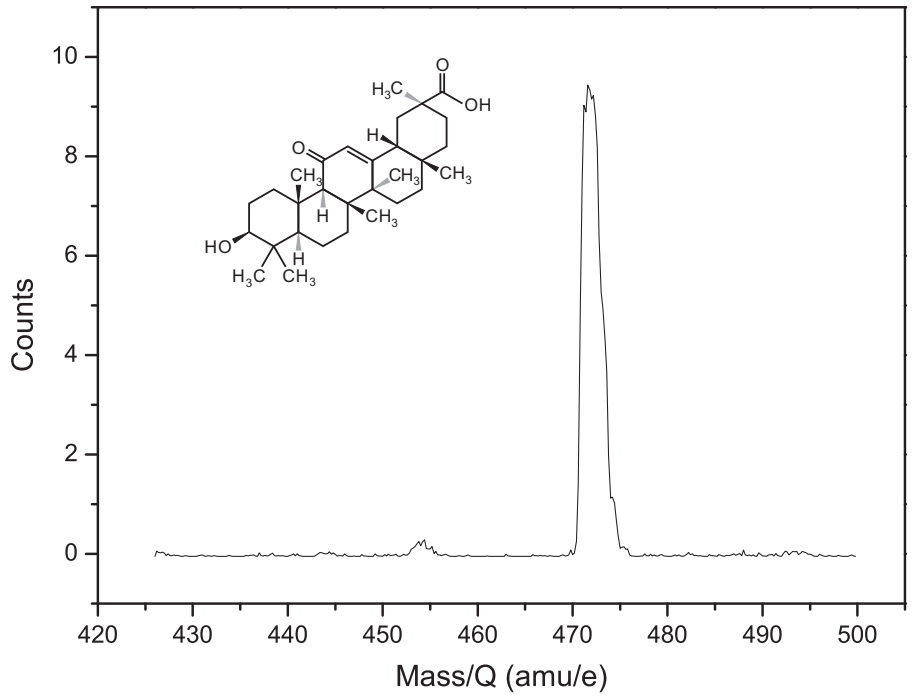

Figure 7.17: Mass spectrum of GA obtained in our ESI system.

150 μm wide. The temperatures of the ion ensembles of $^{138}Ba^{+}$, barium isotopes, and Alex Fluor 350 are 35 mK, 57 mK, and 138 mK, respectively.

This is the first time such big complex molecular ions have been cooled down to the millikelvin regime. The sympathetic cooling technique is proven to be reliable and efficient for cooling medium weight molecular ions.

7.4 Sympathetic cooling of glycyrrhetinic acid ions

For our further investigations we were looking for a molecule which can be loaded easier and which is cheaper and easier to handle. Glycyrrhetinic acid (GA) is the second medium mass compound that was sympathetically cooled in our linear Paul trap. Its molecular formula is $C_{30}H_{46}O_4$, and its molecular weight is 470.74 amu. Fig. 7.17 (inset) shows its molecular structure. This compound is dissolved in a 50 : 50 mixture of

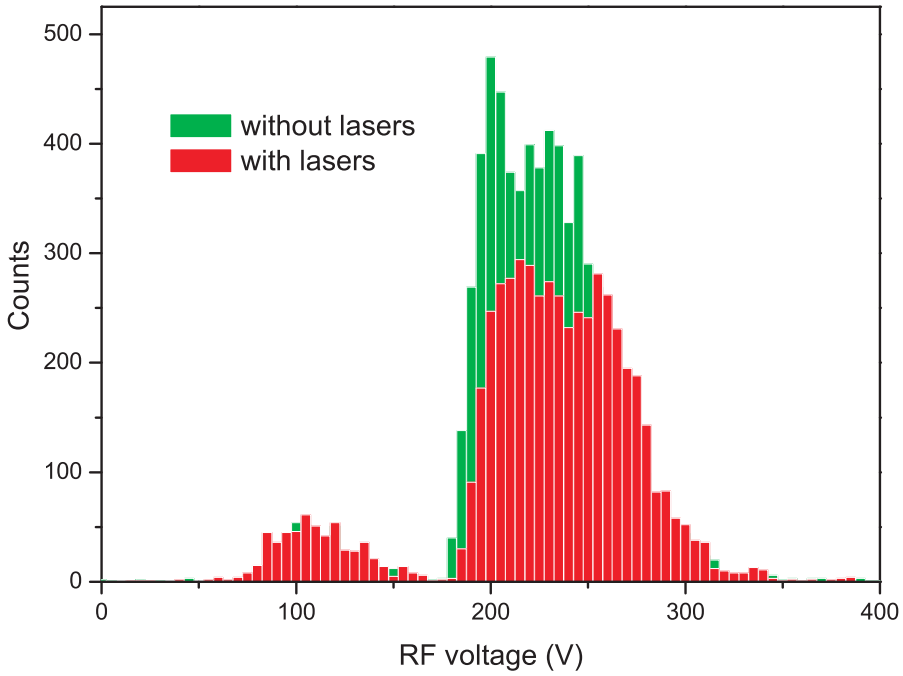

Figure 7.18: Ion extraction spectra of GA^+ molecular ions with and without exposure to the lasers (without barium ions). The small peaks are fragments generated during the loading procedure by collisions of the GA^+ ions with buffer gas atoms. The GA^+ ions are stable in the presence of the cooling laser light as no additional fragments appear(red histogram).

acetonitrile and water solution at a concentration of 10 pmol/μl. Formic acid is added at the concentration of 0.01%. Its mass spectrum from 420 amu/e to 500 amu/e taken by our ESI system is shown in Fig. 7.17. There is a strong peak for the singly charged GA molecules.

We checked the photostability for GA^+ ions in the same way as rhodamine 6G, rhodamine 101 and Alexa Fluor 350 (see Fig. 7.18). Therefore, they can be sympathetically cooled by barium ion ensembles.

In contrast to the other complex molecular ions investigated before, there is another smaller peak on each ion extraction spectrum of a GA^+ ion ensemble after loading. These ions are fragments generated in the loading procedure by collisions of the GA^+ ions with buffer gas atoms. The GA^+ ions are stable in the presence of the cooling laser light as no additional fragments (red histogram). However, they are much lighter than the GA^+ ions, but their masses are quite close to the barium ions. Thus, it is necessary to remove them from the trap before loading the barium ions via the secular excitation cleaning technique. Fig. 7.19 shows an ion extraction spectrum of GA^+ molecular ions after such a cleaning procedure (a frequency scan from 50 to 500 kHz at 120 mV). This spectrum indicates that only GA^+ ions are left in the trap.

The easiest way to check if an ion species is sympathetically cooled is the comparison of two ion extractions of a cooled and a non-cooled ensemble as shown above. Therefore,

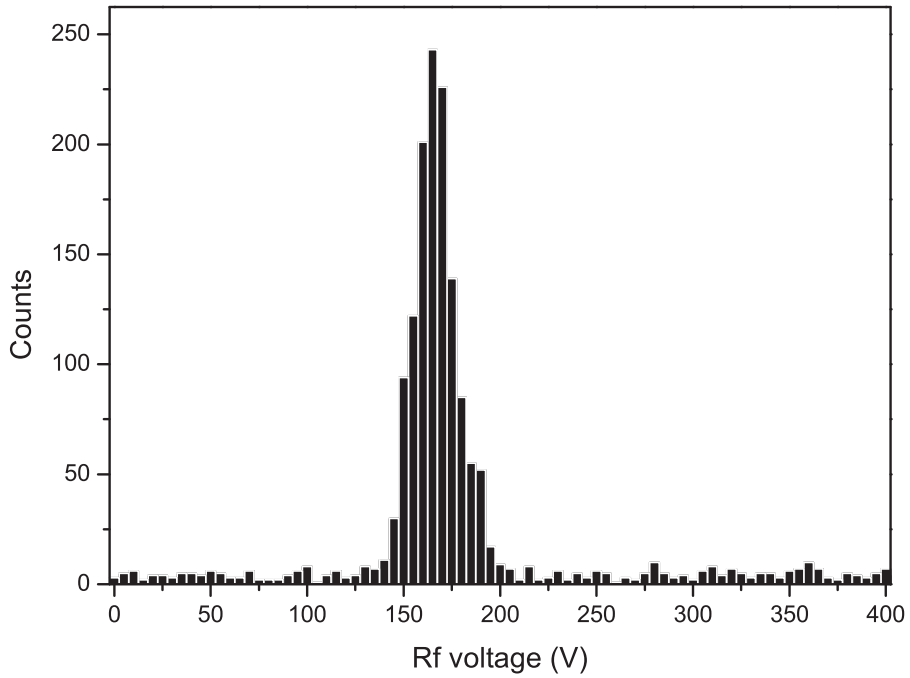

Figure 7.19: Ion extraction spectrum of a GA^+ molecular ion ensemble after removal of the fragments, created during loading.

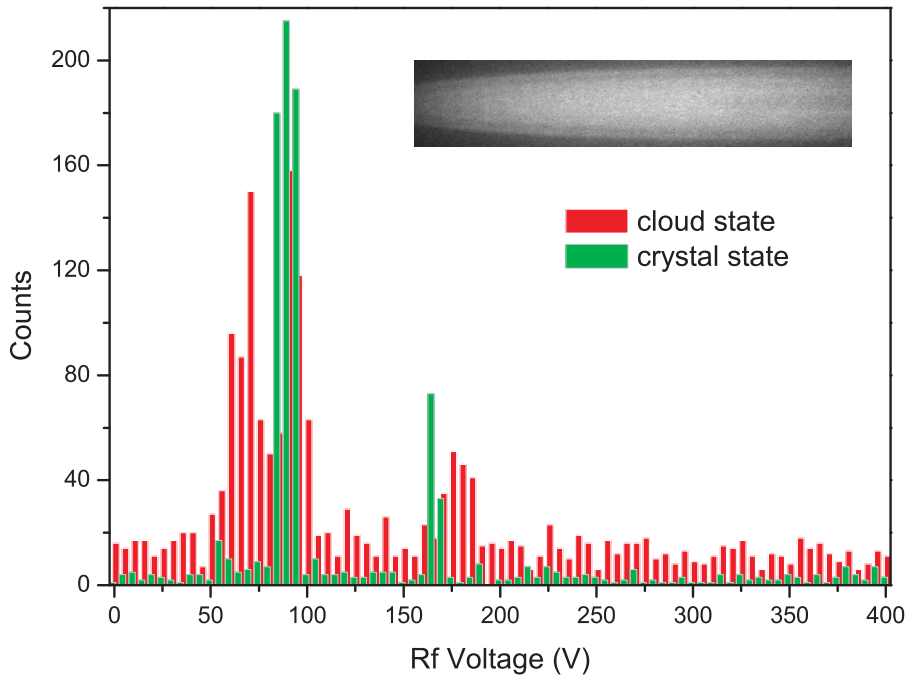

Figure 7.20: Ion extraction spectra with the ions in different states. The peak widths indicate the temperature of each ion species.

after loading GA^+ ions barium ions are loaded with the cooling lasers on. By tuning the lasers to the right wavelengths the barium ions are laser-cooled and the molecular ions are simultaneously sympathetically cooled. We perform this procedure twice and their ion extraction spectra are shown in Fig. 7.20. The red spectrum is the case without

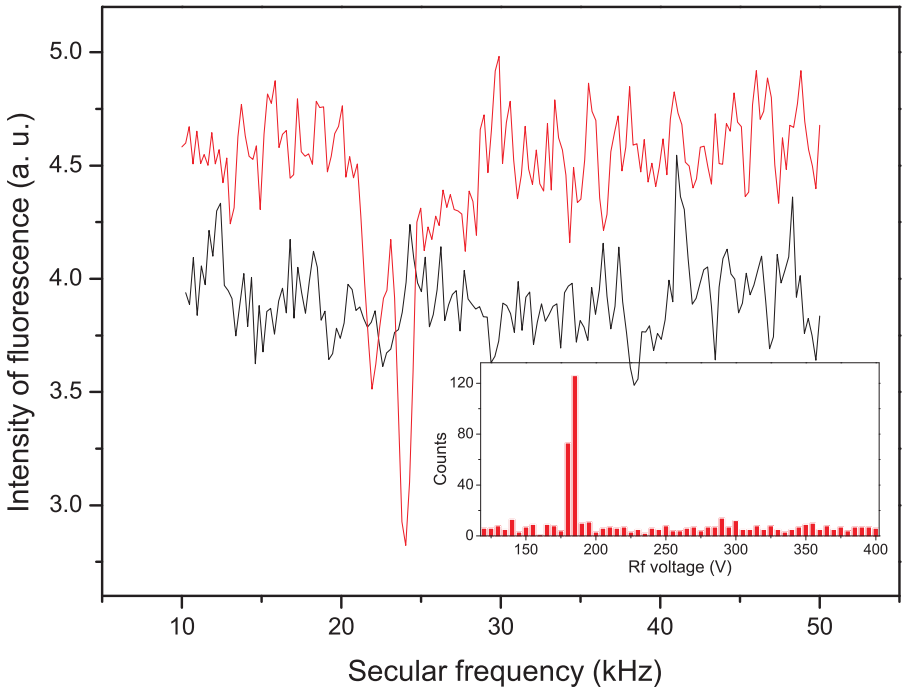

Figure 7.21: Secular excitation spectra with and without GA^+ molecular ions. The dip on the fluorescence curve is a strong evidence of the presence of the GA^+ ions. After the removal of the GA^+ ions, the fluorescence dip does not appear.

cleaning the light ions, which are introduced in the loading of the barium ions. Due to the disturbance of the light ions the barium ion ensemble can only be cooled down to a cloud state. Thus, all the ion species are still relatively hot (the broad widths of the peaks are the evidence). In the case of the green spectrum, most of the lighter mass ions are removed via a secular excitation cleaning process. The barium ion ensemble is finally crystallized as shown in the inset. The temperature of each ion ensemble is reduced now and is reflected in the width of its corresponding ion extraction peak.

To determine the mass-to-charge ratio of the sympathetically cooled molecular ions more accurately, a secular excitation scan with a small amplitude is applied. The frequency is swept from 50 to 10 kHz with an amplitude of 2.3 mV. The intensity of the barium fluorescence is recorded during the frequency scan and shown as the red curve in Fig. 7.21. The dip position of this curve is consistent with the calculated secular frequency for a single GA^+ ion (23 kHz). To prove that this dip is caused by the GA^+ ions, a partial ion extraction spectrum on this ion ensemble is done to remove the GA^+ ions (the spectrum is shown in Fig. 7.21 (inset)). Hereby, the presence of the heavy molecular ions is confirmed. Then, the same frequency scan acts on this pure barium ion ensemble, shown as the black curve in Fig. 7.21. The GA dip does not appear as expected.

It is evident that the GA^+ ions are sympathetically cooled. However, the peak width of the ion extraction spectrum only indicates the temperature qualitatively. How cold the molecular ions still needs to be determined. To obtain the temperature quantitatively, MD simulations need to be performed. As in the case of Alexa Flour 350, two

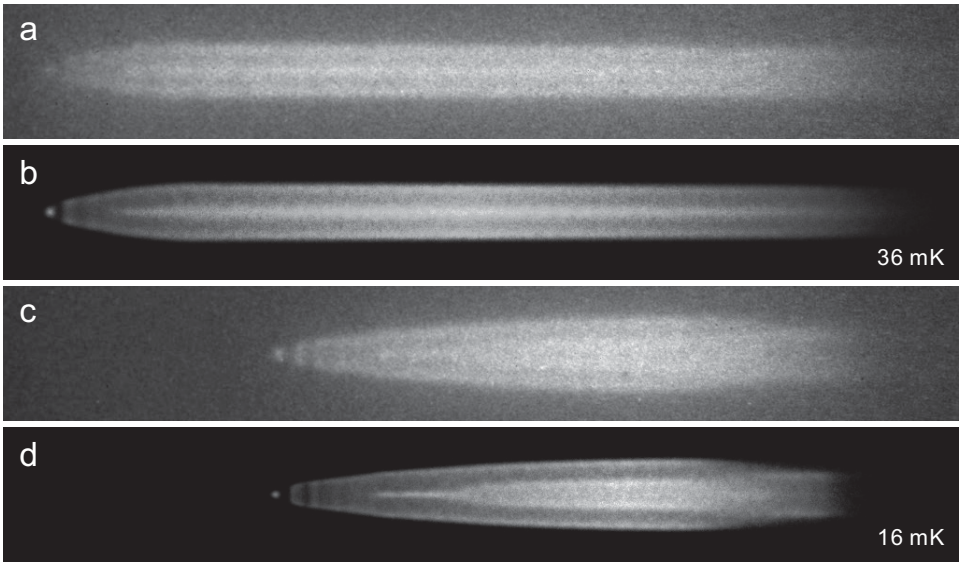

Figure 7.22: CCD images taken from the experiment and their simulated images. (a) CCD image of a barium ion crystal with GA^+ molecular ions. (b) Simulated image to fit the CCD image shown in (a). (c) CCD image after the GA^+ ions removed. (d) Simulated image to fit the CCD image shown in (c).

CCD images of a crystalline barium ion ensemble before and after removing the GA^+ complex molecular ions are required.

Two such CCD images are shown in Fig. 7.22(a) and (c). Since these two CCD images are much clearer and have higher contrast than the CCD images of Fig. 7.13(a) and Fig. 7.13(c), the ion number of each ion ensemble can be determined directly through the MD simulations (see Chapter 9) with a higher accuracy. The partial ion extraction process for the determination of the ion numbers can be omitted here. The barium ion ensemble in Fig. 7.22(a) contains 270 ± 10 $^{138}Ba^+$ ions and 80 ± 10 barium isotopes together with 15 ± 3 light ions, assumed to be CO_2^+, embedded in the barium ion crystal. Additionally, there are 75 ± 10 BaO^+ ions (product of the chemical reactions described in Chapter 6) and 1050 ± 20 GA^+ complex molecular ions stay around the barium crystal. Up to now, our simulation program can only run four ion species at once. Therefore, in the simulation for Fig. 7.22(a) the light ions are replaced by the barium isotopes. The error can be neglected due to the low ion numbers. The simulated $^{138}Ba^+$ ion crystal for Fig. 7.22(a) is shown in Fig. 7.22(b). The crystal is at about 36 mK. The barium ion ensemble in Fig. 7.22(c) contains 210 ± 10 $^{138}Ba^+$ ions and 80 ± 10 barium isotopes together with 15 ± 3 light ions and 75 ± 10 BaO^+ ions. Its simulated image is shown in Fig. 7.22(d). This crystal is at about 16 mK.

Once the ion numbers of all ion species have been determined, the upper temperature limit of the GA^+ molecular ion ensemble can in principle be simulated. However, in our case, either of the ion ensembles has at least four ion species. We have not enough information to determine the heating rate of each ion species. Using the MD simulation method to determine the heating rate of a sympathetically cooled ion species, the heating

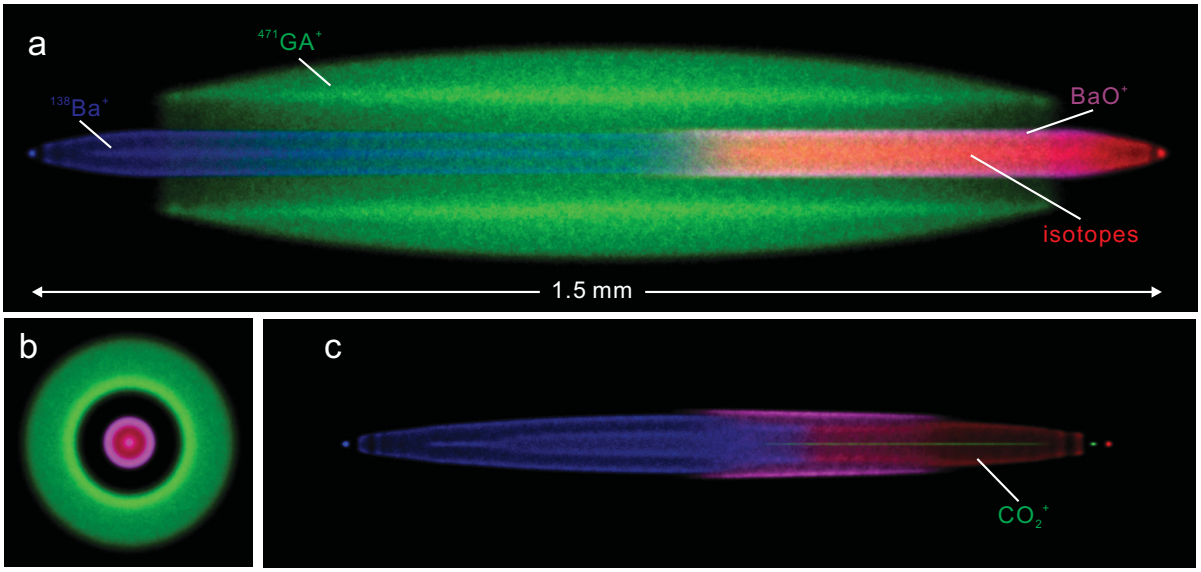

Figure 7.23: Simulated images with all ion species before and after removing the GA^+ ions. (a) Barium ion ensemble together with GA^+ molecular ions. (b) Endview of the ion crystal shown in (a). (c) Ion crystal after removing the GA^+ ions.

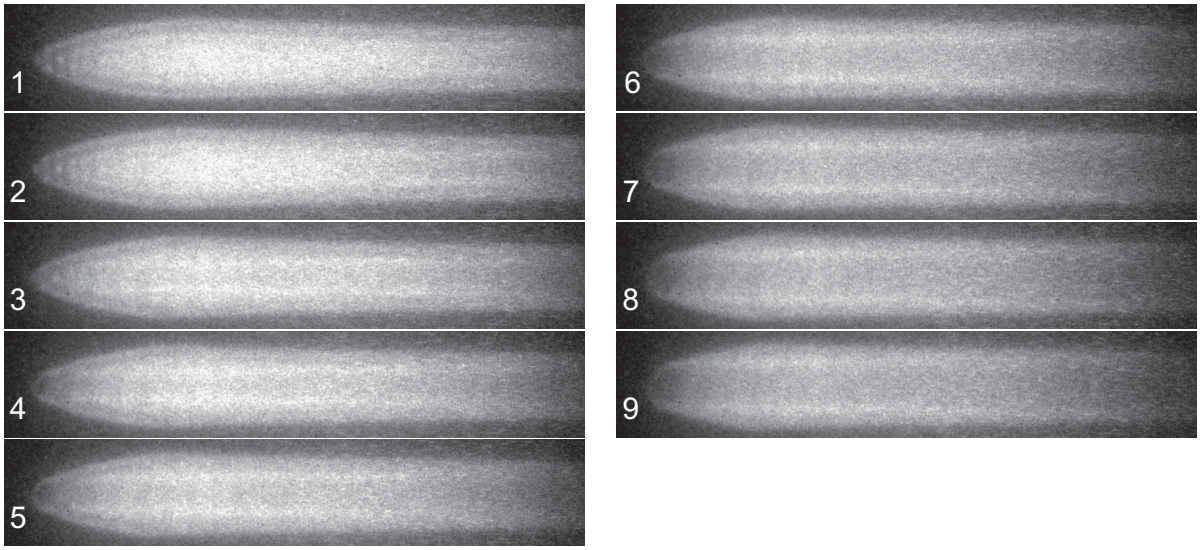

Figure 7.24: Photodissociation of GA^+ complex molecular ions. Initially, the GA^+ ions are located around the barium ion ensemble. When some GA^+ molecular ions are photodissociated, the low mass-to-charge ratio fragments move to the center of the barium crystal and accumulate owe to their smaller mass-to-charge ratio than that of the barium ions.

rates of the other species need to be known and two CCD images with and without this ion species need to be available. Due to the small mass difference between the BaO^+ and the barium ions and the low number of the light ions we assume that all the ion species except the GA^+ ions have the same heating rate.

We fix the laser cooling rate $\beta/m_{\mathtt{Ba}}$ to be 870 s^{-1} to obtain an upper limit temperature (see the temperature determination of the Alexa Fluor 350 ions). To get an image as Fig. 7.22(d), a heating rate of k_B(7.5 K/s) is necessary for all low-mass ion species. In order to obtain an image as Fig. 7.22(b), the heating rate for the GA^+ ions is required to be k_B(5.4 K/s). The final upper limit temperature of the GA^+ ions is found to be 72 mK. The simulated images with all ion species are shown in Fig. 7.23. The length of the barium ion crystal with GA^+ ions is about 1.5 mm. The ratio of the ion numbers of sympathetically cooled GA^+ ions to the laser cooled barium ions is approximately 4:1.

GA^+ ions have a strong absorption peak near 254 nm, which can be excited by a 266 nm laser. When they stay in a vacuum environment, they might be photodissociated similar to the rhodamine 6G and 101 molecular ions, which are sensitive to our 493 nm cooling laser. To show that the GA^+ ions are stable under UV exposition we prepared a cold Ba^+/GA^+ ion ensemble. A 266 nm laser is directed to the ions and a dark core appears at the right end of the CCD image. As time goes on, this dark core grows more and more as shown in Fig. 7.24. Finally, it passes through the whole barium crystal. This indicates that the cold GA^+ molecular ions are destroyed by the 266 nm laser light. Currently in our group experiments are performed to determine the UV dissociation rate for cold GA^+ ions.

8 Sympathetic cooling of proteins

We have discussed the sympathetic cooling of light and two medium weight ion species (411 and 471 amu) in the last two chapters. In this chapter we discuss the sympathetic cooling of a much heavier molecular ion species, cytochrome c, with a mass of about 12000 amu.

8.1 Protein molecule - cytochrome c

Since multiply charged cytochrome c (cyt c) molecular ions have been successfully produced by ESI and transferred to a Paul trap [103], we choose this kind of protein to be sympathetically cooled and to demonstrate the full potential of our apparatus. Cyt c is a small heme protein containing a single polypeptide chain and a single heme group, which is covalently attached to Cys^{14} and Cys^{17}. Unlike other cytochromes, it is a soluble protein. Its primary structure consists of a chain of 100 amino acids and its molecular weight is about 12377 amu. The molecular structure is shown in Fig. 8.1.

Cyt c from horse heart used in our experiment is purchased from Sigma-Aldrich. The compound is dissolved in a 50 : 50 mixture of water and methanol solution at concentration of 10 pmol·μl^{-1} containing 0.5% or 2% acetic acid. The molecules are multiply pronated. Mass spectra from our system are shown in Fig. 8.2 with 0.5% and 2% concentration of acetic acid. The acetic acid helps to charge the molecules, higher concentration leading to a higher charge-to-mass ratio. Here we find a maximum in the charge state +12 for a concentration of 0.5 % and in the charge state +15 for 2 %. Thus,

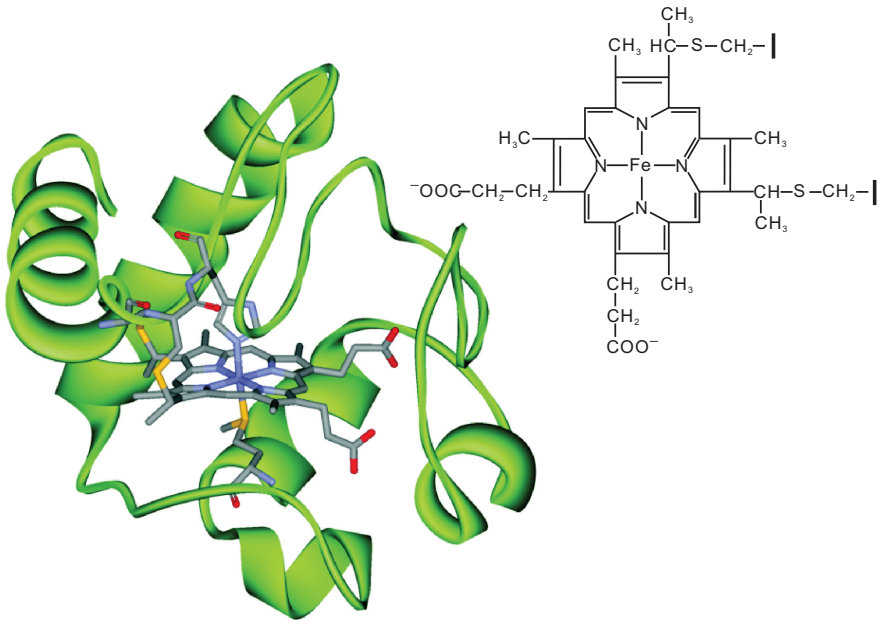

Figure 8.1: Molecular structure of cyt c with heme (net structure) [104].

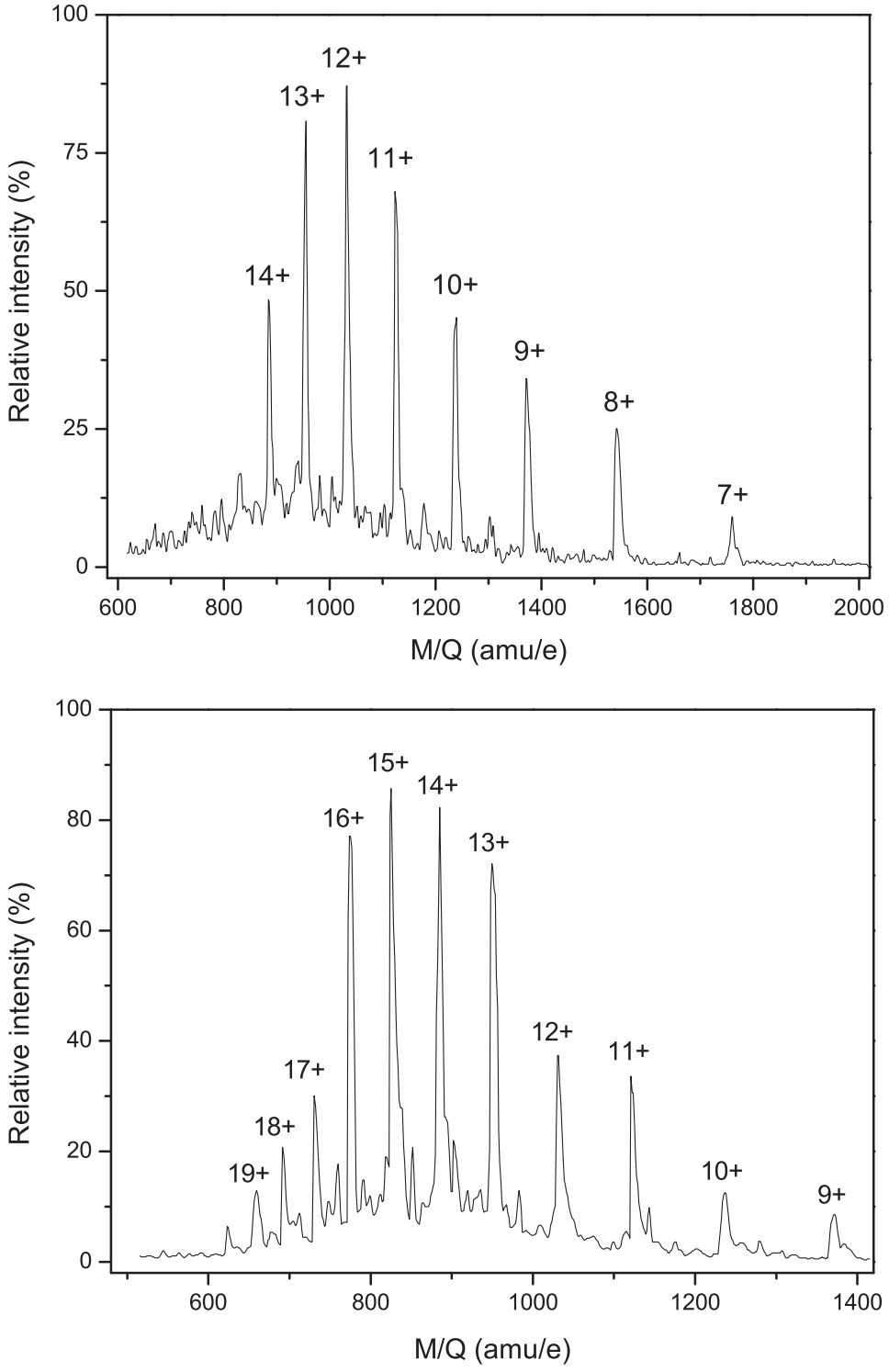

Figure 8.2: Mass spectra of cyt c obtained using our ESI system with 0.5% (a) and 2% concentrations of acetic acid (b).

via the control of the concentration of the acetic acid, maximum ion flux of the cyt c at a different state can be realized. If we use the solution with 2% concentration of acetic acid, cyt c ions in the charge state +17 (cyt17, the cyt c protein ions in the charge state $+N$ are denoted by cyt$N$) can be generated with a sufficiently high ion flux.

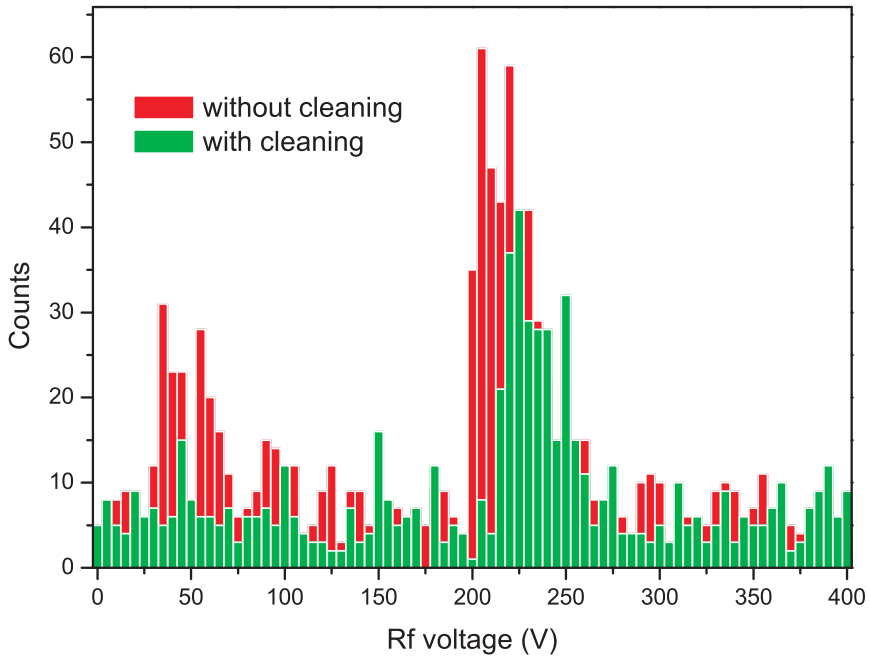

Figure 8.3: Ion extraction spectra of the cyt c ions with and without the removal of the loading fragments.

8.2 Loading of cyt c molecular ions

The mass and charge state of the cyt c ions used in our experiment is different from the singly charged Alexa Fluor 350 and GA molecular ions. However, to load the cyt c protein ions to our trap, except the increase of the needle high voltage of the ESI system, all the parameters for the ion generation and transport are the same as in the case of Alexa Fluor 350 or GA. An ion flux of approximately 1000 counts per second can be detected behind the octopole ion guide. During loading the cyt c protein ions, the endcap voltage at the entrance end is modified to -3 V and the other end is set to be 2.5 V. The helium buffer gas pressure leaked into the main chamber is about 1×10^{-4} mbar. Due to the lower depth of the pseudopotential well for a higher mass-to-charge ratio ion species the rf voltage during the loading time needs to be turned to its maximum value of 500 V.

A typical loading procedure for the cyt c ions works as follows: After loading the cyt c molecular ions with the parameters mentioned above, the endcap voltage at the entrance end is raised up to the same level as on the exit end and the leak valve is closed to remove the buffer gas. At the same time the rf voltage is lowered down to about 400 V to reduce the rf heating.

The loading result can be checked via an ion extraction. The red histogram in Fig. 8.3 shows such an ion extraction spectrum of an ensemble of cyt17 ions. It shows two clear peaks. Since the starting voltage of the ion extraction is 400 V, the center of the main peak is at about 220 V rf voltage, which is much higher than the normal position for the barium ion ensemble (at about 100 V). This means the mass-to-charge ratio of the molecular ions at the main peak is much higher than that of the the singly charged barium ion. The peak at about 220 V should corresponds to the cyt17 ions.

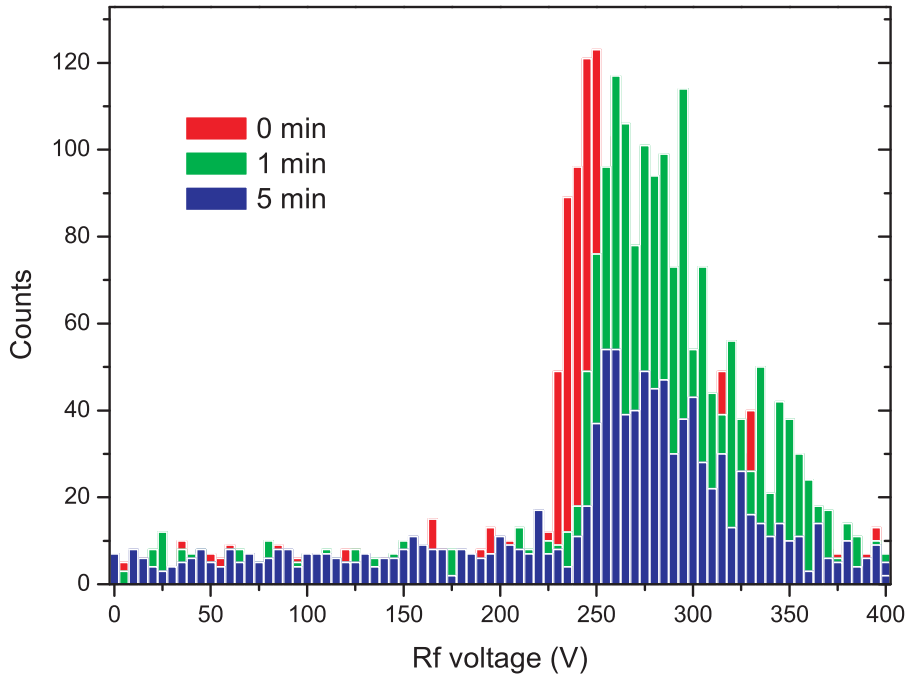

Figure 8.4: Ion extraction spectra of cyt17 ion ensembles with different exposure times to the 493 nm cooling laser only. No fragments are found in the spectra.

During loading, fragments are also captured by the trap (see the red histogram in the lower rf voltage range of Fig. 8.3). Those fragments can easily be removed through the secular excitation method. The green histogram in Fig. 8.3 is the ion extraction spectrum of another cyt17 ion ensemble after removal of the fragments. The ion peaks in the low voltage range disappears.

It is also necessary to check whether the cyt c ions are also sensitive to our lasers or not. Fortunately, we found that they are photostable in the cooling lasers. After loading the cyt17 ions and the removal of the fragments, the 493 nm cooling laser is directed to the ion trap for 1 min. Then, an ion extraction is done. This experiment is repeated but with a longer time (5 min) of cooling laser exposition. The ion extraction spectra are shown in Fig. 8.4. The case without any laser exposure is also plotted, as the red histogram in Fig. 8.4. We found no evidence for photofragmentation of the cyt17 ions by the 493 nm cooling laser. In the case when both lasers are directed on the ions for one and two minutes, we find that the cyt17 ions are also not fragmented by the 650 nm repumping laser. The results are shown in Fig. 8.5.

Therefore, cyt c is a suitable candidate for the demonstration of sympathetic cooling of very heavy molecular ions.

8.3 Sympathetic cooling of cyt17 protein ions

Cyt17 protein ions are sympathetically cooled in our experiment. In this section, our routine procedure to prepare sympathetically cooled cyt c ions is addressed and diverse

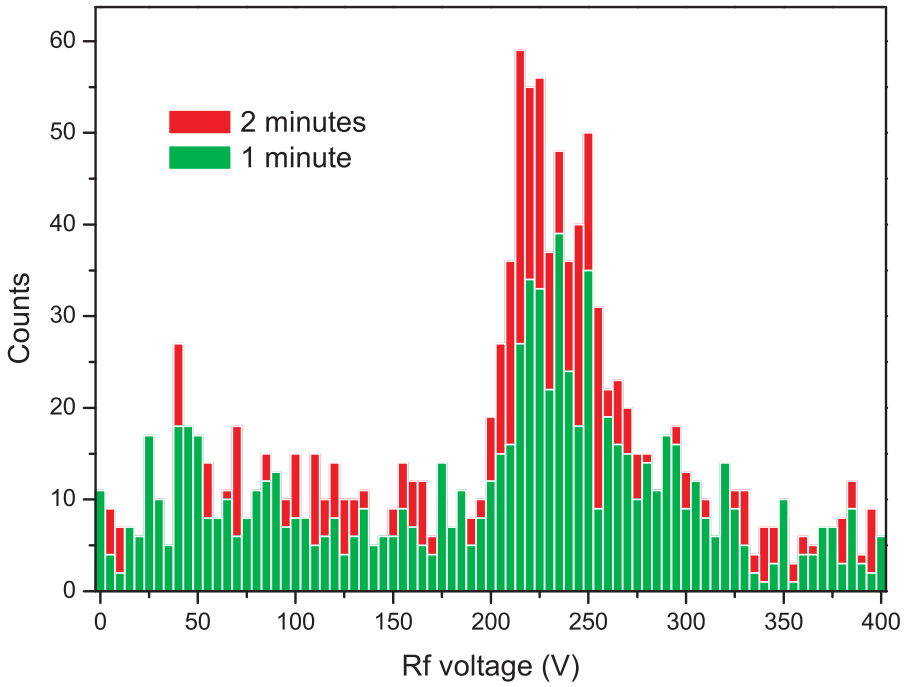

Figure 8.5: Ion extraction spectra of the cyt17 ions with different exposure times to both 493 nm and 650 nm lasers. Ions are photostable in the lasers.

evidences of the existence of the cooling cyt17 protein ions are presented.

8.3.1 Simultaneous trapping of cyt17 and barium ions

To realize our final goal, one prerequisite is to prepare an ion ensemble containing cyt c and barium ions simultaneously in the trap. First, we load cyt17 ions followed by loading barium ions in the usual way with the lasers being blocked. In principle, the two ion species are confined in the ion trap simultaneously. To prove this we do an ion extraction of this ion ensemble, the spectrum is shown in Fig. 8.6. Except for the peaks of the barium and cyt17 ion species, there is a strong peak near 50 V. This is due to CO_2^+ ions, which are always loaded together with the barium ions. As said before, they can be removed by the secular excitation cleaning method. Actually, another secular excitation cleaning process is performed to remove heavier molecular ions such as the products of the chemical reactions of barium and the fragments of the cyt c ions. The ion extraction spectrum after cleaning is shown in Fig. 8.7. It is evident that the light molecular ions are mostly removed. Since the cooling lasers are blocked all the time in this case, the barium ion ensemble is very hot. Thus, the other ion species are also hot as represented in the broadness of the ion extraction peaks.

8.3.2 Evidences of the sympathetic cooling of cyt17 ions

Since the cooling laser and the repumping laser do not photodissociate the cytochrome c ions, all the ions can be loaded with the cooling lasers and the loading efficiency can be improved, as discussed in Chapter 5. When the $^{138}Ba^+$ ions are laser-cooled, all other ions present in the trap are sympathetically cooled simultaneously.

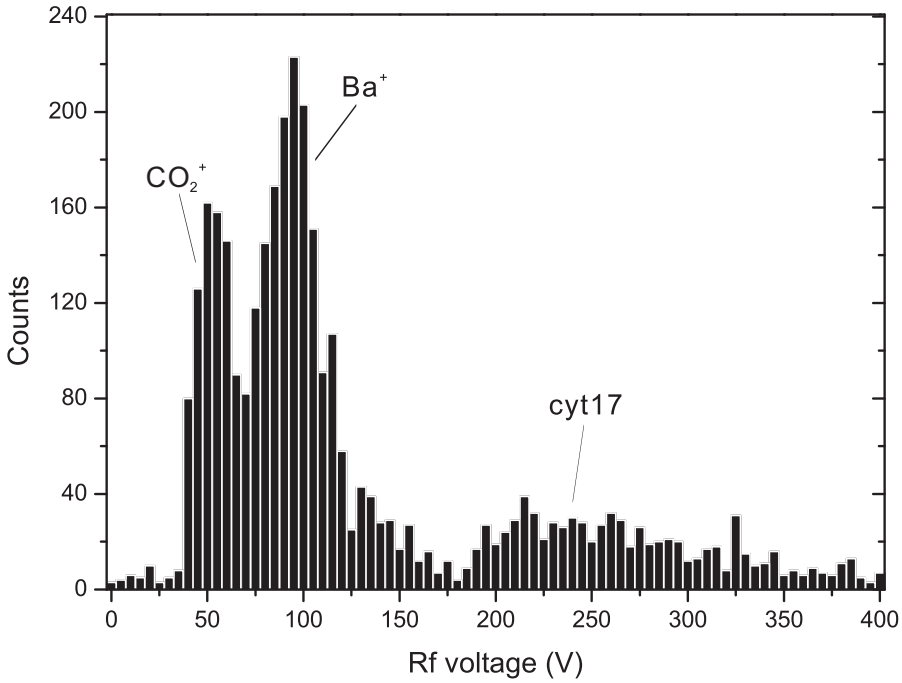

Figure 8.6: Ion extraction spectrum of an ion ensemble consisting of the cyt17 and barium ions, as well as light ions loaded with the barium ions. Here, since all the processes are done without the cooling lasers, the peaks are very wide indicating the ions are hot.

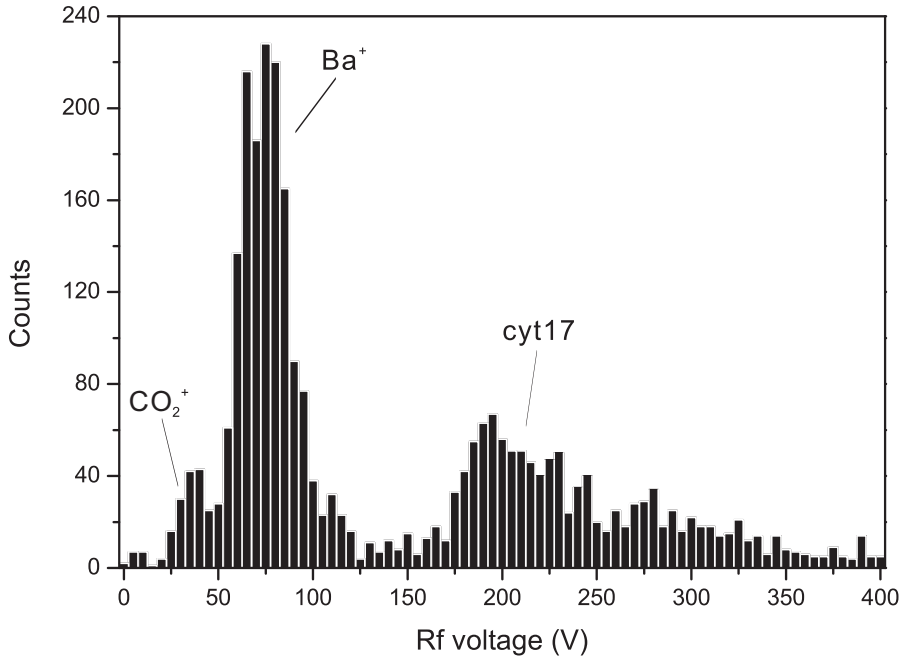

Figure 8.7: Ion extraction spectrum of an ion ensemble consisting of the cyt17 and barium ions after cleaning of the light molecular ions. The CO_2 peak is much smaller than that shown in Fig. 8.6. Here, the cooling lasers are blocked all the time. Thus, the ions are quite hot.

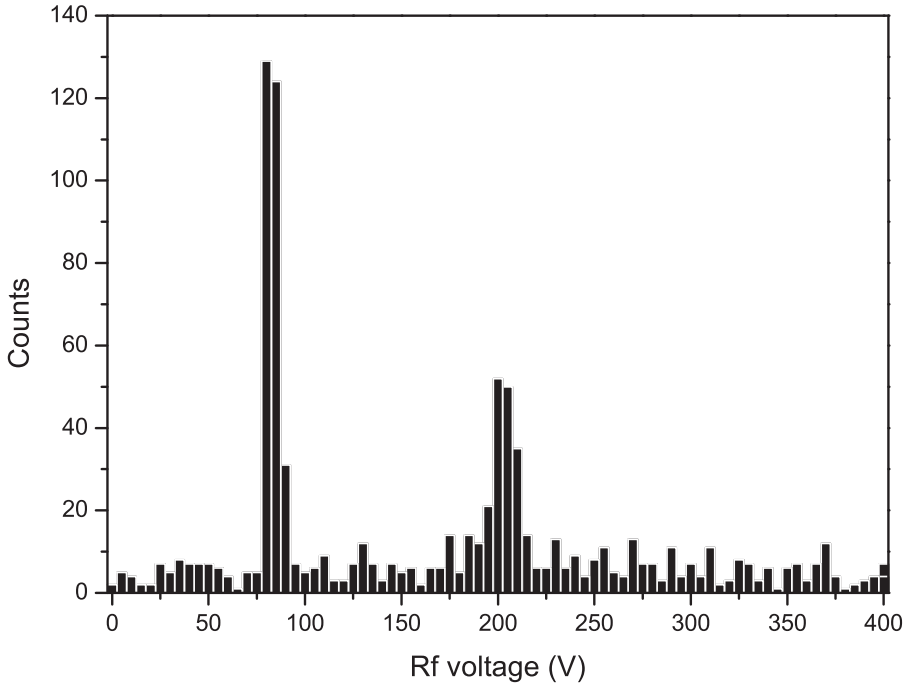

Figure 8.8: Ion extraction spectrum of of a laser-cooled ion ensemble consisting of cyt17 and barium ions. Compared to the spectra in Fig. 8.6 and Fig. 8.7 the peaks are much narrower.

8.3.2.1 Ion extraction

Fig. 8.8 shows an ion extraction spectrum of an ion ensemble consisting of barium and cyt17 ions, which was prepared as described above, but the lasers are unblocked. After the loading of all ions the cooling lasers are fine tuned to achieve the maximum cooling efficiency. Although the barium ion ensemble is not crystallized due to the large number of cyt c ions, both ion species are much colder than in the case without laser cooling. Comparing with the ion extraction spectrum in Fig. 8.6 or Fig. 8.7 the narrower peaks offer a strong evidence for the realization of the sympathetic cooling of the cyt c ions.

8.3.2.2 Visible evidence

If one loads an appropriately low number of cyt c ions, the barium ions can sufficiently cool down the whole ion ensemble to the crystalline state, which can be imaged by our ICCD camera. The cyt c protein ions stay further away from the trap axis and squeeze the barium ion ensemble making it thinner radially and longer longitudinally. Fig. 8.9(a) is a CCD image of barium ion ensemble surrounded by cyt17 ions. Subsequently, a strong frequency sweep from 90 to 5 kHz with an amplitude of 150 mV is performed to remove the cyt c ions. Since the secular frequency of the barium ions is about 100 kHz, the cyt c ions are kicked out from the trap without loss of the barium ions. Fig. 8.9(b) shows the CCD image after cleaning. This barium ion crystal is roughly 50% shorter than the one with the cyt17 ions and has three layers instead of the one-shell structure. Since all the trap parameters are the same all the time, the shape and structure changes only arises from the absence of the cyt17 ions.

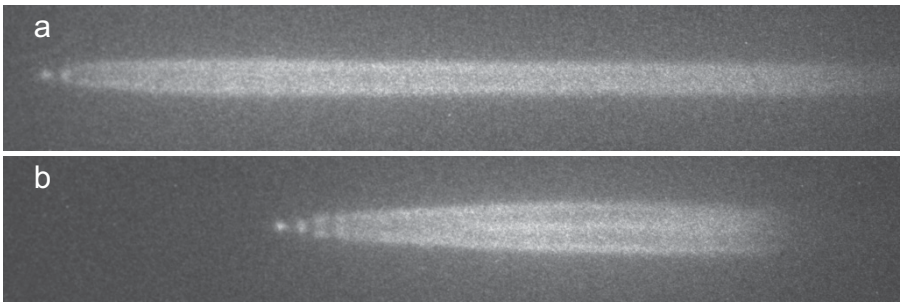

Figure 8.9: CCD images of $^{138}Ba^{+}$ ion crystals. (a) Together with cyt17 ions. (b) After cyt17 ions have been removed via a secular excitation.

Comparing these two CCD images one finds that the barium ion ensemble is much colder after the removal of the protein ions (the barium ion crystal in Fig. 8.9(b) has a clearer structure). This is another indication of the previous presence of the cyt c protein ions in the ion trap.

8.3.2.3 Secular excitation

Another method to detect the cyt c ions is a secular excitation with a small amplitude. An ion ensemble, whose CCD image is shown in Fig. 8.10(a), is excited periodically between 5 and 20 kHz with an amplitude of 3 mV, the repetition frequency being 0.2 Hz. The fluorescence intensity of the ^{138}Ba ion ensemble is recorded and shown as in Fig. 8.10(b). A main fluorescence dip in each scanning period is observed. The main dip is split into two separate dips at about 11.5 and 16.5 kHz due to space charge effects (discussed in Chapter 10). A partial ion extraction is done to remove the cyt17 ions by lowering the rf voltage from 350 V to 165 V. If we continue the frequency scan, no obvious repeatable peaks appear on the fluorescence curve any more (see the green curve). All the frequency scans are operated with 350 V rf voltage. The calculated frequency for a single cyt17 ion here is about 16.3 kHz, which locates between the two dips.

The periodic frequency scan near the resonant frequency of the barium ions is also performed to calibrate the rf voltage. The scanning range is from 90 to 100 kHz with an amplitude of 1 mV and a repetition frequency of 0.1 Hz. The fluorescence curve is shown in Fig. 8.10(c). The resonance frequency is at about 90 kHz, which corresponds to an rf voltage of 346 V (the rf voltage displayed in the oscilloscope is about 322 V).

8.4 Temperature determination via MD simulations

Using the MD simulations the temperature of the sympathetically cooled cyt c ions can determined as done for the Alexa Fluor 350 and GA ions. As usual, two CCD images before and after removing the heavy molecular ions are required. In this case, the two CCD images are shown as Fig. 8.11(a) and Fig. 8.11(b), respectively. This CCD image is taken with an rf voltage of 350 V and an endcap voltage of 6.8 V. A partial ion extraction is performed by lowering the rf voltage from 350 V to 175 V to remove the cyt17 ions. The partial ion extraction spectrum and the final full ion extraction spectrum are show in Fig. 8.12.

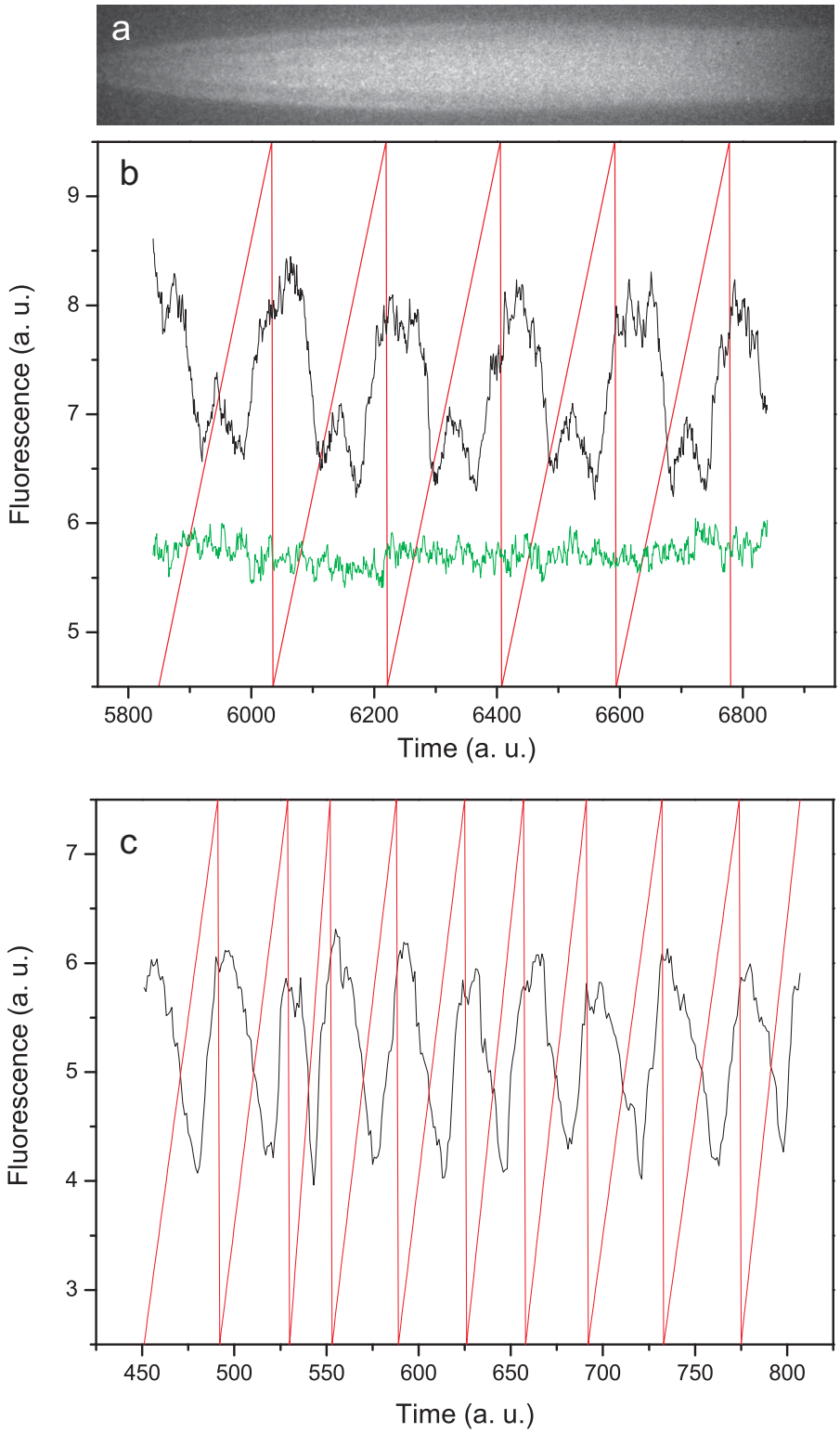

Figure 8.10: Spectra of a periodic secular excitation to detect the presence of cyt17 ions. (a) CCD image of the ion ensemble being scanned. (b) Spectra before (black) and after (green) the removal of the cyt17 ions. (c) Spectrum for the barium ions recorded for calibration with the known Ba^+ frequency.

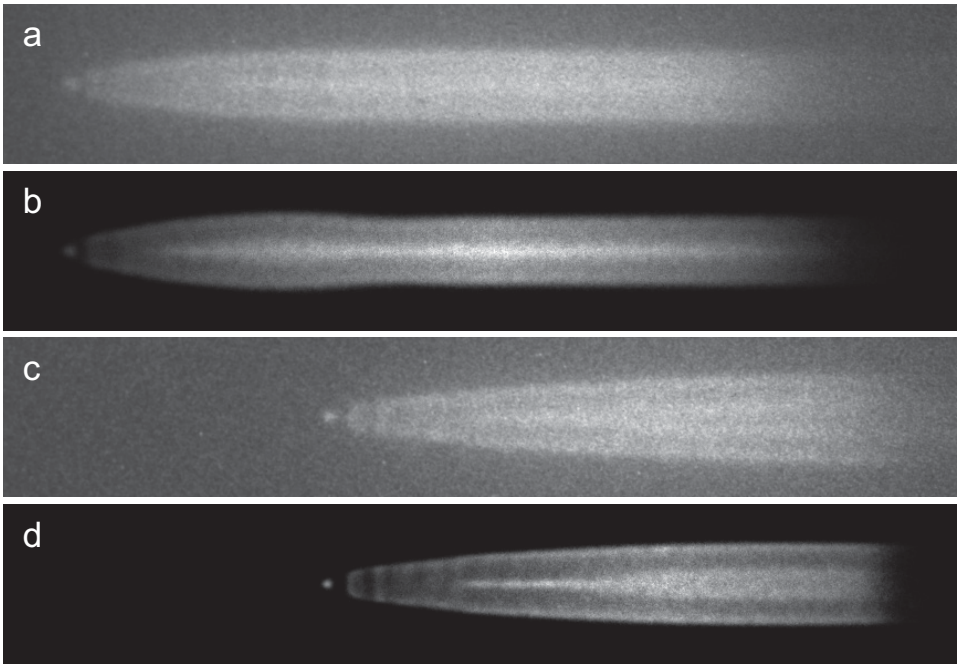

Figure 8.11: Temperature determination of cyt17 ions via molecular dynamics simulations. (a) CCD image of a $^{138}Ba^{+}$ ion ensemble with cyt17 around. (b) Simulated image to fit the CCD image of (a). (c) CCD image after the removal of the cyt17 ions. (d) Simulated image to fit the CCD image of (c).

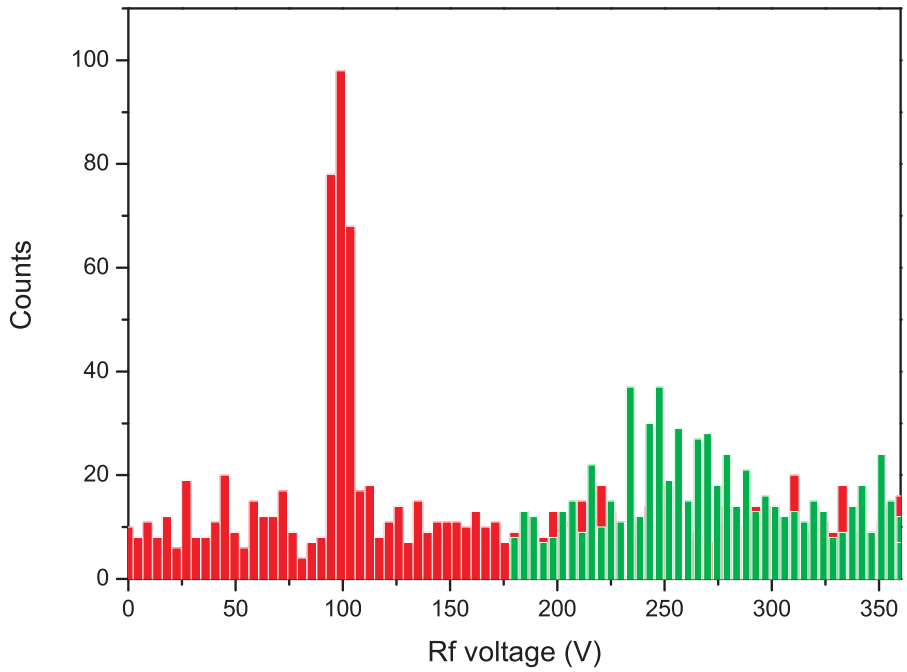

Figure 8.12: A partial (green) and a full ion extraction spectrum (red) for the determination of the ratio of the barium and the cyt17 ion numbers. The signal-to-noise ratio for the cyt17 ions is very low (see the green spectrum)

Usually, the barium ion number of a crystal is obtained through simulations, while

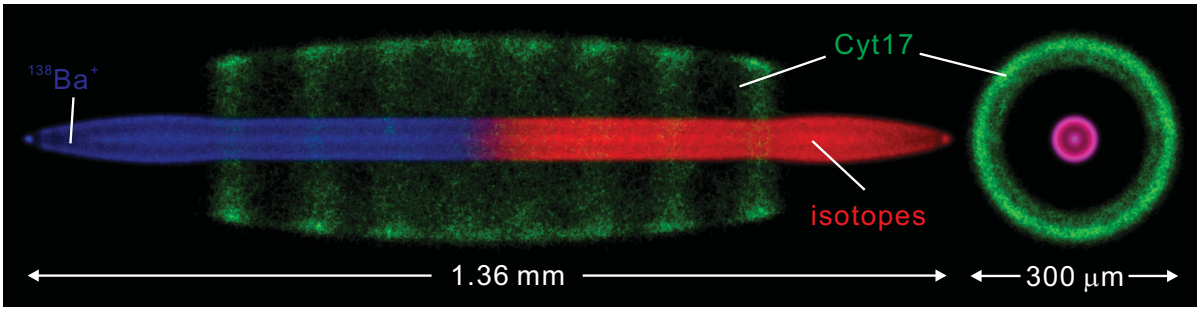

Figure 8.13: Simulated image with all ion species (both sideview and endview are shown here). This ensemble consists of 175 $^{138}Ba^+$ ions, 160 barium isotopes, and 46 cyt17 ions. The temperatures are about 43, 70, and 570 mK, respectively.

the determination of the ion number of heavy molecular ions requires the ion extraction spectra (described in Chapter 7). However, as only ion ensembles of low ion numbers can be crystallized in this case, the number of the cyt17 ions is so low that the signal-to-noise ratio in the corresponding ion extractions is very low (see the green partial ion extraction spectrum in Fig. 8.12). Thus, the error bar for the number determination of the cyt c protein ions is beyond 50%.

Since the cyt c protein ions used here are multiply charged, the Coulomb interaction between the cyt c ions and the barium ions is very strong. This means that the shape of the barium ion ensemble is very sensitive to the cyt17 ion number. Therefore, from the shape of the barium Coulomb crystal in Fig. 8.11(a), we can accurately fit the ion number of the cyt17 ions to 46 ± 3. Thus, the error is significantly lessened to 7%. The barium ion crystals in Fig. 8.11(a) and Fig. 8.11(c) contain 335 ± 10 (175 ± 10 $^{138}Ba^+$ and 160 ± 10 barium isotopes) and 240 ± 10 (145 ± 10 $^{138}Ba^+$ and 85 ± 10 barium isotopes) barium ions, respectively.

To determine an upper limit for the temperature of the cyt17 ions in the ion ensemble shown in Fig. 8.11(a), a simulation is performed with the laser cooling rate for $^{138}Ba^+$ ions set to 870 s^{-1}. Since the $^{138}Ba^+$ ions in Fig. 8.11(c) are at about 15 mK, the heating rate for each barium ion is determined to be $k_B(8.3\ \mathrm{K/s})$, the simulated image for the $^{138}Ba^+$ ion ensemble in Fig. 8.11(c) is shown as Fig. 8.11(d). Then we compensate lost barium ions and assign the obtained heating rate to all barium ions. 46 cyt c protein ions in the 17 charge state are added to the ion trap. A heating rate of $k_B(57\ \mathrm{K/s})$ for the protein ions is required to get a simulated image of the $^{138}Ba^+$ ion ensemble consistent with the experimental one shown in Fig. 8.11(a). The corresponding temperatures are 43, 70, and 570 mK for the $^{138}Ba^+$, barium isotopes, and cyt17 ions, respectively. The cyt c protein ions at this temperature together with the barium ions are shown in Fig. 8.13. This is the first time protein molecular ions have been cooled to millikelvin temperatures by sympathetic cooling.

In the simulated image (Fig. 8.11(b)) the $^{138}Ba^+$ ion ensemble looks sharply squeezed, whereas the experimental image is more smooth. This is due to the strong background, which wash out details. Additionally, in the experiment, the electric noise results in a low-amplitude motion of normal modes. With a long integration time for the CCD

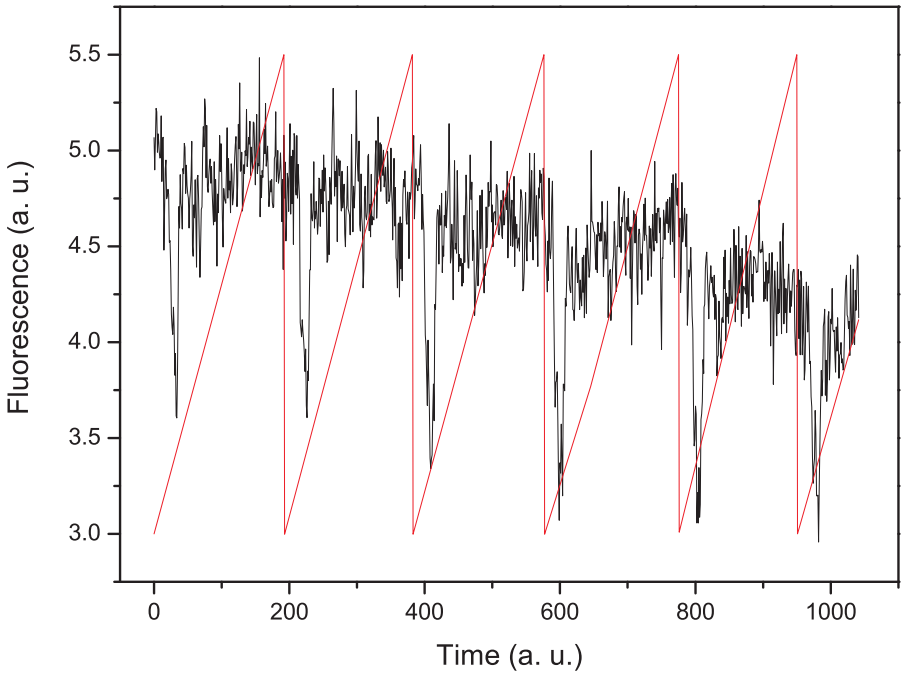

Figure 8.14: Secular frequency scanning spectrum for the detection of the cyt c protein ions in the 12 charge state. The red ramp represents the frequency scan.

images (in our case it is 2 s), the motion of normal modes is included in the CCD images and makes them look more blurred and, thus, warmer. However, in the simulation the integration time is only a few ms to 40 ms. Another factor inducing the blur of the CCD images is rare but strong collisions with residual gas rising the activity of local ion diffusions. Moreover, rf micromotion is another important factor described in Chapter 9.

8.5 Sympathetic cooling of cyt12 ions

As shown in Fig. 8.2, cyt c ions in other charge states can be selected and transferred to our ion trap. However, due to a limited maximum rf voltage of an trap, the cyt c ions in charge states lower than +12 cannot be captured. Thus, in principle, the protein ions in the charge state between +12 and +17 can be trapped and sympathetically cooled. Here, we give an example of the sympathetic cooling of cyt12 ions .

We repeat the ion loading process already used for the cyt17 ions. The only difference is that the mass filter was set for the cyt12 ions to pass. After loading cyt12 and barium ions, the lasers are tuned to make the ion ensembles as cold as possible. To detect the cyt12 ions, a periodic secular frequency sweep is performed. The frequency sweeps from 5 to 65 kHz, the obtained spectrum is shown in Fig. 8.14. The resonance dip of the cyt12 ions always occurs at about 14 kHz, which is close the calculated value of 13 kHz. Here, in each period of the secular excitation only one main peak appears, which is different from the case of the protein ions in the 17 charge state. The reasonable explanation is that due to the higher mass-to-charge ratio the ions in the 12 charge state are more easily pushed further away from the trap axis (for an ion ensemble containing 200 barium ions and 10 cyt c ions, the gap widths between the two ion species are 72 and 89 μm,

respectively, for cyt17 and cyt12 ions) having smaller interactions with the barium ions resulting in a weak secular frequency coupling.

9 Molecular dynamics simulations

In Sec. 9.1 of this chapter a brief introduction to molecular dynamics simulations is given. In Sec. 9.2 the ion's equations of motion and the algorithms are described in detail. In MD simulations, time scales such as time step, thermalization time, determine the computation time and the accuracy of the results. Thus, in Sec. 9.3 the time scales for the barium experiment as well as the beryllium experiment are shown. The initialization of ion ensembles in the trap is discussed in Sec. 9.4 and a heating model is presented in Sec. 9.5. In Sec. 9.6 we explain how to reproduce experimental CCD images and in Sec. 9.7 how to determine the temperatures and numbers of laser-cooled and sympathetically cooled ions. It is studied in Sec. 9.8 how to improve the sympathetic cooling efficiency. Simulations of ion ensembles in the rf field are done in Sec. 9.9, and the results are compared with those obtained in the pseudopotential case. In the last section, Sec. 9.9, ion diffusion in different situations is investigated. Since in our lab there are two specific linear Paul traps - one for barium ions and another for beryllium ions, all the simulations in this thesis are not limited to one particular case.

9.1 Introduction

One of the routine tools in the theoretical study of a many-body system is the method of molecular dynamics (MD) [105, 106, 107] simulations. This is a multidisciplinary method. Its laws and theories stem from mathematics, physics, and chemistry, and it employs algorithms from computer science and information theory. Now it is widely used in physics, chemistry, biology, and material science. This computational method gives direct numerical solutions of the equations of motion of particles and calculates their time dependent behaviors, which allow to check models, offer insights to the experimentalists, assist in the interpretation of new results, predict the properties of the dynamics and other complicated phenomena that cannot be found out in other ways. Moreover, they reveal hidden details behind the experimental measurements. They act as a bridge between microscopic length and time scales and the macroscopic world of the laboratory, and between theory and experiment.

The molecular dynamics simulation method was first introduced by Alder and Wainwright in the 1950's [108, 109]. And the first molecular dynamics simulation of a realistic system was done by Rahman and Stillinger in 1971 [110]. This simulation technique needs extensive numerical calculations because of the approximate and step-by-step procedure. With the help of the rapid development of the computer technology, the application of this method on neutral particles in liquid or solid state [111] was extended to non-neutral plasmas. For liquids or solids, considering the interactions with a few neighbors is sufficient, but for plasmas, because of the long range Coulomb interaction, the interaction of each other particle needs to be counted in. Thus, the computational effort increases greatly. Today, simulations with a few thousand non-neutral particles on a normal personal computer are realistic. In the case the particle number is more than ten thousand,

the simulations need to run on parallel computer systems.

9.2 Basic approach

9.2.1 Equations of motion and forces

In order to perform MD simulations, the definition of a potential energy function is required. The aim of the simulations is to study the properties of a particle ensemble under the interactions of forces, which are usually derived from the potential energy. In our case, as described in Chapter 2, ions are confined in a linear Paul trap by electric fields, but repel each other due to the mutual long-range Coulomb interaction. The laser-cooled ions are slowed down or heated up by the laser light force introduced in Chapter 3. Additionally, ions in a UHV chamber experience some unquantifiable forces such as casual collisions with residual gas or the noise of electric fields. Therefore, the force acting on the ions is the combination of the trap potential force $\boldsymbol{F}_i^{trap}$, the Coulomb interaction force $\boldsymbol{F}_i^{Coulomb}$ due to all other ions, a stochastic force $\boldsymbol{F}_i^{stochastic}$, and the laser light $\boldsymbol{F}_i^{laser}$. Thus, the classical equations of motion (Newton's equations) can be written as

$$\begin{aligned} m_i\ddot{\boldsymbol{r}} &= \boldsymbol{F}_i(\boldsymbol{r}_1, \ldots \boldsymbol{r}_{N_{LC}+N_{SC}}, \boldsymbol{v}_1, \ldots \boldsymbol{v}_{N_{LC}+N_{SC}}, t) \\ &= \boldsymbol{F}_i^{trap} + \boldsymbol{F}_i^{Coulomb} + \boldsymbol{F}_i^{stochastic} + \boldsymbol{F}_i^{laser}, \end{aligned} \tag{9.1}$$

where $i = 1, \ldots, N_{LC} + N_{SC}$ (N_{LC} and N_{SC} are the numbers of the laser-cooled and sympathetically cooled ions, respectively), so there are $3(N_{LC} + N_{SC})$ particle coordinates totally. m_i and $\boldsymbol{r}_i$ are the mass and position vector of particle i, respectively. $\boldsymbol{F}_i(\boldsymbol{r}_1, \ldots \boldsymbol{r}_{N_{LC}+N_{SC}}, \boldsymbol{v}_1, \ldots \boldsymbol{v}_{N_{LC}+N_{SC}}, t)$ is the force acting on particle i and depends on the positions and velocities of all other ions, and the time t.

The trapping potential force $\boldsymbol{F}_i^{trap}$ can have two forms, the pseudopotential force or the rf potential force. In this thesis, in most of the simulations we consider the pseudopotential energy which has the expression of Eq. (2.39) (rf micromotion is averaged out). Only in a small part of our simulations micromotion is taken into accounted in order to do compare with the case of the pseudopotential.

The Coulomb force $\boldsymbol{F}_i^{Coulomb}$ is the repulsive force from all other confined ions and has the form

$$\boldsymbol{F}_i^{Coulomb} = \frac{Q_i}{4\pi\varepsilon_0} \bigtriangledown \sum_{j=1, j\neq i}^{j=N} \frac{Q_j \boldsymbol{r}_{ij}}{r_{ij}}, \tag{9.2}$$

where r_{ij} is the distance between ion i and j. $\boldsymbol{r}_{ij}$ is the unit vector. ε_0 is the permittivity of free space.

The stochastic force $\boldsymbol{F}_i^{stochastic}$ can not be expressed by a simple formula due to the uncertainty of the actions on trapped ions. This force will heat up an ion ensemble. We may consider this force as one kind of heating source and a model to describe this effect is introduced in Sec. 9.5.

9.2.2 Algorithms

The standard method to numerically solve an ordinary differential equation such as Eq. (9.1) is the finite differential approach. The idea is to give the particles' positions $r_i(t)$, velocities $v_i(t)$, and accelerations $a_i(t)$ at time t and from these to calculate the positions, velocities, and accelerations at time $t + \Delta t$.

If the classical trajectory is continuous, an estimate of the positions, velocities and accelerations at time $t + \Delta t$ can be obtained by Taylor expansions in time t. We take a general function $f(t)$ as an example. Its Taylor expansion is:

$$f(t + \Delta t) = f(t) + f'(t)\Delta t + \frac{f''(t)}{2!}(\Delta t)^2 + \frac{f^{(3)}(t)}{3!}(\Delta t)^3 + \cdots , \tag{9.3}$$

from which one obtains the forward differential algorithm

$$f'(t) = \frac{f(t + \Delta t) - f(t)}{\Delta t} - \Theta \tag{9.4}$$

the error Θ is given by

$$\Theta = \frac{f''(t)}{2!}\Delta t + \frac{f^{(3)}(t)}{3!}(\Delta t)^2 + \cdots . \tag{9.5}$$

When Δt is small, Θ is dominated by the first term, which is proportional to Δt.

If we subtract Eq. (9.3) with Δt replaced by $\Delta t/2$ from the same equation with Δt replaced by $-\Delta t/2$, all even powers of Δt vanish.

$$f(t + \frac{\Delta t}{2}) = f(t - \frac{\Delta t}{2}) + f'(t)\Delta t + \frac{2f^{(3)}(t)}{3!}(\frac{\Delta t}{2})^3 + \frac{2f^{(5)}(t)}{5!}(\frac{\Delta t}{2})^5 + \cdots . \tag{9.6}$$

Now the error Θ is given by

$$\Theta = \frac{f^{(3)}(t)}{24}(\Delta t)^2 + \frac{f^{(5)}(t)}{1920}(\Delta t)^4 + \cdots . \tag{9.7}$$

If Δt is small, then Θ is dominated by the first term, which is proportional to $(\Delta t)^2$ (much smaller than Δt). This means that the slope of a curve between two points is better approximated by that at the midpoint than at either end point.

9.2.3 The leapfrog algorithm

The idea mentioned above is used to solve the particles' Newton's equations of motion and to obtain:

$$\boldsymbol{r}(t + \Delta t) = \boldsymbol{r}(t) + \boldsymbol{v}(t + \frac{\Delta t}{2})\Delta t \tag{9.8}$$

$$\boldsymbol{v}(t + \frac{\Delta t}{2}) = \boldsymbol{v}(t - \frac{\Delta t}{2}) + \boldsymbol{a}(t)\Delta t \tag{9.9}$$

$$\boldsymbol{a}(t) = \frac{\boldsymbol{F}_i(t)}{m_i} \tag{9.10}$$

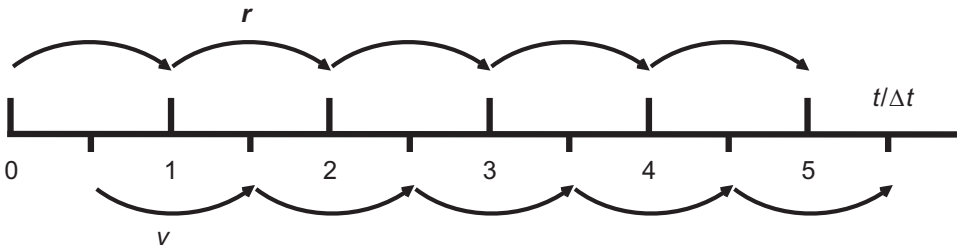

Figure 9.1: Leapfrog Verlet algorithm

If $\boldsymbol{r}(t)$ and $\boldsymbol{v}(t+\Delta t/2)$ are known, the position at $t+2\Delta t$, $t+3\Delta t$, ... can be derived step by step, as well as the velocity $\boldsymbol{v}(t)$. Thus, $\boldsymbol{r}$ and $\boldsymbol{v}$ leapfrog over each other as shown in the Fig. 9.1 [112, 113, 114].

Since the approximate error of $\boldsymbol{r}(t+\Delta t) - \boldsymbol{r}(t)$ is proportional to $(\Delta t)^3$ in each integration time Δt (see Eq. (9.6)), after a finite computation time (integration steps times Δt), the overall error is proportional to $(\Delta t)^2$, which is in the same order as the second order Runge-Kutta method [115, 116].

9.2.4 The velocity Verlet algorithm

The leapfrog shown in Eq. (9.8) starts with $\boldsymbol{v}(t+\Delta t/2)$. However, we only have the initial velocity $\boldsymbol{v}(t)$. The simplest solution to get $\boldsymbol{v}(t+\Delta t/2)$ is doing a single half step revolution by $\boldsymbol{v}(t+\Delta t/2) = \boldsymbol{v}(t) + \boldsymbol{a}\Delta t/2$. This is not a midpoint method with an error of $(\Delta t)^2$. Fortunately, we only use this once, it does not increase the order of the whole error by one order. Usually, to characterize a particle at time t', ($\boldsymbol{r}(t')$, $\boldsymbol{v}(t')$) are used instead of ($\boldsymbol{r}(t')$, $\boldsymbol{v}(t'+\Delta t)$) or ($\boldsymbol{r}(t')$, $\boldsymbol{v}(t'-\Delta t)$). Thus, $\boldsymbol{v}(t')$ is taken as the mean of two adjacent mid-step velocities [117]

$$\boldsymbol{v}(t') = \frac{1}{2}[(\boldsymbol{v}(t'+\frac{1}{2}\Delta t) + \boldsymbol{v}(t'-\frac{1}{2}\Delta t)]. \tag{9.11}$$

The algorithm for determining the position and velocity at the same moment in the way mentioned above is called velocity Verlet or position Verlet algorithm. It can be written as

$$\boldsymbol{v}(t+\frac{1}{2}\Delta t) = \boldsymbol{v}(t) + \frac{1}{2}\boldsymbol{a}(t)\Delta t \tag{9.12}$$

$$\boldsymbol{r}(t+\Delta t) = \boldsymbol{r}(t) + \boldsymbol{v}(t+\frac{1}{2}\Delta t)\Delta t \tag{9.13}$$

$$\boldsymbol{v}(t+\Delta t) = \boldsymbol{v}(t+\frac{1}{2}\Delta t) + \frac{1}{2}\boldsymbol{a}(t+\frac{1}{2}\Delta t)\Delta t \tag{9.14}$$

or

$$\boldsymbol{r}(t+\frac{1}{2}\Delta t) = \boldsymbol{r}(t) + \frac{1}{2}\boldsymbol{v}(t)\Delta t \tag{9.15}$$

$$\boldsymbol{v}(t+\Delta t) = \boldsymbol{v}(t) + \boldsymbol{a}(t+\frac{1}{2}\Delta t)\Delta t \tag{9.16}$$

$$\boldsymbol{r}(t+\Delta t) = \boldsymbol{r}(t+\frac{1}{2}\Delta t) + \frac{1}{2}\boldsymbol{v}(t+\Delta t)\Delta t \tag{9.17}$$

The most important advantage of the leapfrog algorithm is its simplicity at second order of accuracy. Additionally, it is time reversal invariant; the particle's trajectory forward in time is overlapped with that backward.

9.3 Time scales

With a specific computational power to simulate a certain number of particles, the time interval for each integration step (integration time or time step, Δt) and the computation time need to be well chosen in order to ensure minimum computation steps with an acceptable accuracy. Since the equations of motion are solved on a step-by-step basis, the time step should be sufficiently small to avoid discretization errors (i.e. much smaller than the period of the fastest motional process in the system). However, if Δt is too small, the number of computation steps for a finite computation time (inversely proportional to Δt) increases greatly. This means it will cost a much longer time for a computer to do the simulation. Additionally, a small Δt increases the roundoff error.

Generally, the time scale of the macromotion (secular motion) period of ions in our experiment (using $^{138}Ba^{+}$ as the coolant to cool heavier complex molecular ions) is in the order of 10 μs, and for that of their micromotion (rf driving field) it is in the order of 100 ns. Tens to hundreds computation steps for one oscillation period are acceptable in order to simulate ensembles in the millikelvin temperature regime. For example, for a $^{138}Ba^{+}$ ion ensemble with the secular oscillation frequency at 100 kHz at a temperature of 20 mK, if we set Δt to 400 ns, a secular oscillation containing 25 computation steps (see Fig. 9.2) is accurate enough to represent the secular motion of the ion ensemble. In a higher temperature regime, ions move faster and the moving distance in each time step is accordingly bigger, which sometimes results in a serious acceleration fluctuation and gives the ion ensemble a high kinetic energy, which breaks the law of energy conservation. Thus, at high temperatures a smaller time step should be applied. For the same reason, lighter ions such as $^{9}Be^{+}$, at 20 mK, have a much higher average velocity than heavier ions, such as $^{138}Ba^{+}$ ions. Therefore, 25 computation steps per period are not enough. Normally, the secular oscillation frequency for $^{9}Be^{+}$ ion our trap is approximately 250 kHz. We set the time step to 50 ns at 20 mK, thus, it is about 80 computation steps for each oscillation period.

We should also have some idea of the time scale for an ion cluster reaching its equilibrium state to help us to choose an appropriate simulation time. Actually, this time scale varies depending on the initial temperatures, ion densities, and mass difference of the ion ensembles. When all ion species included in the ion cluster have close masses, due to the strong Coulomb interaction it reaches an equilibrium state within microseconds. Fig. 9.3 shows a simulation of the thermalization process. The broken thermal states are recovered in about 14 μs. When the mass difference between two ion species is big, they are far away from each other resulting in a weak mutual interaction. Thus, a longer time is necessary for such a system to reach the equilibrium state. In our case, simulation /

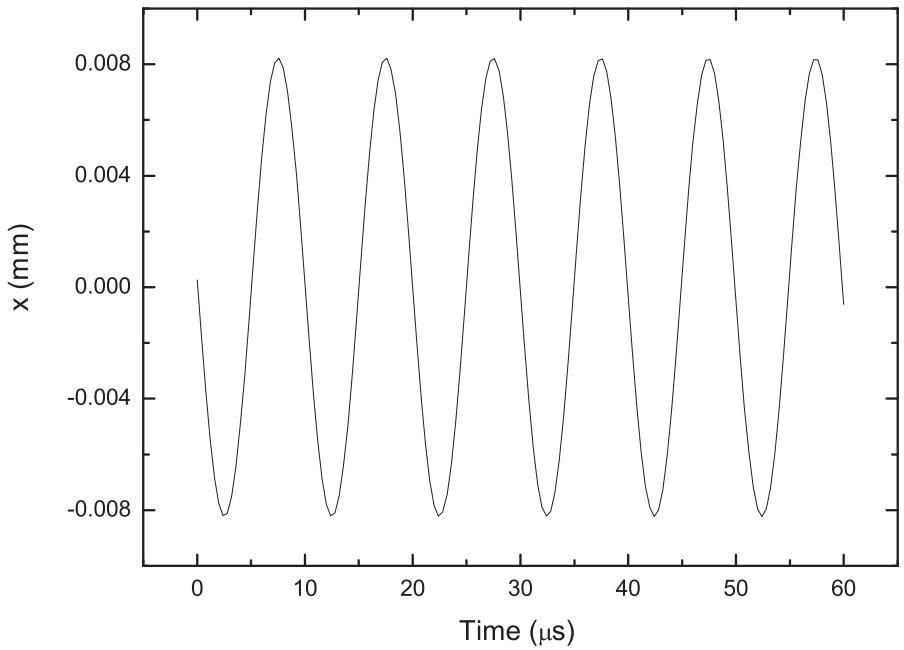

Figure 9.2: A barium ion oscillates in a linear Paul trap with a trap secular frequency of 100 kHz, the time step of 400 ns is small enough to describe the ion's trajectory smoothly.

cooling times of several ms are normal.

9.4 Initial conditions

As mentioned in Sec. 9.2, in order to obtain the positions and velocities of particles at any moment, we need to know their initial positions and velocities. So before running the simulations an initialization has to be done. Since the velocity distribution of particles in any direction at a certain temperature is a Gaussian distribution, the standard way is to assign a value from a Gaussian random generator as the velocity of a particle. However, the initialization of the positions depends on the temperature of the particle system. At high temperatures, the spatial distribution of a particle system is also a Gaussian distribution, so that the positions can be initialized in the same way as the velocities. At very low temperatures, particles are arranged in shells but move (diffuse) randomly over the surface of the shells. This can be characterized "as a crystal in the direction perpendicular to the shells and as a liquid on the shells" [118]. At even lower temperatures, diffusion decreases and an ordered structure forms on the shells [119], so the ensemble is no longer following the Gaussian distribution and the positions cannot be assigned directly. Generally, we can set the initial positions and velocities at a higher temperature with the Gaussian distribution, then let the particle system evolve for a long time, which can be some thousand oscillation periods, including friction. The thermal kinetic energy will be dissipated gradually, and the temperature of the ensemble decreases. Via the control of the magnitude of the friction force we can stop the system at any target temperature (no matter if it is in liquid or crystal state).

In principle, this method can be simplified. One initializes each ion at a random po-

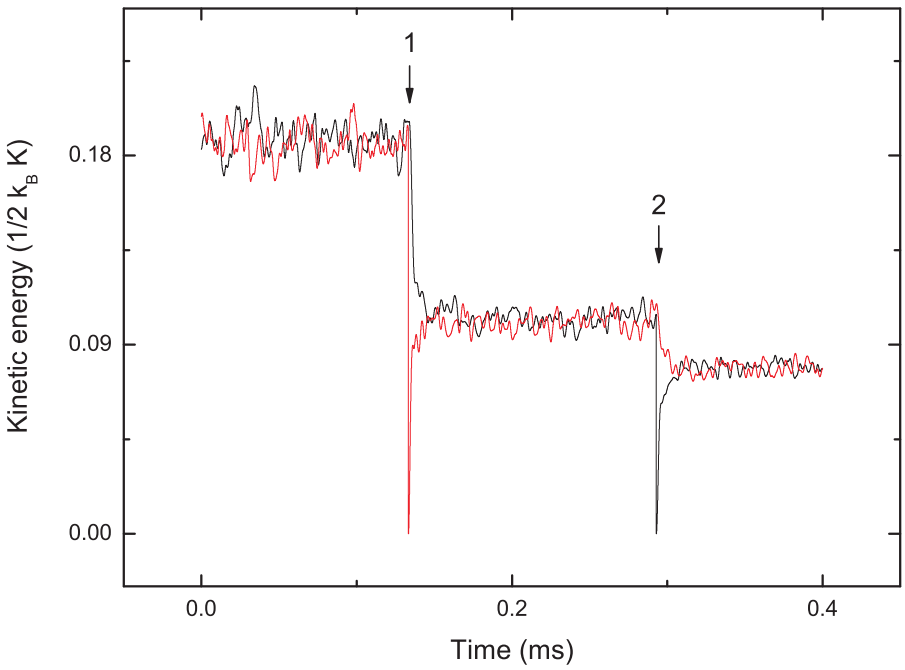

Figure 9.3: Simulation of a thermalization process. A barium ion ensemble containing 1000 ions is in the ion trap. Its averaged kinetic energies in the x and axial (z) directions are equal as shown in red and black. At time point 1 the velocities in x direction are set to be 0. Due to the Coulomb interaction, the kinetic energy is redistributed in all directions. The time of the redistribution process is quite short, about 14 μs. We repeat this in the axial direction at time point 2. The thermalization time is similar.

sition with zero velocity (or a random value) in a limited spatial region, i.e. in the trap area. Then we let the ensemble evolve with a frictional force for a long time. This initialization process is very similar to the loading of the barium ions into the ion trap with our cooling lasers in the experiment. This method is suitable for a system with a large number of ions. Otherwise, a strong random motion in normal modes is usually induced due to the insufficient samples (the initial ion distribution is hard to be homogenous). This complicates the study of the dynamics properties such as CCD image simulations and temperature determination of ensembles.

Moreover, in the process of laser cooling the ion ensemble from a high temperature to a very low temperature, some ions are mainly sympathetically cooled (the laser cooling rate depends on the average temperature of the ion ensemble; at a low average temperature, a few hot ions mainly dissipate their energy through the Coulomb interaction with the cold ions). Some ms computation time for them is probably needed to reach the thermal equilibrium state.

To avoid these difficulties we set the ions in their minimum potential energy state with zero velocities (temperature at absolute zero with the ground potential energy) [120, 96], then start to heat this ultracold ion crystal to a target temperature based on the fact that the cooling and heating processes are time reversible (in the simulations cooling is simulated by a viscous force, not by photon recoil processes). An ion crystal with the

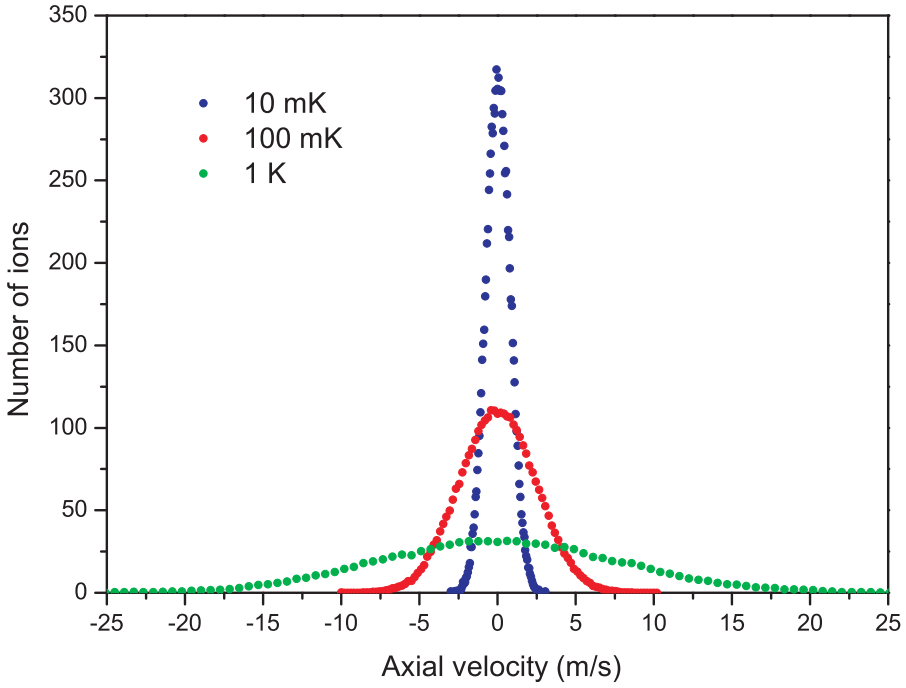

Figure 9.4: Axial velocity distributions of three barium ion ensembles with 1000 ions at 10, 100, and 1000 mK after have been heated up from absolute zero. They have distributions that are Gaussian.

ground potential energy at $T = 0$ is realized in the simulation as follows: (1) only assign the coordinates to each ion; (2) move one ion to a testing position ($\alpha + \Delta\alpha$, α can be x, y, and z) and calculate the potential energy of the ion ensemble (trap potential plus Coulomb potential among ions) to compare with the potential before moving. If it is smaller, the coordinate of this ion is updated by this new position and double the distance offset $\Delta\alpha$. Otherwise, we move the ion to ($\alpha - \Delta\alpha$) and make a new comparison. If the energy is smaller, the coordinate of this ion is assigned as the new testing position and double the distance offset. If the result is still bigger, we keep this ion at the original position and replace $\Delta\alpha$ by $\Delta\alpha/2$. (3) switch to another ion and repeat the calculations.

This model is checked in Fig. 9.4. In the beginning, 1000 $^{138}Ba^{+}$ ions are set to the ground potential energy state without any kinetic energy, then the ion ensemble is heated up (see Sec. 9.5.2). The velocity distribution in axial direction at different temperatures are recorded. They have perfect Gaussian distributions, which shows that this initialization approach works very well.

9.5 Simulation models

In this section, the possible heating sources are studied and a model for the heating effects is presented. The laser cooling model is also presented here.

9.5.1 Heating effects

In order to characterize the temperature of an ion crystal one has to distinguish between the energy contributions of the micromotion and of the secular motion. The secular energy, where the micromotion oscillation is averaged out, can be taken as an indication of the temperature of the ion crystal, since it arises from the disordered motion of the interacting ions in the time-averaged trap potential. In contrast, the micromotion contribution to the total energy arises from a driven motion, which is limited to the radial direction in the linear ion traps considered here.

The root-mean-square (rms) velocity of one particular ion, $(v_{i\alpha}^{rms})^2 = \frac{1}{J}\sum_{j=1}^{J} v_{i\alpha}^2$, is a measure of the kinetic energy averaged over one rf period. $\alpha = x, y, z$ denotes the directions, j and J are the time step number and the number of time steps in one rf period, respectively. The secular velocity is defined by averaging over one rf period, $\bar{v}_{i\alpha} = \frac{1}{J}\sum_{j=1}^{J} v_{i\alpha}$.

Fig. 9.5 shows these two quantities for a large ensemble of ions containing a single species. The curves are averages over single-period histograms. The secular velocities $\bar{v}$ show a Gaussian distribution corresponding to that of a gas in thermal equilibrium, and the variances of the axial and radial velocities are equal. Thus a secular temperature of an ion ensemble can be introduced as

$$\frac{2}{3k_B}E_{sec} = T_{sec} = \frac{1}{3Nk_B}m\sum_{i}^{N}(\langle\bar{v}_{ix}^2\rangle + \langle\bar{v}_{iy}^2\rangle + \langle\bar{v}_{iz}^2\rangle), \tag{9.18}$$

where $\langle\ldots\rangle$ denotes an average over many rf periods and N is the total ion number.

The time-averaged micromotion energy can be defined as the difference between the time-averaged total energy

$$E_{tot} = \frac{1}{2N}m\sum_{i}^{N}(\langle(v_{ix}^{rms})^2\rangle + \langle(v_{iy}^{rms})^2\rangle + \langle(v_{iz}^{rms})^2\rangle), \tag{9.19}$$

and the secular energy E_{sec}. Unlike in the case of ion strings on the trap axis (where micromotion would be zero), in large ensembles at mK temperatures considered here, the total energy is a few orders larger than the secular energy, as a comparison of the histograms in Fig. 9.5(b) indicates. Thus, the micromotion energy can be approximated by the total energy Eq. 9.19.

The micromotion leads to rf heating (see Chapter 2). Fig. 9.6 shows how the secular temperature of an ion ensemble rises due to rf heating only. In this simulation, where micromotion is included, an ensemble of 1250 $^{138}Ba^+$ ions was set to $T_{sec} = 600$ mK, then all cooling and heating sources were switched off and the ensemble was left evolving. As rf heating rises with temperature [94], the temperature increase is slow in the beginning, with an rf heating rate $dT_{sec}/dt \approx k_B(2.93\ \mathrm{K/s})$ at 600 mK, and much faster at higher temperatures, with a rate of $\approx k_B(39.29\ \mathrm{K/s})$ at 10 K. In our experiments, the ion ensembles are generally in the crystal state at temperatures from 5 to 100 mK with small

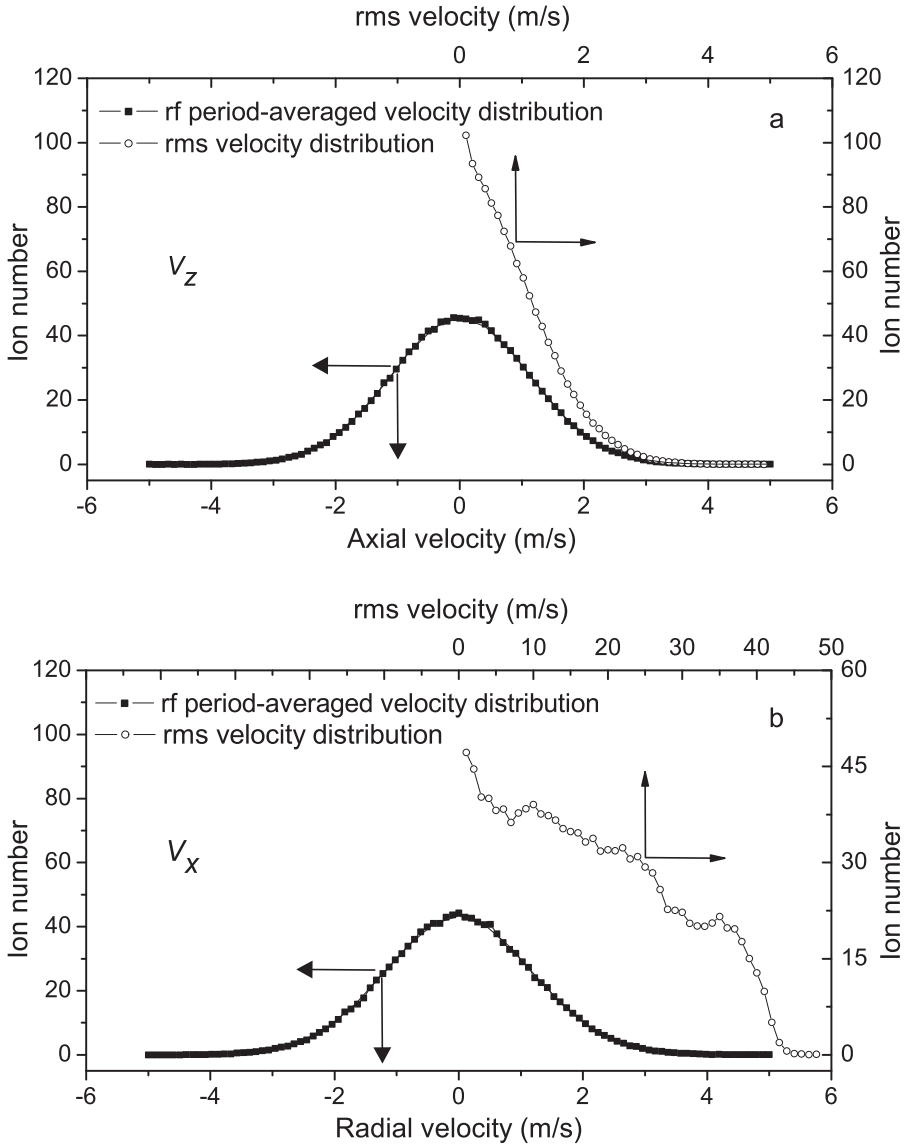

Figure 9.5: Velocity distributions for an ion ensemble containing 1250 $^{138}Ba^{+}$ ions at $T_{sec} \approx 13$ mK. The rf averaged and rms velocity distributions are shown for (a) the axial and (b) a radial direction. The simulation included micromotion.

q parameters (≈ 0.11) and low ion numbers (less than 3000 ions). Under these conditions, the simulations show that rf heating rates are almost negligible ($\ll k_B(1\ \mathrm{K/s})$) [45].

However, trap imperfections as a result of rf phase shifts or stray fields can lead to an increased rf heating [44]. To obtain an upper limit of this effect, we implemented an additional rf phase shift of 0.1 rad between neighboring electrodes and a DC offset of 5 V in x-direction applied to the central electrodes in our simulations (see [121, 100] for details on our linear Paul traps). An ensemble of 1250 $^{138}Ba^{+}$ ions was set to $T_{sec} = 36.5$ mK, and then let evolve with cooling and heating sources switched off. As Fig. 9.7 shows, the rf heating rate is very low ($\approx k_B(0.00234\ \mathrm{K/s})$) in this typical temperature regime, even in the case of a strongly imperfect trap.

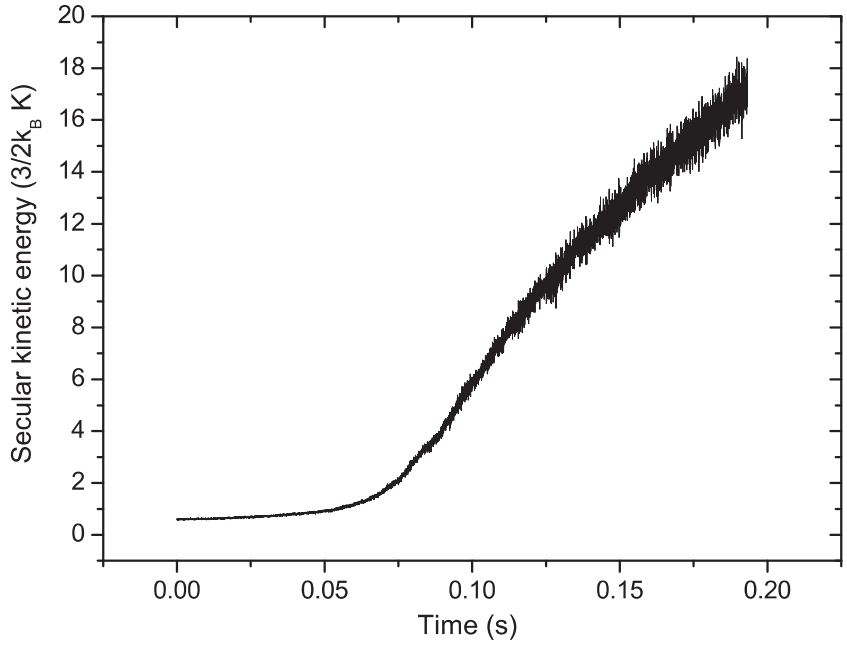

Figure 9.6: Rf heating. After the laser cooling is switched off (at $t = 0$) the secular energy of an ion ensemble (1250 $^{138}Ba^{+}$ ions, $q = 0.119$) rises in a nonlinear fashion from $\approx$ 600 mK to $\approx$ 17 K in about 0.2 s purely due to rf heating.

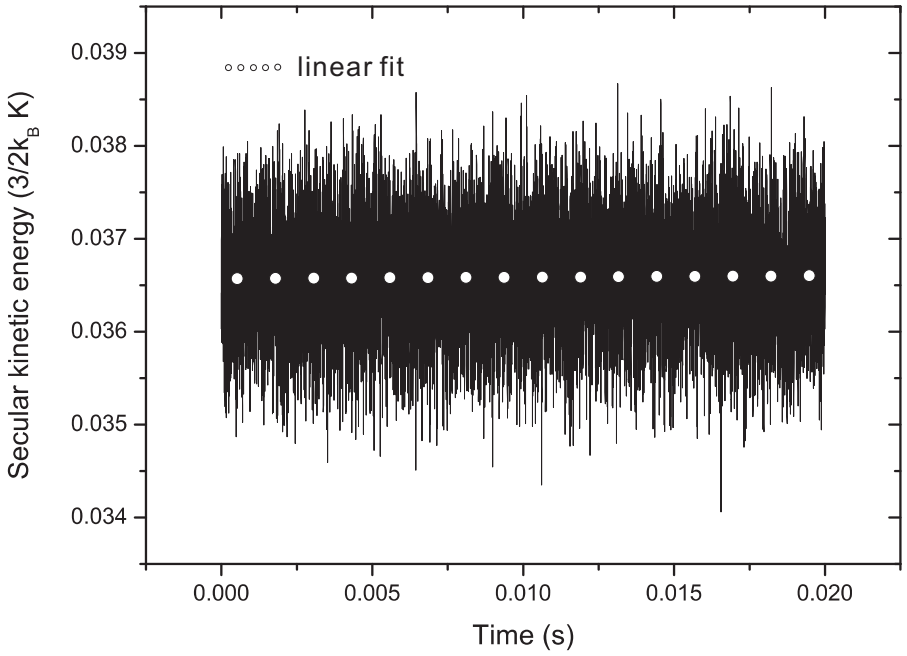

Figure 9.7: Rf heating in an imperfect trap. The simulation includes an additional rf phase shift of 0.1 rad between neighboring electrodes and a DC offset of 5 V in x-direction applied to the central electrodes. The plot shows the temperature of an ion ensemble (1250 $^{138}Ba^{+}$ ions, $q = 0.083$) in absence of laser cooling and other heating. A linear fit (open circles) yields a heating rate of $\approx k_B(0.00234$ K/s), which is so small that it can be neglected.

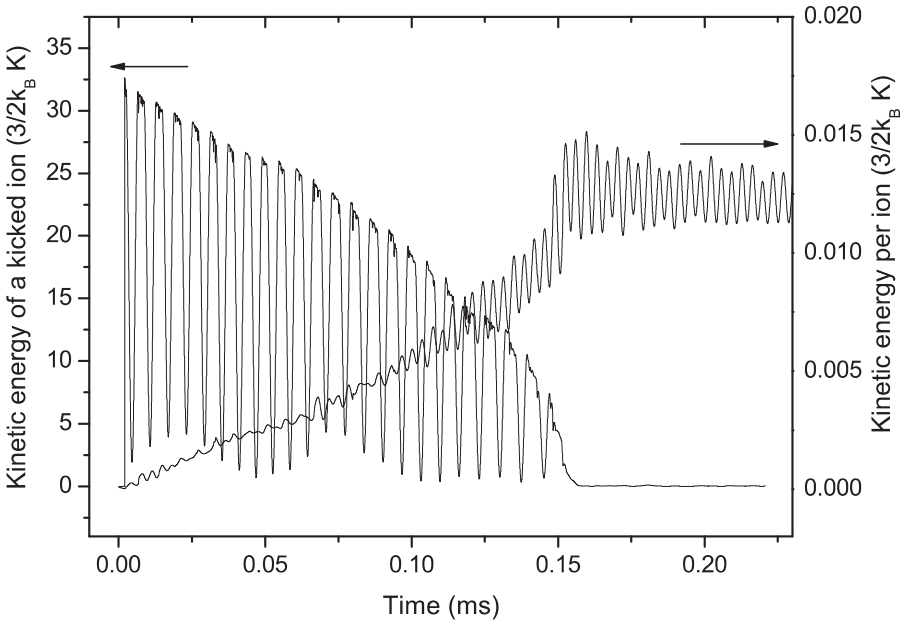

Figure 9.8: Ion-neutral head-on collision. After its collision with a neutral helium atom a barium ion gradually transfers its gained kinetic energy (left scale) to the whole ion ensemble, whereupon the kinetic energy per ion (right scale) increases. The simulation was performed without micromotion.

Another heating source which can be substantial also at low temperatures are collisions with residual gas molecules. From Eq. (3.38) we know that when the ions are hotter than the room temperature (T_n), they can be cooled by the neutral gas, otherwise, they are heated. In a background gas of N_2 at 300 K and a pressure of 1×10^{-9} mbar the average $^{138}Ba^+$ N_2 elastic collision rate is $\gamma_{\text{elastic}} \approx 0.017$ s^{-1}. In each collision the average energy transfer is $\approx k_B$ (128 K), leading to a heating rate $h_{coll} = k_B(2.2$ K/s), which increases linearly with the residual gas pressure.

Finally, electric noise on the electrodes can also lead to heating. It is hard to be formulated but its effect considered to be quite weak. [122, 123].

9.5.2 Modelling of heating effects

Consider the case of an ion colliding with a residual gas atom or molecule. The velocity magnitude change Δv can exceed 100 m/s. This is so strong that the ion leaves the ion crystal and moves in the whole trap volume. Each time the ion passes through the ion cluster, it transfers some energy to it, with the energy loss rate being the lower, the faster the ion is [124]. Fig. 9.8 shows the kinetic energies of an ensemble of 1249 barium ions (initially at zero temperature) and of a single ion after the latter has suffered a head-on collision along the x-direction with a helium atom of $\frac{3}{2}k_B(300$ K) kinetic energy. The colliding barium ion suddenly gains a large velocity (76.8 m/s) and starts to oscillate in the trap. Its kinetic energy is periodically transformed into potential energy and back. It gradually leaks to other ions until the whole ensemble reaches an equilibrium state with increased potential and kinetic energies per ion (see Fig. 9.11). In final equilibrium state, the total kinetic energy of the ion ensemble is about $\frac{3}{2}k_B(15$ K), which is approxi-

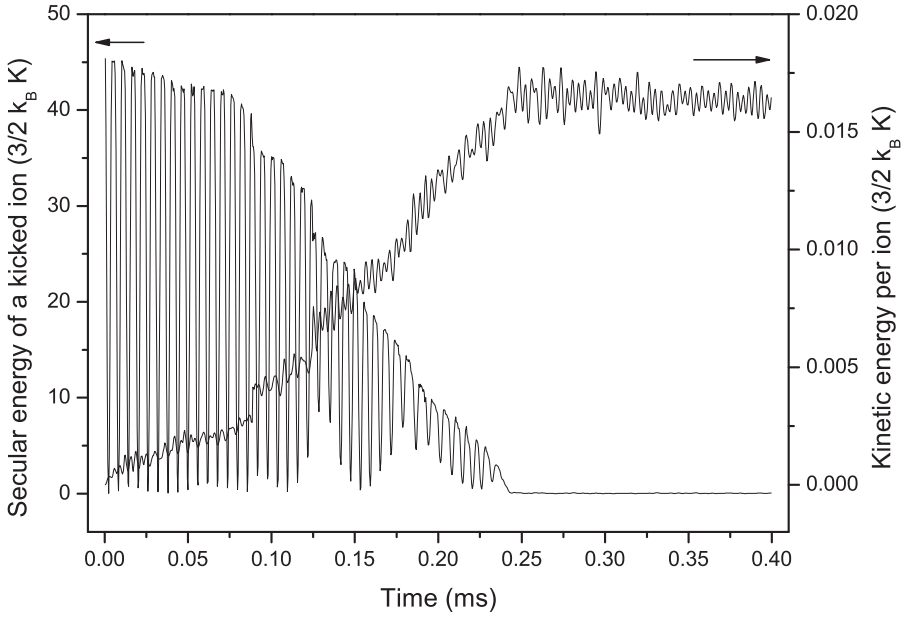

Figure 9.9: Ion-neutral head-on collision in the case of included micromotion. After its collision with a neutral helium atom a barium ion gradually transfers its gained kinetic energy (left scale) to the whole ion ensemble, whereupon the kinetic energy per ion (right scale) increases.

mately the same as the potential increase. Thus, the final overall energy is about $\frac{3}{2}k_B$(33 K), which is consistent with the original kinetic energy of the ion which experienced the collision, $\frac{3}{2}k_B$(32.6 K). For a typical crystal, as considered here, the thermalization time is $\tau \approx 0.2$ ms, which is much longer than the value (≈ 14 μs) mentioned in Sec. 9.3. The difference arises from the fact that in the present case the colliding barium ion spends most time staying quite far away from the remaining ions and therefore the return to equilibrium takes longer.

A similar result is obtained when the rf micromotion is included. In this simulation, the colliding barium ion, near the trap axis, initially gains a velocity of 76.8 m/s as above. However, due to the presence of the rf driven motion the rf heating effect is activated, especially, on this kicked barium ion, which is quite hot. In the final equilibrium state, the secular temperature of the ions is about 16.3 mK, thus, the total gained secular energy in this collision process is about $\frac{3}{2}k_B$(42.6 K) (secular kinetic energy plus potential energy, which is almost the same amount as the secular kinetic energy), which is evident bigger than the transferred energy directly from the colliding helium atom. The difference energy, $\frac{3}{2}k_B$(9.6 K), came from the rf field, i.e. rf heating occurred.

Another similar simulation is done as well. In this case, the colliding ion is moved to the outmost layer and stays near the x axis. When the ion reaches the point farthermost away from the trap center, a head-on collision occurs with a helium atom along the x-direction. The following thermalization process is shown in Fig. 9.9. The final gained energy is about $\frac{3}{2}k_B$(44.6 K), thus, the rf heating is about $\frac{3}{2}k_B$(12 K). Therefore, in the experiments a barium ion ensemble can not be cooled to the Doppler cooling limit. At least, the collisions of barium ions with background neutral gas and the corresponding

rf heating keep the barium ion ensemble at a few millikelvin.

The collision heating of an ensemble of N ions will be essentially continuous if the time between two collisions in the whole ensemble, $1/N\gamma_{elastic}$, is smaller than the thermalization time τ, i.e. for ion numbers $N > 1/(\gamma_{elastic}\tau)$. For a typical value of $\gamma_{elastic} = 0.02$ s^{-1}, this condition is fulfilled for $N > 250000$ ions. Thus, much smaller ensembles can appear significantly colder in a single CCD image than the actual time-averaged temperature, if the CCD exposure time is less than $1/(N\gamma_{elastic})$. With a typical exposure time of 2 s this is the case for $N < 25$ ions. Indeed, our experience is that small clusters show a lower temperature (as found from the CCD images) than larger ones.

Ion ensembles considered here are usually large ($N > 2000$) and the CCD camera exposure times are long enough, so that collision heating due to the relatively rare collision events (as well as other heating processes) can be implemented by a more continuous heating in the simulations. Choosing more frequent velocity kicks with appropriately low velocity kick magnitudes, computing time can be saved because equilibrium states are reached much faster (within a few ms of simulated time).

Thus, we consider a model in which each ion experiences a velocity kick $\boldsymbol{w}_k$ at each integration step with a fixed magnitude in a random direction. It is described by the function

$$\boldsymbol{w}_k(t) = v_{l,0}\hat{\boldsymbol{w}}_k(t). \tag{9.20}$$

Here, $v_{l,0}$ is a constant velocity kick magnitude that in general may differ from species to species l, $\hat{\boldsymbol{w}}_k(t)$ is a unit vector whose direction is chosen randomly for each ion at each integration step. The average change in kinetic energy per ion for a particular species l from one integration step (duration Δt) to the next is, in absence of any forces,

$$\begin{aligned}\langle \Delta E_l \rangle &= \frac{m_l}{2}\langle \boldsymbol{v}_k^2(t+\Delta t) - \boldsymbol{v}_k^2(t)\rangle \\ &= \frac{m_l}{2}\langle 2\boldsymbol{v}_k(t)\boldsymbol{w}_k(t) + \boldsymbol{w}_k^2(t)\rangle = \frac{m_l}{2}\langle \boldsymbol{w}_k^2(t)\rangle,\end{aligned} \tag{9.21}$$

since the ion velocities and the velocity kicks are uncorrelated. The kinetic energy increase rate per ion (heating rate) is therefore

$$h_l = \frac{\langle \Delta E_l \rangle}{\Delta t} = \frac{1}{2} m_l v_{l,0}^2/\Delta t. \tag{9.22}$$

In a more general approach, at each integration step $N_{l,kick}$ ions of each species are randomly chosen and given random velocity kicks. Then, the heating rate is

$$h_l = \frac{1}{2} m_l \frac{N_{l,kick}}{N_{l,total}} \widetilde{v}_{l,0}^2/\Delta t. \tag{9.23}$$

Here, $N_{l,total}$ is the total number of ions of species l, and the $\widetilde{v}_{l,0}$ are the $v_{l,0}$ from Eq. (9.22) chosen in such a way that h_l is equal to h_{coll}.

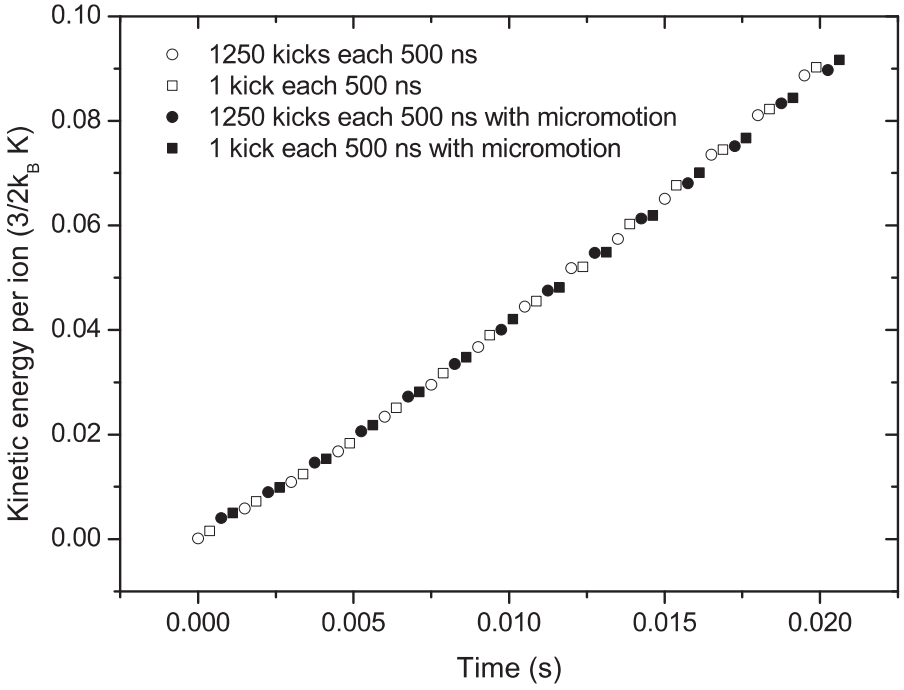

Figure 9.10: Heating with velocity kicks. A specific heating rate was realized with different velocity kick frequencies $N_{l,kick}/(N_{l,total}\Delta t)$ by adjusting kick magnitudes accordingly (open circles and squares). The filled circles and squares show the temperature evolution in presence of micromotion.

Thus, a given heating rate can be implemented in different ways - by frequent kicks with small velocity kick amplitudes $v_{l,0}$ or by rare ones with large amplitudes. Fig. 9.10 illustrates this. Here, an ensemble of 1250 barium ions was set to 0 K and then let evolve without any cooling and with a heating rate $h = k_B(11.95\ \mathrm{K/s})$. In the first case (open circles) all ions were kicked after each time step ($\Delta t = 500$ ns) with kick magnitude $v_0 = 2.68 \times 10^{-2}$ m/s and in the second case (open squares) just one ion ($N_{l,kick} = 1$) was kicked per time step, with an appropriately higher magnitude $\widetilde{v}_0 = 0.949$ m/s. As expected, in both cases the rate of increase of the kinetic energy per ion is the same. Additionally, these simulations were performed including micromotion in the time-dependent trap potential $V(x, y, z, t)$ (see Eq. (9.2)), but using the same kick parameters (filled circles and squares). We find the same heating rate. This is due to the fact that the implemented kicks change the velocities of the ions (several m/s, see Fig. 9.5) only by small amounts, and thus preserve the phase of their micromotion. Thus, rf-heating is negligible for secular temperatures $\ll 1$ K. Note that in the simulation velocity kicks of constant magnitude have been used, and not a Maxwellian distribution.

The heating rate used in Fig. 9.10 clearly does not lead to a linear increase of the kinetic energy per ion, as expected from Eq. (9.23). This is due to the fact that the definition considers an equilibrium state of heating and cooling effects, whereas Fig. 9.10 shows a dynamic process with heating only. Here, the rising temperature leads to an increase of the ion ensemble's volume whereupon the potential energy of the ensemble increases non-linearly. Due to energy conservation it is the total energy of the ensemble which increases linearly with time when applying a certain heating rate. Both the kinetic energy

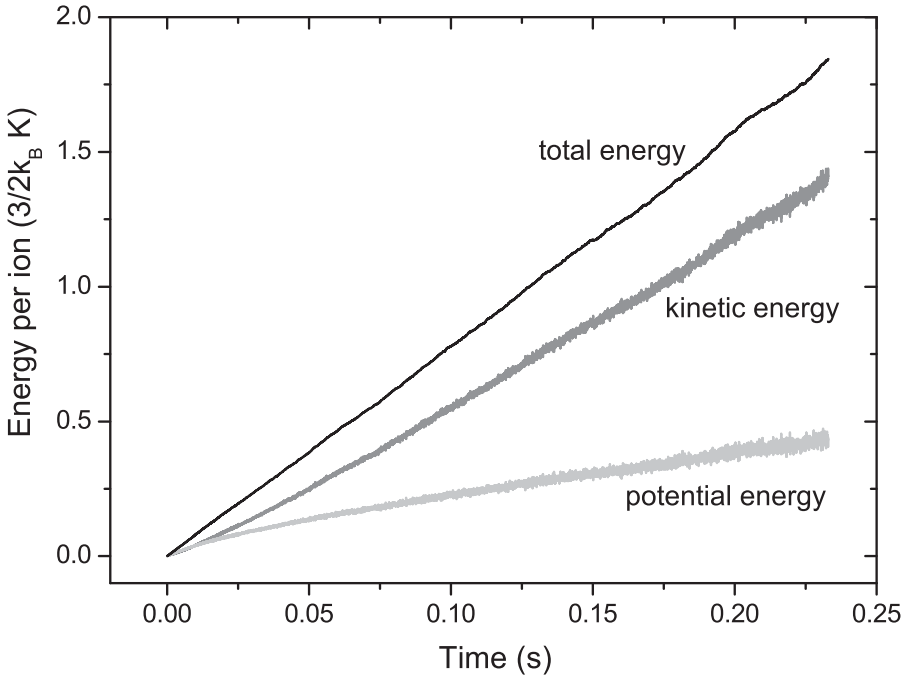

Figure 9.11: Energy distribution. The total energy per ion (black) increases linearly according to the implemented heating rate in the velocity kick model (micromotion not included). However, the kinetic (grey) and the potential (light grey) energy grow nonlinearly due to a growth of the ion ensemble's volume.

and the potential energy increase nonlinearly. This is shown in Fig. 9.11 for an ensemble of 1250 barium ions heated with $h = k_B(11.95\ \mathrm{K/s})$ without any cooling. The grey curve shows the nonlinear change of the kinetic energy, and the light grey curve the one of the potential energy. Here, the ground potential energy (the mutual Coulomb energy of the ions at zero temperature plus their trap potential energy), $k_B(70.75\ \mathrm{K})$, was set as reference energy. The black curve is the total energy change due to the velocity kicks. It is linear with a slope of $k_B(11.6\ \mathrm{K/s})$, which agrees well with the applied heating rate h.

The appropriateness of the kick model can also be verified by comparing theoretical collision heating rates with those extracted from experimental data via simulations.

Experimentally, CCD images of an ensemble of $^{138}Ba^+$ ions at different N_2 pressures were taken. Assuming a realistic cooling rate $\beta = 2 \times 10^{-22}$ kg/s (see Sec. 9.7.4), at each pressure we fitted the heating rate that yields the best agreement of simulated and experimental image. Fig. 9.12 shows these experimental values (circles) together with the collision heating rate h_{coll} (black line) for $^{138}Ba^+$ ions and N_2 molecules, rising linearly with the N_2 pressure. Here, $T_n - T_c$ (see Eq. (3.38)) was set to 300 K. For pressures above 1×10^{-9} mbar, the experimental values agree well with the theoretical heating rate given by Eq. (3.38), with $\alpha_{N_2} = 4\pi\epsilon_0(1.76 \times 10^{-24}\,\mathrm{cm}^3)$ (α_{N_2} is molecular polarizability of N_2 gas).

The agreement is not complete at the lowest pressures. To a lesser extent, this could

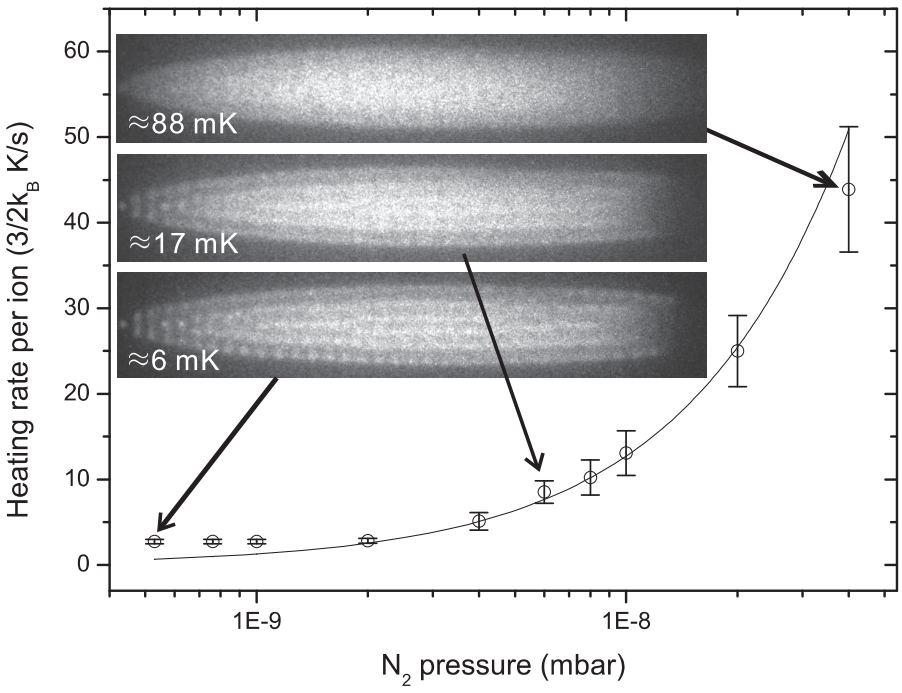

Figure 9.12: Collision heating. The black curve shows the theoretical collision heating rates for collisions of $^{138}Ba^+$ ions and N_2 molecules, the circles show the heating rates extracted from the experiment.

be due to the finite spatial resolution of our imaging system, which naturally leads to blurring of the crystal. However, we believe that other heating sources besides the considered rf and collision heating are present, such as electric field noise and possibly additional collision heating due to ion micromotion. As we cannot quantify them, they are not implemented in our simulations directly, but their effect can be included in the velocity kick model as a pressure-independent contribution to $\widetilde{v}_0$.

9.5.3 Cooling model

As laser cooling force $\boldsymbol{F}_i^{laser}$ we consider a linear viscous damping force plus a constant light pressure force $\boldsymbol{F}_i^{laser}$ (see Eq. (3.17))

$$\boldsymbol{F}_i^{laser} = -\beta_i \dot{\boldsymbol{r}}_i + \boldsymbol{F}_i^{lp}, \tag{9.24}$$

here we rewrite β as $-\beta$ to ensure that it is positive in the red detuning of the cooling laser.

The light pressure force $\boldsymbol{F}_i^{lp}$ pushes the laser-cooled ion ensemble in the laser beam direction and gives a spatial offset from the potential well center. The cooling force reduces the velocity magnitude of the laser-cooled ions, so the kinetic energy change rate per ion is

$$\Delta E_i = \frac{1}{2} m_i v_i^2(t+\Delta t) - \frac{1}{2} m_i v_i^2(t) = \frac{1}{2} m_i v_i^2(t) \left[\left(\frac{\beta \Delta t}{m_i} \right)^2 - 2 \frac{\beta \Delta t}{m_i} \right]. \tag{9.25}$$

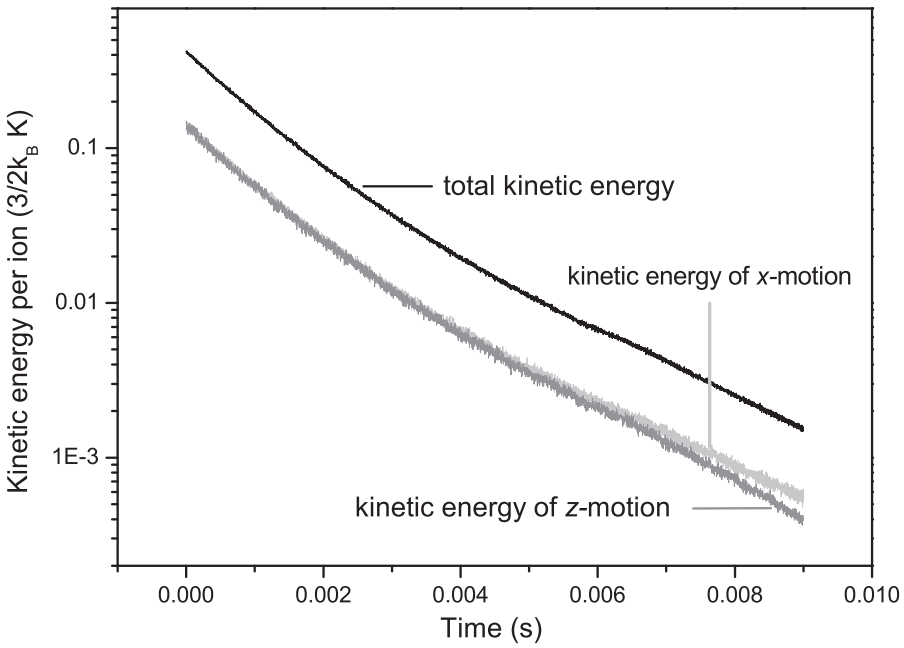

Figure 9.13: Simulation of viscous cooling of an ion ensemble. 1250 barium ions are cooled by only one laser beam along the trap axis ($\beta = 2 \times 10^{-22}$ kg/s, no heating applied, micromotion not included). The kinetic energy is effectively reduced in all dimensions.

Because the friction coefficient β is very small ($\beta_{max} \approx \pi^2\hbar/\lambda^2 \approx 4 \times 10^{-21}$ kg/s for transitions at optical wavelengths λ [125]), the first term in the parenthesis can be neglected. Thus, the kinetic energy decrease rate per ion ("cooling rate") of a species l is

$$c_l = \frac{\langle \Delta E_i \rangle}{\Delta t} = -\frac{2\beta}{m_l}\langle \frac{1}{2} m_l v_i^2(t) \rangle = -\frac{2\beta}{m_l}\langle E \rangle_l. \tag{9.26}$$

The temperature of the ion species l, T_l, is obtained from $\frac{3}{2}k_B T_l = \langle E \rangle_l$, where $\langle E \rangle_l$ is the time- and ensemble-averaged kinetic energy. The temperature decrease rate of an ion ensemble l is

$$\frac{\mathrm{d}T_l}{\mathrm{d}t} = -\frac{2\beta}{m_l} T_l \tag{9.27}$$

This holds when the cooling is along all three spatial directions simultaneously. If the ion ensemble is cooled by only one laser beam along the axial direction z, then in the expression for c_l in Eq. (9.10) v_i is to be replaced by $v_{i,z}$, and E_i by $E_{i,z}$. Thus, the temperature reduction rate should be divided by 3 to get

$$\frac{\mathrm{d}T_l}{\mathrm{d}t} = -\frac{2}{3}\frac{\beta}{m_l} T_l. \tag{9.28}$$

Indeed, cooling with only one laser beam is sufficient to reduce the secular motion of the ions in all dimensions, because their mutual Coulomb interaction leads to a fast thermalization. This is also conventionally implemented in experiments. To demonstrate the effect of the damping, Fig. 9.13 shows an ensemble of 1250 barium ions cooled with a friction coefficient $\beta = 2 \times 10^{-22}$ kg/s along the axial direction without applying any

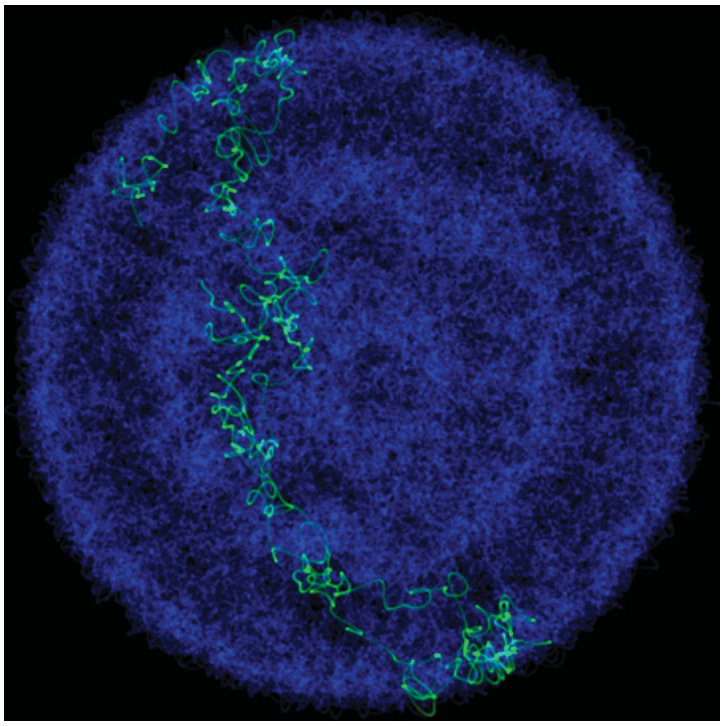

Figure 9.14: Diffusion in an ion crystal. In this axial view of a time-averaged ion crystal at 6 mK the trajectory of a single ion is shown in green. During the "exposure time" of 5 ms the ion traveled about 5.3 mm. In this simulation, no heating and cooling was applied.

heating. The secular kinetic energy per ion in radial (x or y) and axial (z) direction decreases by two orders of magnitude within less than 10 ms. As the radial secular motion is reduced indirectly, its decrease is slightly slower than that of the axial secular motion which is most obvious in the mK regime, since the thermalization time becomes longer at lower temperatures.

9.6 Simulation of CCD images

When taking CCD images of laser-cooled ion ensembles our typical exposure times are in the order of 0.5 to 2 s. During that time the ions' trajectories span several meters due to their residual secular kinetic energy (see Fig. 9.14). As a result, the images appear blurred and can be considered as probability density plots, rather than as images of individual particles.

To reproduce these CCD images by simulations, the positions of all ions for every time step of the simulation are projected to a plane perpendicular to the desired line of sight. (In our setups, the line of sight is radial, i.e. perpendicular to the z-axis and at 45° to the x- and y-axis.) A density plot of this plane corresponds to a CCD image observed.

A completely realistic simulation of the CCD images would require simulation times as long as the exposure times and a more accurate implementation of the ions' collisions with the background gas, i.e. rare and strong collisions (compare Sec. 9.5.2), leading to

long computing times. With our more continuous velocity kick model equilibrium states are reached after simulated times of a few ms and the experimental CCD images can be reproduced with good agreement. The reason for this is the CCD exposure time, which is much longer than the thermalization time, and the short inter-site diffusion time for the temperatures considered here.

In contrast to the experiment, simulations can also visualize ions which are not laser-cooled and therefore do not fluoresce. Fig. 7.16 shows a multi-species ion crystal consisting of 830 laser-cooled $^{138}Ba^+$ ions, 420 singly charged barium isotopes ($m = 137$ amu), and 200 singly protonated Alexa Fluor 350 molecules ($m = 410$ amu). Because the radial confinement for ions with a higher mass-to-charge ratio is weaker, the heavier Alexa Fluor 350 ions are located around the $^{138}Ba^+$ ions, as shown in the axial view on the right-hand side of Fig. 7.16. The lighter barium isotope ions would arrange inside the $^{138}Ba^+$ crystal and form a core (see Fig. 9.20 for the much lighter $CO_2{}^+$ ions), but as the mass difference is small and the light pressure pushes the $^{138}Ba^+$ ions to the left, they arrange on the right side of the crystal and only slightly leak into the $^{138}Ba^+$ crystal.

9.7 Ion number and temperature determination

9.7.1 Determination of ion numbers

Shape and structure of an ion crystal are determined by the trap potentials applied, the number of ions, the ion species, the light pressure force, and the temperatures. Ion numbers and temperatures can be obtained from comparison of experimental and simulated images of the ion crystals.

Firstly, the number of the trapped ions are determined. For ion crystals consisting of laser-cooled ions only the procedure is as follows: As the magnification of the imaging system is known (100 pixels in a CCD image corresponds to about 104 μm), one just needs to adjust the number of ions until the simulated crystal has the same dimensions as the observed one. Here (mK regime), the volume of the crystal is not significantly influenced by the temperature of the ions. Therefore, the ion number can be fit without considering the temperature.

For ion crystals containing sympathetically cooled ion species in addition, the determination of ion numbers is more complicated. Ions with higher mass-to-charge ratios arrange around the laser-cooled ion ensemble and therefore modify its shape. If the species is known and the mass-to-charge ratio is still close to that of the laser-cooled ions, one can find its number by reproducing the observed deformation. However, for a species with a much higher mass-to-charge ratio, the deformation induced is not sufficient (see Fig. 7.13 and Fig. 9.20). A reliable determination of the ion numbers is by extraction from the trap and counting [126], but this is a destructive method. As ions with a lower mass-to-charge ratio are located inside the laser-cooled ensemble and form a core, their number can be determined, in a non-destructive manner, from the size of the core.

In both cases it is essential to consider the light pressure force which shifts the laser-

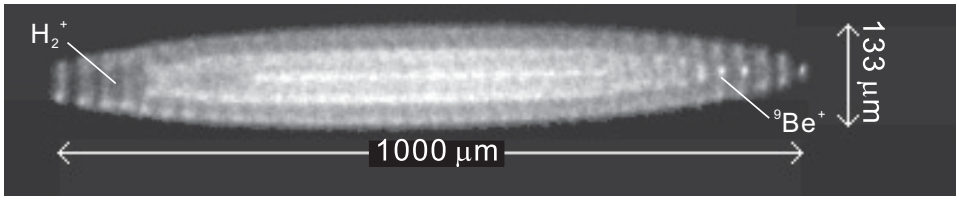

Figure 9.15: CCD image of a typical laser-cooled $^9Be^+$ ion crystal in a linear Paul trap containing sympathetically cooled molecular hydrogen ions. The cooling laser propagates to the right, the crystal is at $T_{sec} \approx 6$ mK and consists of 435 ± 10 $^9Be^+$ and 7 H_2^+ ions.

cooled ions out of the trap center and causes strong asymmetries. For example, the

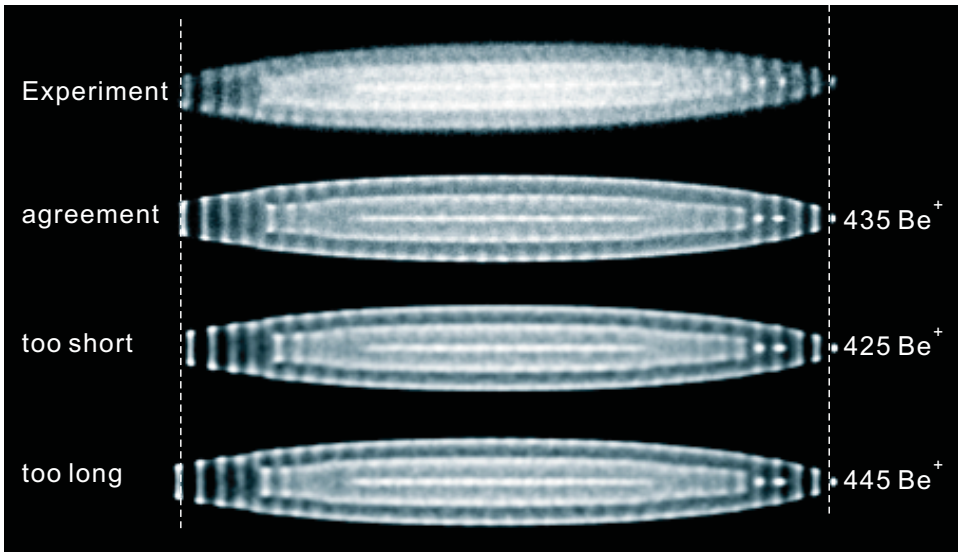

Figure 9.16: Determination of ion numbers. The experimental image of a beryllium ion crystal is compared with simulated images with different ion numbers. The best fit is achieved for a number of 435 $^9Be^+$ ions and 7 H_2^+ at the left side.

beryllium ion crystal shown in Fig. 9.15 contains H_2^+ ions that are located on the left side of the crystal, because the beryllium ions are shifted to the right. To determine the ion numbers in this crystal we simulated crystals with different ion numbers and compared them with the experimental CCD image (see Fig. 9.16). The best fit is achieved for 435 ± 10 $^9Be^+$ and 7 H_2^+ ions, when a light pressure force of 8×10^{-21} N is assumed.

9.7.2 Sympathetic heating and cooling

If other ion species are confined in the trap simultaneously with laser-cooled ions, they can be sympathetically (indirectly) heated or cooled via their mutual long-range Coulomb interaction.

To quantify this interaction, Fig. 9.17 shows a simulation of the various forces acting on the multi-species ion ensemble from Fig. 7.16. Initially, all species were set to a (secular) temperature of 0 K and in the spatial configuration of the lowest potential energy. Then

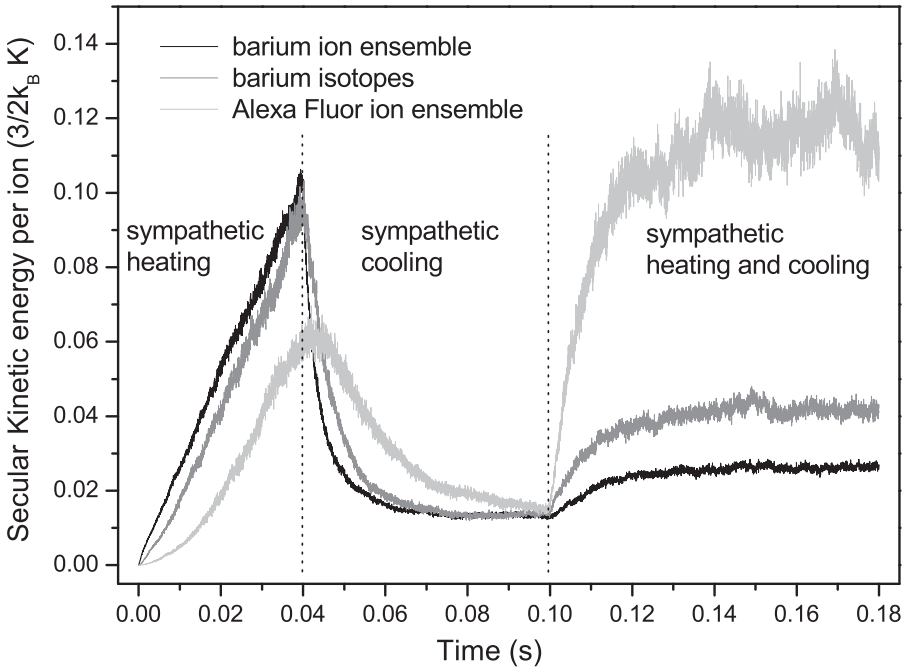

Figure 9.17: Sympathetic heating and cooling in a multi-species ion ensemble. The ion composition is the same as in Fig. 7.16. After all species were set to a secular temperature of 0 K, heating is implemented only for the $^{138}Ba^+$ ions starting at $t = 0$ s, and the other ions are sympathetically heated. At $t = 0.04$ s the laser cooling of $^{138}Ba^+$ is added, and the $^{138}Ba^+$ temperature decreases. The $^{138}Ba^+$ ions now sympathetically cool the other ions, and the ensemble reaches an equilibrium state at nonzero temperature. Finally at $t = 0.1$ s, heating is also turned on for the barium isotopes and the Alexa Fluor 350 ions, which increases the temperatures of all species until they reach the equilibrium state.

a heating rate of $h_{138Ba} = k_B(11.55\ \mathrm{K/s})$ is applied to the $^{138}Ba^+$ ions. Their temperature increases (black curve), and due to the sympathetic interaction the temperatures of the other two ion species increase as well. Because the mass-to-charge ratio of the barium isotope ions is very close to that of the $^{138}Ba^+$ ions, these two species couple very well and the energy transfer efficiency is high. Thus, the temperature of the barium isotope ions (grey curve) closely follows that of the $^{138}Ba^+$ ions. However, for the Alexa Fluor 350 ions the coupling to the $^{138}Ba^+$ ions is lower due to their larger radial separation caused by the significant mass-to-charge ratio difference. So, their temperature increase is weaker (light grey curve). After 40 ms the laser cooling is switched on with a friction coefficient $\beta = 2 \times 10^{-22}$ kg/s. As the cooling of the $^{138}Ba^+$ ions is higher than the heating h_{138-Ba}, their temperature starts to decrease. When their temperature becomes lower than that of the other species, these start to be cooled sympathetically until all species reach an equilibrium state with nearly equal temperatures. At $t = 100$ ms, realistic conditions are established by switching on the heating for the barium isotopes and the Alexa Fluor 350 ions (with heating rates of $k_B(11.47\ \mathrm{K/s})$ and $k_B(25.14\ \mathrm{K/s})$, respectively). Their temperatures increase above the $^{138}Ba^+$ temperature, which in turn causes a sympathetic heating of the $^{138}Ba^+$ ions. Finally, the whole ensemble reaches an equilibrium state with stable, but species-dependent temperatures, i.e. temperature

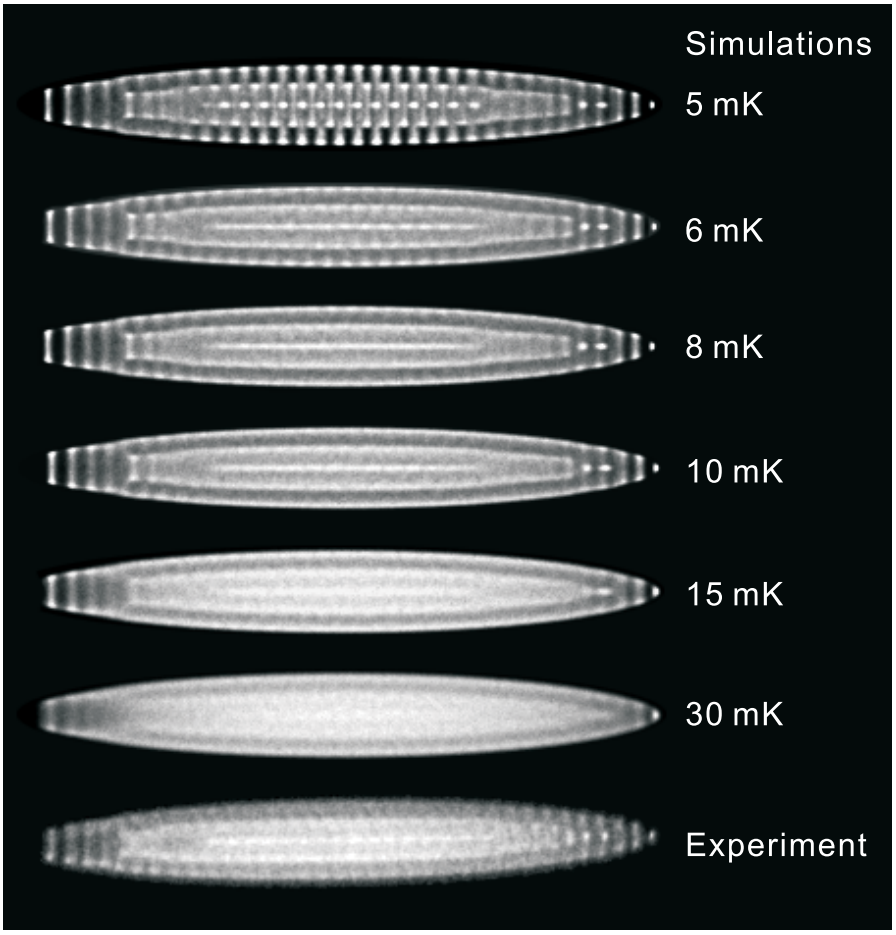

Figure 9.18: Temperature determination of laser-cooled ions. A series of simulated ion crystals at different temperatures is compared to the experimental CCD image (bottom, same as Fig. 9.15). The best agreement is achieved for a temperature of about 6 mK.

gradients are present.

9.7.3 Temperature determination of laser-cooled ions

In order to determine the temperature of the laser-cooled ions, a series of ion crystals at different temperatures is simulated and visually compared with the experimental CCD image. Due to scattered light and the limited resolution of our imaging system the experimental CCD images look blurred. Thus, the crystals appear warmer than they actually are. There are, however, details in the crystal structure, which are used to find the closest temperature. In Fig. 9.18, for example, the experimental image of a beryllium crystal (lowermost image) shows two concentric ellipsoidal shells with a string in the middle. The string displays discrete spots which are, comparing with the simulated images above, only visible for temperatures lower than 8 mK. But, these spots are not as distinct as in the simulated image at 5 mK. Thus, the best fit is achieved for a temperature of 6 mK.

As discussed above, these discrete spots usually do not correspond to single or individual ions, but to a high probability density for ions at a certain location during the

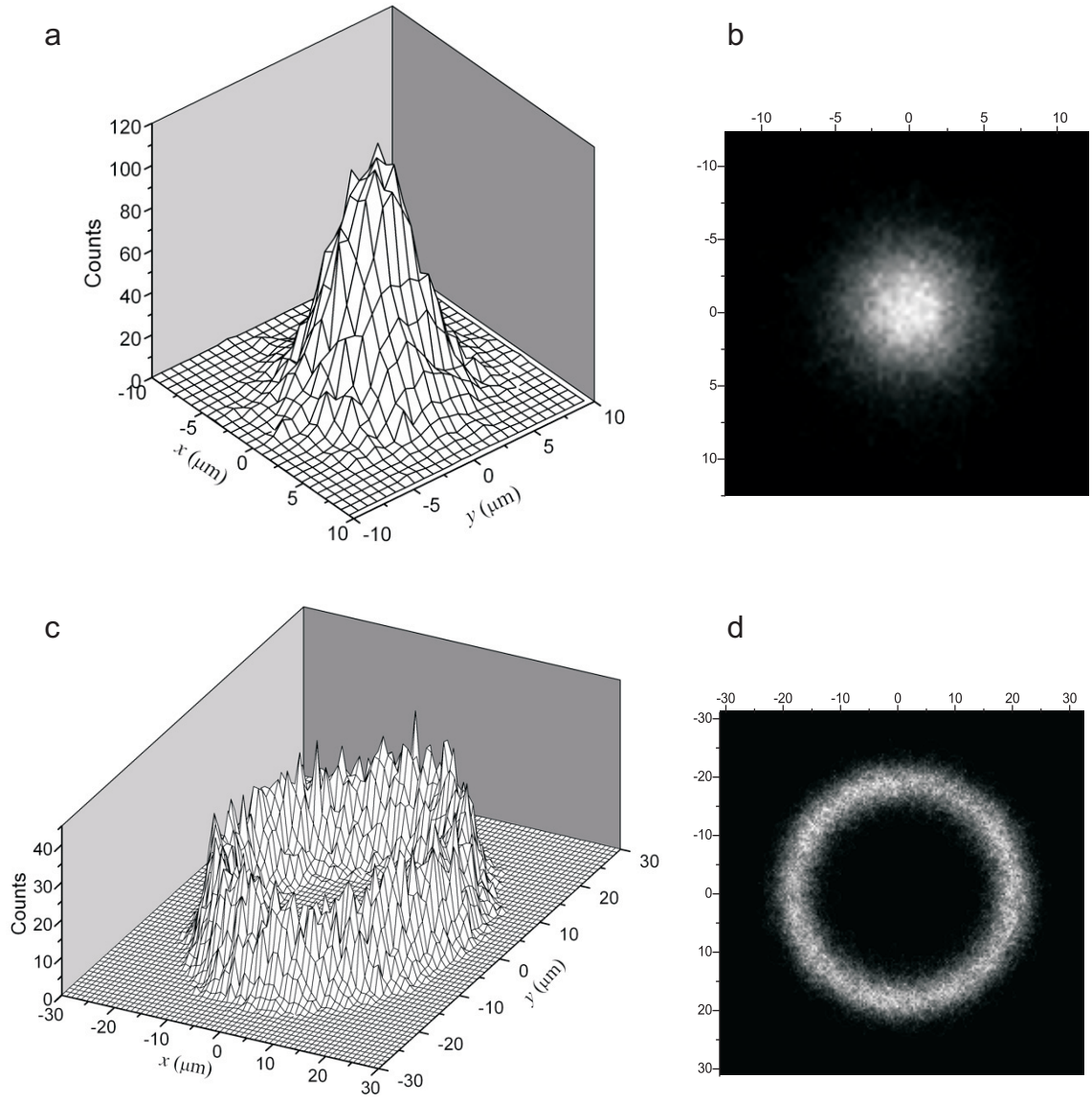

Figure 9.19: Probability density of ion trajectories within particular slices $(z_0 - \Delta z, z_0 + \Delta z)$ of the crystal. (a) for the right end spot and (b) image mode of (a). (c) for the two neighboring spots of the beryllium crystal in Fig. 9.15 ($T_{sec} = 6$ mK). (d) image mode of (c). The simulation time is 200000 time steps of 50 ns.

exposure time, except for special sites and very low temperature.

In contrast to the experiment, in the simulations one can image ion crystals from any direction and with arbitrary magnification. Even specific sites of the crystals can be studied in detail. For example, Fig. 9.19(a) shows the spatial radial distribution of the spot at the right end of the beryllium crystal shown in Fig. 9.15. The spatial distribution has a Gaussian shape and a full width at half maximum of 6 μm. Fig. 9.19(b) shows the spatial distribution of the neighboring two spots. They cannot be ascribed to two ions, but to an average of three ions moving diffusively and due to residual rotation of the crystal around the z-axis.

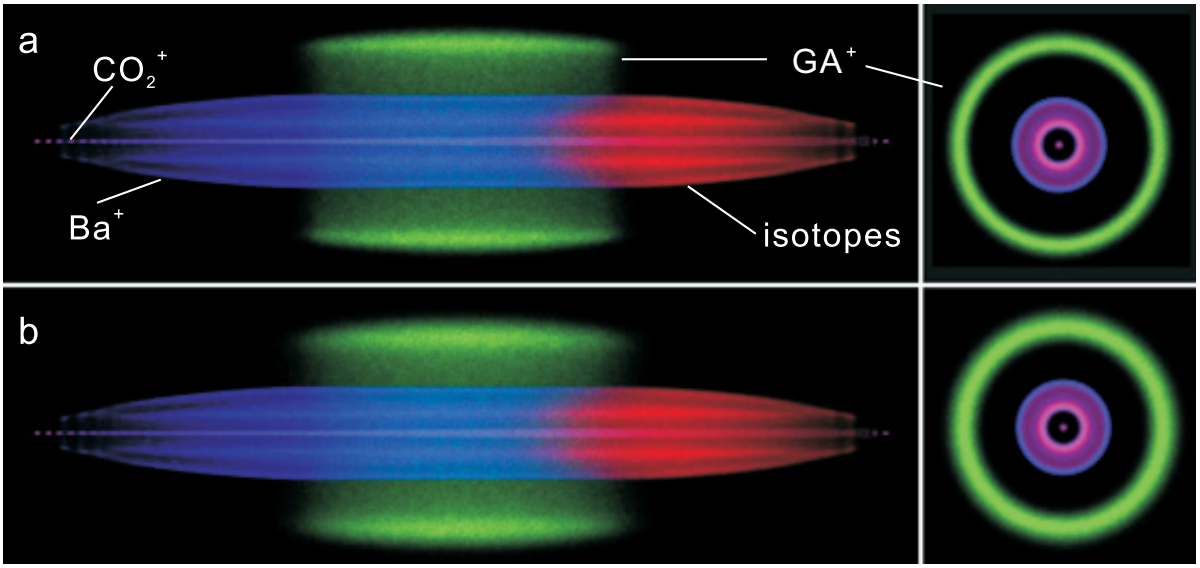

Figure 9.20: Temperature determination of sympathetically cooled ions. If a higher laser cooling rate is used in the simulations (b), the heating rate of the laser-cooled ions was increased so as to keep the same temperature in (a) and the heating rate of the sympathetically cooled ions was increased as well. Finally, one obtains higher temperatures for the sympathetically cooled species (green) than in (a) (the GA^+ molecular ions have a broader distribution).

9.7.4 Temperature determination of sympathetically cooled ions

The temperature of sympathetically cooled ions cannot be determined as described above, because they do not fluoresce and are therefore invisible to the CCD camera. In order to find their temperature, two CCD images are required. One is taken when the laser-cooled and the sympathetically cooled ions are trapped together, the other is taken when there are only the laser-cooled ions, i.e. before loading or after extracting the sympathetically cooled ions. The temperature of both ion ensembles is different, as the heating rate h_{sc} of the sympathetically cooled ions acts as an additional heating source for all ions. By simulating the CCD image of the pure laser-cooled ion ensemble its heating rate h_{lc} is found. In the simulation of the whole ensemble h_{lc} is kept constant for the laser-cooled species. Then, the heating rate h_{sc} for the sympathetically cooled species is varied in order to heat the laser-cooled ion ensemble to the observed temperature. When the right parameters are found, the temperature of the sympathetically cooled ions can be obtained from the simulation data.

In principle, a specific temperature of a laser-cooled ion ensemble can be achieved with a continuous set of pairs of appropriate laser-cooling and heating rates. The simulated temperature of the sympathetically cooled ion ensemble strongly depends on the actual laser cooling rate. When a higher laser cooling rate is applied, the heating rates for all involved species need to be increased in order to keep the temperature of the laser-cooled ion ensemble constant at the observed level. However, this leads to a higher temperature of the sympathetically cooled ions as illustrated in the following example: Fig. 9.20 shows a four-species ion crystal consisting of 700 laser-cooled barium ions (blue, 138 amu), 300 barium isotope ions (red, 137 amu), 100 CO_2^+ ions (pink, 44 amu), and 200

singly protonated glycyrrhetinic acid molecules (denoted as GA^+, green, 470 amu). In case (a), the friction coefficient β is set to 1×10^{-22} kg/s. To keep the crystal at 20 mK, the corresponding heating rate for barium ions and isotopes is $\approx k_B(5.94$ K/s). After loading the GA^+ ions, we set their heating rate to $\approx k_B(8.25$ K/s), which heats the barium ion ensemble to 25.6 mK. The temperature of the GA^+ ion ensemble in this equilibrium state is ≈ 130 mK. In case (b), a higher friction coefficient $\beta = 4 \times 10^{-22}$ kg/s is set. To heat the barium ion ensemble to the same 20 mK and 25.6 mK values, higher heating rates are required: $\approx k_B(23.9$ K/s) for the barium ions and $\approx k_B(33.6$ K/s) for the GA^+ ions. Here, the final equilibrium temperature of the GA^+ ions ensemble is ≈ 300 mK.

Thus, in order to obtain a concrete temperature value for the sympathetically cooled ion ensemble, the friction coefficient needs to be determined independently. From laser cooling theory

$$\beta = 2 \sum_i \frac{\hbar k_i^2}{2} \Gamma_i \frac{\partial \rho_e}{\partial \Delta_i}|_{\Delta_i}. \tag{9.29}$$

The wavenumbers k_i and partial decay rates Γ_i for the laser transitions are constants, whilst the change in the excited state population ρ_e with laser detunings Δ_i is calculated from 8-level Bloch equations using our measured laser saturation parameters and detunings [127]. The value for $^{138}Ba^+$ in our experiments was determined to $\approx 1.75 \times 10^{-22}$ kg/s in good agreement with [128].

9.8 Advanced cooling of complex molecular ions

Sympathetic cooling in a Paul trap is most efficient for species with similar mass-to-charge ratio, as their radial separation is small.

In one of our experiments, we used laser-cooled $^{138}Ba^+$ ions to sympathetically cool complex molecular ions with masses of several hundred amu produced with an electrospray ion source [89]. Here, the efficiency of sympathetic cooling is relatively low due to the high radial separation of the ion species and the difference between the temperatures of the species is substantial, as discussed above. A possibility to enhance the sympathetic cooling is the reduction of the mass-to-charge ratio difference, which can be realized by using multiply protonated molecules from the electrospray ionization source. Another option is to raise the trap voltage so as to increase the radial confinement of all ions. However, higher trap voltages also cause a higher rf heating [94, 100]. Yet another possibility is a reduction of the total ion number, in order to reduce the repulsive forces between the ion species.

A different approach is to add a (sympathetically cooled) intermediate species layer between the laser-cooled and the sympathetically cooled ions, see Fig. 9.21. This layer acts as a "conducting layer" and helps to transfer the energy from the sympathetically cooled ions of interest to the laser-cooled ions. Such ions of intermediate mass may be loaded into the trap deliberately or they may be produced by photodissociation of the molecular ions. Fig. 9.22 shows an example for the sympathetic cooling process, in which 200 Alexa Fluor 350 ions are sympathetically cooled by 1250 $^{138}Ba^+$ ions – with

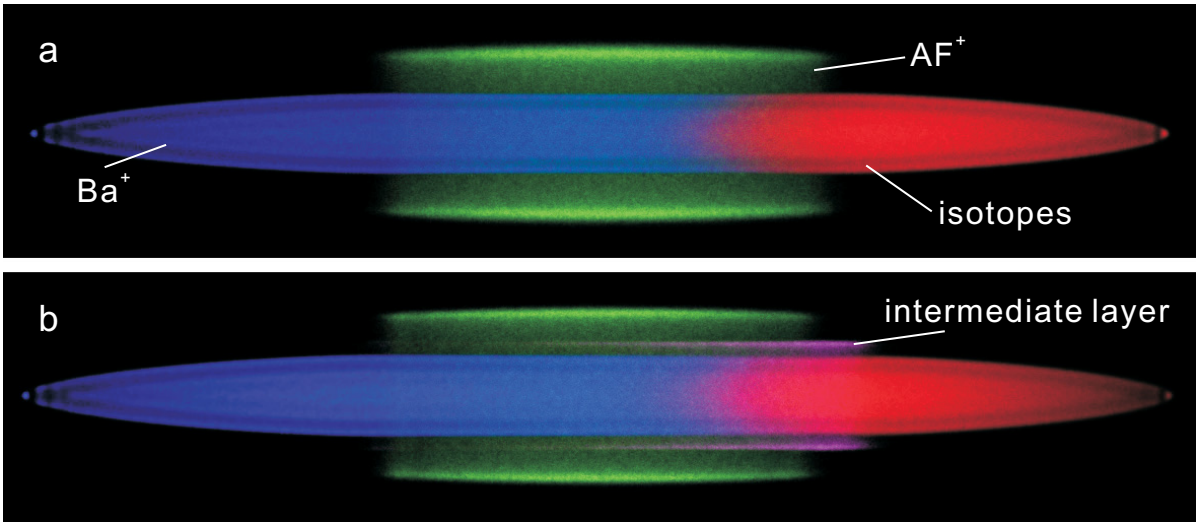

Figure 9.21: Sympathetic cooling in presence of an intermediate layer. The images show a multi-species ion ensemble consisting of barium ions (blue, 138 amu), Alexa Fluor 350 ions (green, 410 amu) and barium isotope ions (red, 137 amu) – (a) without and (b) with an intermediate species layer (pink, 200 amu), which helps to cool the Alexa Fluor 350 ions more efficiently.

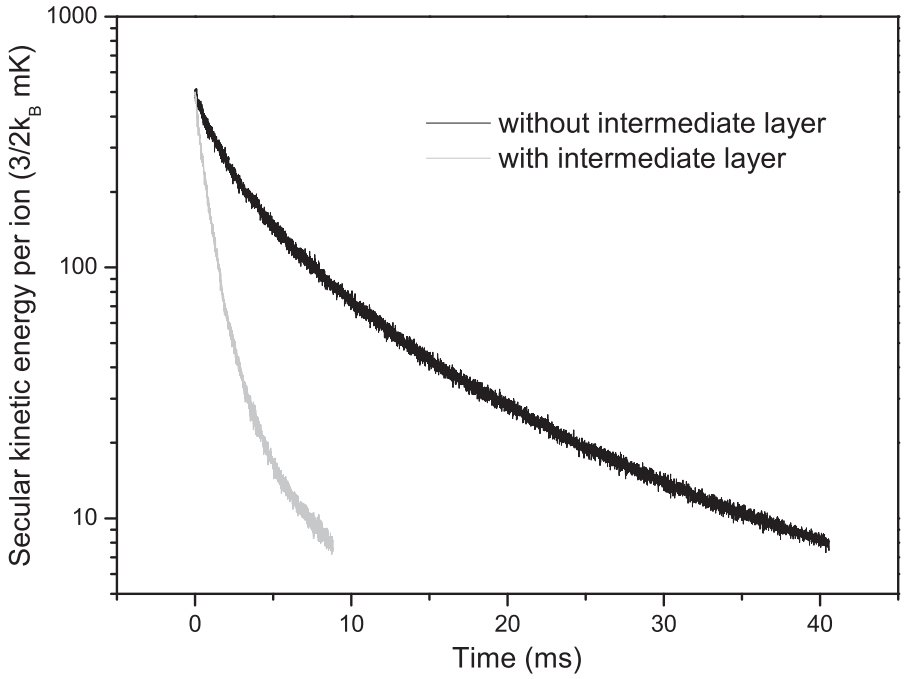

Figure 9.22: Sympathetic cooling with an intermediate layer. With an additional intermediate ion species (compare Fig. 9.21(b)) the sympathetic cooling of the Alexa Fluor 350 ions is much faster (grey) than without (black). Note that in this case no heating was applied to the Alexa Fluor 350 ions and they would consequently reach the same temperature with or without intermediate layer.

and without intermediate layer. Initially, the barium ions are kept at very low temperature (< 3 mK) by applying a high cooling rate ($\beta = 200 \times 10^{-22}$ kg/s), while the Alexa Fluor 350 ions are kept at about 490 mK. Then, the heating for the Alexa Fluor 350 ions is turned off and their temperature decreases due to sympathetic cooling. It takes about 40.6 ms to cool them to ≈ 8 mK, but only 8.8 ms when 50 ions with an intermediate mass (200 amu) are added. Thus, the sympathetic cooling rate can be substantially increased.

Under realistic conditions (heating effects present), the final temperature of the sympathetically cooled ions can be significantly lower with the intermediate species layer. For the case shown in Fig. 9.21, 200 Alexa Fluor 350 ions are sympathetically cooled by 830 $^{138}Ba^{+}$ ions. With an intermediate layer (50 ions, 200 amu), the final temperature of the Alexa Fluor 350 ions is reduced from ≈ 114 mK to ≈ 58 mK (see Fig. 9.21(b)).

9.9 Micromotion effect

Our simulations are a useful tool for the interpretation of experiments with sympathetically cooled molecules. For the determination of ion numbers and temperatures or the simulation of ion crystal structures and secular excitation spectra it is not necessary to include the micromotion in the simulations. To save computing time we solve Newton's equations of motion in the pseudopotential approximation. However, there are some aspects related to micromotion, which cannot be neglected and are considered in the following.

An aspect of relevance for high-resolution spectroscopy is a possible direct coupling of radial micromotion to the axial direction which would lead to the appearance of motional sidebands in the spectrum and thus a loss of spectral resolution. To study this effect, a barium ion from a cold ion ensemble (830 $^{138}Ba^{+}$ ions, 420 barium isotope ions, and 200 Alexa Fluor 350 ions) was randomly selected and its axial position $z(t)$, one component of the radial position $x(t)$, and its axial velocity $v_z(t)$ were recorded (see Fig. 9.23). The solid curve $x(t)$ clearly shows the slow radial secular oscillation (≈ 40 kHz) with the superimposed fast micromotion at the rf driving frequency of 2.5 MHz (see inset). There is no apparent rf oscillation in the axial motion $z(t)$ (dashed curve) and the axial velocity $v_z(t)$ (dotted curve). Thus, we find that under the typical conditions considered here (small q parameter, as evidenced by the small amplitude of the micromotion compared to the average radial distance), the micromotion in radial direction does not couple to the axial direction. Nevertheless, at much higher secular temperature, the micromotion causes an increase of the secular energy of both radial and axial motions. The only possibility for an energy transfer of micromotion to the axial motion is an indirect coupling via rf heated ions which distribute their kinetic energy to the axial direction through the thermalization process.

Finally, we have studied the influence of the micromotion on the simulated images. Fig. 9.24 compares structural details of an ion ensemble consisting of 500 $^{138}Ba^{+}$ ions at $T_{sec} = 12$ mK in the pseudopotential approximation (c, e and g) and including the micromotion (a, b, d and f).

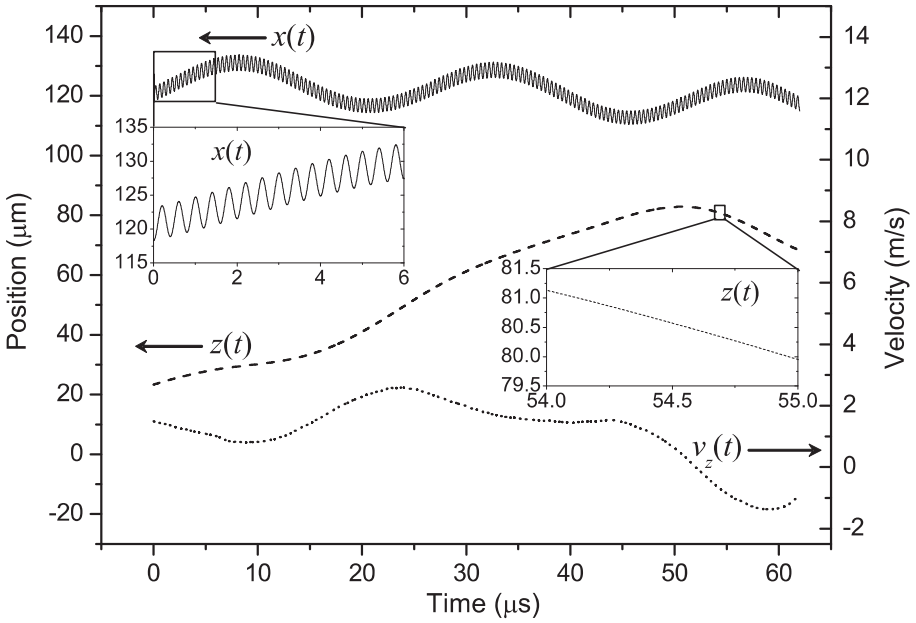

Figure 9.23: Micromotion of an individual ion within an ensemble. In a simulation including micromotion the x-component of the motion clearly shows the fast micromotion (solid curve, the inset is a magnification). The z-component of the motion and the velocity (dashed and dotted curve) do not show any effect of micromotion. The secular temperature of the barium ion ensemble was ≈ 30 mK.

If the ions are close to the x- or y-axis, their micromotion is parallel to the corresponding axis. This is shown in (d) for a simulated time which is long enough to reproduce the experimental images, and - just for demonstration - in (f) for an unrealistic, much shorter simulated time where this effect is more obvious. The ions' motional amplitude is the larger, the further away they are from the trap center (z-axis). Image (a) is taken along the x-axis, so the center is dominated by ions moving perpendicularly to the image plane without a visible effect. The outer two shells are dominated by ions moving up and down in the image plane, so they appear blurred. However, the relevant radial line of sight for the CCD camera is between the electrodes as shown in (b). Here, the blurring is weaker and homogeneous (compare with image (d)).

In general, the images from simulations including micromotion appear more blurred than those from simulations in the pseudopotential. But due to the limited resolution of our imaging systems, this weak effect is not visible in our CCD images. It is an open question whether a higher resolution imaging system could resolve the micromotion details.

9.10 Ion diffusion

In Fig. 9.14 we showed a trajectory of a barium ion. Although that barium crystal is evolving at a very low temperature of about 6 mK, this trajectory tells us that each ion does not stay at a specific lattice point all the time. They diffuse randomly. It is evident that the activity of a ion diffusion depends on the temperature of the ion species, since

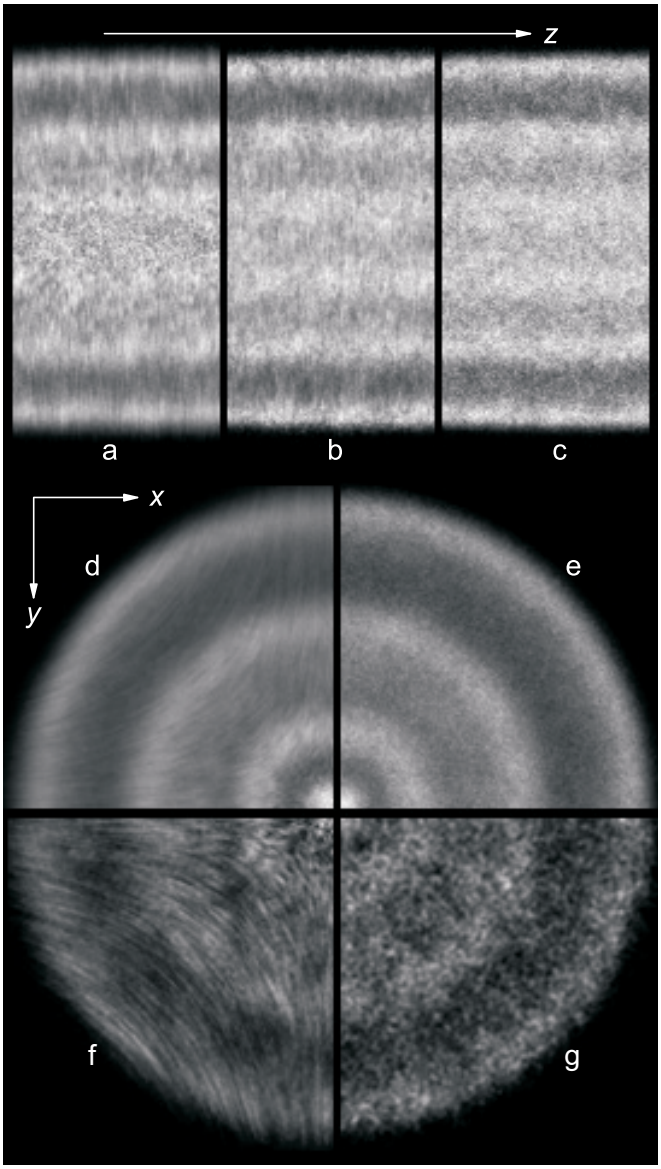

Figure 9.24: Micromotion in simulated images. Here, sections from simulated images of a cold ensemble consisting of 500 barium ions are shown - simulated including micromotion (a, b, d and f) and in the pseudopotential approximation (c, e and g). (d) - (g) show sections of axial views, (a) - (c) sections of radial views, while (a) is a view along the x-axis and (b) and (c) correspond to the line of sight of the CCD camera (at 45° to the x- and y-axis). In fact, as the pseudopotential is radially symmetric, (c) shows the view along any angle perpendicular to the axial direction. (f) and (g) show the same as (d) and (e) but for a 20 times shorter simulated time of 0.5 ms in order to highlight the different nature of images from simulations with and without micromotion.

the crystal structure washes out with the temperature increase. Here, we consider the relationship with the crystal structure. As a first case, we consider 200 $^9Be^+$ ions and 30 HD^+ ions in the trap. Here, the HD^+ ions stay along the trap axis in a line and the beryllium ions sit around the HD^+ string. This ion system is heated to about 48

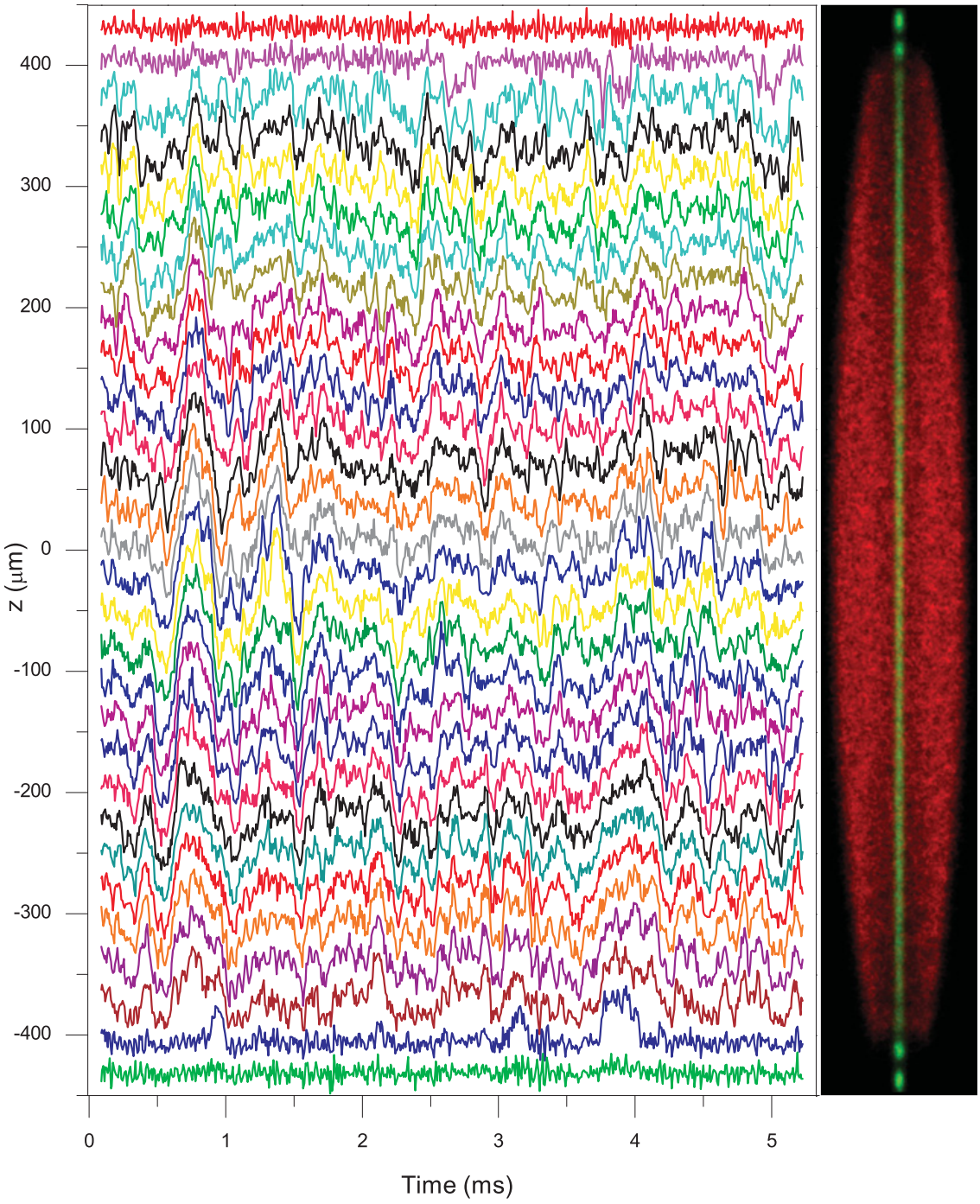

Figure 9.25: z coordinates of 30 HD^+ ions as a function of time. The image at the right side is the simulated image of the ion ensemble containing 200 $^9Be^+$ ions and 30 HD^+ ions at about 48 mK. These 30 HD^+ ions align as a string. The trajectories show that although the HD^+ ions are quite active, they stay in order and no ions exchange there positions.

mK slowly. Then the z coordinate of each HD^+ ion is monitored for more than 5 ms as shown in Fig. 9.25. Although sometimes the ions drift a lot (in groups, and by more than the next-neighbor distance), no position exchange happens. As a second case, we add another 30 HD^+ ions into the ion trap and let the ion system evolve at 8.5 mK.

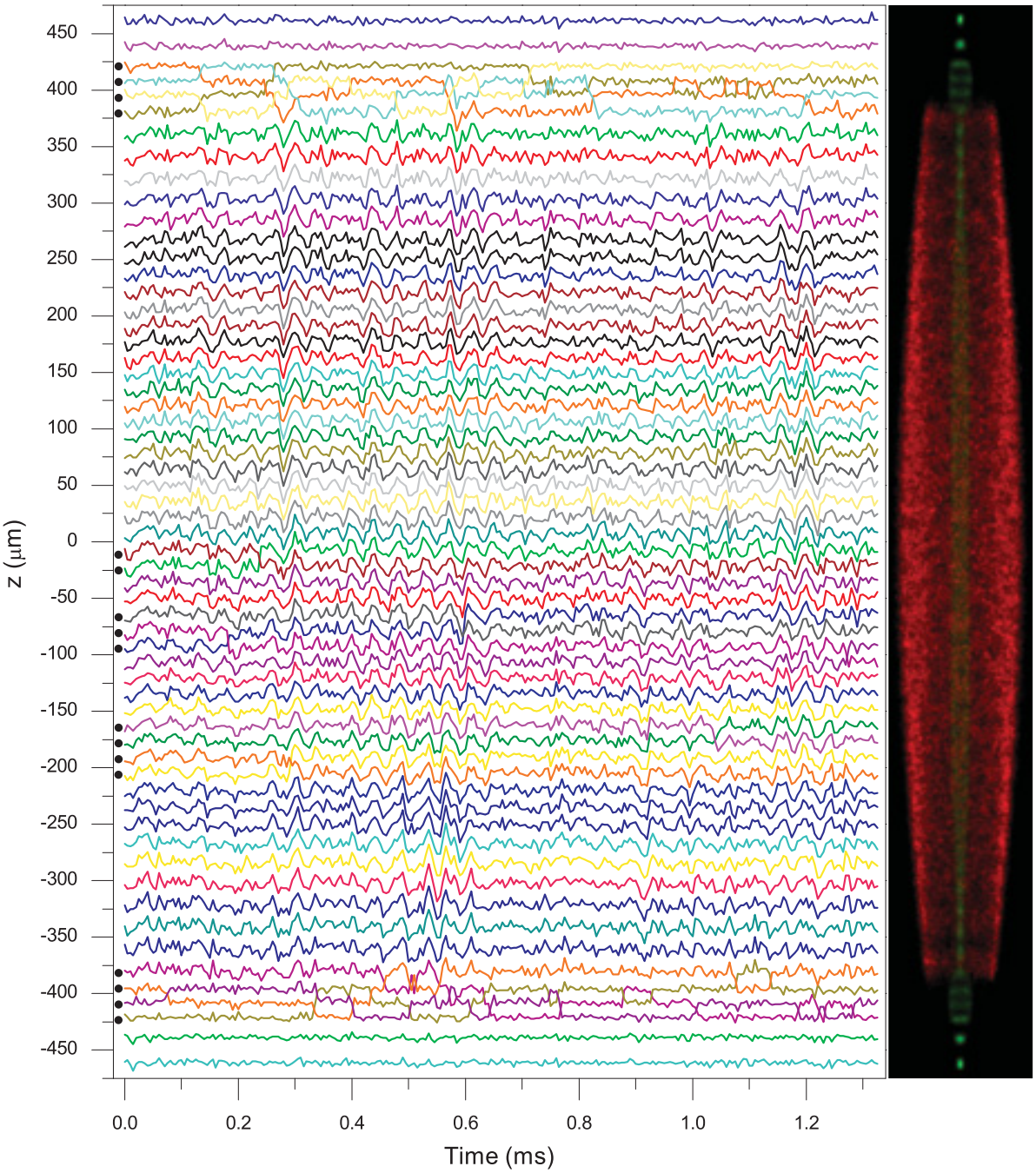

Figure 9.26: z coordinates of 60 HD^+ ions as a function of time. The image at the right side is the simulated image of the ion ensemble containing 200 $^9Be^+$ ions and 60 HD^+ ions at about 8.5 mK. Some parts of the HD^+ ion ensemble have a two-layer structure, where the position exchange among ions occur. The ions that exchanged their positions are marked by black dots on the left side.

The z coordinate of each HD^+ ion is shown in Fig. 9.26. Some parts of the HD^+ ion ensemble have a two-layer structure (see the left image in Fig. 9.25). Ions at these parts have a high possibility of exchanging positions. However, the ions at the end of the ion ensemble do not fluctuate too much. They are very stable. This is also indicated in

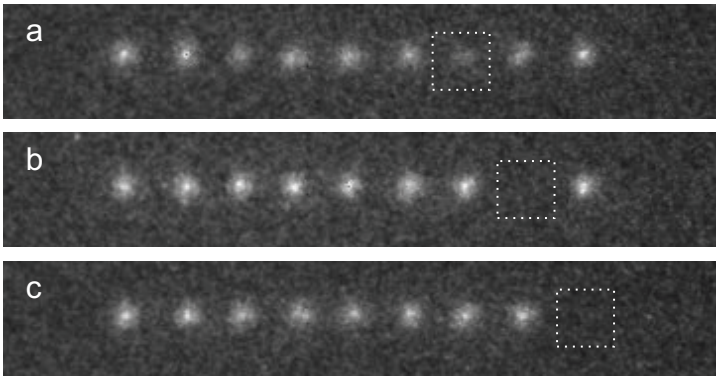

Figure 9.27: Barium ion diffusions due to the collisions with residual gas observed experimentally. Since the ion chain is colder than 50 mK, ions should move around their crystal lattice spots. Here, jumps of a dark crystal lattice spot (occupied by a non-fluorescing barium isotope ion) are observed. In (a) the framed lattice is weaker than others. The explanation is that in the integration time of our ICCD camera (2 s) this lattice was occupied by one or two or even more different laser-cooled ions temporally.

many of our CCD images - these single spots are always the last ones to be washed out, when the temperature increases.

Usually, in simulations we only model mild velocity kicks as a heating source, these kicks are not strong enough to make position exchanges among ions at very low temperatures. However, the collisions of the ions with the residual gas molecules are very strong and the ions can gain enough energy to make position exchanges occasionally. In the experiment, in a cold barium chain these position exchanges have been observed by jumps of dark lattice spots (barium isotopes) as shown in Fig. 9.27. In a background gas of N_2 at the pressure of 1×10^{-9} mbar, the collision rate for this ion ensemble is about 0.153 s^{-1}. Without collisions at such a low temperature (less than 50 mK) the kinetic energies of these barium ions are not high enough to exchange positions. They should move around their crystal lattice spots.

9.11 Conclusion

In this chapter, basic approach of molecular dynamics simulation is briefly introduced. Time scales and trap settings fitting our linear Paul traps (one is for barium experiment and the other one is for beryllium experiment) are represented. Heating and cooling models, as well as the initialization of ion ensembles, are described. In our simulations, Newton's equations of motion for all trapped ions are solved for the exact rf trap potential as well as in the rf averaged pseudopotential approximation to investigate the influence of rf micromotion. It shows that rf micromotion does not change the simulated (long time exposure) images of ion crystals and does not lead to strong rf heating effects for ion crystals at secular temperatures below 100 mK. Thus, simulations in the pseudopotential approximation with their much shorter computing times can be used to reproduce and interpret experimental data.

Several applications of our simulation model are shown. It can be used to extract temperatures and numbers of laser-cooled and sympathetically cooled ions from experimental CCD images of ion crystals. It also allows detailed studies of the sympathetic cooling process which helps to understand and improve our experimental work. Furthermore, ion diffusions are studied here as well.

10 Simulation of secular excitation spectra

10.1 Introduction

The motion of individual, isolated ions in a linear Paul trap is characterized by two secular frequencies, an axial and a radial frequency, as expressed in Eq. (2.15) and (2.36). Therefore, the ions can be excited resonantly at either of these two frequencies [129, 130, 131, 132, 37]. This excitation is done electrically and the easiest way is to use an external electrode with a sine voltage applied to it. In most cases, the electric circuit is connected to the electrodes in the same way as the rf circuit, and the excitation is then a quadrupole excitation [130]. On the other hand, when only two electrodes are connected, the excitation is a dipole excitation. The axial electrical excitation in linear Paul trap is always a dipole excitation with a voltage applied to the endcap electrodes at one end and another one with an opposite phase to the other end. In this chapter, in all the simulations a dipole excitation is assumed, which is close to our experiment (the amplitude of the rf voltage on the two middle top electrodes is modulated).

Actually, this problem is just concerned with the driven oscillator such as LC circuits. The equation of motions has the form

$$m\ddot{x} + m\omega_x^2 = QV_{external}e^{i\omega t} = F_0 e^{i\omega t}, \tag{10.1}$$

here m and Q are the mass and charge of an ion, respectively. $V_{external}$ is the amplitude of the excitation voltage. $QV_{external}$ is denoted by F_0. ω is the excitation frequency. The solution for this equation can be found in many physics books and the amplitude of the oscillation in steady state is given here as

$$x_0 = \left| \frac{F_0}{m(\omega_0^2 - \omega^2)} \right|. \tag{10.2}$$

Confined ions gain significant energy from the excitation field at resonance conditions. Either a long excitation time or a high excitation amplitude can cause a loss of ions (ions can be kicked out of the trap and most of them are lost on the electrodes). When the ions are excited at frequencies away from resonance, they oscillate with a low amplitude, which is determined by the amplitude of the excitation and its frequency. To demonstrate this, a simulation is performed with an ion ensemble containing 1000 barium ions, which was excited at its resonance frequency (about 100 kHz) and at two other frequencies (98 and 95 kHz) in the x-direction, as shown in Fig. 10.1(b), (c), and (d). This ion ensemble is initially released from a start point (0, 200 μm, 0) at rest. Thus, the restoring force towards the trap center makes it oscillate harmonically like a pendulum along the y-direction with the radial secular frequency of ω_y. The trajectory of the center-of-mass is plotted in Fig. 10.1(a). No oscillation occurs in the x-direction and the oscillations along the x- and y-directions are independent. In the simulation

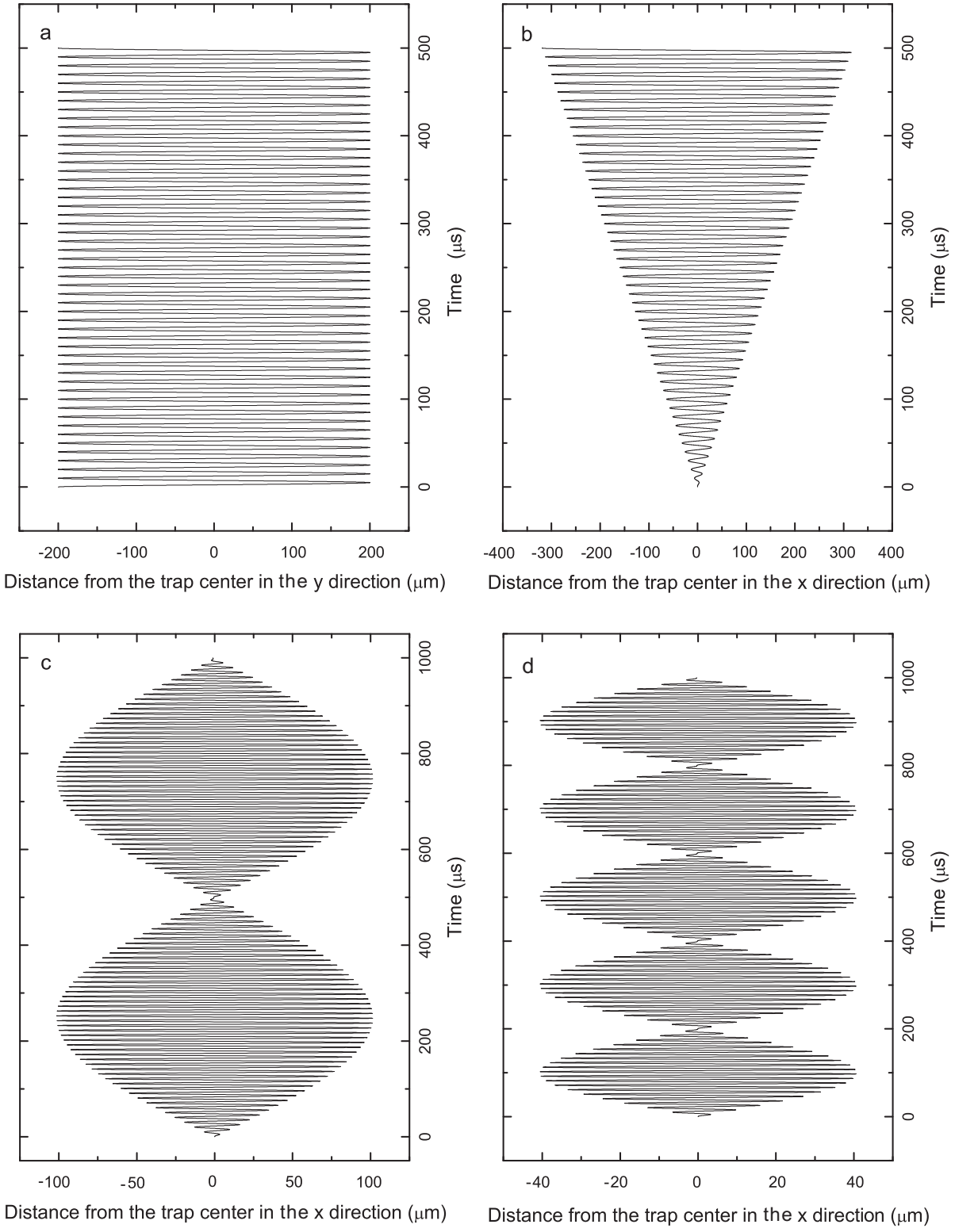

Figure 10.1: Center-of-mass positions of a barium ion ensemble with different radial excitation frequencies. (a) The ion ensemble oscillates freely in y-direction with the radial secular frequency. (b) The ion ensemble is excited in x-direction at its resonance frequency (the radial secular frequency, 100 kHz). (c) Excited in x-direction at 98 kHz. (d) Excited in x-direction at 95 kHz.

when this ion ensemble is excited at its resonance frequency (100 kHz) with about 10 mV excitation voltage along the x-direction, its oscillation amplitude in x-direction increases linearly, as shown in Fig. 10.1(b). The bigger the offset from the resonance frequency, the more smaller oscillation amplitude. Meantime the oscillation along the y-direction is the same as shown in Fig. 10.1(a). If we excite the ion ensemble at 98 or 95 kHz, it stays relatively undisturbed in the trap as shown in Fig. 10.1(c), and (d)). The beats in Fig. 10.1(c), and (d)) arise from the initial conditions (the position and velocity).

Thus, by controlling of the parameters of the excitation this technique can be used in many aspects [37]. In our case, we are interested in two main aspects.

- Removal of the unwanted ion species. For example, as described in the Chapter 5, 6, 7, and 8, when the barium ions are loaded from the oven, some light ions like CO_2^+ are trapped as well. Since these ions keep the barium ions hot, they need to be removed. This is done with a secular excitation with the frequency sweep covering the resonance frequencies of the light ions only. The amplitude of the excitation field is a few hundred mV at least, while the frequency scanning time is a few seconds.

- Identification of the ion species. The excitation by a frequency sweep covering a broad range with a low excitation amplitude can strongly heat up the ion species at their resonance frequencies in a short time. The laser-cooled ion ensemble can be heated directly at its own resonance frequency. When other ion ensembles are heated up at their own resonance frequencies, a part of the gained energy is transferred to the laser-cooled ion species via the Coulomb interaction. Therefore, the secular excitation at any resonance secular frequency of the ion species in the trap can rise the temperature of the laser-cooled ion species, which results in a Doppler shift. The reduction of the laser cooling efficiency is represented by a drop of the laser-induced fluorescence intensity. When the excitation frequency is swept over the resonance frequency, the gained energy is extracted by the cooling lasers again and the intensity of fluorescence returns to the previous level. Therefore, if the intensity of the fluorescence is monitored, dips occur on the fluorescence curve, consistent with the resonance frequency of each ion species. Fig. 5.4 shows a secular excitation spectrum of a cold pure barium ion ensemble. If the ion ensembles become too hot, due to the excitation, the Doppler shift of the laser-cooled ions will be far away from the cooling laser frequency: the Doppler broadenings of a barium ion ensemble at 10 mK are about 3.7 and 2.8 MHz at the wavelengths of 493 and 650 nm, respectively, while at a temperature of 10 K the broadenings increase to 117.2 and 88.9 MHz correspondingly. Then, the ion ensemble will stay hot or will be cooled down again very slowly, since the excitation frequency is out of the resonance. In this case, a step or a broad dip occur on the fluorescence intensity curve.

  Actually, in the experiment the monitored rf voltage is not the exact value acting on the trap electrodes, so it needs to be calibrated. Since the secular frequency of a pure barium ion ensemble should be close to the calculated value for a single barium ion, the experimental value can be used to calibrate the rf voltage.

In this chapter, we only focus on the second aspect.

10.2 Model for the secular excitation

All the ion species in the ion trap have their own secular frequencies (see Eq. (2.15) and (2.36)). However, in the presence of other ions, the characteristic frequencies are shifted and broadened due to the strong space charge effects. Thus, it is necessary to simulate their characteristic secular frequencies in a specific ion system. A simple way to simulate the coupled secular frequencies is to give a small disturbance to an equilibrium ion system and to record the trajectory of the system. The trajectory includes the information about the secular frequencies of all ion species, which can be extracted via a fast Fourier transformation (FFT). The disturbance can be realized through a displacement of the ion ensemble by several μm in the radial or axial direction (the direction depends on which kind of spectrum we study) or by applying an additional small force (by an AC or DC voltage) to the ions for a short period of time. In order to speed up the computation of the FFT spectrum (using the base-2 logarithm), a power of two computation time steps is used. In our case, we usually record 32768 data points. Fig. 10.2 shows an example. Each peak corresponds to a resonance frequency or a coupling frequency. The details of Fig. 10.2 will be explained in the following section.

10.3 Space charge effects

Generally, for an ion ensemble, we take the motional frequency of a single ion in a harmonic trap as the resonance frequency. Actually, when there are more than one ion in the ion trap, beside the harmonic trap potential, each ion is affected by the Coulomb potential from all others. This is called space charge effect. A large ion crystal has a bigger volume and the space charge effects are strong. Thus, the pseudopotential well for particle i (Eq. (2.39)) is modified

$$\psi_i(x,y,z) = \frac{eV_0^2}{m\Omega^2 r_0^4}(x^2+y^2) + \frac{\kappa V_{ec}}{2z_0^2}\left(2z^2-x^2-y^2\right) + \frac{Q_i}{4\pi\varepsilon_0}\sum_{j=1,j\neq i}^{j=N}\frac{Q_j}{r_{ij}}. \tag{10.3}$$

The secular frequency on a specific ion depends on the instantaneous position of the ion. For huge ion systems, many ions are pushed further away from the trap center, so the external trap potentials acting on these particles are no longer treated as perfect harmonic. In this case, the space charge effects are very important. In our experiments, only ion systems with less than 3000 ions are studied. The nonharmonic terms of the trap potential near the trap center are negligible. For cold, tiny, and single-species ion crystals, the couplings among these ions are very strong, thus, they move like a rigid body under a external field, so the calculated secular frequency for only one ion can still be taken as the resonance frequency of the whole crystal.

The model becomes much more complicated in the case of multi-component ion systems [133]. Normally, ion species with different mass-to-charge ratios are spatially strongly separated from each other, their motional modes are coupled, and the coupling strength depends on the temperature of the ion systems (and thus on its state: gas, fluid or crystalline)[134].

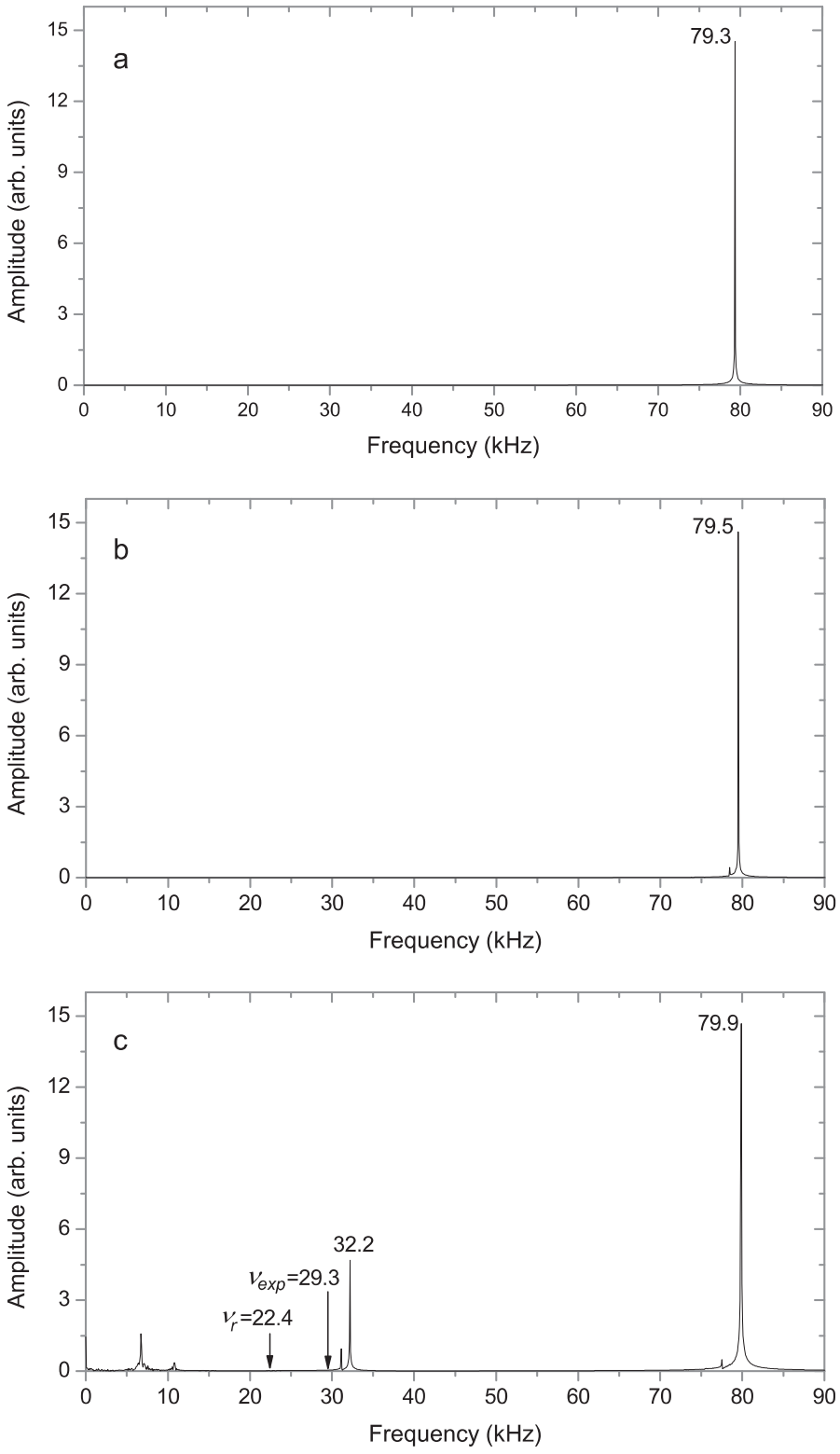

Figure 10.2: Simulated radial secular excitation spectra. For equal trap parameters ($q(^{138}Ba^+) = 0.091$) different crystal compositions were considered: (a) only $^{138}Ba^+$ ions, (b) $^{138}Ba^+$ ions and isotopes, (c) $^{138}Ba^+$ ions, isotopes and GA^+ molecular ions. In (c) ν_r indicates the calculated single-ion frequency for a GA^+ ion and ν_{exp} the experimentally determined value.

10.3.1 Weak coupling

In the high temperature regime (in the gas state) ions have a Gaussian spatial distribution. Thus, the force on one ion from all other ions is approximated by the interaction of the ion with a mean space charge field derived from a Gaussian charge density $\rho(R)$ field [135]. The corresponding electrostatic potential is

$$\varphi(x,y,z) = \int \frac{1}{4\pi\varepsilon_0} \frac{\rho(R')}{|\mathbf{R}-\mathbf{R}'|} d^3R', \tag{10.4}$$

where R is the distance from the trap center. The shape of the distribution is determined by the trap potential ψ given by Eq. 2.39. In an equilibrium state, the charge density is approximated by

$$\rho(R) = Qn(R) = Qn_0 e^{-Q\psi(R)/kT}, \tag{10.5}$$

where n_0 is the peak ion density for the cloud containing N ions and can be written as

$$n_0 = N\left(\frac{M}{2\pi kT}\right)^{3/2} \omega_r^2 \omega_z. \tag{10.6}$$

When the charge density is in a low range ($n_0 \leq 10^8$ ions·cm^{-3}), this approximation is accurate enough. Normally, space charge effects cause a resonance frequency red-shift. More details and examples are described in Ref. [135].

Qualitatively, the presence of other ions fills the bottom of the harmonic well and makes it shallower resulting in red-shift of the resonance frequency. The weak coupling is also studied in another experiment in our group which uses laser-cooled beryllium ions as the coolant [133].

10.3.2 Strong coupling

In our work, in most cases, all ion species are cooled down to a crystalline state, and our main goal is to investigate the properties of the sympathetically cooled ion species. Thus, our simulations focus on the strong coupling between the laser-cooled barium ions and sympathetically cooled complex molecular ions.

At low temperatures these ion species are spatially separated forming a concentric structure: heavier complex molecular ion species are located outside, as shown in the image of Fig. 9.20. The coupling of the ion species becomes very strong (a small oscillation of one ion species will drive all other species). The trap potential for each ion species is also strongly modified leading to large resonance frequency shifts. In this subsection the potential deformations are analyzed and the modifications on the resonance frequencies are described.

1D potential deformation

In a simplified picture, the potential change can be illustrated by comparing the ideal harmonic pseudopotential with the one modified by the space charge of the trapped ions.

In Fig. 10.3, for example, a cold ion crystal containing 1200 $^{138}Ba^+$ ions and 500 GA^+ molecular ions are considered. The effect of the GA^+ ions on the barium ion ensemble is shown in Fig. 10.3(a). The shape of the potential well is almost unchanged. There is only an offset to higher potential energies which does not influence the barium ions' secular frequency too much. However, as shown in Fig. 10.3(b), the presence of the barium ions causes a drastic change of the potential well for GA^+ ions. The harmonic pseudopotential is modified to a double well potential. These potential wells are steeper, so that the GA^+ ions have a higher secular frequency. To quantify this, we performed fits with harmonic functions to the wells. The asymmetric double wells can be described by the functions $y = 11.5 \cdot 10^{-8}(x-160)^2 + 0.006$ and $y = 6.3 \cdot 10^{-8}(x-160)^2 + 0.006$ for the outer part, while the potential for a single trapped GA^+ ion in absence of $^{138}Ba^+$ is described by $y = 3.9 \cdot 10^{-8}x^2$. Thus, the radial frequency of a GA^+ ion can be up to $\sqrt{11.5/3.9} = 1.7$ times higher than the one calculated with the single-ion formula, Eq. (2.15) and (2.36).

2D potential deformation

Now we consider the 2-dimensional case of the GA^+ ion ensemble (the same crystal as discussed in Fig. 10.3). Fig. 10.4(a) shows the modified trap potential well in the xy-plane, intersecting with the trap center. Supposing the AC excitation field is along the x-direction, a GA^+ ion located at a different place has a different modified potential well along the x-direction. The farther away from the x-axis, it is the lower the potential well is. For the GA^+ ions near the y-axis, no potential well exists, and on the other hand, the original potential well even becomes flatter resulting in the secular frequency being lower than the calculated value. Consequently, the calculated secular frequency splits into two broad frequency groups (see Fig. 10.6(c)), which are observed in our experiment. The modified potential well along the xz-plane is shown in Fig. 10.4(b).

Simulated secular frequency spectra are shown in Fig. 10.2 for different ion crystals with the same trap settings ($q(^{138}Ba^+)$=0.091) as a example. For a pure $^{138}Ba^+$ ion crystal (Fig. 10.2(a)) the simulated frequency $\nu_{sim} = 79.3$ kHz is consistent with the calculated single-ion frequency $\nu_r = 79.2$ kHz. In comparison, the spectrum of a crystal consisting of $^{138}Ba^+$ ions and isotopes (Fig. 10.2(b)) is not much different because the ion masses are quite similar. However, due to the coupling of the ions' oscillation modes there are additional small peaks beside the main peak, which is slightly shifted to a higher frequency of 77.5 kHz. Fig. 10.2(c) shows the excitation spectrum of an ion crystal containing barium ions with isotopes and GA^+ ions. The experimentally determined secular frequency of the GA^+ ions $\nu_{exp} = 29.3 \pm 1.3$ kHz differs substantially from the single-ion frequency $\nu_r = 22.4$ kHz, but is consistent with the simulated value $\nu_{sim} = 32.2$ kHz. The difference may be due to the dependency of the experimental frequency on the excitation amplitude in the experiment and the ion numbers.

The small additional peaks around 10 kHz in Fig. 10.2(c) are the resonance frequencies of the GA^+ ions further away from the x-axis. With our simplified excitation model, we cannot characterize in detail these additional coupling modes. This could be done by performing simulations with an additional homogeneous field oscillating at the respective

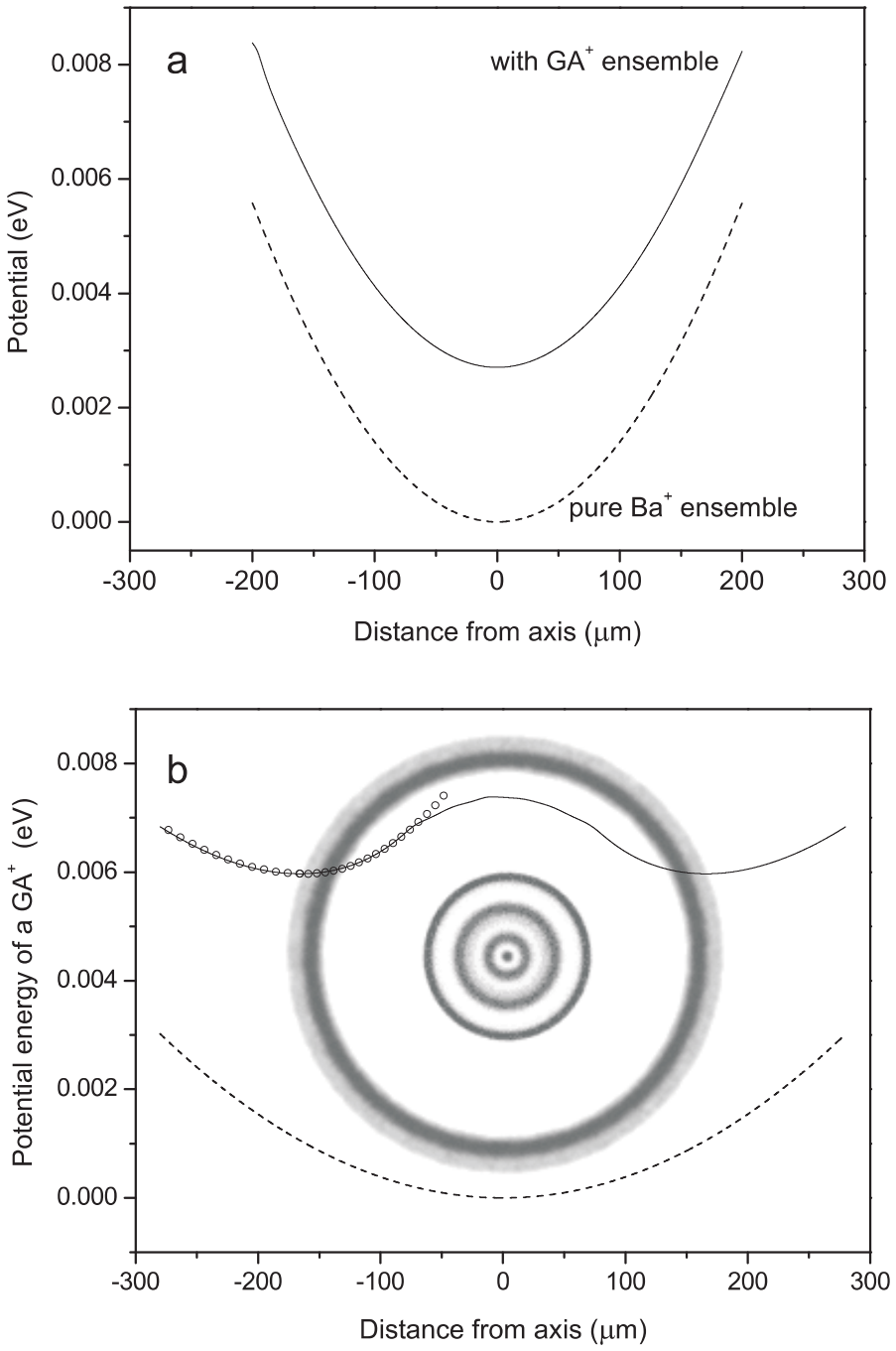

Figure 10.3: Space charge effects and trap potentials. Here, we consider a cold ion crystal containing 1200 $^{138}Ba^+$ ions and 500 GA^+ molecular ions. (a) Potential wells for a single barium ion in the ideal harmonic trap potential (dashed curve) and influenced by the space charge of heavier GA^+ ions (solid curve). (b) Potential well for a single GA^+ ion in the ideal harmonic trap potential (dashed curve) and double well potential caused by the barium ions (solid curve). Superimposed is an axial view of the considered ion crystal.

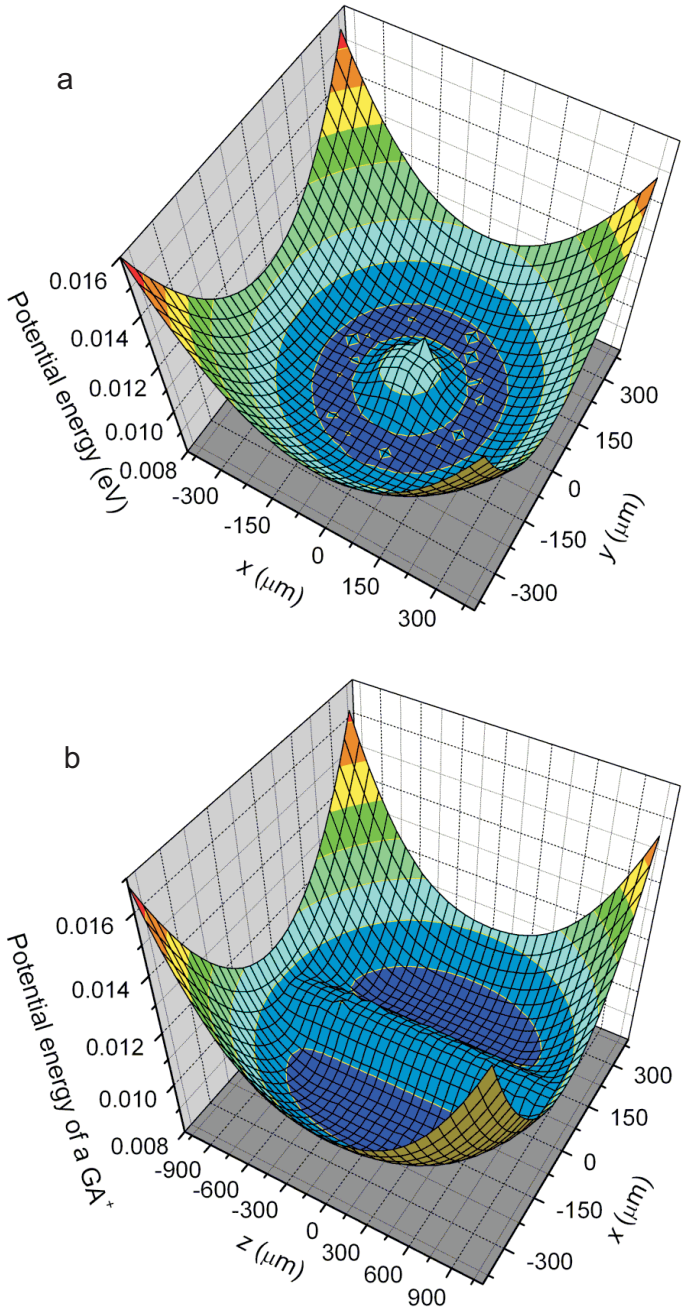

Figure 10.4: Modified 2-dimensional potential well for a GA^+ ion ensemble in the presence of 1000 barium ions and 500 GA^+ ions. (a) view is in the xy-plane. (b) View is in the xz-plane.

mode frequency found above and analyzing the amplitudes and phases of the forced oscillations of the individual species.

Effects of ion number

When the trap parameters are fixed, ion numbers determine the space charge distribution. Changing the number of one ion species the positions and shapes of all the ion

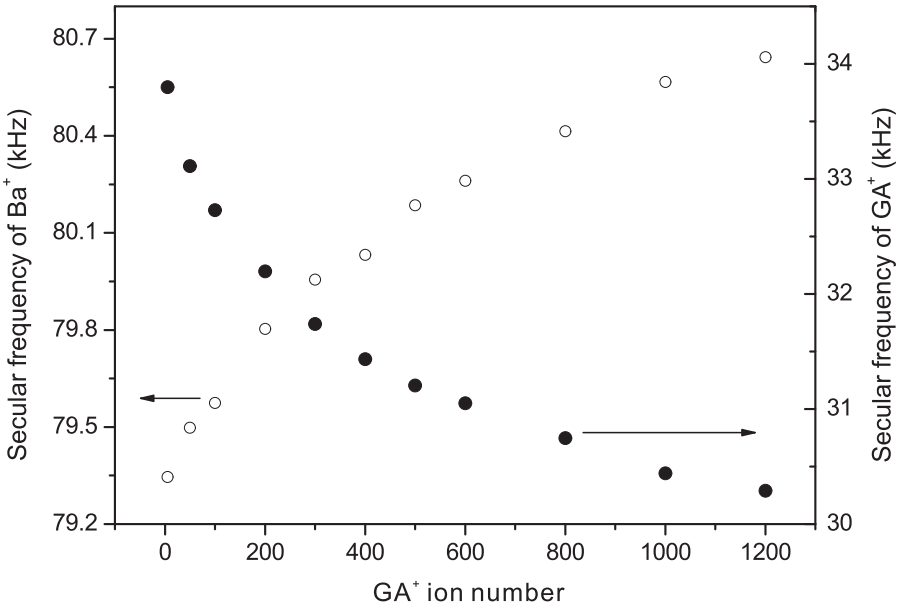

Figure 10.5: Secular frequencies of barium and GA^+ ion ensembles with a different number of the GA^+ ions. The ion number change leads to a modification of the potential, which is reflected in the shifts of the resonance frequency of each ion species.

species will be modified, and their resonance frequencies change accordingly. This can be shown in simulations. For example, if an ion ensemble containing 1000 barium ions is prepared (the radial resonance frequency is at 79.22 kHz), different numbers of heavier GA^+ molecular ions are added to the trap. More GA^+ ions means that the force squeezing the barium ion ensemble is larger and correspondingly its potential well becomes steeper. As a result the resonance frequency of the barium ion ensemble becomes higher. When 1200 GA^+ ions are added, the resonance frequency of the barium ion ensemble shifts to 80.64 kHz. On the other hand, the radial shrinking of the barium ion ensemble results in the GA^+ ions moving to the trap axis, which leads to a lower resonance frequency of the GA^+ ion ensemble. The shift is about 3.5 kHz (from 33.80 kHz to 30.29 kHz along with the GA^+ ion number from 5 to 1200 ions). The changes of the resonance frequencies as a function of the GA^+ ion number are shown in Fig. 10.5. It seems that the shift becomes weaker with increase of the GA^+ ion number. This is due to the fact that it becomes more and more difficult to squeeze the barium ion ensemble.

Effects of symmetry

For an ideal trap if all the middle electrodes have perfect rf potential, the effective trap potential is radially harmonic with axial symmetry and the crystallized ion species arrange in concentric shells around the symmetry axis. In the experiment electrostatic potentials on different electrodes might drift or are set to be different from zero on purpose. In this case, the axial symmetry is broken and the ion species with higher mass-to-charge ratios are displaced stronger. Thus, the ion spatial distribution is changed leading to the change of the secular excitation spectrum. To demonstrate this we use the ion ensemble shown in Fig. 10.2, but an additional DC voltage of 0.25 V is applied to one middle electrode. The laser-cooled barium ions and the sympathetically cooled

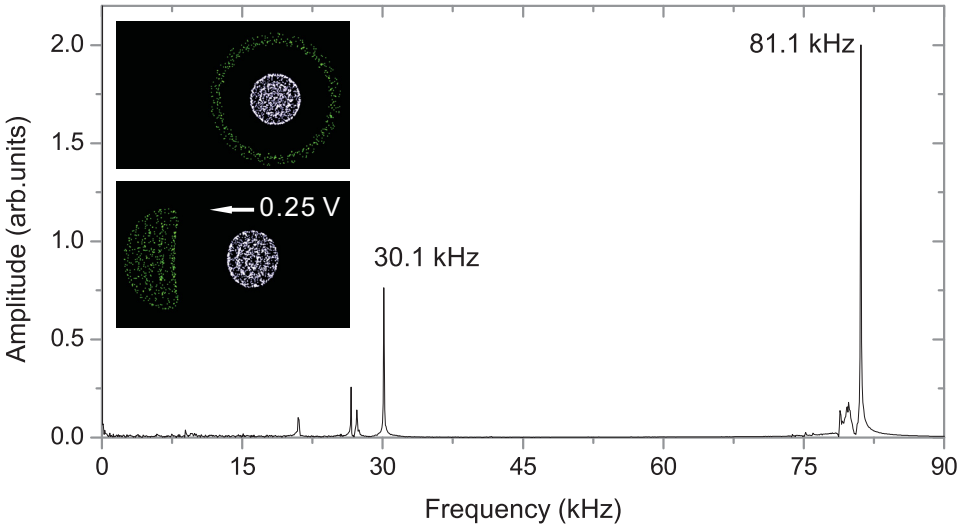

Figure 10.6: Secular frequencies of barium and GA^+ ions in an asymmetric trap. A DC voltage is applied to displace the ion ensembles from the trap center and separates them more strongly. The excitation direction is taken to be the same as that of the displacement. Since all the GA^+ ions share a similar potential well along the excitation direction, the low resonance frequencies vanish. The two ion species are located further away leading to a weakening of space charge effects and the main resonance frequency of the GA^+ ions becomes lower comparing to Fig. 10.2.

GA^+ ions are displaced from the trap center. The GA^+ ions have a larger displacement and are more compact compared to the symmetric case. Thus, the barium ion ensemble is no longer surrounded by the GA^+ ions (see the inset of Fig. 10.6). A simulation of the secular frequency spectrum of this ion ensemble is performed by giving a small position offset along the direction of the ion displacement. Since all the GA^+ ions almost share the same potential well, the low frequencies for the GA^+ ions (see Fig. 10.2(c)) vanish, as expected (see Fig. 10.6). The fact that the two ion species stay away from each other leads to a weakening of their coupling. Therefore, the main resonance frequency of the GA^+ ions moves close to the calculated value (22.4 kHz).

10.4 Alternative model for the secular excitation

The model for the simulation of the secular excitation spectra used above has some disadvantages. From Eq. (2.6) we know that the applied excitation voltage is also not homogenous, but the above model assumes the excitation field being homogenous. Thus, for a pure ion ensemble, no matter how big or how hot it is, the simulated resonance frequencies are always the same. The collective oscillates as a rigid body. Moreover, in multi-species cases, after giving a position offset for one or all ion species, the eigen-oscillation of each species is damped by other species. Thus, the secular oscillation energy transfers to the thermal energy in a short time leading to a poor resolution in the spectrum, so most of the simulations are done with small disturbances and the ensembles are set to very low temperatures (less 1 mK) to improve the resolution.

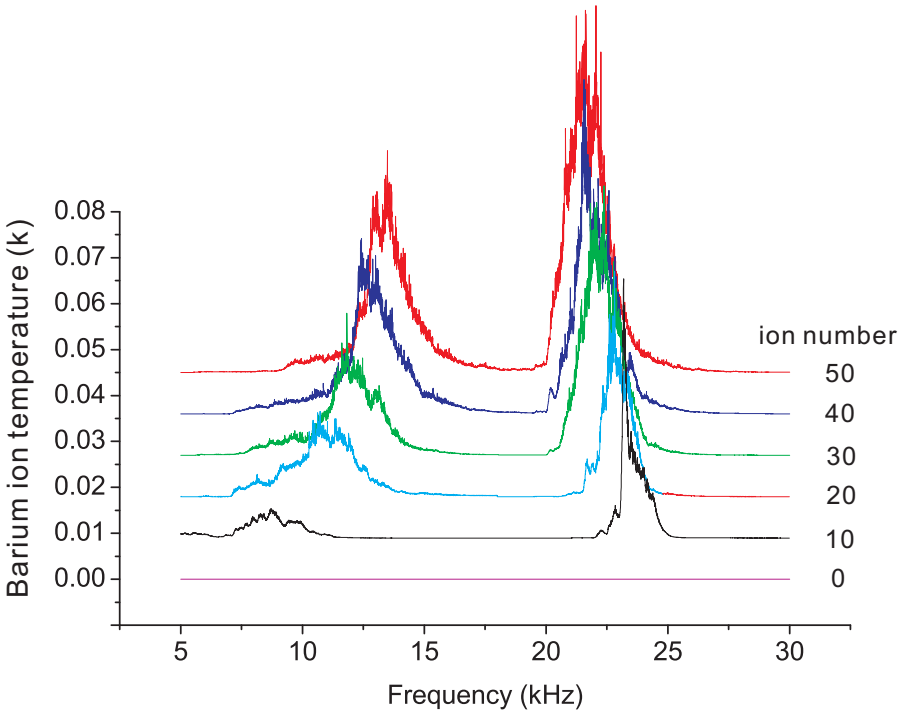

Figure 10.7: Simulated secular excitation spectra of an ion ensemble containing 400 barium ions and different numbers of cyt17 ions. Due to space charge effects the resonance frequency of the cyt17 ions is split. The space charge effects depend on the number of ions, and the resonance frequency of each ion species changes accordingly.

Normally, in experiment the frequency sweep time is several seconds, which is too long for the simulations. However, sometimes it is worth to do simulations in this way to obtain more realistic spectra. To realize this goal, the parameters in the simulations were changed as follows to shorten the computing time: a higher excitation amplitude is implemented to shorten the scan time, and the laser cooling rate is increased to keep all ions in the trap. Moreover, only the interesting frequency range is simulated. If we use an ion ensemble consisting of barium ions and the cyt17 ions (cytochrome c molecules in the 17 charge state and a mass of about 12400 amu, for details see Chapter 8) as an example, the interesting frequency range is from 5 to 30 kHz (usually the rf voltage is about 400 V and the q-factor is approximately 0.11 for the barium ions; the calculated radial secular frequency for a single cyt17 ion is about 17 kHz, but due to space charge effects the resonance frequency split, thus, the frequency range from 5 to 30 kHz is chosen to include all possible resonance frequencies.). The frequency step is 500 Hz and at each frequency 25000 computing steps are integrated to let the ion ensemble reach an equilibrium state. The temperature of the barium ion ensemble is recorded vs. time instead of the fluorescence intensity as in the experiment. The time step for this case is 400 ns, so the total computing time is 500 ms. For a small ion system, for example, 500 ions, about 10 hours are necessary for a usual PC (2-GHz AMD Dual-Core Processor, 1-Gb memory).

Fig. 10.7 shows the simulated secular excitation spectra of an ion ensemble containing 400 barium ions and different numbers of cyt17 ions (0, 10, 20, 30, 40, and 50). The

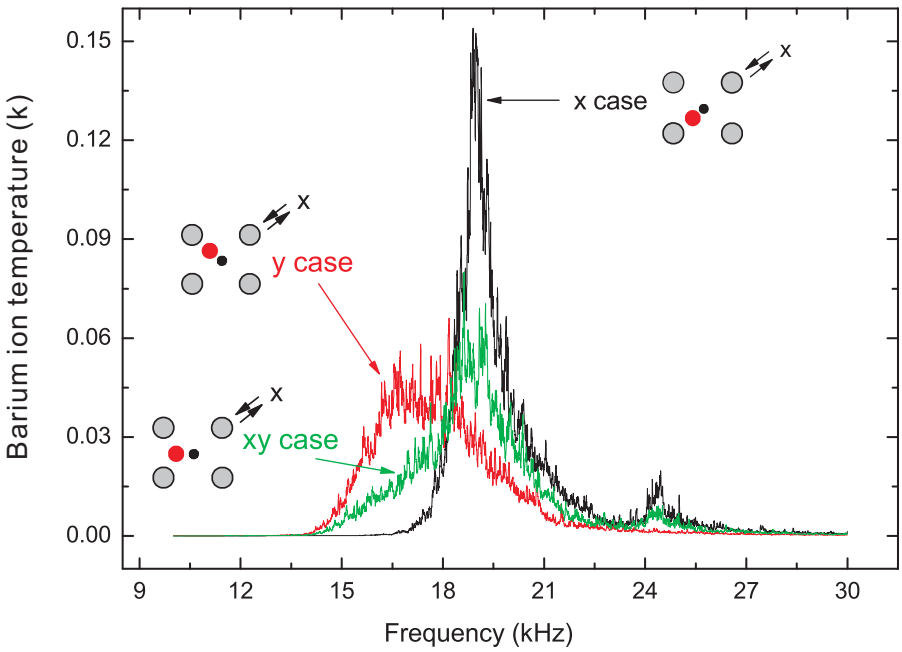

Figure 10.8: Simulated secular excitation spectra of an asymmetric ion ensemble containing 400 barium ions and 50 cyt17 ions excited along the same direction, but with different equilibrium positions. Due to the space charge effects the excitation spectra are different. The small figures show simplified cross-sectional views of the ion ensemble, with red indicating the location of the cyt17 ions and black the barium ions.

laser cooling rate used here is 1750 s^{-1} and the excitation voltage is 30 mV. For a pure barium ion ensemble, when it is excited radially, there are no peaks between 5 to 30 kHz. Therefore, the peaks are attributed to the presence of cyt c protein ions. Here this frequency splits into two peaks consistent with the analysis in Sec. 10.3. When more cyt c ions are added to the ion trap, the two peaks move closer. This means the barium ion ensemble is squeezed and its induced potential well modification becomes smaller. A similar result was already shown in Fig. 10.5.

Simulations using this model have also been performed for asymmetric traps. As an example, 400 barium ions and 50 cyt17 ions are trapped simultaneously and a constant DC offset of 175 mV is applied on the x-, y-, and xy-directions, respectively. The ions are excited along the x-direction, with an amplitude of 30 mV. The simulation results are shown in Fig. 10.8. Compared to the red curve shown in Fig. 10.7, the excitation spectrum is completely different due to the change of the spatial charge distribution. The black curve represents the temperature change as a function of the excitation frequency when the excitation is performed along the direction of the ion displacement. The perpendicular case is shown in red. In this case, the peaks stay in a lower frequency region. When the direction of the ion displacement is at a 45° degree angle with the excitation direction, the main peak is close to the peak for the parallel case (cyt17 ions are driven towards the barium ions back and forth, thus, the barium ions are heated up easier). This confirms that for a multi-species ion system at low temperatures due to the space charge effects, the heavy ions at different positions have different resonance

frequencies, which leads to the split in the secular excitation spectra or frequency shifts.

11 Simulation of nondestructive state-selective detection and spectroscopy

Secular excitation can be used to study ro-vibrational spectroscopy via $(1+1')$ resonance-enhanced multi-photon dissociation (REMPD) [136, 137]. Since detection is based on the method of secular ion excitation by an external AC electric field, in experiment when a target ion species is excited, all other species are excited as well with different amplitudes. This lowers the signal-to-noise ratio of the measurements. Moreover, in some cases, a strong excitation voltage is necessary to obtain a resolvable signal. Subsequently, the ion ensemble is heated to a much higher temperature regime (the ion crystal is melted to a liquid or a gaseous state). Thus, the measured results do not reflect the original ion system and cannot reach a precise measurement. The most important aspect is that REMPD is a destructive measurement. This means in the experiment the ions have to be reloaded periodically.

On the other hand, a strongly focused laser beam, far-detuned from the resonance of a microscopic dielectric object as small as an atom, can generate an optical dipole force (optical tweezer) [138, 139], which has the ability to manipulate this microscopic object and has been widely used in atomic physics for optical dipole traps. This approach is also used with trapped ions but only in connection with quantum logic experiments in atomic ions [140]. In principle, its application can be extended to cold molecular ions. It is possible to be used to resonantly excite sympathetically cooled molecular ions, where the relevant transitions are ro-vibrational transitions. For this purpose, the behavior of cold ion plasmas experiencing a time varying dipole force were simulated in order to investigate the feasibility of the application of the nondestructive optical dipole excitation to spectroscopy. It should be suitable for complex molecular ions as well. Since the mass of a HD^+ ion is relatively small, it can be excited more easily. Here, we use HD^+ ions as an example.

HD^+ molecular ions have been sympathetically cooled down to tens of mK, which is useful for high resolution spectroscopy [137]. Since the HD^+ molecule is one of the simplest molecular ions, containing just a single electron, the precise measurement of its vibrational transition frequencies will ultimately allow to

1. test theoretical methods of precision calculation of molecular levels;
2. establish a new system allowing to measure QED effects / test QED theory in molecules;
3. determine the ratio of electron-to-proton mass in a novel way and with potentially higher precision than with alternative methods;
4. measure nuclear properties such as quadrupole moments;
5. test the time-independence of nuclear mass ratios.

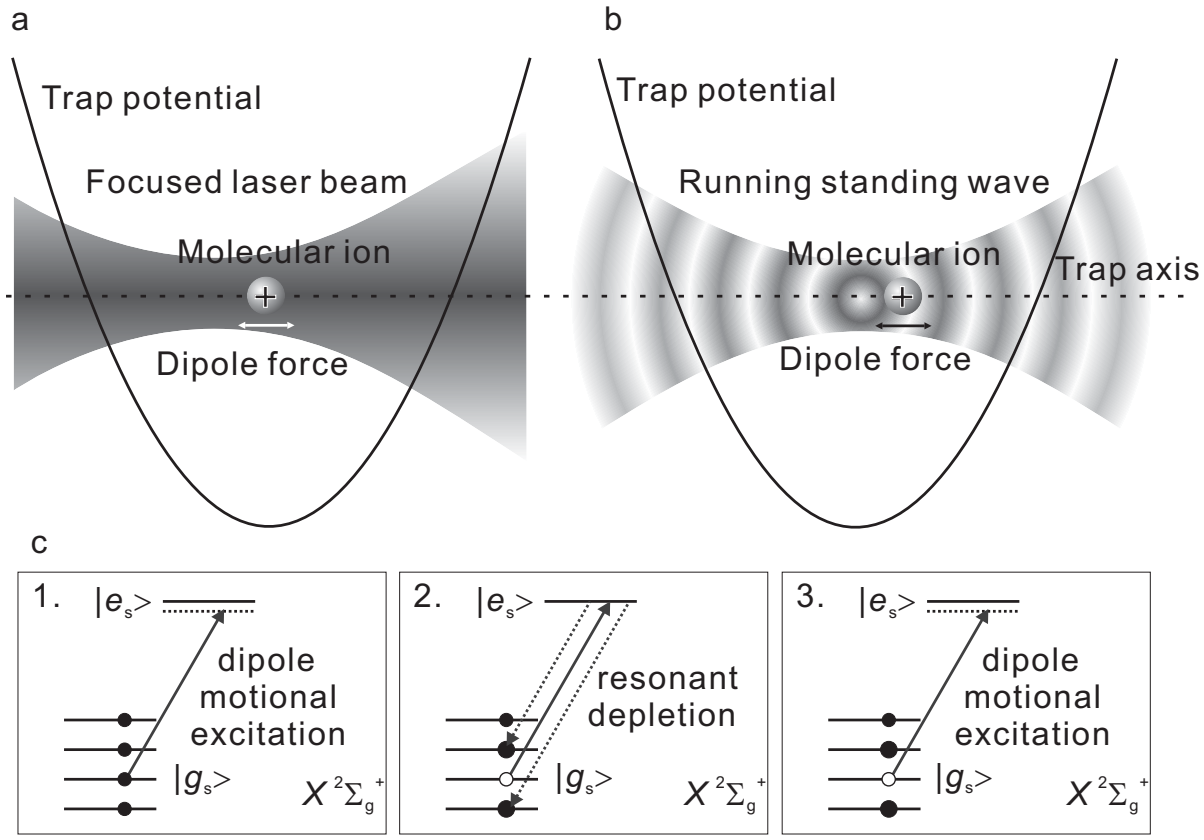

Figure 11.1: Simplified depiction of spectroscopy using nondestructive rotational state detection. (a) principle of internal molecular state detection via the intensity modulation of a single laser beam. A molecular ion is trapped. The intensity modulation of the laser beam exerts a periodic force on the molecular ion only if it is in the appropriate internal (rotational-vibrational) state and the dipole excitation is resonant thus avoiding decay from $|e_s\rangle$ to other levels. Some portion of kinetic energy will transfer to other ions such as laser-cooled ions, which can be detected via the fluorescence produced by a near-resonant laser (not shown). (b) Internal molecular state detection via the modulation of a standing wave. (c) The detection can also be applied to an ensemble of molecular ions distributed among different rotational levels (the sizes of the black circles indicate the relative population in the rotational levels).

The basic idea of the optical dipole excitation is that by modulating the intensity of a focused laser beam the optical dipole force is periodically changed. With a appropriate modulation frequency the HD^+ can be resonantly excited as illustrated in Fig. 11.1(a). For this purpose, the laser beam has to be split into two counterpropagating beams producing a running standing wave, as shown in Fig. 11.1(b). The optical dipole force can be modulated via beam intensity modulation or frequency offset of one individual beam. In fact, only the trap motion of those HD^+ molecular ions in a particular ro-vibration level can be resonantly excited. Due to the strong Coulomb interaction, the coherent motion of the molecular ions will be converted into other internal trap energies such as thermal energy, and transfer a portion of them to the laser-cooled $^9Be^+$ ions, which leads to a change of the fluorescence intensity, i.e. an atomic photonic signal proportional to

the number of the molecular ions in a particular ro-vibrational state is produced. Thus, the relative population in the rotational levels can be obtained nondestructively.

The ratio of the populations of a particular ro-vibrational level before and after depletion can be measured as well. Fig. 11.1(c) gives an example. Step 1: The optical frequency of the excitation laser beam is tuned off-resonantly to a particular ro-vibrational transition $\langle g_s| \rightarrow \langle e_s|$ in the electronic ground state of the molecular ion. The number of ions in the level $\langle g_s|$ is measured nondestructively. Step 2: A transition is induced by resonant irradiation. The ions in the level $\langle g_s|$ can be excited to the level $\langle e_s|$ and decay to other ground sub-levels leading to the reduction of the population of the ions in the state $\langle g_s|$. Step 3: The new population is measured nondestructively. The ratio of final to initial population is a measure of the spectroscopic excitation efficiency. This cycle is repeated for different resonant frequencies, yielding a spectrum. In practice, the upper level for the dipole excitation force and the upper level for the spectroscopy transition may be different.

Therefore, this nondestructive method can be used for precision spectroscopy, with possible rotational resolution: the dependence of the force on the detuning ensures this. The spacing between neighboring ro-vibrational transitions is at least 600 GHz. Since the dipole force is inversely proportional to the laser detuning Δ (see Eq. 11.13), the atomic fluorescence signal resulting from the HD^+ ions in other rotational states is at least 600 times weaker.

In the following sections the optical dipole force is described (in Sec. 11.1) and the simulation of the effects of the optical dipole excitations by a single laser beam and a running standing wave are presented (in Sec. 11.2).

Another issue, the simulations of the linewidths for the spectroscopy of a string HD^+ ion ensemble in a crystal state, is discussed in Sec. 11.5. Both axial and radial directions are simulated as well as the case of excess micromotion along the axial direction.

11.1 Optical dipole potential

In order to study the optical dipole excitation via MD simulations, the optical dipole potential resulting from the interaction between the ions and the laser far detuned from a particular transition frequency needs to be modeled. According to Ref. [141] the optical dipole potential between the ground and excited states U_{dip} is expressed as

$$U_{dip}(x,y,z) = -\frac{3\pi c^2}{2\omega^3}\left(-\frac{\Gamma}{\Delta}+\frac{\Gamma}{\omega+\omega_0}\right) I(x,y,z), \tag{11.1}$$

which is determined by the dipole matrix element d,

$$\Gamma = \frac{\omega^3 d^2}{3\pi\epsilon_0\hbar c^3}. \tag{11.2}$$

Here, ω is the frequency of the excitation laser and $\Delta = \omega - \omega_0$ is the detuning of this laser from the particular transition frequency of the molecular ion ω_0. Γ is the natural

linewidth of the transition, which usually is much smaller than Δ (the natural linewidth for the $v = 2, J = 0$ level is about 5 Hz, while Δ would conveniently be chosen to be about 100 MHz). The term $\Gamma/(\omega+\omega_0)$ is much smaller than Γ/Δ, so it can be neglected. ϵ_0 and c are the vacuum permittivity and speed of light, respectively, and their product is denoted by $1/R_{vac}$. Thus, the optical dipole potential is final given as

$$U_{dip}(x, y, z) = \frac{d^2 R_{vac}}{2\hbar\Delta} I(x, y, z), \tag{11.3}$$

For a Gaussian beam, the amplitude of the driving electric field of the laser wave $E_0(x, y, z)$ can be expressed by the intensity of the beam:

$$E_0(x, y, z) = \sqrt{\frac{2I(x, y, z)}{\epsilon_0 c}} = \sqrt{2I(x, y, z)R_{vac}}. \tag{11.4}$$

The total squared electric field of two counterpropagating laser beams along the z-direction with the same polarization direction is given as

$$E^2_{sum}(x, y, z, t) = \frac{E^2_0(x, y, z)}{2}[\cos(kz - \omega_{opt}t) + \cos(-kz - \omega_{opt}t + \omega_{run}t)]^2, \tag{11.5}$$

where k is the wavenumber of the excitation laser. ω_{opt} and ω_{run} are the angular frequency of the laser beams and the angular frequency difference between the two individual beams, respectively. The power of these two beams are equal and they come from one beam, but $E_0(x, y, z)$ is the electric field of the original beam, so a factor $1/2$ is induced in Eq. (11.5). Fast terms in the expansion of this equation with ω_{opt} can be averaged out ($\omega_{opt} \gg \omega_{run}$). Then, Eq. (11.5) can be simplified as

$$E^2_{sum}(x, y, z, t) = E^2_0(x, y, z)\cos^2\left(kz - \frac{1}{2}\omega_{run}t\right). \tag{11.6}$$

If the minimum waist of the laser beam w_0 is located at $z = 0$ and the laser beam propagates along the axial direction, the beam waist at z is

$$w_z = w_0\sqrt{1 + \frac{z^2\lambda^2}{\pi^2 w_0^4}}. \tag{11.7}$$

Thus, the distribution of the beam intensity is given by

$$I(x, y, z) = \frac{2P}{\pi w_z^2}\exp\left(-2\frac{x^2 + y^2}{w_z^2}\right), \tag{11.8}$$

where P is the beam power. When the beam propagates along an arbitrary direction, the intensity distribution Eq. (11.8) and the square of the electric field of a standing

wave Eq. (11.6) are rewritten as:

$$I(x,y,z) = \frac{2P}{\pi w_0^2 + \frac{\lambda^2(k_x x+k_y y+k_z z)^2}{\pi w_0^2}} \exp\left[-2\frac{(yk_z - zk_y)^2 + (zk_x - xk_z)^2 + (xk_y - yk_z)^2}{w_0^2 + \frac{\lambda^2(k_x x+k_y y+k_z z)^2}{\pi^2 w_0^2}}\right], \tag{11.9}$$

and

$$E_{sum}^2(x,y,z,t) = E_0^2(x,y,z)\cos^2\left[(k_x x + k_y y + k_z z)k - \frac{1}{2}\omega_{run}t\right]. \tag{11.10}$$

here, $\mathbf{k} = (k_x, k_y, k_z)$ is the propagation direction of the laser beam, while $k = \omega/c$. Therefore, the optical dipole potential arising from a single beam or two counterpropagating beams can be expressed as

$$\begin{aligned} U_{srw}(x,y,z) =& \frac{PR_{vac}d^2\cos^2[\omega_{mod}t]\cos^2[(k_x x + k_y y + k_z z)k - \frac{1}{2}\omega_{run}t]}{\hbar\Delta\left[\pi w_0^2 + \frac{\lambda^2(k_x x+k_y y+k_z z)^2}{\pi w_0^2}\right]} \times \\ & \exp\left[-2\frac{(yk_z - zk_y)^2 + (zk_x - xk_z)^2 + (xk_y - yk_z)^2}{w_0^2 + \frac{\lambda^2(k_x x+k_y y+k_z z)^2}{\pi^2 w_0^2}}\right]. \end{aligned} \tag{11.11}$$

P is the total power (power of the single laser beam or power of both beams together). In this equation a possible additional intensity modulation of the laser beams, with the angular frequency of ω_{mod}, is also included. Thus, the molecular ions can be excited in two ways: intensity modulation or frequency detuning of one individual beam in the standing wave. When $\cos^2\left[(k_x x + k_y y + k_z z)k - \frac{\omega_{run}t}{2}\right]$ is replaced by 1, we obtain the case of the single beam.

From Eq. (11.11) the optical dipole force acting on the molecular ion in x-, y-, and z-directions can be derived as -$\frac{\partial U_{srw}}{\partial x}$, -$\frac{\partial U_{srw}}{\partial y}$, and -$\frac{\partial U_{srw}}{\partial z}$, respectively.

To obtain a strong dipole force, sufficient laser power and large dipole matrix elements are necessary. A mW-power source on the $\Delta v = 1$ transition at 5.5 μm would be ideal. Quantum cascade lasers may in the near future provide such power levels. Alternatively, we can consider the overtone transition $\Delta v = 2$. For example, the transition between the levels $(v = 0, J = 0)$ and $(v = 2, J = 1)$ has the wavelength 2.65 μm and this is obtainable via OPO techniques. The dipole matrix element d for this particular transition is about 0.011 Debye [142]. The expected power is higher than 100 mW and with 200 MHz detuning, useful dipole forces can be achieved, as will be shown below.

11.2 Simulations of the optical excitation with different beam configurations

11.2.1 Modulated single beam case

When a single laser beam propagates along the trap axis and is strongly focused (minimum waist is 30 μm), the gradient of the intensity leads to the dipole force. Fig. 11.2

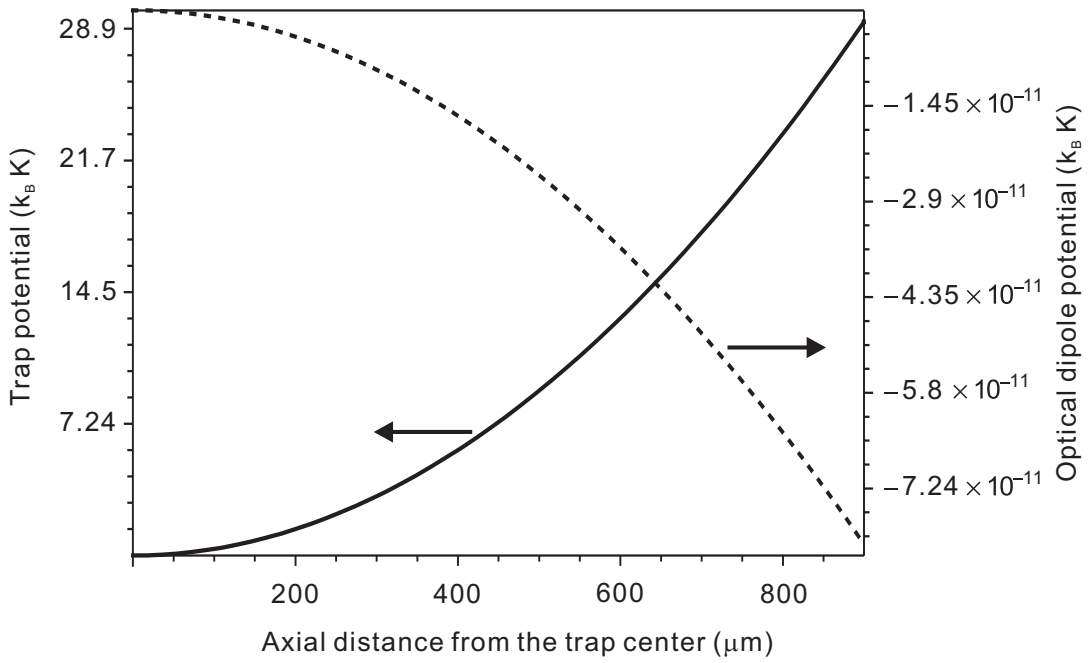

Figure 11.2: Single-beam optical dipole potential $U_{srw}(0,0,z) - U_{srw}(0,0,0)$ and trap potential near the trap center. The excitation laser at 2.65 μm with 100 mW power runs along the trap axis and its focus is at the trap center. The minimum waist is 30 μm.

shows the dipole potential near the trap center along the axial direction, as well as the trap potential. Here, the focus point of the laser beam is in the trap center and the trap parameters chosen here are typical for our trap: 380 V rf voltage, 14.2 MHz rf frequency, 1 V endcap voltage, and $\kappa = 0.192$. The optical dipole potential is serval orders smaller than the trap potential.

Although this optical dipole potential is smaller than the trap potential, it still can resonantly excite the HD^+ ions efficiently. To demonstrate this effect, an HD^+ ion is in the trap center, initially at rest, and a single excitation laser beam is directed onto the ion along the trap axis. The beam waist is set about 900 μm away from the trap center to achieve a dipole force. Via intensity modulation of the laser beam with $\omega_{mod} = \frac{1}{2}\,\omega_z$ (ω_z is the axial resonance frequency of the HD^+ ion, $2\pi(40.38$ kHz) for 1 V endcap trap voltage) the ion is excited resonantly. In our simulations the depth of the modulation is always 1. The z-trajectory is plotted in Fig. 11.3. The oscillation amplitude increases linearly and was confirmed also for larger t. Thus, the kinetic energy increases quadratically with time. The maximum kinetic energy along the z-direction is about $k_B(0.0007$ mK) after 1 ms, and $k_B(7$ mK) after 100 ms.

However, when more ions are added to the trap, due to the strong Coulomb interaction the ions can not be resonantly excited any more. Fig. 11.4 gives an example. 600 $^9Be^+$ and 200 HD^+ at zero temperature are prepared in the trap and no laser cooling is applied to the $^9Be^+$ ions. Then, the laser beam is added and its intensity is modulated with $2\pi(20.19$ kHz) ($\frac{1}{2}\,\omega_z$). No matter whether the beam has an offset from the trap center or not the temperature of the HD^+ ion ensemble does not increase significantly. Simulations

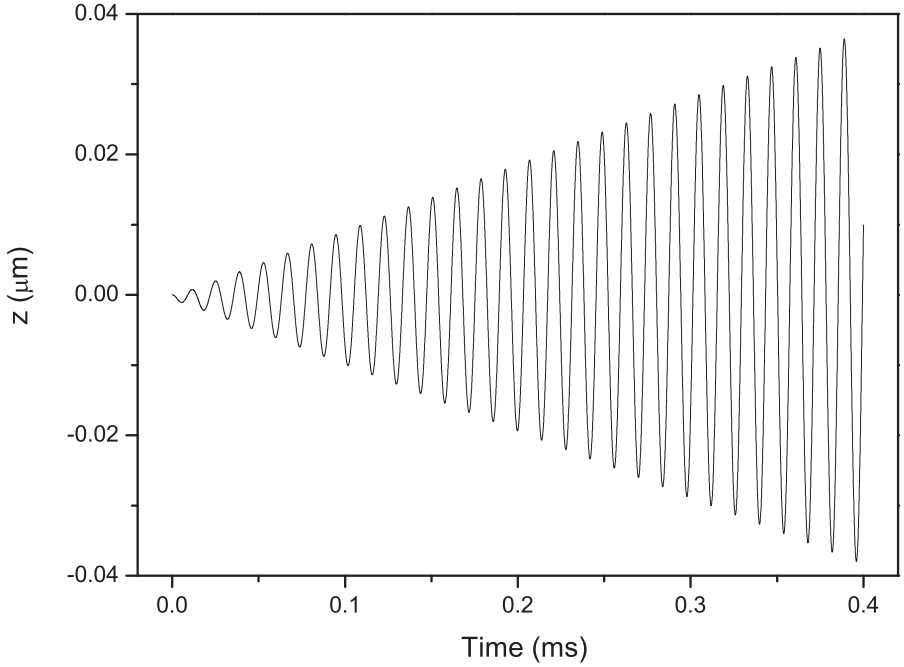

Figure 11.3: Optical dipole force excitation of a single HD^+ ion, which initially is at the trap center, by modulating the intensity of a 2.65 μm laser, whose focus point is 900 μm away from the trap center. The laser power used here is 100 mW. The oscillation amplitude of the ion increases linearly with time, and its kinetic energy increases quadratically with time.

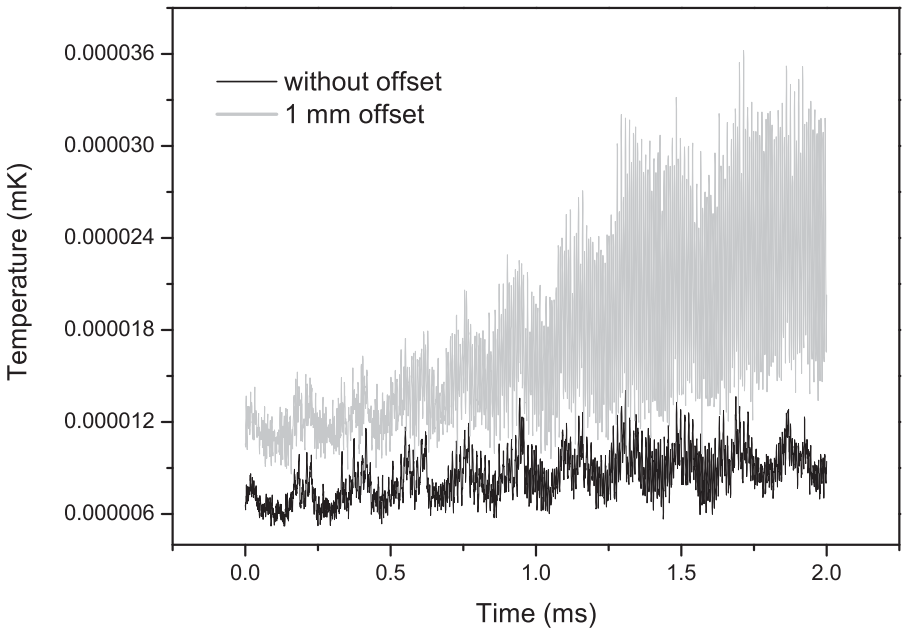

Figure 11.4: Optical excitation of an ensemble of HD^+ ions (200 HD^+ together with 600 $^9Be^+$ ions). The case of focus of the laser beam at the trap center and 1 mm away along the trap axis are simulated. The temperature of the HD^+ ion ensemble does not increase significantly.

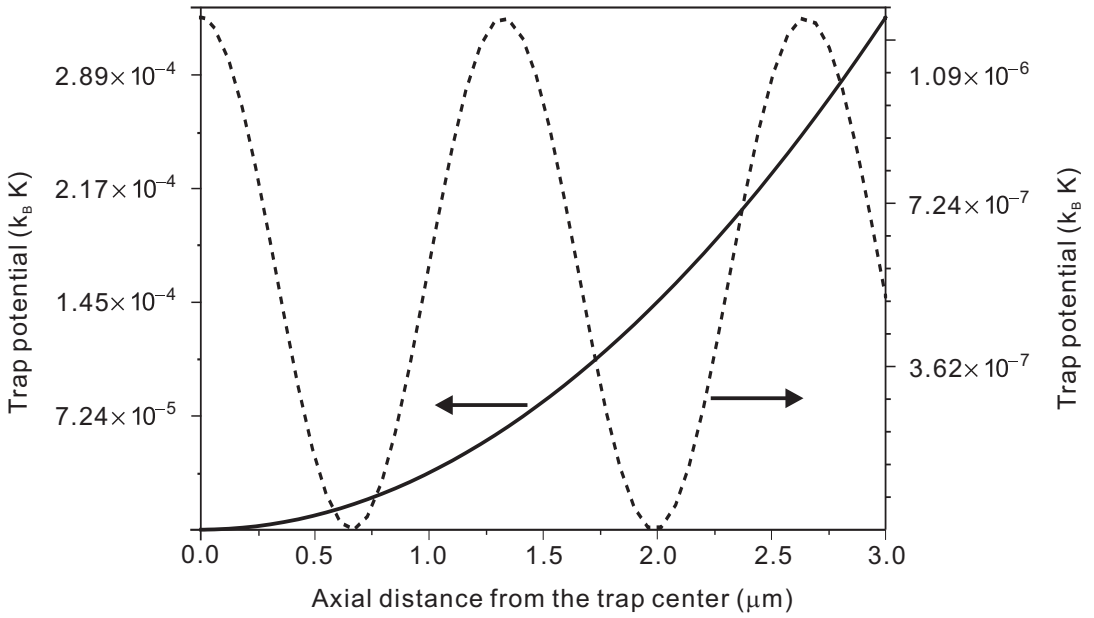

Figure 11.5: Optical dipole potential $U_{srw}(0, 0, z)$ and trap potential near the trap center. The optical dipole potential approximately has a cosine form and its amplitude is quite small comparing to the trap potential, but larger compared to single beam.

with higher modulation frequencies ($10\,\omega_z$ and $100\,\omega_z$) show similar results. Thus, the intensity modulation of a single laser beam can not resonantly excite an ion ensemble.

11.2.2 Standing-wave case

Another option is to use a standing wave. Since the force is the negative gradient of the potential in the standing wave configuration, it is much larger than that in a single running wave. When the standing wave propagates along the trap axis and has the minimum waist (30 μm) at the trap center, the corresponding optical dipole potential is shown as the dashed curve in Fig. 11.5. The cosine form dipole potential is much larger than the case of a single beam. In principle, the dipole potential can be modulated by intensity or frequency. In the following, both the simulations with the modulation intensity and frequency detuning of one individual beam are studied.

11.2.2.1 Intensity modulation

Firstly, the simulations with the intensity modulation are performed on an HD^+ ion ensemble containing 200 HD^+ ions with the cooling force switched on. This ion ensemble is surrounded by 600 $^9Be^+$. The trap parameters are kept the same as above and the modulation frequency ω_{mod} is $\frac{1}{2}\,\omega_z$. Since the dipole force is proportional to the power of the laser beam, we set the power to be 1 W to amplify the resonance process. The simulated result is shown as the black curve in Fig. 11.6. Due to the Coulomb interaction the actual resonance frequency for each HD^+ ion is no longer ω_z, but is shifted towards higher frequencies. Although the HD^+ ion ensemble is heated up, the process is very slow. The heating rate is about $k_B(0.248\ \mathrm{K/s})$. Thus, the temperature change is too small to be observed in experiment. So simulations with higher modulation frequencies

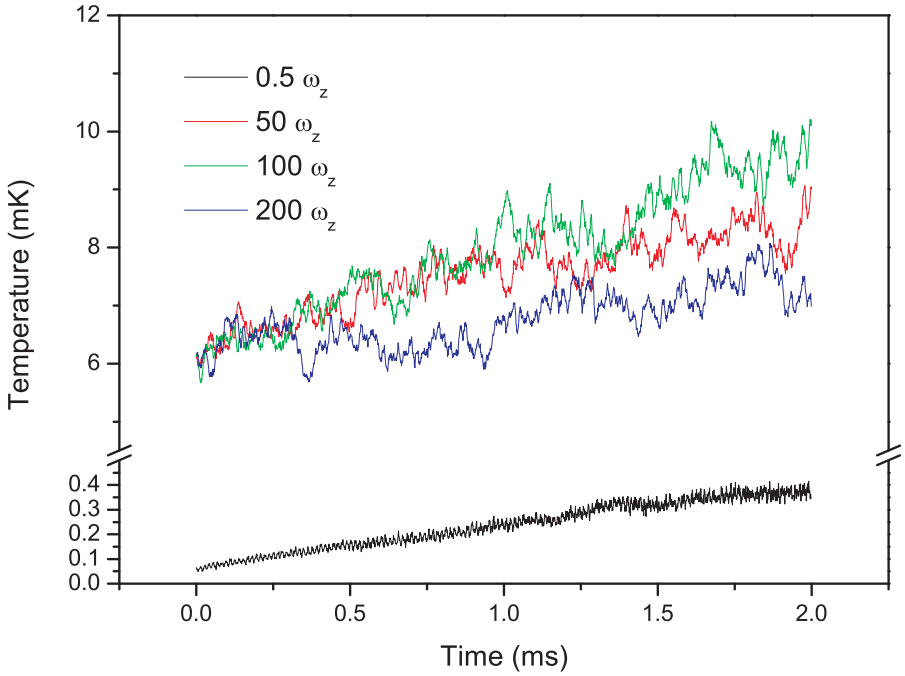

Figure 11.6: Optical dipole excitation of the HD^+ ion species in an ion ensemble consisting of 600 $^9Be^+$ and 200 HD^+ ions for different frequencies of intensity modulation ω_{mod}. The ion ensemble is initially at nearly absolute zero or 6 mK, without any cooling and heating effects. When the modulated standing wave is switched on, the temperatures of the HD^+ ions are recorded. For ω_{mod} set to $50\,\omega_z$, $100\,\omega_z$, or $200\,\omega_z$, the fitted heating rates are $k_B(2.1$ K/s), $k_B(2.667$ K/s), and $k_B(0.998$ K/s), respectively. In the case of $\omega_{mod} = \frac{1}{2}\omega_z$, the heating rate from the dipole excitation is negligible.

$50\,\omega_z$, $100\,\omega_z$, and $200\,\omega_z$ are performed, as shown in Fig. 11.6 as well. The fitted heating rates are $k_B(2.1$ K/s), $k_B(2.667$ K/s), and $k_B(0.998$ K/s), respectively. The optimal modulation frequency for the highest heating rate should be found in further simulations in the future. Due to the strong Coulomb interaction when the HD^+ ions are heated, the $^9Be^+$ ions are also heated to a similar temperature. Therefore, the gained kinetic energy of the HD^+ ion ensemble is approximately 1/8 of the actual energy generated in the optical dipole excitation process (1/8 for the potential energy increase of the HD^+ ion ensemble (see Fig. 9.11), the remaining $3/8 + 3/8$ are are transferred to the $^9Be^+$ ion ensemble).

11.2.2.2 Frequency detuning of one individual beam

Simulations with the frequency detuning of one individual beam of the standing wave are also performed. We use the same ion ensemble as for the intensity modulation. The ion ensemble is initially evolving at 6 mK without any cooling and heating sources. Then the running standing wave is applied on the HD^+ ions with the frequency offset of one individual beam (ω_{run}). The temperature of the HD^+ ions is recorded. The simulation results with $\omega_{run} = \omega_z$, $10\,\omega_z$, $50\,\omega_z$, and $100\,\omega_z$ are plotted in Fig. 11.7. When the HD^+ ions are heated, the $^9Be^+$ ions are sympathetically heated to a similar temperature due to the fast thermalization process (see Chapter 9). To demonstrate this effect, the

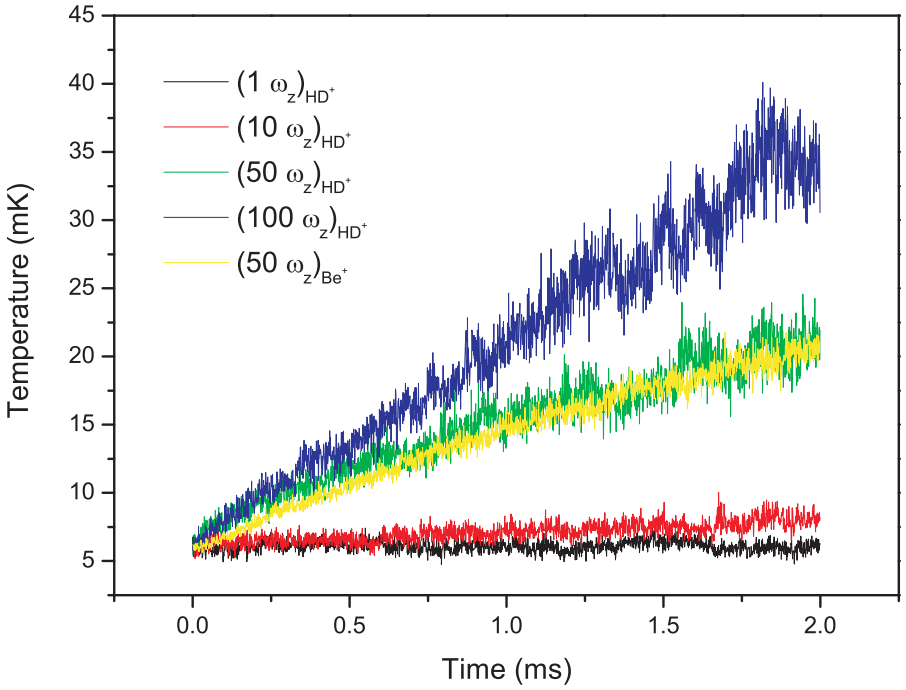

Figure 11.7: Optical dipole excitation of the HD^+ ion species via frequency detuning of one individual laser beam of the standing wave by ω_{run}. The ion ensemble (600 $^9Be^+$ and 200 HD^+ ions) is initially evolving at 6 mK without any cooling and heating effects.For frequency offsets of ω_z, $10\,\omega_z$, $50\,\omega_z$, and $100\,\omega_z$, respectively, the temperature evolutions of the HD^+ ion ensemble are recorded.

temperature change of the $^9Be^+$ ions in the case of $\omega_{run} = 50\ \omega_z$ is recorded as well and shown as the yellow curve in Fig. 11.7. It almost overlaps with the green curve, which is the temperature evolving curve of the HD^+ ions at the same modulation frequency ($\omega_{run} = 50\ \omega_z$).

Since the temperature increase due to the excitation is close to linear in time, the heating rates were again fitted as indicated in Fig. 11.8. The heating rate rises approximately linearly with the increase of the frequency offset ω_{run}. If we consider the energy absorption of the $^9Be^+$ ions as well, the heating rate from the optical dipole excitation is about $k_B(22.1{\times}8$ K/s). Here, 1 W total power for the two laser beams is used. Normally, a power of 100 mW is realistic. Thus, this heating rate is larger compared to the background rate we found under typical experiment conditions.

The relationship between the heating rate and the wavelength of the excitation laser is also investigated here. In the simulations the same ion ensemble as above (200 HD^+ and 600 $^9Be^+$ at 6 mK without any heating and cooling) is prepared and evolves with 1, 2, 2.65, 4, and 5 μm wavelengths of the excitation laser, respectively. The dipole matrix element is kept constant. The first three wavelength values correspond roughly to the fifth, third, second vibrational overtone, the last to the fundamental transition. The temperatures of the HD^+ ion ensemble as a function of time are plotted in Fig. 11.9(a) and the (linearly) fitted heating rate for each curve is shown in Fig. 11.9(b) as the function

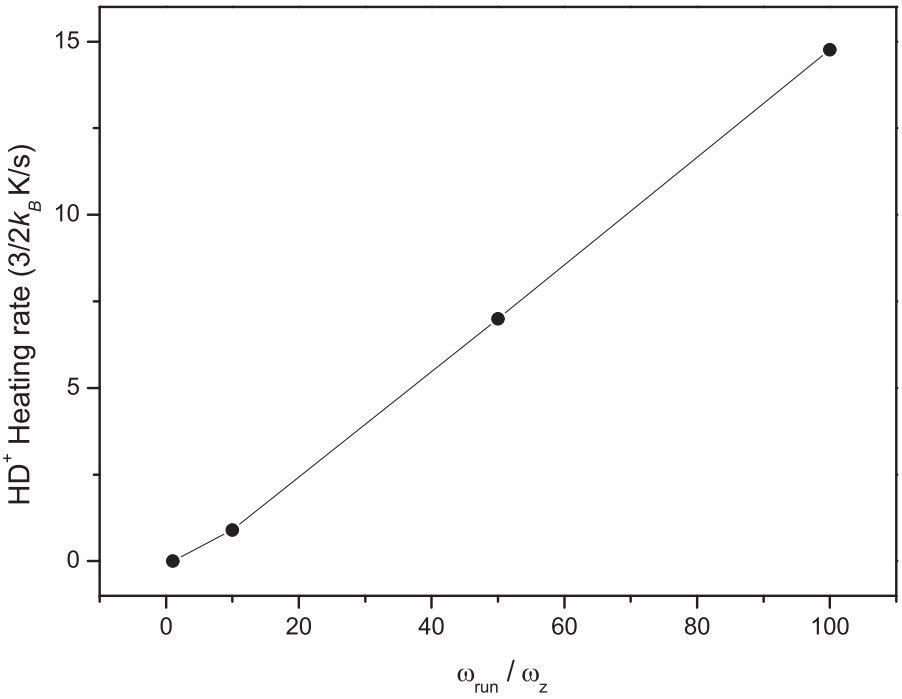

Figure 11.8: Fitted heating rates of the optical dipole excitation with different modulation frequencies (from the temperature curves shown in Fig. 11.7). The heating rate is approximately proportional to the modulation frequency. The line is a guide for the eye.

of the wavelength of the excitation laser λ. It appears that the heating rate decreases exponentially with the rising of λ. The explanation is that a smaller wavelength corresponds to a higher number of potential antinodes for the running standing wave in a finite length leading to a higher potential force, which is the minus derivative of the dipole potential). Since the dipole matrix element decrease with decreasing λ, one has to consider the combined effect. For example, in going from the $\lambda = 1.1$ μm overtone transition in HD^+ ions to the $\lambda = 1.8$ μm overtone transition, d^2 increases by approximately a factor of 80, thus offsetting the wavelength effect.

For comparison, simulations with different beam waists and endcap voltages are performed, as shown in Fig. 11.10. Here, the initial ion ensemble is evolving at close to absolute zero. The frequency offset of one individual beam is $20\,\omega_z$. Note that a different endcap voltage corresponds to a different axial secular frequency ω_z. As mentioned above when $V_{ec} = 1$ V, ω_z is about 34.4 kHz, while it is about 70 kHz with $V_{ec} = 3$ V. The comparison between the black and red or the blue and green curves shows that although the modulation frequency is approximately doubled for $V_{ec} = 3$ V, the heating rates do not change too much. The reason is that when we lift up the endcap voltage and correspondingly increase the laser detuning ω_{run}, the oscillation frequencies of the HD^+ ions at their lattices are increased as well. A bigger waist lowers the intensity gradient of the laser beams resulting in a smaller heating rate. Fig. 11.10 shows the results obtained, confirming the expectations.

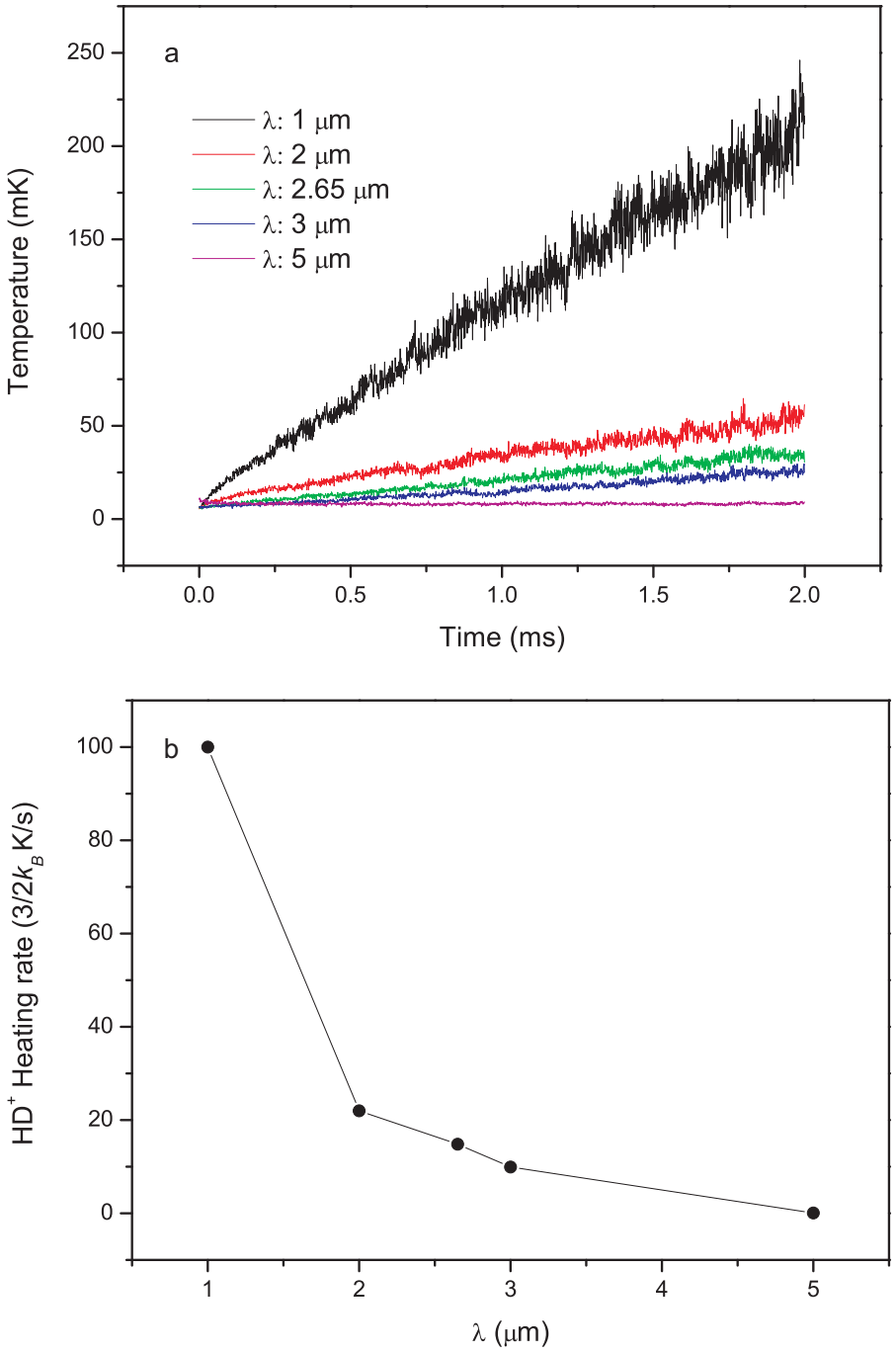

Figure 11.9: Temperature evolution upon optical dipole excitation as a function of the wavelength of the excitation laser λ. (a) Temperature changes of the HD^+ ion ensemble with different λ. (b) Fitted heating rate for each heating curve shown in (a). The heating rate due to the dipole excitation decreases approximately exponentially with wavelength.

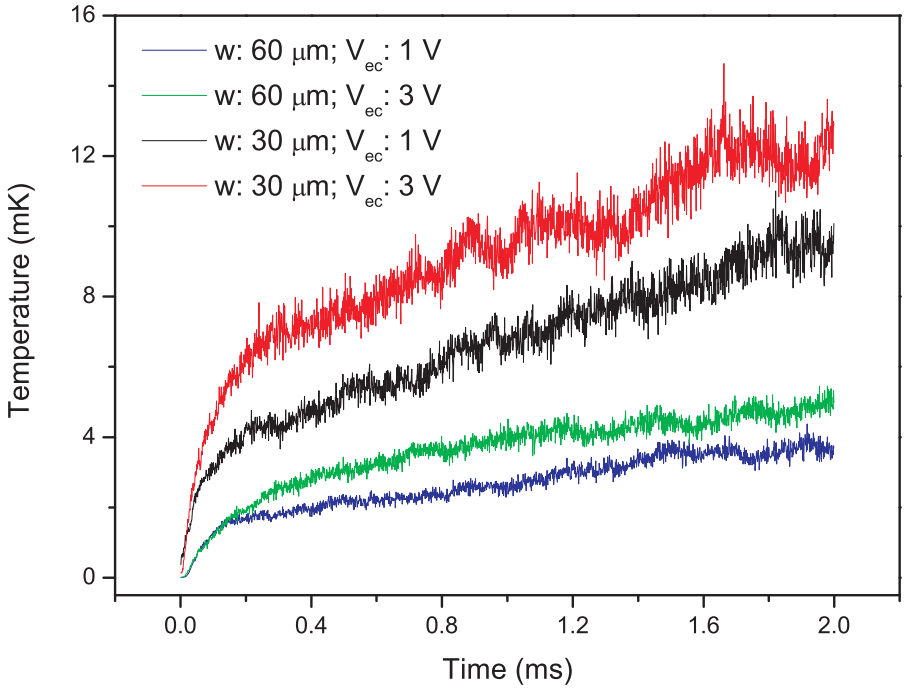

Figure 11.10: Optical dipole excitation of HD^+ ions in an ion ensemble consisting of 600 $^9Be^+$ and 200 HD^+ ions, via frequency detuning of one individual laser beam by ω_{run}. The ion ensemble is initially evolving at absolute zero without any cooling and heating effects. The excitations with different minimum beam waists and endcap voltages are performed with the frequency modulation of $\omega_{run} = 20\,\omega_z$. The increase of the endcap voltage can not improve the heating rate due to the rising of the axial trap potential. The increase of the minimum beam waist leads to the lowering of the heating rate.

11.3 Conclusion of the optical dipole excitation

In this chapter, the optical dipole force is described and simulated. The resonance excitation of a single HD^+ ion by the optical dipole force of a single laser beam via intensity modulation is studied. The oscillation amplitude of this ion increases linearly. However, the following simulations show that an HD^+ ion ensemble (200 HD^+ ions with 600 $^9Be^+$ ions outside) cannot be effectively excited due to the strong Coulomb interactions. Thus, we consider the standing wave, which can offer a larger optical dipole force. The optical excitations of the HD^+ ion ensemble via intensity modulation and frequency detuning of one individual beam are simulated. In both cases, the ion ensemble can be well excited. The simulations with different parameters such as the endcap voltage and the excitation laser wavelength are also performed.

11.4 Simulation of HD^+ vibrational spectroscopy

In the MD simulations, the trajectory of each ion confined in a linear Paul trap can be monitored. This offers a way to investigate the line broadening of an ion ensemble at each possible transition via summing the power spectrum (PS) of the calculated FFT (fast Fourier transform) of each ion [143]. If ions are irradiated by a monochromatic laser beam of frequency ω_0 (transition frequency) propagating along the z-direction, the electric field of this laser beam is given by

$$E(z_i, t) = E_0 e^{i\phi_i(t)} = E_0 e^{ikz_i(t) - i\omega_0 t}. \tag{11.12}$$

Here, $z_i(t)$ is the trajectory of ion i and k is the wavelength of the laser beam. The frequency spectrum of this field is obtainable by a FFT

$$E_(\omega) \propto \int_{-\infty}^{\infty} e^{-i\omega_0 t} e^{ikz(t)} dt. \tag{11.13}$$

The line profile will be proportional to the square of its magnitude. In this section we demonstrate this method by using HD^+ ion ensembles as examples. The transition wavelengths used here are 1.4 μm (ro-vibrational transition $v = 0 \rightarrow v = 4$ for HD^+ ions) and 5.1 μm (the transition $v = 0 \rightarrow v = 1$ is about 5.5 μm).

The HD^+ ion ensembles can be sympathetically cooled down to a few ten mK regime. At these temperatures the confinement of the HD^+ ions might be in the Lamb-Dicke regime (the region to which the particle confinement is much smaller than the optical wavelength), especially for the transition wavelength of 5.1 μm. The harmonic motions of the HD^+ ions can be distinguished. In this case, in the frame of the ions, the laser field is modulated. The phase of the electric field in the ion frame is modified by

$$\phi_i(t) = kz_{i0}\cos(\omega t) + kz_i(t) - \omega_0 t. \tag{11.14}$$

Except for the random thermal motion $z_i(t)$, ion i has harmonic oscillation with frequency ω and amplitude z_{i0}. Therefore, the line profile for an ion ensemble can be expressed as

$$\begin{aligned}\sum_i \left|\mathrm{FFT}\{E_0 e^{i\phi_i t}\}\right|^2 &\propto \sum_i \left| \int_{-\infty}^{\infty} e^{-i\omega_0 t} e^{ik[z_{i0}\cos(\omega t) + z_i(t)]} dt \right|^2 \\ &= \sum_i \left| \sum_{n=-\infty}^{+\infty} i^n J_n(kz_{i0}) \int_{-\infty}^{\infty} e^{i(n\omega - \omega_0)t} e^{ikz_i(t)} dt \right|^2, \end{aligned} \tag{11.15}$$

where J_n is the nth Bessel function. Instead of a single, Doppler broadening spectrum, the spectrum takes the form of a series of discrete resonances, each having a width equal to the Doppler broadened width, which are separated by the frequency of harmonic motion ω. They are the motional sidebands and their amplitudes are proportional to the Bessel functions $J_n(kz_{i0})$. Thus, simulations at different temperatures are performed. The ion ensemble used in our simulations includes 30 HD^+ ions and 200 $^9Be^+$ ions. The q parameter for HD^+ ions is 0.165 and the endcap voltage is 3 V. In this case the HD^+ ions are aligned as a string along the axis direction, so that they have different trap potentials along the axial and radial directions. Hence, simulations in both directions

are performed. Actually, in the experiment, axial micromotion of about 300 nm peak-to-peak amplitude was observed, so that simulations including the rf micromotion are performed as well.

Firstly, the spectrum of the HD^+ ion ensemble was simulated along the axial direction. An ion ensemble is prepared initially and let evolve at 16 mK. The z-coordinates of each HD^+ ion are recorded for 1.33 ms (time step is 5 ns). Subsequently, the FFT of $exp(ikz_i)$ is used to obtain the power spectrum of each HD^+ ion at the wavelengths of 1.4 or 5.1 μm. Finally, the 30 power spectra are added up, as shown in Fig. 11.11(a) and (b), which are the spectra corresponding to the wavelengths of 1.4 and 5.1 μm, respectively. They have the Gaussian shape and their Gaussian fits are shown as circles with about 10.9 and 2.95 MHz linewidths (FWHM), respectively. Actually, the Doppler shift in frequency of the thermal motion of a particle can be directly derived as

$$P(f)df = \sqrt{\frac{mc^2}{2\pi k_B T f_0^2}} \exp\left[-\frac{mc^2(f-f_0)^2}{2k_B T f_0^2}\right] df, \tag{11.16}$$

here, $P(f)df$ is the fraction of particles with frequency component f to $f + df$. c is the speed of light, T is the temperature, k_B is the Boltzmann constant and m the mass of the particle. f_0 is the central transition frequency. Eq. 11.16 is a typical Gaussian equation. Thus, the FWHM of the distribution is

$$\Delta f_{FWHM} = \sqrt{\frac{8k_B T \ln 2}{mc^2}} f_0. \tag{11.17}$$

If one knows the temperature of an ion ensemble, the width of the Doppler broadened spectrum is obtained. In our case, the HD^+ ion ensemble is at 16 mK. The calculated linewidth is about 11.2 and 3.07 MHz for the laser wavelengths of 1.4 and 5.1 μm, respectively. They are consistent with the simulated values.

The simulations for a lower temperature (1.75 mK) are performed as well and the results are shown in Fig. 11.11(c) and (d). Due to the decrease of the temperature the Doppler broadening becomes smaller, which is reflected in the narrowing of the linewidth of the spectra. Fig. 11.11(c) shows that the linewidth for the transition wavelength of 1.4 μm is reduced from 9.21 MHz at 16 mK to 3.39 MHz. Since at 1.75 mK the oscillation amplitude of the HD^+ is smaller than the 5.1 μm, the HD^+ ions are in the Lamb-Dicke regime. Thus, the spectrum for the 5.1 μm wavelength is no longer a simple Gaussian profile as shown in Fig. 11.11(d).

The HD^+ ions aligned as a string have different trap potentials along the axial and radial directions. Thus, simulations of the ion ensemble at 6.8 mK along the x-direction are also performed, as shown in Fig. 11.12(a) and (b). The Doppler broadening for the wavelength of 1.4 μm is similar then for the axial cases having a Gaussian shape with a linewidth of about 7.46 MHz (see Fig. 11.12(a)). Since in x-direction the ion potential is much larger than the axial one (the radial secular frequency for an HD^+ is about 822 kHz, while the axial secular frequency is about 121 kHz.), the radial oscillation amplitude of each HD^+ ion is smaller. Therefore, at 6.8 mK the confinement of the HD^+ ions

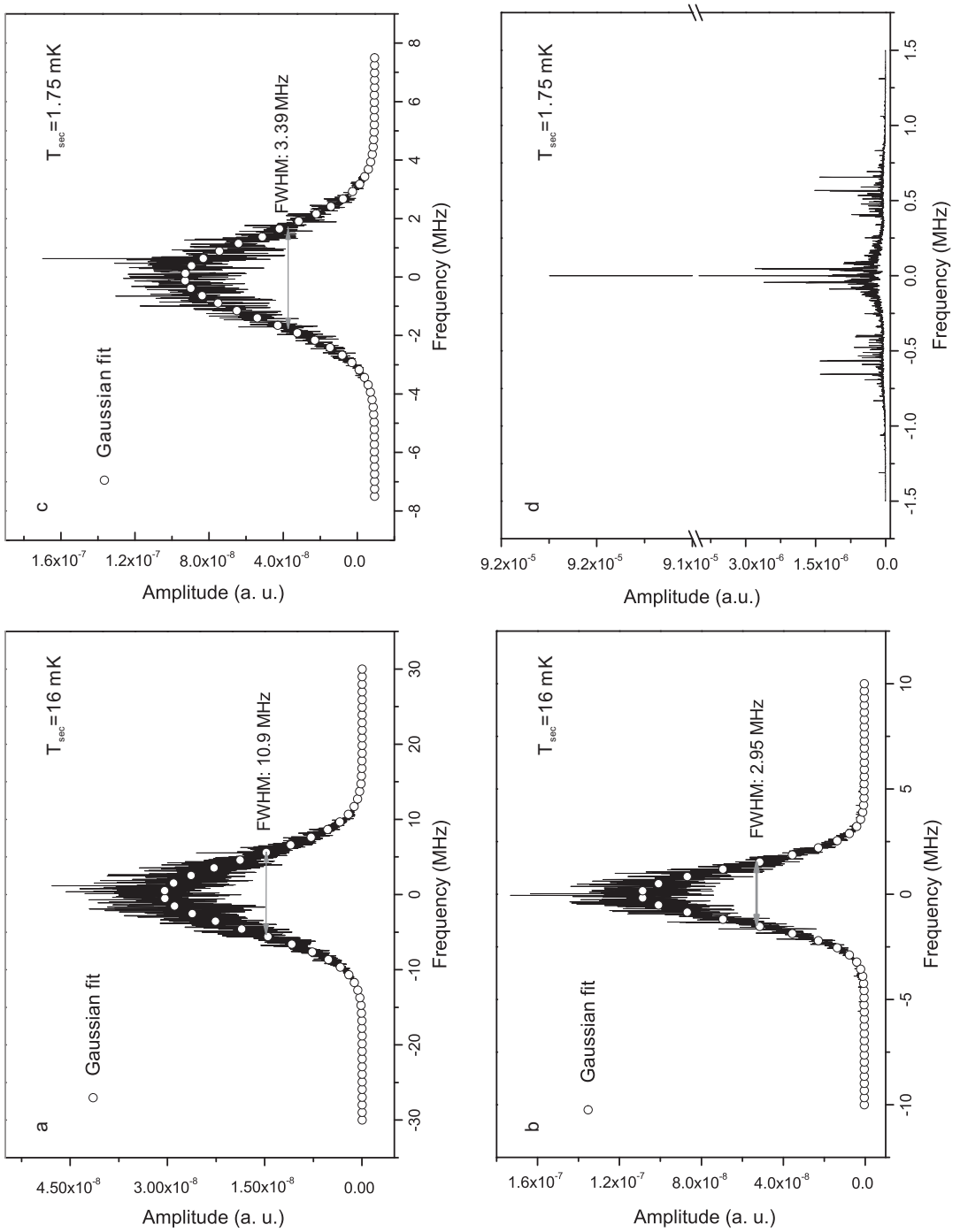

Figure 11.11: Simulated spectrum of the Doppler broadening of an HD^+ ion ensemble along the axial direction at 16 and 1.75 mK (the spectroscopy laser is along the axial direction). The Doppler broadening of the spectrum is a function of the laser wavelength. (a) Spectrum at the wavelength of 1.4 μm. The fitted linewidth of the Doppler broadening $\approx$ 10.9 MHz (b) Spectrum at the wavelength of 5.1 μm. The fitted linewidth is about 2.95 MHz. (c) Spectrum at the wavelength of 1.4 μm. The circle curve is the Gaussian fit, from which we obtain that the linewidth of the Doppler broadenings is about 3.39 MHz. The linewidth becomes smaller due to the decrease of the temperature. (d) Spectrum at the wavelength of 5.1 μm. The confinement of the HD^+ ions in the Lamb-Dicke regime, the spectrum is no longer a simple Gaussian profile.

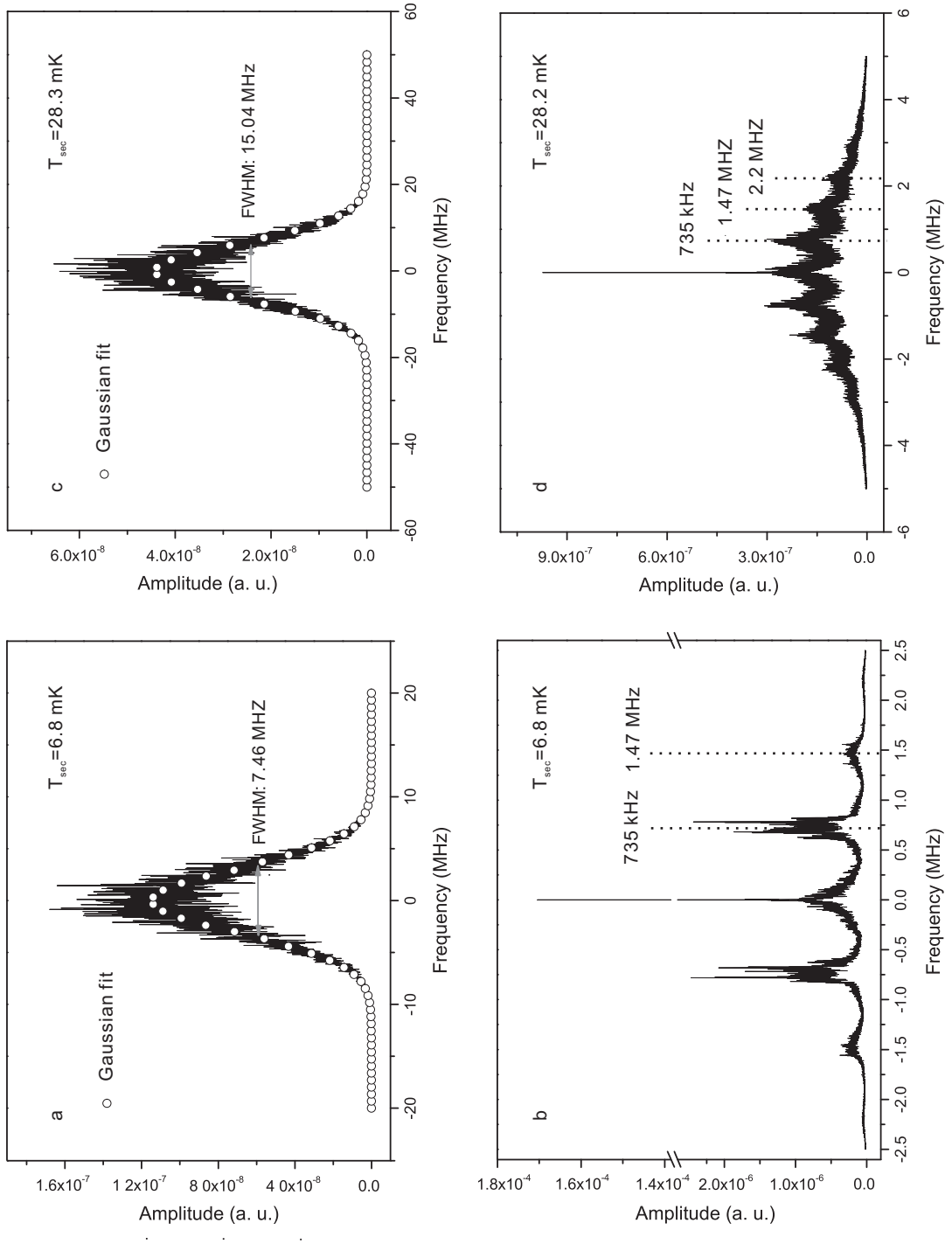

Figure 11.12: Simulated Doppler broadening of an HD^+ ion ensemble in x-direction (**radial direction**) at 6.8 and 28.2 mK. (a) Spectrum at the wavelength of 1.4 μm. The circles represent the Gaussian fit, from which we obtain that the linewidths of the Doppler broadened spectrum is about 7.46 MHz. (b) Spectrum at the wavelength of 5.1 μm. Due to the confinement of the HD^+ ions in the Lamb-Dicke regime, the spectrum shows obvious sidebands. (c) Spectrum at the wavelength of 1.4 μm. The circles are the Gaussian fit, from which we obtain a Doppler broadening of approximately 15.04 MHz, which is almost double compared to the case of 6.8 mK. (d) Spectrum at the wavelength of 5.1 μm. The discrete sideband structure starts to be washed out.

in x-direction is already in the Lamb-Dicke regime for the wavelength of 5.1 μm. Apart from the peak around 0, there are two strong sidebands at about 735 kHz (due to the space charge effect the actual secular frequency is different from the calculated one for a single ion) and other higher-order sidebands as shown in Fig. 11.12(b). Comparing this spectrum to that in Fig. 11.11(d), the sidebands are much clearer. The reason is that due to the string structure in the radial direction all the HD^+ ions share a similar confining potential (trap potential plus the Coulomb interaction with the $^9Be^+$ ions), while in the axial direction (except for the endcap trap potential) the interactions among the HD^+ ions are very strong (ions stay more close), leading to different confining potentials for each HD^+ ion. Thus, the sidebands in the radial direction are enhanced but in the axial direction they are washed out.

Fig. 11.12(c) and (d) show the simulations of the spectroscopy in x-direction at 28.2 mK. As expected the Doppler broadening is wider for the wavelength of 1.4 μm (see Fig. 11.12(c)) and the discrete peak structure for the wavelength of 5.1 μm (see Fig. 11.12(d)) is washed out and starts to have to a Gaussian profile.

In the experiment, due to the imperfect construction of the linear Paul trap, the rf micromotion might arise from phase differences between the rf fields on different electrodes (central and endcap electrodes). According to measurements in experiment, a 300 nm peak-to-peak amplitude rf micromotion for HD^+ ions can occur. Therefore, it is necessary to study the influence of this effect on the spectroscopy. To study this effect, in our simulations an additional rf field with $2\pi\times14.2$ MHz angular frequency is applied in axial direction to excite the HD^+ ions with about 300 nm peak-to-peak amplitude. The resulting spectra for the wavelengths of 1.4 and 5.1 μm at 6 mK are shown in Fig. 11.13(a) and (b), respectively. Due to the strong rf micromotion, the middle peak in Fig. 11.13(a) is covered by the sidebands. The overall linewidth is larger than the reported value (40 MHz) in Ref. [137]. In fact, in the simulations we can see that the second order and even third order sidebands make a significant contribution to the linewidth broadening. This was not evidently shown in the experiment. Thus, we can say that 300 nm peak-to-peak rf motion is an overestimated value. The rf motion along the trap axial direction is probably weaker.

The Gaussian fit for each peak in Fig. 11.13(b) shows that the linewidth is about 1.96 MHz. For a temperature of the ion ensemble of 48 mK, the spectra are shown in Fig. 11.13(c) and (d). The discrete peak structure shown in Fig. 11.13(a) is washed out in Fig. 11.13(c) and the peaks in Fig. 11.13(d) become broader (the Gaussian fits give the linewidth about 5.3 MHz).

11.5 Conclusion of the simulations of the spectroscopy

In this section the Doppler broadening of an HD^+ vibrational spectrum at transition wavelengths of 1.4 and 5.1 μm are investigated via MD simulations and the results were compared with calculated values. They are consistent. Simulations at different temperatures along axial and radial directions were also performed. At low temperatures, HD^+ ions are confined in the Lamb-Dicke regime, thus, sidebands in the spectra were observed. In the Lamb-Dicke regime first order Doppler effects can be reduced significantly leading

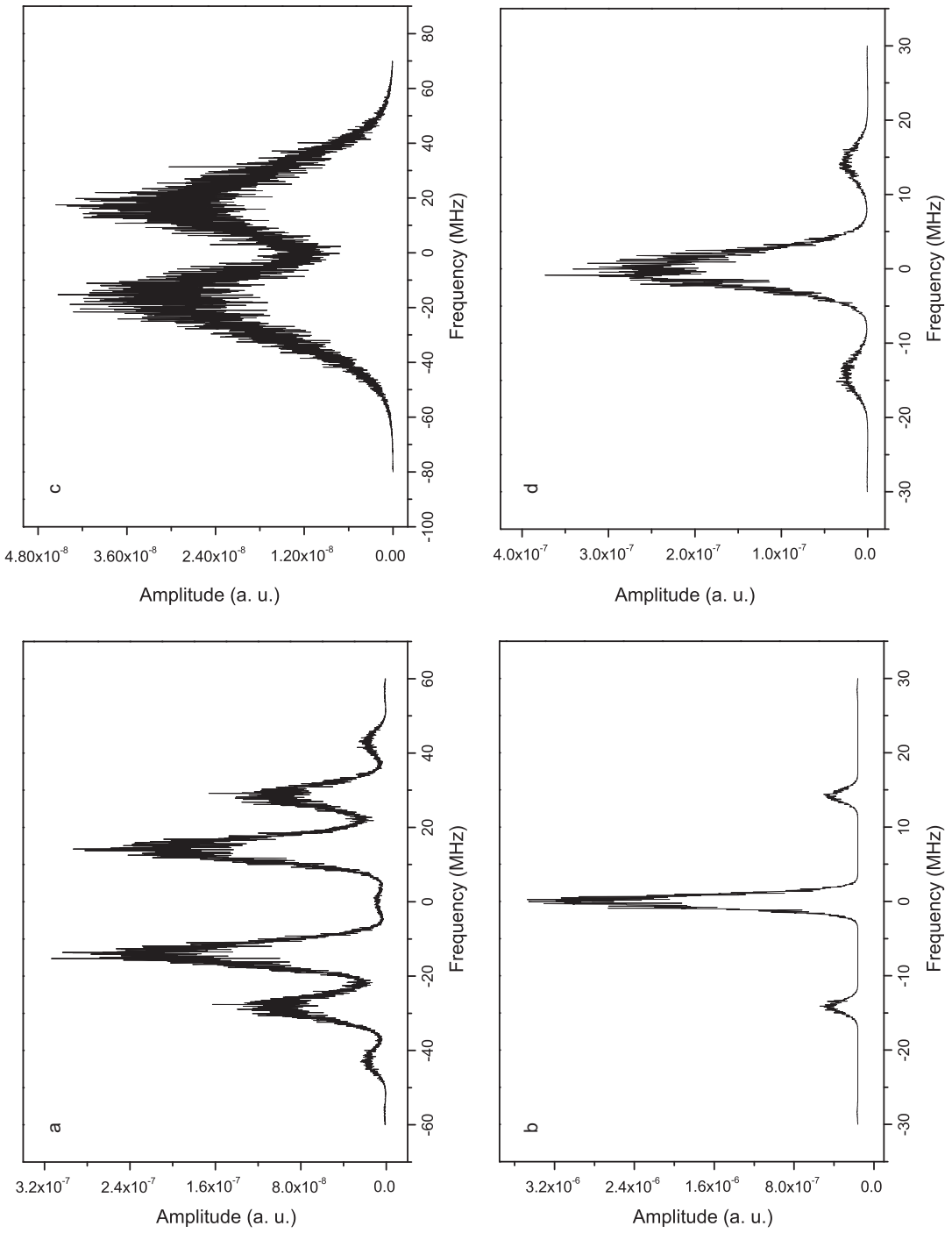

Figure 11.13: Simulated Doppler broadening of an HD^+ ion ensemble in the axial direction at 6 and 48 mK with an additional axial rf field. (a) Spectrum at the wavelength of 1.4 μm and the temperature of 6 mK. (b) Spectrum at the wavelength of 5.1 μm and the temperature of 6 mK. The Gaussian fit for each peak shows that the Doppler broadening is 1.96 MHz. (c) Spectrum at the wavelength of 1.4 μm at 48 mK. The discrete sideband structure is washed out. (d) Spectrum at the wavelength of 5.1 μm at 48 mK. The Gaussian fit for each peak shows that the Doppler broadening is about 5.3 MHz.

to high precision spectroscopies. A case with an rf voltage along the trap direction was studied as well. Due to the strong rf amplitude, with the transition wavelength of 1.4 μm the higher order sidebands are very obvious at 6 mK and make a significant contribution to the broadening of the spectrum at a higher temperature (48 mK). Thus, lowering the temperatures of ion ensembles and reducing the magnitude of the rf micromotion are very helpful for obtaining high resolution spectroscopies.

12 Summary

This thesis presents the work on the production and sympathetic cooling of complex molecular ions.

In this work a universal cooling method - sympathetic cooling, was used to cool molecular ions. In order to cool a variety of molecular ions more efficiently, the laser-cooled atomic ions needs to be well chosen. Thus, laser-cooled beryllium ions (mass 9 amu) are used to cool low mass molecular ions (masses from 1 to 200 amu) and barium ions to cool heavy molecular ions (masses from 32 to more than 20000 amu). Experimentally, this work only focused on the barium case. An important part of this work is the partial development of the experimental setup, which was described in Chapter 4. The preparation of pure, cold, and different-sized laser-cooled $^{138}Ba^+$ ion ensembles was described in Chapter 5. Their properties such as secular frequencies, ion spatial distribution and lifetime, together with the effects of laser detunings and trap parameters were discussed as well.

In Chapter 6 chemical reactions of the Ba^+ ions with different neutral gases such as He, N_2, H_2, O_2, CO_2 and N_2O, at room temperature were investigated. We found that H_2, O_2, CO_2 and N_2O molecules can react with $^{138}Ba^+$ ions. Chemical reaction are not observed when leaking in O_2 or CO_2 gas without the 650 nm laser or without both cooling lasers. Thus, chemical reactions of the $^{138}Ba^+$ ions with O_2 and CO_2 molecules are photo-chemical reactions and only occur when the $^{138}Ba^+$ ions are excited to the $^2P_{1/2}$ state. Since the reaction cross section with H_2 is small, the main products of the chemical reactions of the $^{138}Ba^+$ ions with residual background gas of the main vacuum chamber are $^{138}BaO^+$ ions.

If chemical reactions occur at a very low temperature of the Ba^+ ions (the initial Ba^+ ion ensemble is crystallized), the products of the chemical reactions remain cold even for a large ratio of the numbers of sympathetically cooled (produced) molecular ions and laser-cooled $^{138}Ba^+$ ions. For example, a cold barium ion ensemble containing 450 $^{138}Ba^+$ ions and 120 isotopes at approximately 7 mK was prepared in the trap. After leaking in CO_2 gas for more than one hour, only about 20 $^{138}Ba^+$ ions were left as coolants and 430 $^{138}Ba^+$ ions were converted to sympathetically cooled $^{138}BaO^+$ ions. In this case, only 3.5% of the ions are laser-cooled, 96.5% are sympathetically cooled, but all the ions are still quite cold (the CCD image of the $^{138}Ba^+$ ion ensemble showed that the temperature was at about 25 mK).

The back-reaction with CO was also studied in Chapter 6. The back-reaction of $^{138}Ba^+$ ions from $^{138}BaO^+$ ions was observed via the change of the size of the $^{138}Ba^+$ ion ensemble and the increase of the fluorescence intensity at 493 nm.

In Chapter 7 and 8 sympathetic cooling of medium size organic molecular ions (Alexa

Fluor 350 and GA^+ ions) and mass 12300 amu molecular ions (17 and 12 fold charged protein molecular ions - cytochrome c, cyt). Via MD simulations, we determined an upper limit for the temperatures of the molecular ion ensembles, which are 138, 72, and 570 mK, respectively. This proves that sympathetic cooling is a reliable technique to cool complex molecular ions to the sub-Kelvin regime. The transfer of the molecular ions to the gas phase and the loading of the ions to the ion trap is described in these chapters as well. We also made a step towards photodissociation spectroscopy of the GA^+ molecular ions.

In Chapter 9 our MD simulation models were introduced. A MD simulation program was developed. With this program, CCD images can be simulated, which offers a way to determine the ion numbers and temperatures of different ion species. Ion dynamics, such as micromotion and ion diffusion, were also studied via MD simulations.

Due to space charge effects the secular radial frequency of an ion ensemble shifts, especially, in multi-species ion ensembles. Thus, in Chapter 10, the changes of the secular frequencies of the ion ensembles in a 2-species ion system were analyzed. Two different models were developed, separately, to simulate the secular frequencies. Each one has its own advantages and disadvantages.

In Chapter 11 the feasibility of nondestructive detection via optical dipole excitation was studied using the MD simulations. Molecular ions can be resonantly excited by a laser beam at the wavelength far-detuned from one of their ro-vibrational transitions. Although a single HD^+ ion could be excited by intensity modulation of a focused laser beam at the wavelength of 2.65 μm, an HD^+ ion ensemble containing many ions (200 HD^+ ions and 600 $^9Be^+$ ions) was no longer excited efficiently, due to strong Coulomb interactions. Thus, excitation via a running standing wave, which can offer a larger optical dipole force, was studied. The optical excitations of an ion ensemble via the intensity modulation of both and frequency detuning of one individual beam were simulated. In both cases, the ion ensemble can be excited well, for example, in the conditions of 1 V endcap voltage and 1 W laser power, a heating rate of approximately $k_B(177\ \mathrm{K/s})$ was achieved when the HD^+ ion ensemble was excited via the frequency detuning of one individual beam by $100\,\omega_z$. The simulations with different parameters such as the endcap voltage and the excitation laser wavelength were also performed. The increase of the endcap voltage from 1 to 3 V did not improve the excitation efficiency evidently, while the increase of the wavelength of the excitation laser reduced the heating rate (in the simulations the according increase of the dipole matrix element was not considered).

The lineshapes of ro-vibrational transitions in HD^+ molecular ions at the transition wavelengths of 1.4 and 5.1 μm were also studied via MD simulations. The results were compared with calculated values and were found to be consistent with them. Simulations at different temperatures along axial and radial directions were also performed. At 1.75 and 6.8 mK in the axial and radial directions HD^+ ions were already in the Lamb-Dicke regime, respectively, thus, sidebands in the spectra were observed for wavelength < 5.1 μm. In this regime, high precision spectroscopy appears possible. A case with an rf voltage (arising from the movement of the $^9Be^+$ ions with a 300 nm peak-to-peak amplitude) along the trap direction was performed and compared to measured results in

an experiment showing that the rf peak-to-peak amplitude in the experiment should be less than 30 nm. Simulations also told us that high rf micromotion worsens the resolution of spectroscopies.

Bibliography

[1] A. L. Migdall, J. V. Prodan, W. D. Phillips, T. H. Bergeman, and H. J. Metcalf. First observation of magnetically trapped neutral atoms. *Phys. Rev. Lett.*, 54:2596–2599, 1985.

[2] R. N. Watts P. D. Lett, C. I. Westbrook, D. Phillips, P. L. Gould, and H. J. Metcalf. Observation of atoms laser cooled below the Doppler limit. *Phys. Rev. Lett.*, 61:169–172, 1988.

[3] M. H. Anderson, J. R. Ensher, M. R. Matthews, C. E. Wieman, and E. A. Cornell. Observation of Bose-Einstein condensation in a dilute atomic vapor. *Science*, 269(5221):198–201, 1995.

[4] S. Schiller and V. Korobov. Tests of time independence of the electron and nuclear masses with ultracold molecules. *Phys. Rev. A*, 71:032505, 2005.

[5] M. D. Di Rosa. Laser-cooling molecules. *Eur. Phys. J. D*, 31(15):395–402, 2004.

[6] C. A. Regal, C. Ticknor, J. L. Bohn, and D. S. Jin. Creation of ultracold molecules from a Fermi gas of atoms. *Nature*, 424:47, 2003.

[7] C. A. Regal, M. Greiner, and D. S. Jin. Observation of resonance condensation of fermionic atom pairs. *Phys. Rev. Lett.*, 92:040403, 2004.

[8] S. Dürr, T. Volz, A. Marte, and G. Rempe. Observation of molecules produced from a Bose-Einstein condensate. *Phys. Rev. Lett.*, 92:020406, 2004.

[9] A. Fioretti, D. Comparat, A. Crubellier, O. Dulieu, F. Masnou-Seeuws, and P. Pillet. Formation of cold Cs_2 molecules through photoassociation. *Phys. Rev. Lett.*, 80(20):4402–4405, 1998.

[10] J. C. Pearson, L. C. Oesterling, Eric Herbst, and F. C. De Lucia. Pressure broadening of gas phase molecular ions at very low temperature. *Phys. Rev. Lett.*, 75:2940–2943, 1995.

[11] S. E. Barlow, G. H. Dunn, and M. Schauer. Radiative association of CH_3^+ and H_2 at 13 k. *Phys. Rev. Lett.*, 52:902–905, 1984.

[12] D. M. Egorov. *Buffer-gas cooling of diatomic molecules*. PhD thesis, Harvard University, 2004.

[13] S. A. Rangwala, T. Junglen, T. Rieger, P. W. H. Pinkse, and G. Rempe. Continuous source of translationally cold dipolar molecules. *Phys. Rev. A*, 67(4):043406, 2003.

[14] J. D. Weinstein, R. deCarvalho, T. Guillet, B. Friedrich, and J. M. Doyle. Magnetic trapping of calcium monohydride molecules at millikelvin temperatures. *Nature*, 395:148–150, 1998.

[15] H. L. Bethlem, G. Berden, and G. Meijer. Decelerating neutral dipolar molecules. *Phys. Rev. Lett.*, 83(8):1558–1561, 1999.

[16] H. L. Bethlem, A. J. A. van Roij, R. T. Jongma, and G. Meijer. Alternate gradient focusing and deceleration of a molecular beam. *Phys. Rev. Lett.*, 88:133003, 2002.

[17] D. J. Larson, J. C. Bergquist, J. J. Bollinger, W. M. Itano, and D. J. Wineland. Sympathetic cooling of trapped ions: a laser-cooled two-species nonneutral ion plasma. *Phys. Rev. Lett.*, 57(1):70–73, 1986.

[18] R. E. Drullinger, D. J. Wineland, and J. C. Bergquist. High-resolution optical spectra of laser cooled ions. *Appl. Phys.*, 22:365–368, 1980.

[19] R. Folman, P. Kruger, D. Cassettari, B. Hessmo, T. Maier, and J. Schmiedmayer. Controlling cold atoms using nanofabricated surfaces: atom chips. *Phys. Rev. Lett.*, 84(20):4749–4752, 2000.

[20] E. A. Hinds and I. G. Hughes. Magnetic atom optics: Mirrors, guides, traps, and chips for atoms. *Journal of Physics D:*, 32(18):R119, 1999.

[21] J. Doyle, B. Friedrich, R.V. Krems, and F. Masnou-Seeuws. Editorial: Quo vadis, cold molecules? *The European Physical Journal D*, 31(2):149–164, 2004.

[22] P. K. Ghosh. *Ion Traps*. Clarendon, Oxford, 1995.

[23] H. Dehmelt. Radiofrequency spectroscopy of stored ions. I: Storage. *Adv. At. Mol. Phys.*, 5:53–72, 1967.

[24] H. Dehmelt. Radiofrequency spectroscopy of stored ions. II: spectroscopy. *Adv. At. Mol. Phys.*, 5:109–154, 1969.

[25] E. Fischer. Die dreidimensionale Stabilisierung von Ladungsträgern in einem Vierpolfeld. *Z. Phys.*, 156(1):1–26, 1959.

[26] J. E. P., Syka, and W. J. Jr. Fies. Fourier transform quadrupole mass spectrometer and method, 1988. United States Patent US 4755670.

[27] J. D. Prestage, G. J. Dick, and L. Maleki. New ion trap for frequency standard applications. *J. Appl. Phys.*, 66(3):1013–1017, 1989.

[28] B. E. King. *Quantum state engineering and information processing with trapped ions*. PhD thesis, University of Colorado, 1999.

[29] Kristian Møhave. Construction of and experiments with a linear Paul trap. Master's thesis, University of Aarhus, March 2000.

[30] S. R. Jefferts, C. Monroe, E. W. Bell, and D. J. Wineland. A coaxial-resonator-driven rf (Paul) trap for strong confinement. *Phys. Rev. A*, 51:3112–3116, 1995.

[31] P. H. Dawson. *Quadrupole mass spectrometry and its application*. Elsevier, Amsterdam, 1976.

[32] R. E. March and R. J. Hughes. *Quadrupole storage mass spectrometry.* Wiley Interscience Publications, New York, 1989.

[33] M. G. Raizens, J. M. Gilligan, J. C. Bergquist, W. M. Itano, and D. J. Wineland. Linear trap for high-accuracy spectroscopy of stored ions. *J. Mod. Opt.*, 39(2):233–242, 1992.

[34] D. R. Denison. Operating parameters of a quadrupole in a grounded cylindrical housing. *J. Vac. Sci. Technol.*, 8:266–269, 1971.

[35] H. Schnitzler. *Development of an experiment for trapping, cooling, and spectroscopy of molecular hydrogen ions.* PhD thesis, Universität Konstanz, 2001.

[36] M. Drewsen and A. Brøner. Harmonic linear Paul trap: Stability diagram and effective potentials. *Phys. Rev. A*, 62(4):045401, 2000.

[37] R. E. March. An introduction to quadrupole ion trap mass spectrometry. *J. Chem. Phys.*, 32:351–369, 1997.

[38] M. D. Barrett, B. Demarco, T. Schaetz, D. Leibfried, J. Britton, J. Chiaverini, W. M. Itano, B. Jelenković, J. D. Jost, C. Langer, T. Rosenband, and D. J. Wineland. Sympathetic cooling of $^{9}Be^{+}$ and $^{24}Mg^{+}$ for quantum logic. *Phys. Rev. A*, 68(4):042302, 2003.

[39] R. Alheit, K. Enders, and G. Werth. Isotope separation by nonlinear resonances in a Paul trap. *Appl. Phys. B: Lasers and Optics*, 62:511–513, 1996.

[40] R. Blümel, C. Kappler, W. Quint, and H. Walther. Chaos and order of laser-cooled ions in a Paul trap. *Phys. Rev. A*, 40(2):808–823, 1989.

[41] J. D. Prestage, A. Williams, L. Maleki, M. J. Djomehri, and E. Harabetian. Dynamics of charged particles in a Paul radio-frequency quadrupole trap. *Phys. Rev. Lett.*, 66(23):2964–2967, 1991.

[42] H. Walther. volume 31 of *Advances in Atomic, Molecular and Optical Physics*, pages 137–182. Academic Press, Inc., New York, 1993.

[43] J. Hoffnagle and R. G. Brewer. Two-ion chaos. *Physica Scripta*, T59:380–386, 1995.

[44] D. J. Berkeland, J. D. Miller, J. C. Bergquist, W. M. Itano, and D. J. Wineland. Minimization of ion micromotion in a Paul trap. *J. Appl. Phys.*, 83(10):5025–5033, 1998.

[45] C. B. Zhang, D. Offenberg, B. Roth, M. A. Wilson, and S. Schiller. Molecular-dynamics simulations of cold single-species and multispecies ion ensembles. *Phys. Rev. A*, 76:012719, 2007.

[46] L. E. Sadler, J. M. Higbie, S. R. Leslie, M. Vengalattore, and D. M. Stamper-Kurn. Spontaneous symmetry breaking in a quenched ferromagnetic spinor Bose-Einstein condensate. *Nature*, 443:312–315, 2006.

[47] M. H. Holzscheiter. Cooling of particles stored in electromagnetic traps. *Physica Scripta*, T22:73–78, 1988.

[48] B. J. André. Étude théorique de l'influence des collisions élastiques sur un gaz dilué de particules chargées, confinées par un champ de radio-fréquence à symétrie quadrupolaire. *J. Phys.*, 37(6):719, 1976.

[49] D. J. Wineland and H. Dehmelt. Proposed 10^{14} $\delta\nu < \nu$ laser fluorescence spectroscopy on Tl^+ mono-ion oscillator III (sideband cooling). *Bull. Am. Phys. Soc.*, 20:637, 1975.

[50] T. W. Hänsch and A. L. Schawlow. Cooling of gases by laser radiation. *Opt. Commun.*, 13:68–69, 1975.

[51] R. H. Dicke. The effect of collisions upon the Doppler width of spectral lines. *Phys, Rev.*, 89(2):472–473, 1953.

[52] R. Loudon. *The Quantum Theory of Light*. Oxford University Press., New York, 1983.

[53] S. Kryszewski. Quantum optics. Lecture notes in Unveristy of Gdańsk, 2004.

[54] H. J. Metcalf and P. van der Straten. *Laser Cooling and Trapping*. Springer-Verlag, New York, 1999.

[55] G. Audi, O. Bersillon, J. Blachot, and A. H. Wapstra. The nubase evaluation of nuclear and decay properties. *Nucl. Phys. A*, 729(1):3–128, 2003.

[56] A. H. Wapstra, G. Audi, and C. Thibault. Ame2003 atomic mass evaluation - I. *Nucl. Phys. A*, 729(1):129–336, 2003.

[57] G. Audi, A. H. Wapstra, and C. Thibault. Ame2003 atomic mass evaluation - II. *Nucl. Phys. A*, 729(1):337–676, 2003.

[58] O. H. Arroe. Hyperfine structure and isotope shift in barium. *Phys. Rev.*, 79(5):836–838, 1950.

[59] D. F. V. James. Quantum dynamics of cold trapped ions with application to quantum computation. *Appl. Phys. B*, 66:181–190, 1998.

[60] A. Gallagher. Oscillator strengths of Ca II, Sr II, and Ba II. *Phys. Rev.*, 157(1):24–30, 1967.

[61] A. Ostendorf. *Sympathetische* K*ühlung von* M*olekülionen durch lasergekühlte* B*ariumionen in einer linearen* P*aulfalle*. PhD thesis, Heinrich-Heine-Universität Düseldorf, 2004.

[62] L. A. Lugiato. *Theory of Optical Bistability*, volume XXI of *Progress in Optics*. North-Holland, Amsterdam, 1984.

[63] D. Reiß, A. Lindner, and R. Blatt. Cooling of trapped multilevel ions: A numerical analysis. *Phys. Rev. A*, 54:5133–5140, 1996.

[64] Y. Stalgies, I. Siemers, B. Appasamy, T. Altevogt, and P. E. Toschek. The spectrum of single-atom resonance fluorescence. *Europhys. Lett.*, 35(4):259–264, 1996.

[65] H. Oberst. Resonance fluorescence of single barium ions. Master's thesis, Leopold-Franzens-Universität Innsbruck, 1999.

[66] P. Banks. Collision frequencies and energy transfer: electrons. *Planet. Space Sci.*, 14:1105–1122, 1966.

[67] F. Herfurth, J. Dilling, A. Kellerbauer, G. Bollen, S. Henry, H.-J. Kluge, E. Lamour, D. Lunney, R. B. Moore, C. Scheidenberger, S. Schwarz, G. Sikler, and J. Szerypo. A linear radiofrequency ion trap for accumulation, bunching, and emittance improvement of radioactive ion beams. *Nucl. Instrum. Meth. A*, 469:254–275, 2001.

[68] J. J. Bollinger, D. J. Heinzen, S. L. Gilbert W. M. Itano, and D. J. Wineland. Progress at NIST toward absolute frequency standards using storedions. *IEEE Trans. Instrum. Meas.*, 40:126–128, 1991.

[69] J. J. Bollinger, D. J. Heinzen, M. W. Itano, S. L. Gilbert, and D. J. Wineland. Test of the linearity of quantum mechanics by rf spectroscopy of the $^9Be^+$ ground state. *Phys. Rev. Lett.*, 63(10):1031–1034, 1989.

[70] H. Imajo, K. Hayasaka, R. Ohmukai, U. Tanaka, M. Watanabe, and S. Urabe. High-resolution ultraviolet spectra of sympathetically-laser-cooled Cd^+ ions. *Phys. Rev. A*, 53(1):122–125, 1996.

[71] I. Waki, S. Kassner, G. Birkl, and H. Walther. Observation of ordered structures of laser-cooled ions in a quadrupole storage ring. *Phys. Rev. Lett.*, 68(13):2007–2010, 1992.

[72] T. Baba and I. Waki. Cooling and mass-analysis of molecules using laser-cooled atoms. *Japn. J. Appl. Phys.*, 35(9A):1134–1137, 1996.

[73] K. Mølhave and M. Drewsen. Formation of translationally cold MgH^+ and MgD^+ molecules in an ion trap. *Phys. Rev. A*, 62(1):011401, 2000.

[74] L. Hornekær. *Single- and multi-species Coulomb ion crystals: structures, dynamics and sympathetic cooling*. PhD thesis, University of Aarhus, 2000.

[75] T. Baba and I. Waki. Laser-cooled fluorescence mass spectrometry using laser-cooled barium ions in a tandem linear ion trap. *J. Appl. Phys.*, 89(8):4592–4598, 2001.

[76] D. J. Wineland, C. Monroe, W. M. Itano, D. Leibfried, B. E. King, and D. M. Meekhof. Experimental issues in coherent quantum-state manipulation of trapped atomic ions. *J. Res. Natl. Inst. Stand. Technol.*, 103(3):259–328, 1998.

[77] V. L. Ryjkov, X. Z. Zhao, and H. A. Schuessler. Sympathetic cooling of fullerene ions by laser-cooled Mg^+ ions in a linear rf trap. *Phys. Rev. A*, 74:023401, 2006.

[78] B. Roth. Production, manipulation and spectroscopy of cold trapped molecular ions. Habilitation thesis, Univ. Düsseldorf. January 2007.

[79] T. Baba and I. Waki. Sympathetic cooling rate of gas-phase ions in a radio-frequency-quadrupole ion trap. *Appl. Phys. B*, 74:375–382, 2002.

[80] B. Roth, U. Fröhlich, and S. Schiller. Sympathetic cooling of $^4He^+$ ions in a radio-frequency trap. *Phys. Rev, Lett.*, 94:053001, 2005.

[81] B. Roth, J. C. J. Koelemeij, H. Daerr, and S. Schiller. Rovibrational spectroscopy of trapped molecular hydrogen ions at millikelvin temperatures. *Phys. Rev. A*, 74:040501, 2006.

[82] S. Gulde, D. Rotter, P. Barton, F. Schmidt-Kaler, R. Blatt, and W. Hogervorst. Simple and efficient photo-ionization loading of ions for precision ion-trapping experiments. *Appl. Phys. B: Lasers and Optics*, 73:861–863, 2001.

[83] A. Benninghoven, F. G. Rüdenauer, and H. W. Werner. *Secondary Ion Mass Spectrometry: Basic Concepts, Instrumental Aspects, Applications, and Trends*. Wiley, 1987.

[84] H. D. Beckey. *Field ionization mass spectrometry*, volume 42 of *Monographs in Analytical Chemistry*. Pergamon Press, Oxford, 1971.

[85] Torgerson D. F, R. P. Skowronski, and R. D. Macfarlane. New approach to the mass spectroscopy of non-volatile compounds. *Biochem. Biophys. Res. Commun.*, 60:616–621, 1974.

[86] Torgerson D. F and R. D. Macfarlane. Californium-252 plasma desorption mass spectroscopy. *Science*, 191:920–925, 1976.

[87] M. Karas and F. Hillenkamp. Laser desorption ionization of proteins with molecular masses exceeding 10,000 daltons. *Anal. Chem.*, 60(20):2299–2301, 1988.

[88] S. Nguyen and J. B. Fenn. Inaugural article: gas-phase ions of solute species from charged droplets of solutions. *Proceedings of the National Academy of Sciences*, 104(4):1111–1117, 2007.

[89] J. B. Fenn, M. Mann, C. K. Meng, S. F. Wong, and C. M. Whitehouse. Electrospray ionization for mass spectrometry of large biomolecules. *Science*, 246:64–71, 1989.

[90] D. Gerlich. *Inhomogeneous* RF *fields: a versatile tool for the study of processes with slow ions*, volume 82 of *Advances in Chemical Physics*. John Wiley & Sons, Inc, 1992.

[91] R. V. Pound. Electronic frequency stabilization of microwave oscillators. *Rev. Sci. Instrum.*, 17(11):490–505, 1946.

[92] R. W. P. Drever, J. L. Hall, F. V. Kowalski, J. Hough, G. M. Ford, A. J. Munley, and H. Ward. Laser phase and frequency stabilization using an optical resonator. *Appl. Phys. B*, 31:97–105, 1983.

[93] E. D. Black. An introduction to Pound-Drever-Hall laser frequency stabilization. *Am. J. Phys.*, 69(1):79–87, 2001.

[94] V. L. Ryjkov. *Laser cooling and sympathetic cooling in a linear quadrupole rf trap.* PhD thesis, Texas A&M University, 2003.

[95] J. Vasut, T. Hyde, and L. Barge. Finite Coulomb crystal formation. In *34th COSPAR Scientific Assembly*, volume 34 of *COSPAR, Plenary Meeting*, 2002.

[96] D. H. E. Dubin. Minimum energy state of the one-dimensional Coulomb chain. *Phys. Rev. E*, 55(4):4017–4028, 1997.

[97] J. P. Schiffer. Melting of crystalline confined plasmas. *Phys. Rev. Lett.*, 88(20):205003, 2002.

[98] Edmond Murad. The reactions of ba^+ ions with o_2 and h_2o. *J. Chem. Phys*, 77:2057–2060, 1982.

[99] K. G. Spears and F. C. Fehsenfeld. Termolecular association reactions of mg, ca, and ba ions. *J. Chem. Phys. 56*, 56:5698–5705, 1972.

[100] B. Roth, A. Ostendorf, H. Wenz, and S. Schiller. Production of large molecular ion crystals via sympathetic cooling by laser-cooled Ba^+. *J. Phys. B: At. Mol. Opt. Phys.*, 38:3673–3685, 2005.

[101] H. Du, R. A. Fuh, J. Li, A. Corkan, and J. S. Lindsey. Photochemcad: A computer-aided design and research tool in photochemistry. *Photochemistry and Photobiology*, 68:141–142, 1988.

[102] T. Baba and I. Waki. Spectral shape of in situ mass spectra of sympathetically cooled molecular ions. *J. Appl. Phys.*, 92(7):4109–4116, 2002.

[103] O. Y. Zheng, Z. Takáts, T. A. Blake, B. Gologan, A. J. Guymon, J. M. Wiseman, J. C. Oliver, V. J. Davisson, and R. G. Cooks. Preparing protein microarrays by soft-landing of mass-selected ions. *Science*, 301:1351–1354, 2003.

[104] http://upload.wikimedia.org/wikipedia/commons/0/07/Cytochrome_c.png.

[105] J. M. Haile. *Molecular dynamics: elementary methods.* John Wiley and Sons, New York, 1997.

[106] M. P. Allen and D. J. Tildesley. *Computer simulation of liquids.* Oxford, 1987.

[107] G. Ciccotti, D. Frenkel, and I. R. McDonald. *Simulation of liquids and solids.* Elsevier Science Pub. Co., 1987.

[108] B. J. Alder and T.E. Wainwright. Phase transition for a hard sphere system. *J. Chem. Phys.*, 27:1208–1209, 1957.

[109] B. J. Alder and T. E. Wainwright. Studies in molecular dynamics. I. General method. *J. Chem. Phys.*, 31(2):459–466, 1959.

[110] A. Rahman and F. H. Stillinger. Molecular dynamics study of liquid water. *J. Chem. Phys.*, 55:3336–3359, 1971.

[111] M. P. Allen. Introduction to molecular dynamics simulation. *Computational Soft Matter: From Synthetic Polymers to Proteins,*, 23:1–28, 2004.

[112] R. W. Hockney. The potential calculation and some applications. *Methods Comput. Phys.*, 9:136–211, 1970.

[113] D. Potter. *Computational physics, Chapter 5.* John Wiley and Sons, New York, 1972.

[114] R. P. Feynman. *The Feynman Lectures on Physics*, volume Vol. 1, Sec. 9-6. 1970.

[115] M. W. Kutta. Beitrag zur näherungsweisen Integration totaler Differentialgleichungen. *Z. Math. Phys*, 46:435–453, 1901.

[116] J. H. E. Cartwright and O. Piro. The dynamics of Runge-Kutta methods. *Int. J. Bifurcation and Chaos*, 2(3):427–449, 1992.

[117] P. Young. Leapfrog method and other "symplectic" algorithms for integrating Newton's laws of motion, Lecture notes in University of california, santa cruz.

[118] D. H. E. Dubin and T. M. O'Neil. Computer simulation of ion clouds in a penning trap. *Phys.Rev. Lett.*, 60:511–514, 1988.

[119] A. Rahman and J. P. Schiffer. Structure of a one-component plasma in an external field: a molecular-dynamics study of particle arrangement in a heavy-ion storage ring. *Phys. Rev. Lett.*, 57(9):1133–1136, 1986.

[120] R. Rafac, J. P. Schiffer, J. S. Hangst, D. H. E. Dubin, and D. J. Wales. Stable configurations of confined cold ionic systems. *Proc. Natl. Acad. Sci. USA*, 88(8):483–486, 1991.

[121] B. Roth U. Fröhlich and S. Schiller. Ellipsoidal Coulomb crystals in a linear radio-frequency trap. *Physics of Plasmas*, 12:073506, 2005.

[122] D. J. Wineland, C. Monroe, W. M. Itano, D. Kielpinski, B. E. King, C. J. Myatt, Q. A. Turchette, and C. S. Wood. Quantum computation, spectroscopy of trapped ions, and Schrödinger's cat, 1998.

[123] D. Kielpinski, B. E. King, C. J. Myatt, C. A. Sackett, Q. A. Turchette, W. M. Itano, C. Monroe, and D. J. Wineland. Sympathetic cooling of trapped ions for quantum logic. *Phys. Rev. A*, 61:032310, 2000.

[124] M. Bussmann, U. Schramm, D. Habs, V. S. Kolhinen, and J. Szerypo. Stopping highly charged ions in a laser-cooled one component plasma of $^{24}Mg^{+}$ ions. *Int. J. Mass Spectrom.*, 251(1):179–189, 2006.

[125] S. Schiller and C. Lämmerzahl. Molecular dynamics simulation of sympathetic crystallization of molecular ions. *Phys. Rev. A*, 68:053406, 2003.

[126] A. Ostendorf, C. B. Zhang, M. A. Wilson, abd B. Roth D. Offenberg, and S. Schiller. Sympathetic cooling of complex molecular ions to millikelvin temperatures. *Phys. Rev. Lett.*, 97:243005, 2006.

[127] Ch. Raab, J. Eschner, J. Bolle, H. Oberst, F. Schmidt-Kaler, and R. Blatt. Motional sidebands and direct measurement of the cooling rate in the resonance fluorescence of a single trapped ion. *Phys. Rev. Lett.*, 85:538–541, 2000.

[128] P. Bushev, A. Wilson, J. Eschner, Ch. Raab, F. Schmidt-Kaler, C. Becher, and R. Blatt. Forces between a single atom and its distant mirror image. *Phys. Rev. Lett.*, 92:223602, 2004.

[129] A. L. Michaud, A. J. Frank, C. Ding, X. Z. Zhao, and D. J. Douglas. Ion excitation in a linear quadrupole ion trap with an added octopole field. *J. Am. Soc. Mass Spectrom.*, 16:835–849, 2005.

[130] M. Sudakov, N. Konenkov, D. J. Douglas, and T. Glebova. Excitation frequencies of ions confined in a quadrupole field with quadrupole excitation. *J. Am. Soc. Mass Spectrom.*, 11:10–18, 2000.

[131] M. A. N. Razvi, X. Z. Chu, R. Alheit, G. Werth, and R. Blümel. Fractional frequency collective parametric resonances of an ion cloud in a Paul trap. *Phys. Rev. A*, 58:R34–R37, 1998.

[132] R. Alheit, X. Z. Chu, M. Hoefer, M. Holzki, and G. Werth. Nonlinear collective oscillations of an ion cloud in a Paul trap. *Phys. Rev. A*, 56(5):4023–4031, 1997.

[133] B. Roth, P. Blythe, and S. Schiller. Motional resonance coupling in cold multispecies Coulomb crystals. *Phys. Rev. A*, 75:023402, 2007.

[134] K. Jungmann, J. Hoffnagle, R. G. Devoe, and R. G. Brewer. Collective oscillations of stored ions. *Phys. Rev. A*, 36:3451–3454, 1987.

[135] J. H. Parksa and A. Szöke. Simulation of collisional relaxation of trapped ion clouds in the presence of space charge fields. *J. Chem. Phys.*, 103(4):1422–1439, 1995.

[136] B. Roth, P. Blythe, H. Daerr, L. Patacchini, and S. Schiller. Production of ultracold diatomic and triatomic molecular ions of spectroscopic and astrophysical interest. *J. Phys. B: At. Mol. Opt. Phys.*, 39:S1241–S1258, 2006.

[137] J. C. J. Koelemeij, B. Roth, A. Wicht, I. Ernsting, and S. Schiller. Vibrational spectroscopy of HD^+ with 2-ppb accuracy. *Phys. Rev. Lett.*, 98:173002, 2007.

[138] A. Ashkin. Acceleration and trapping of particles by radiation pressure. *Phys. Rev. Lett.*, 24:156–159, 1970.

[139] S. Chu, J. E. Bjorkholm, A. Ashkin, and A. Cable. Experimental observation of optically trapped atoms. *Phys. Rev. Lett.*, 57:314–317, 1987.

[140] J. I. Cirac and P. Zoller. Quantum computations with cold trapped ions. *Phys. Rev. Lett.*, 74(20):4091–4094, 1995.

[141] R.Grimm, M. Weidemueller, and Y. B. Ovchinnikov. Optical dipole traps for neutral atoms. *Atomic Physics*, 42:95–170, 2000.

[142] E. A. Colbourn and P. R. Bunker. Accurate theoretical vibration-rotation energies and transition moments for HD^+, HT^+, and DT^+. *J. Mol. Spect.*, 63:155–163, 1976.

[143] W. M. Itano, J.C. Bergquist, and D.J. Wineland. Coulomb clusters of ions in a Paul trap. Workshop on Crystalline Ion Beams, pages 241–249, Wertheim, W. Germany, 1989.

Acknowledgements

In the past couple of years I had an interesting and challenging time in Düsseldof, so I would like to use this opportunity to thank all the people who have helped me to do my thesis work for a Doctor's degree. Without your selfless assistance I could not get so many wonderful experimental and simulation results.

First of all, I would like to thank my supervisor, Prof. Stephan Schiller, for supporting this work and his guidance throughout my research period as a doctoral student. Numerous skills obtained from him will help me to succeed in my future career path.

I would like to gratefully acknowledge Dr. Bernhard Roth for his great efforts on this work. He guided me into this interesting research field and taught me many useful skills. Many good discussions and close cooperations with him were the prerequisites to finish this work. His keen helps kept me away from many diary life problems arising from the communications in German and his good humour brought us boundless happiness.

My special thanks go to David Offenberg for his contribution to this work. I am very happy to have worked with him on this project in the past few years. I would say that our cooperation was very successful. I also thank him for revising this thesis.

I would also like to thank all other former and present members involving in this project: Postdocs Alex Wilson for his excellent experience in the laser cooling of barium ions, good discussions with me about the development of the simulation program, and our friendship. Our electronic technician, Peter Dutkiewicz, for building state-of-the-art electronics and his patience when speaking German to international colleagues like me. Our former doctoral student, Alexander Ostendorf, made the main contribution to building this unique experimental setup.

I would also like to express my appreciation to Christian Eisele, Ulf Bressel, Rainer Gambke, Dr. Sergey Vasilyev, Ingo Ernsting, and all other former and present colleagues of our institute. They created a family atmosphere and made my time in Düssedorf enjoyable.

The DAAD and DFG have my thanks as well for the financial support.

Most importantly, I would like to thank my wife, Fanzhen Meng, who made so many sacrifices and as a physicist gave me many constructive suggestions for this work. I am also greatly indebted to my parents for their constant support and encouragement. Without the strong support from my family, this doctoral study would not have been possible.